Interplay of Electronic Correlations and Topology in the Hubbard Model

Dissertation
zur Erlangung des Doktorgrades
der Naturwissenschaften

vorgelegt beim Fachbereich Physik
der Johann Wolfgang Goethe-Universität
in Frankfurt am Main

von
Dominik Leßnich
geboren in Groß-Gerau

Frankfurt am Main, August 2023
(D 30)

Vom Fachbereich Physik
der Johann Wolfgang Goethe-Universität
als Dissertation angenommen.

Dekan:

Prof. Dr. Roger Erb

Gutachter:

Prof. Dr. Roser Valentí

Prof. Dr. André-Marie Tremblay

Datum der Disputation: 26. Januar 2024

Acknowledgements

I would like to thank professor Roser Valentí for giving me the opportunity to make a PhD in her group and entrusting with my work during my time as a PhD student. I thank professor André-Marie Tremblay for giving me the opportunity to make an internship in his group and to work with him at Université de Sherbrooke two times once for four month and once for two month. I enjoyed this time very much and it impacted me very positively. Thank you also for your supervision during that time and many long and illuminating discussions during my time in Sherbrooke and after that helped me a lot with my research. I thank professor Steve Winter for many insightful discussions and help with my first paper and exact diagonalization, that were crucial for this work. I thank Chloé Gauvin-Ndiaye to whom I owe so much personally and professionally. Professionally, I thank you for explaining me things, help coding, help fixing my code or my thinking when something did not work and proofreading many things I wrote. Personally, I thank you for your compassion, your advice, your calm and direct way of approaching things and making so many things possible that otherwise seem impossible. Thank you for so many things. I thank Olivier Gingras for inviting me to the Flatiron institute in New York City for a three week visit giving me the opportunity to present and discuss my research there. I thank my colleagues in Frankfurt, my colleagues in Sherbrooke and the predocs at the Flatiron institute for many interesting discussions and many fun activities during my time there. I thank all students who visited my tutorials. I thank you for all the active discussions, questions and your motivation to learn new things. I always enjoyed giving these tutorials and also giving these tutorials teached myself so much. I wish you all the best for your future. I also thank Mrs. Metz, Mrs. Karl, Mrs. Lamoureux and Mrs. Moisan for helping me making the exchanges to Sherbrooke possible. Finally, I would like to thank my family and my friends for their support.

Zusammenfassung

Um die Eigenschaften eines Materials zu beschreiben oder vorherzusagen ist es notwendig, die Elektronen in dem Material zu beschreiben. Das Verhalten der Elektronen wird mithilfe von Quantenmechanik beschrieben. Dies geschieht mathematisch durch das Lösen der Schrödingergleichung. Für idealisierte nicht-wechselwirkende Elektronen ist die Lösung der Schrödingergleichung gegeben durch eine Slater-Determinate der Einteilchenzustände. Die Einteilchenzustände ergeben sich aus der Lösung der entsprechenden Einteilchen-Schrödingergleichung. Aufgrund des Bloch-Theorems haben die Einteilchenzustände die Form von Bloch-Funktionen. Die dazugehörigen Einteilchenenergie führen dann zum sogenannten Bändermodell von Festkörpern. In Materialien in denen die Effekte der Elektron-Elektron-Wechselwirkung schwach ist oder in denen die Elektron-Elektron-Wechselwirkung in einer Molekularfeld (englisch mean-field) Näherung behandelt werden kann, können gut mit dem Bändermodell beschrieben werden. Numerisch können solche Materialien daher oft erfolgreich mit Dichtefunktionaltheorie beschrieben werden.

Wenn Wechselwirkungen jedoch stark werden und die Elektronen korreliert werden, dann bricht dieses einfache Bild zusammen. Unter dem Begriff elektronische Korrelation sind all jene Effekte zusammengefasst, die sich nicht mehr mit einer Slater-Determinante aus Einteilchenzuständen beschreiben lassen. Diese Effekte sind numerisch und analytisch schwierig zu beschreiben. Jedoch sind sie für einige interessante physikalische Phänomene in Materialien verantwortlich. Beispiele sind Supraleitung, Magnetismus, Mott-Isolatoren oder der fraktionale Quanten-Hall-Effekt. Viele dieser Zustände sind immer noch nicht gut theoretisch verstanden. Gerade deshalb sind elektronische Korrelation jedoch seit vielen Jahren ein aktives Forschungsfeld.

Um solche Materialien und Zustände zu beschreiben ist es jedoch notwendig mehr als nur die Standard ab inition Methoden, wie die Dichtefunktionaltheorie, zu verwenden. Eine Art korrelierte Materialien zu beschreiben ist das Hubbard-Modell welches 1963 simultan von Hubbard, Kanamori und Gutzweiler eingeführt wurde. Das Hubbard-Modell ist ein Gittermodell, in welchem die Elektronen von Gitterplatz zu Gitterplatz hüpfen können. Zwei Elektronen am selben Gitterplatz wechselwirken mit der sogenannten Hubbard-Wechselwirkung. Die Hubbard-Wechselwirkung ist eine drastische Vereinfachung der in Realität langreichweitigen Coulomb-Wechselwirkung der Elektronen. Physikalisch lässt sich die Näherung, die Wechselwirkung als lokal zu beschreiben, jedoch in manchen Fällen dadurch rechtfertigen, dass die Präsenz anderer Elektronen die Wechselwirkung zweier weit entfernter Elektronen abschirmt.

Das Hubbard-Model mit einem Band auf dem Quadratgitter ist ein viel studiertes Modell. Es wird oft zur Modellierung von Hochtemperatursupraleitern, die auf Kupfer basieren, den sogenannten Cupraten, verwendet. Cuprate haben ein schmales Band an der Fermienergie, welches hauptsächlich den Charakter eines Kupfer d-Orbitals und eines Sauerstoff p-Orbitals besitzt. Gerade wegen der elektronischen Korrelation besitzen Cuprate ein Phasendiagramm mit vielen verschieden Phases. Durch veränderung der Temperatur oder Dotierung lassen sich supraleitende Phasen, ein Antiferromagnet, ein Metall, das sich durch eine Fermi-Flüssigkeit beschreiben lässt oder es lässt sich eine Pseudobandlücke realisieren. Das Hubbard-Modell wurde auch auf anderen Gittern wie die Kagome-Gitter, dem hexagonale Gitter oder dem Dreiecksgitter studiert. Das Hubbard-Modell auf dem Dreiecksgitter spielt eine zentrale Rolle in der Modellierung von organischen Supraleitern und das hexagonale Gitter hat Ähnlichkeiten mit Graphen.

Trotz seiner Einfachheit ist das Hubbard-Modell in der Praxis schwierig zu lösen. Exakte Lösungen sind nur für wenige Grenzfälle, wie in einer Dimension, in unendlich vielen Dimensionen oder für kleine Systemgrößen, in welchen sich das Hubbard-Modell mit exakter Diagonalisierung lösen lässt, bekannt.

Um trotzdem approximative Lösungen für das Hubbard-Modell zu finden, wurden mit der Zeit einige Methoden entwickelt um Näherungslösungen zu erhalten. Ein Beispiel für eine solche Methode ist die Zweiteilchen Selbstkonsistenz Methode (englisch Two-Particle Self-Consistent approach, TPSC). Jede dieser Methoden hat ihre eigenen Stärken, Schwächen und numerischen Rechenaufwand.

Ein relativ junges Teilgebiet der Festkörperphysik ist das Teilgebiet der Topologie, welches sich mit der topologischen Klassifikation von Phasen und Materialien beschäftigt. Topologie ist ursprünglich ein Teilgebiet der Mathematik, das sich unter anderen mit invarianten Eigenschaften von Objekten unter stetigen Verformungen beschäftigt. Seit den 1980er Jahren hat Topologie jedoch viele Anwendungen in der Festkörperphysik gefunden. Im Jahr 2016 wurde Nobelpreis für Physik an Kosterlitz, Thouless und Haldane verliehen „für theoretische Entdeckungen topologischer Phasenübergänge und topologischer Materiephasen“.

In dem idealisierten Bild der wechselwirkungsfreien Elektronen können Bandstrukturen mithilfe der Theorie der Bandtopologie klassifiziert werden. Die Idee ist, die Bloch-Funktionen selbst als eine Funktion der Wellenzahl aufzufassen, welche Werte in der ersten Brillouin-Zone annimmt. Mathematisch betrachtet ist die erste Brillouin-Zone nichts anderes als ein in d-Torus. Die Aufgabe besteht nun darin, die Abbildung vom d-Torus auf die Bloch-Funktionen topologisch zu klassifizieren. Die entsprechende mathematische Struktur wird Faserbündel genannt.

In der Festkörperphysik sind topologische Invarianten für topologische Isolatoren Größen die invariant unter stetigen Deformierungen des Hamiltonian sind während die Bandlücke geöffnet bleibt. Mathematisch betrachtet ist eine solche stetige Deformation eine Homotopie. Die Chernzahl ist das bekannteste Beispiel einer solchen topologischen Invarianten. Die Chernzahl ist direkt proportional zu der Hall-Leitfähigkeit beim Quanten-Hall-Effekt bei welchem die Hall-Leitfähigkeit immer ein ganzzahliges vielfaches von $\frac{e^2}{h}$. Damit ist der Wert der Hall Leitfähigkeit allein durch Naturkonstanten und die Chernzahl bestimmt. Andere Beispiele, in denen physikalische Observablen direkt mit einer topologischen Klassifizierung der Bänder zusammenhängen, sind elektrische Polarisation und der Quanten-Spin-Hall-Effekt.

Ein physikalischer Effekt, der oft die Ursache dafür ist, dass ein Material topologisch nichttrivial ist, das bedeutet eine nichttriviale topologische Invariante besitzt ist, ist die Spin-Bahn-Kopplung. Die Spin-Bahn-Kopplung ist ein relativistischer Effekt, der in einem vereinfachten Bild daher kommt, dass im Ruhesystem eines Elektrons es so aussieht, als würde sich die Atomkerne bewegen. Das resultierende Magnetfeld der bewegten Atomkerne koppelt an das magnetische Moment des Elektrons und daher an den Spin des Elektrons. Die Spin-Bahn Kopplung ist stärker für Elemente mit einer hohen Ordnungszahl. Für Elemente mit kleiner Ordnungszahl ist die Spin-Bahn-Kopplung schwach und wird daher oft vernachlässigt. Spin-Bahn-Kopplung ist verantwortlich für eine Reihe interessanter Phänomene in Materialien. Beispiele sind der Spin-Hall-Effekt, Spin-Texturen in Cupraten, kollektive Spin-Anregungen in Graphen oder sie können auch generell wichtig sein um, die elektronische Struktur eines Materials zu beschreiben, wie zum Beispiel in dem unkonventionellen Supraleiter Sr_2RuO_4.

Diese Arbeit beschäftigt sich mit mehreren Teilaspekten, welche durch das Zusammenspiel von Spin-Bahn-Kopplung, Topologie und elektronischer Korrelation entstehen. Diese Arbeit ist folgendermaßen aufgebaut. Kapitel 1 ist eine Einführung in die oben genannten Konzepte, Spin-Bahn-Kopplung, Topologie, elektronischer Korrelation und deren Zusammenspiel. Dort ist auch eine Übersicht über die Struktur dieser Arbeit gegeben.

Kapitel 2 ist eine Einführung in das Hubbard-Modell und den Formalismus der Greenschen Funktionen, um es zu beschreiben. In diesem Kapitel werden die Konzepte der retardierten Greenschen Funktion, der Matsubara Greenschen Funkftion, der Spektraldarstellung, der Selbstenergie und das Konzept eines erzeugenden Funktionals, um Korrelationsfunktionen zu erhalten, besprochen. Diese Konzepte sind essenziell für den Rest dieser Arbeit.

In Kapitel 3 wird untersucht, wie sich das Konzept der elementaren Banddarstellungen (englisch elementary band representation, EBR) auf Greensche Funktionen anwenden lässt, um topologische Isolatoren mit Wechselwirkungen zu identifizieren.

Ein wichtiges Konzept in der topologischen Klassifikation von Festkörpern ist die das Schützen einer topologischen Phase mit einer Symmetrie. Die Idee hier ist, dass man unter den stetigen Deformierungen des Hamiltonoperators kein Brechen dieser Symmetrie zulässt. Hierfür kommen die Symmetrien der Cartan-Altland-Zirnbauer-Klassen, die da wären Zeitumkehr, Teilchen-Loch Symmetrie und chirale

Symmetrie, sowie räumliche Symmetrien, infrage. In dieser Arbeit wird der Formalismus der topologische Quantenchemie (englisch topological quantum chemistry, TQC) verwendet. Dieser Formalismus nutzt räumliche Symmetrien und die daraus resultierenden EBRs, um topologische Phasen zu identifizieren. Dieses Konzept funktioniert jedoch nur für Systeme ohne Wechselwirkungen, in denen das Bändermodell anwendbar ist. Wenn wir jedoch wechselwirkende Systeme betrachten, dann ist das Bändermodell und damit Bandtopologie nicht mehr anwendbar und die topologische Klassifizierung von Festkörpern wird sehr viel komplizierter und ist ein aktives Forschungsfeld. Eine Möglichkeit Konzepte aus der Topologie auf wechselwirkende System zu übertragen ist die Matusbara Green's Funktion topologisch zu charakterisieren.

Um EBRs für die Greensche Funktion in einem Isolator zu definieren, untersuchen wir zunächst die analytischen Eigenschaften einer Greenschen Funktion in einem Isolator und welche Konsequenzen sich daraus für den sogenannten topologischen Hamiltonian, einem effektiven nicht wechselwirkenden Hamiltonian, ergeben. Wir geben einen Überblick über Darstellungen räumlicher Symmetrien in Festkörpern, EBRs und TQC. Wir zeigen dann, wie die Greensche Funktion unter den Darstellungen der räumlichen Symmetrien transformiert. Diese Eigenschaften können dann genutzt werden um EBRs für die Greensche Funktion zu definieren. Dies geschieht über den sogenannten topologischen Hamiltonian. Somit können räumliche Symmetrien genutzt werden, um die Greensche Funktion topologisch zu klassifizieren.

Wir finden, dass sich diese Klassifizierung nur dann ändern kann, wenn sich die Lücke in der Spektralfunktion bei Frequenz null schließt, die Greensche Funktion einen Eigenwert mit dem Wert null bei Frequenz null besitzt oder die Greensche Funktionen eine der schützenden Symmetrien bricht. Eine genaue Korrespondenz zwischen der topologische Klassifizierung der Greenschen Funktion und dem Konzept der Symmetrie geschützte topologische (englisch symmetry protected topological, SPT) Phasen bleibt jedoch eine offene Frage.

Als Beispiel demonstrieren wir EBRs für die Greensche Funktion anhand des Su-Schriefer-Heeger-Modells mit Hubbard-Wechselwirkung, für welches wir mithilfe exakter Diagonalisierung die Greensche Funktion berechnen. Dieses Modell besitzt einen topologischen Phasenübergang welcher sich durch einen null Eigenwert der Greenschen Funktion bei Frequenz null auszeichnet. Obwohl wir den Formalismus in nur einer Dimension demonstrieren, lässt sich das Vorgehen mit dem Formalismus der TQC direkt auf höhere Dimensionen übertragen. Der entwickelte Formalismus ermöglicht unter gewissen Bedingungen topologische Zustände anhand räumlicher Symmetrien zu erkennen, auch in der Präsenz von Wechselwirkungen. Die Ergebnisse dieses Kapitels sind in Referenz [1] veröffentlicht.

Kapitel 4 beschäftigt sich mit der Erweiterung von TPSC, so dass sich Spin-Bahn-Kopplung beschreiben lässt. Die erweiterte Methode wird dann genutzt, um das Zusammenspiel von Hubbard-Wechselwirkung und Spin-Bahn-Kopplung exemplarisch im Kane-Mele-Hubbard-Modell zu untersuchen. Dies ermöglicht weiterhin in Kapitel 5 den Spin-Hall-Effekt im Kane-Mele-Hubbard-Modell zu untersuchen.

TPSC ist eine Methode, die gut zur Beschreibung von schwachen und mittelstarken elektronischen Korrelationseffekten geeignet ist. TPSC berechnet eine approximative Selbstenergie für das Hubbard-Model aus den Ladungs- und Spin-Fluktuationen. Die Idee von TPSC ist, Spin- und Ladungs-Vertices, welche als lokal und konstant angenommenen werden, selbstkonsistent mit Hilfe von Summenregeln zu bestimmen. TPSC ist so konstruiert, dass es das Pauliprinzip, das Mermin-Wagner-Theorem und Erhaltungsgesetze für Ladung und Spin erfüllt. Die Methode hat einen geringen Rechenaufwand und ist konzeptionell einfach, was ein transparentes Verständnis der zugrunde liegeneden Physik erlaubt. Ein Nachteil der Methode ist, dass sie nicht dazu geeignet ist, starke Wechselwirkungen zu beschreiben, außer bei hohen Temperaturen.

Zunächst erklären wir in diesem Kapitel, was Spin-Bahn-Kopplung ist und wann und in welchen Materialien sie relevant ist. Wir geben auch eine Übersicht über die Methode TPSC und erklären ihre Funktionsweise. Der Effekt der Spin-Bahn-Kopplung lässt sich nicht direkt in TPSC einbauen, da der Effekt die Spinrotationssysmmetrie bricht. Die ursprüngliche Formulierung von TPSC basiert auf dieser Symmetrie. In diesem Kapitel leiten wir daher neue TPSC Selbstkonsistenzgleichungen für den Fall mit Spin-Bahn-Kopplung her. Eine Symmetrie, die in der Präsenz von Spin-Bahn-Kopplung erhalten ist und welche notwendig ist um die neuen Selbstkonsistenzgleichungen herzuleiten, ist Zeitumkehrsymmetrie. Wir zeigen daher, wie sich Zeitumkehrsymmetrie in der zweiten Quantisierung einbauen lässt und welche Konsequenzen sie für verschiedene Korrelationsfunktionen und Erwartungswerte hat.

Mithilfe einer Ansatzgleichung für einen der Spin-Vertices und den Summenregeln lässt sich nun ein Selbstkonistenzproblem für die nun drei verschiedene Spin-Vertices und einen Ladungs-Vertex herleiten. Spin-Bahn-Kopplung sorgt dafür, dass Spin und Ladung nun aneinander Koppeln. Die neuen TSCP Selbstkonistenzgleichungen sind daher ein gekoppeltes System an Gleichungen. Die insgesamt vier Vertices sind die Lösungen dieses Selbstkonsistenzproblems. Nachdem dieses Problem gelöst ist, lässt sich aus der Lösung eine Selbstenergie konstruieren. Ohne Spin-Bahn-Kopplung reduzieren sich die hergeleiteten Gleichungen wieder auf die ursprünglichen TPSC Selbstkonsistenz Gleichungen. Numerisch wird all dies mithilfe eines im Rahmen dieser Arbeit entwickelten Python Codes erreicht.

Als Testmodell wird in dieser Arbeit das Kane-Mele-Hubbard-Modell mit TPSC studiert, um besser das Wechselspiel zwischen Hubbard-Wechselwirkung und Spin-Bahn-Kopplung zu verstehen. TPSC findet die Instabilität zu einem XY-Antiferromagnet bei hinreichend großer Hubbard-Wechselwirkung in welchem die Spins in der x-y-Ebene orientiert sind. Gemischte Ladung-Spin-Fluktuationen sind klein im Vergleich zu reinen Spin- und Ladungsfluktuationen. Weiterhin sind die zwei transversalen Spin-Vertices stärker renormiert als der longitudinale Spin-Vertex. Eine stärkere Spin-Bahn-Kopplung sorgt dafür, dass Spin-Fluktuationen kleiner werden und sich der Übergang zu einem XY-Antiferromagnet zu größeren Werten der Hubbard-Wechselwirkung verschiebt. In der Nähe des Phasenübergangs zeigt die Selbstenergie eine starke Impulsabhängigkeit, welche von den starken Spinfluctuationen stammt. Ein Konsistenz-Check für die Selbstenergie zeigt, dass TPSC am Phasenübergang oder bei zu starker Hubbard-Wechselwirkung seine Gültigkeit verliert.

Kapitel 5 beschäftigt sich mit dem Spin-Hall-Effekt in Abhängigkeit von Temperatur, Hubbard-Wechselwirkung und Spin-Bahn-Kopplung. Hierfür wird das Kane-Mele-Hubbard-Modell mit TPSC studiert. Insbesondere wird die Bedeutung von Vertexkorrekturen im Spin-Hall-Effekt bzw. der dazugehörigen Leitfähigkeit untersucht.

Zunächst wird ein Überblick darüber gegeben, wie das zu einem elektrischen Feld dazugehörige Vektorpotenzial an ein Gittermodell koppelt. Dies wird benutzt, um einen Ausdruck für die Spin-Hall-Leitfähigkeit für endliche Temperaturen herzuleiten. Dafür wird wieder den Formalismus der Greenschen Funktionen verwendet. Es wird analytisch gezeigt, dass im Limes unendlich kleiner Temperaturen die Spin-Hall-Leitfähigkeit proportional zu einer topologischen Invarianten der Greenschen Funktion ist. Es wird beschrieben, wie der Ausdruck für die Spin-Hall-Leitfähigkeit für endliche Temperaturen numisch mit TPSC ausgewertet wird.

Wir studieren wieder das Kane-Mele-Hubbard-Modell welches am absoluten Temperaturnullpunkt einen Phasenübergang zwischen dem Quanten-Spin-Hall-Isolator und dem XY-Antiferromagnet hat. In unseren Simulationen identifizieren wir den Punkt des Phasenübergangs durch eine Divergenz der antiferromagnetischen Korrelationslänge. Dies erlaubt es uns mit Hilfe von TPSC ein Phasendiagram in Abhängigkeit der Hubbard-Wechselwirkung und der Stärke der Spin-Bahn-Kopplung zu berechnen.

Wir berechnen die Spin-Hall-Leitfähigkeit einmal mit impulsabhängigen Vertexkorrekturen und einmal ohne. Die Vertexkorrektoren in TPSC für den Spin-Hall Effekt können als Maki-Thompson Beiträge identifiziert werden. Die Vertexkorrekturen in TPSC können physikalisch als Anregung und anschließende Reabsorbtion einer Spin-, Ladungs- oder gemischten Spin-Ladungs-Anregung interpretiert werden. Es zeigt sich, dass für alle Temperaturen die Vertexkorrekturen einen hohen Beitrag zu der Spin-Hall-Leitfähigkeit haben. In der Nähe des Phasenübergangs verdoppeln sie den Wert der Spin-Hall-Leitfähigkeit sogar. Die Vertexkorrekturen sind notwendig, um den quantisierten Wert von $-2e^2/h$ im Limes unendlich kleiner Temperaturen zu erhalten. Weiterhin, sinkt bei nichtverschwindener Temperatur der Wert der Spin-Hall-Leitfähigkeit durch Erhöhen der Hubbard Wechselwirkung. Unsere Ergebnisse deuten darauf hin, dass der Grund hierfür die Streuung von Elektronen an antiferromagnetischen Spin-Fluktuationen ist, welche stärker werden, je näher das System am Phasenübergang ist. Diese antiferromagnetischen Spin-Fluktuationen sorgen für eine Renormierung der Bandlücke im System. Dieses Verkleinern der Bandlücke kann effektiv auch als eine Erhöhung der Temperatur betrachten werden und einer damit einhergehenden stärkeren Besetzung des Leitungsbandes, was wiederum den Wert der Spin-Hall-Leitfähigkeit verkleinert. Es folgt, dass wenn antiferromagnetische Spin-Fluktuationen groß sind, niedrigere Temperaturen erforderlich sind, um den Quanten-Spin-Hall-Effekt zu beobachten.

Auch, wenn das Kane-Mele-Hubbard-Modell ein stark vereinfachtes Modell ist, erlaubt es systematisch das Wechselspiel zwischen elektronischen Korrelationen, hier modelliert durch die Hubbard-Wechselwirkung, die zu einem Phasenübergang zu einer magnetisch geordneten Phase führt und einer

topologischen Transportgröße, die hier durch die Spin-Hall-Leitfähigkeit gegeben ist. Dieses Verständnis kann eventuell nützlich sein bei Spintronikanwendungen basierend auf dem Spin-Hall-Effekt. Die Ergebnisse dieses Kapitels wurden in Referenz [2] veröffentlicht.

In Kapitel 6 sind die Ergebnisse dieser Arbeit zusammengefasst und es wird ein Ausblick auf mögliche künftige Forschungsprojekte gegeben.

Die in dieser Arbeit gewonnen Erkenntnisse und entwickelten Methoden bieten zahlreiche weitere Anwendungen. Die Anwendung von EBRs auf Greensche Funktionen kann hilfreich sein bei der Suche nach weiteren topologisch nichttrivialen Materialien. Insbesondere deshalb, weil es nur notwendig ist, die Greensche Funktion an einigen wenigen Hochsymmetriepunkten zu berechnen, anstatt auf einem dichten Gitter im Impulsraum. Auch wenn der Formalismus nur in einer Dimension mit exakter Diagonalisirung demonstriert wurde, ist die Anwendung prinzipiell auch in höheren Dimensionen mit jeder Vielteilchenmethode denkbar, die eine Berechnung der Matsubara Greenschen Funktion ermöglicht.

Auch die Erweiterung von TPSC so, dass sie Spin-Bahn-Kopplung beinhaltet, bietet viele weitere Anwendungsmöglichkeiten außer dem Spin-Hall-Effekt, die durch das Wechselspiel der Spin-Bahn-Kopplung und der Hubbard-Wechselwirkung verursacht werden. Einige Beispiele sind die oben genannten Spin-Texturen in Cupraten, kollektive Spin-Anregungen in Graphen, magnetische Anisotropie oder die Realisierung eines p-Wellen-Supraleiters an der Grenzfläche eines Supraleiters und eines topologischen Isolators. Auch in verschiedene Materialien wie zum Beispiel dem unkonventionelle Supraleiter Sr_2RuO_4 muss die Spin-Bahn-Kopplung berücksichtigt werden, um die elektronische Struktur zu beschreiben. Viele dieser Anwendungen erfordern auch weitere Methodenentwicklungen, wie zum Beispiel die Kombination der Multi-Orbital-Erweiterung von TPSC mit Spin-Bahn-Kopplung. Auch hier leistet diese Arbeit einen wichtigen Schritt.

Das Fazit dieser Arbeit ist, dass das Zusammenspiel von elektronischer Korrelation, Spin-Bahn-Kopplung und Topologie eine Fülle von interessanten Phänomenen hervorbringt. TPSC ist eine gute Methode für schwache bis mittelstarke Wechselwirkungen diese Phänomene zu studieren.

List of publications

Publications that chapters of this thesis are based on

Dominik Lessnich, Stephen M. Winter, Mikel Iraola, Maia G. Vergniory, and Roser Valentí. Elementary band representations for the single-particle Green's function of interacting topological insulators. Phys. Rev. B, 104:085116 (2021) [1]

D. Lessnich, C. Gauvin-Ndiaye, Roser Valentí, A.-M.S. Tremblay. Spin Hall conductivity in the Kane-Mele-Hubbard model at finite temperature. Phys. Rev. B, 109:075143 (2024) [2]

D. Lessnich et al. Interplay of spin-orbit coupling and electronic correlation effects with the two-particle self-consistent approach. In preparation [3]

Other publications

Mikel Iraola, Niclas Heinsdorf, Apoorv Tiwari, Dominik Lessnich, Thomas Mertz, Francesco Ferrari, Mark H. Fischer, Stephen M. Winter, Frank Pollmann, Titus Neupert, Roser Valentí, and Maia G. Vergniory. Towards a topological quantum chemistry description of correlated systems: The case of the Hubbard diamond chain. Phys. Rev. B, 104:195125, (2021) [4]

Karim Zantout, Steffen Backes, Aleksandar Razpopov, Dominik Lessnich, and Roser Valentí. Improved effective vertices in the multiorbital two-particle self-consistent method from dynamical mean-field theory. Phys. Rev. B, 107:23510 (2023) [5]

C. Gauvin-Ndiaye, J. Leblanc, S. Marin, N. Martin, D. Lessnich and A.-M.S. Tremblay. The Two-Particle Self-Consistent Approach for Multiorbital models: application to the Emery model. arXiv:2308.14091 (2023) [6]

Code published

D. Lessnich. TPSC code for the Kane-Mele-Hubbard model and the calculation of the spin Hall conductivity. Github, `https://github.com/Dominik-Lessnich/TPSC_KMH` (2023)

Contents

Chapter 1

Introduction

The field of condensed matter physics is concerned with the description and prediction of properties of condensed matter, which especially includes liquid and solid phases of matter. To describe the physical properties of condensed matter or of a certain material it is necessary to describe the behavior of electrons. Electrons are described quantum mechanically by the Schrödinger equation. For non-interacting electron systems, the solution of the Schödinger equation is given by a Slater determinant of single-particle states. In the case of a crystal, that in an idealized picture is described as a periodic arrangement of atoms, Bloch's theorem tells us that the single-particle states are given by Bloch functions. This then leads to the band theory for solids. Materials in which the electron-electron interaction, i.e. the Coulomb interaction, has a small effect or in which the interactions can be successfully treated in a mean-field way, are well described within band theory. Such systems can be studied numerically with density functional theory (DFT).

1.1 Electronic correlations

When interaction effects such between the electrons become significant and the electrons in the system become correlated, this simple picture breaks down. Electronic correlation effect are all those effects that cannot be described with a Slater determinant of single-particle states. Although difficult to describe analytically and numerically, electronic correlation effects can lead to many interesting phenomena such as magnetism, superconductivity, the Mott transition or interacting topological phases such as the fractional quantum Hall state. Many of these phases are not well characterized yet and their study is one of the most active research areas in condensed matter physics.

1.1.1 The Hubbard model

To model systems with electronic correlations, it is necessary to go beyond standard ab initio techniques. One way to model such systems is the Hubbard model that was introduced simultaneously in 1963 by Hubbard, Kanamori and Gutzwiller [7–9]. A recent review can be found in Ref. [10]. The Hubbard model is a lattice model in which the electrons can hop from site to site with a certain hopping amplitude. Two electrons on the same site interact via the Hubbard interaction U. The Hubbard model is a simplified way of modeling the Coulomb interaction that in reality is long range. The physical justification of modeling the Coulomb interaction by a short range interaction is that the Coulomb interaction for further apart electrons is screened due to the presence of other electrons.

The single-band Hubbard model on a 2D square lattice has often been applied to model cuprate high-temperature superconductors. These cuprates have a single narrow band at the Fermi level with copper d and oxygen p orbital character. In this narrow band, correlation effects are large. Due to electronic correlations, cuprates possess a rich phase diagram. Varying doping and temperature, it is possible to realize regions in which the system is either a superconductor, an antiferromagnet, possesses a pseudogap, shows strange metal behavior (linear in temperature resistivity) or Fermi liquid behavior. The Hubbard model has also been studied on other lattices such as the honeycomb lattice

due to its connection to graphene [11]. It also has been studied on the Kagome lattice, which is used to model several candidate materials to observe a spin liquid [12–16]. The Hubbard model also has been studied on the triangular lattice to model organic superconductors [13, 17–19]. Similar to cuprates, organic superconductors possess a rich phase diagram with regions of antiferromagnetism and superconductivity. Multi-orbital extensions of the Hubbard model also include interorbital interactions U' and Hund's coupling J [8]. In this way, materials with more then one band near the Fermi level can be modeled such as ruthenates or iron-based superconductors [20].

Although the Hubbard model is a simplified model, exact solutions are only known for special cases such as in one dimension [21], in infinite dimensions with dynamical mean-field theory (DMFT) [22–24] or for limited cluster sizes with exact diagonalization. The reason is that the size of the Hilbert space grows exponentially with the number of orbitals considered. To approximately solve the Hubbard model, many different many-body methods have been developed over the years such as density matrix renormalization group (DMRG) [25, 26], DMFT [22–24, 27], the two-particle self-consistent approach (TPSC) [28–30], the dynamical vertex approximation (DΓA) [31] or the dual Fermion approach (DF) [32]. Each of them comes with their own strengths, weaknesses and computational costs.

1.1.2 The Two-Particle Self-Consistent approach

In this thesis, we focus on TPSC which we extend to include spin-orbit coupling (SOC). TPSC is a weak to intermediate coupling approach to the Hubbard model capable of calculating a frequency- and momentum-dependent self-energy from spin and charge fluctuations. The idea of TPSC is to determine spin and charge vertices, which are assumed to be local and constant, in a self-consistent way with the help of sum rules. TPSC satisfies conservation laws for spin and charge, the Pauli principle and the Mermin-Wagner theorem. It is computationally inexpensive and conceptually simple, which often allows for a transparent understanding of the underlying physics of the studied phenomena. For a review of TPSC see Refs. [30, 33, 34]. TPSC has been used to study a variety of systems and phenomena that can be described by the Hubbard model such as the antiferromagnetic pseudogap in electron-doped cuprates [30, 35], optical conductivity in the Hubbard model [36] and resilience of Fermi liquid quasiparticles on cold parts of the Fermi surface [37]. The main limitation of TPSC is that it is not valid in the strong coupling limit, except at very high temperature [38] or deep in the renormalized classical regime, where the energy of the characteristic spin fluctuations becomes smaller than the characteristic energy scale given by the temperature and the spin correlation length grows exponentially [28, 30].

1.2 Topological classification of phases of matter

A relatively young and branch of condensed matter physics is the topological classification of solids. Topology is a branch of mathematics that since the 1980s has found many applications in the description physical phenomena and characterization of solids. In 2016, Haldane, Kosterlitz and Thouless were awarded the Nobel prize in physics 'for theoretical discoveries of topological phase transitions and topological phases of matter' [39].

In the simplified case of non-interacting electrons, solids can be classified topologically in terms of band topology [40–44]. The fundamental idea of the topological classification of band structures is to understand the Bloch states as a function of the wave vector which takes values in the first Brillouin zone. Mathematically, the first Brillouin zone is a d-torus. So the problem one is concerned with is the topological characterization of a map from a d-torus to a set of orthonormal Bloch states. The corresponding mathematical structure is called a fiber bundle.

Topological invariants in the condensed matter contexts are characteristics of a band structure that are invariant under continuous changes of the Hamiltonian while maintaining the gap. In mathematics, such a deformation is called a homotopy. The Chern number is the most common example for such a topological invariant [45]. In the quantum Hall effect, the Hall conductivity is an integer multiple of $\frac{e^2}{h}$. The integer the conductivity is proportional to is given by the Chern number of the occupied band space. Other notable examples for physical observables and phenomena that are directly related

to topological characterization of the bands are the electric polarization [46, 47], the quantum spin Hall effect [48, 49] and the orbital magnetization [50, 51].

Another important concept is the protection of topological phases due to symmetries. All non-interacting topological phases protected by combinations of time reversal symmetry, particle-hole symmetry and chiral symmetry, that are enumerated in the Cartan-Altland-Zirnbauer (CAZ) symmetry classes [52], have been classified by K-theory [53, 54]. Another important class of topological insulators are topological crystalline insulators which are protected by spatial symmetries [55]. In three dimensions non-interacting topological crystalline insulators have been systematically investigated in the formalism of topological quantum chemistry (TQC) [56, 57] in terms of elementary band representations (EBRs) [58–60] or equivalently in the formalism of symmetry indicators [61, 62] or the algorithm in Ref. [63].

When interactions are introduced, the simple picture of a band structure breaks down and the topological classification of a solid becomes more complicated. A phenomenon that is only possible with interactions is the fractional quantum Hall state [64]. The fractional quantum Hall state is an example for topological order [65]. Investigating the interplay of electronic correlation effects and topology is topic of active research. A minimal generalization of the topological characterization to interacting systems are so called symmetry protected topological (SPT) phases [66–72]. Another way to generalize topological concepts to interacting system is to topologically characterize the Matsubara Green's function [73–80].

1.3 Spin-orbit coupling

Often, the driving effect that makes a system become topologically nontrivial is spin-orbit coupling (SOC). This usually happens by the SOC causing a band inversion making the bands to become topological. Spin-orbit coupling (SOC) is a relativistic effect that originates from the movement of an electron around the ionic cores in a material. In a simplified picture, one can imagine that in the rest frame of the electron the atom core moves around the electron. The electrons magnetic dipole moment associated to the spin couples to the resulting magnetic field. For elements with a small atomic number, SOC is small and hence is often neglected. However, SOC can lead to a number of interesting phenomena in materials, where interplay with electronic correlations can become important. Notable phenomena in materials caused by SOC are spin textures in cuprates [81, 82], collective spin excitations in graphene [83–88] or the (quantum) spin Hall effect [48, 49, 89–91]. Generally the electronic structure determining a material's properties can become crucially influenced by SOC such as for example in Sr_2RuO_4 [92–99]. To appropriately describe such a material and its properties SOC has to be taken into account.

1.4 Outline of this thesis

In this thesis, we are concerned with certain aspects of the interplay of electronic correlation effects, topological properties and spin-orbit coupling. The model we consider is the Hubbard model, once in one dimension for the Su-Schriefer-Heeger model with Hubbard interactions (SSH+U) and once in two dimensions for the Kane-Mele model with Hubbard interactions (KMH). The SSH+U model we solve numerically exactly with exact diagonalization (ED) for a limited number of 12 sites. We then investigate how the formalism of EBRs can be applied to interacting systems via the Matsubara Green's function and demonstrate it on the example of the SSH+U model. The KMH model we investigate with TPSC which we extend to the case with SOC. In the KMH we are interested in two aspects. First we study systematically the interplay of SOC and Hubbard interaction. Second we study the spin Hall effect that is caused by SOC in the presence of Hubbard interaction at finite temperature. Here, TPSC allows us to study the effect of vertex corrections on the spin Hall conductivity, that are linked to the momentum dependence of the self-energy. Hence, the outline of this thesis is the following.

In Chap. 2 review the Hubbard model and the Green's function formalism we use throughout this thesis. Therefore, we first explain our notation and conventions. Then, we define the Hubbard model and review important concepts such as the Green's function, spectral representation and self-energy that

we use study the Hubbard model in this thesis. We then present a formalism which allows to calculate correlation functions as functional derivatives of a generating functional.

In Chap. 3 we investigate how the formalism of elementary band representations can be applied to the Matsubara Green's function to study interacting topological insulators and demonstrate it at the example of the SSH+U model. Therefore, we first investigate the analytical properties of the Matsubara Green's function in an insulator that allow us to define an effective non-interacting Hamiltonian, namely the topological Hamiltonian. We then review band representations for spatial symmetries and the concept of an EBR for the non-interacting case. We then show that the Green's function transforms under spatial symmetries with the band representations. This then allows us to define EBRs for the Matsubara Green's function via the topological Hamiltonian. We discuss the meaning and the limitations of applying the concept EBRs to the Green's function. We demonstrate the formalism at the simplest possible example, namely the SSH+U model which we solve numerically exactly with ED.

In Chap. 4 we extend TPSC to include SOC, which we then use to investigate the interplay of SOC and Hubbard interaction in the KMH model. We first derive the self-consistency equations in the presence of SOC including the ansatz equation and the sum rules. Throughout the derivation we make use of time reversal symmetry, a symmetry that is preserved in the presence of SOC. We hence explain how TR is incorporated in the second quantization formalism and which consequences TR has for correlation functions and expectation values. In the second level approximation we derive an expression for the self-energy. We show that our derived equations reduce to the original TPSC equations when SOC vanishes. We then define the KMH model. In this model the SOC is proportional to the S_z component of the spins. This makes it a simple example to study the interplay of SOC and the Hubbard interaction. We do so by studying the dependence of the renormalized vertices, double occupation, correlation function, Green's function and self-energy for different values of the Hubbard interaction strength of SOC and temperature.

In Chap. 5 we study the effect of vertex corrections on the spin Hall conductivity at finite temperature in the KMH model. Therefore, we first derive an exact expression for the spin Hall conductivity in the presence of interactions in terms of the Matsubara Green's function for finite temperature that takes vertex corrections into account. We explain that in the zero temperature limit the derived expression becomes a topological invariant of the Green's function, which allows the spin Hall conductivity in that limit only to take quantized values. We explain how the finite temperature expression for the spin Hall can be evaluated with TPSC. We then present results for the spin Hall conductivity as a function of Hubbard U strength of SOC and temperature. Further, we calculate a phase diagram as a function of SOC and Hubbard U, the correlation length for the antiferromagnetic spin fluctuations and the band gap renormalization. We also explain how the antiferromagnetic spin fluctuations renormalize the band gap when increasing Hubbard U.

In Chap. 6 we conclude this thesis with the summary of the findings and an give an outlook on possible future research avenues.

Chapter 2

The Hubbard model

In this thesis we will be concerned with finding approximate solutions to the Hubbard model to analyse its properties. In this chapter we will hence first give the definition of the Hubbard model and also the definition of the correlation functions such as the Green's function that we use to investigate the properties of the Hubbard model. We will also review the spectral representation of the Green's function, the self-energy and the Bethe-Salpeter equation.

In Sec. 2.1 we give the notation and conventions we use throughout this thesis. In Sec. 2.2 we give the definition of the Hubbard model we are concerned with in this thesis. In Sec. 2.3 we discuss the retarded Green's function and its properties. In Sec. 2.4 we discuss the Matsubara Green's function and its relation to the retarded Green's function. In Sec. 2.5 we review how correlation functions can be obtained from functional derivatives of a generating functional. We use them to derive the Bethe-Salpeter equation for susceptibilities and an expression for the self-energy in terms of a four-point correlation function.

This chapter is based on Refs. [100–103] that offer a good introductions into the Green's functions formalism.

2.1 Notation and conventions

In this theses we use the following notations and conventions listed in this section.

- We set $\hbar = k_{\mathrm{B}} = 1$ unless stated otherwise.
- $e = |e|$ is the elementary charge.
- We use $\beta = \frac{1}{T}$ where T is the temperature.
- $\omega_n = (2n+1)\pi T$ with n being an integer, are the Fermionic Matsubara frequencies.
- $q_m = 2m\pi T$ with m being an integer, are the Bosonic Matsubara frequencies.
- $k = (i\omega_n, \boldsymbol{k})$ for Fermions and $q = (iq_m, \boldsymbol{q})$ for Bosons, where $\boldsymbol{k}$ and $\boldsymbol{q}$ are k-points inside the first Brillouin zone.
- $1 = (\tau_1, \boldsymbol{R}_{i_1}, a_1, \sigma_1)$ where τ_1 is imaginary time, $\boldsymbol{R}_{i_1}$ is the lattice vector of the unit cell i_1, a_1 labels the orbitals in the unit cell and σ_1 is the spin index.
- We use the following shorthand notation for summation and integration

$$\phi(\bar{1})\psi(\bar{1}) = \sum_{\boldsymbol{R}_{i_1}} \sum_{a_1} \sum_{\sigma_1} \int_0^\beta d\tau_1 \phi_{\boldsymbol{R}_{i_1} a_1 \sigma_1}(\tau_1)\psi_{\boldsymbol{R}_{i_1} a_1 \sigma_1}(\tau_1). \tag{2.1}$$

- We denote infinitesimal time shifts by $1^+ = (\tau_1 + \epsilon, \boldsymbol{R}_{i_1}, a_1, \sigma_1)$ and $1^- = (\tau_1 - \epsilon, \boldsymbol{R}_{i_1}, a_1, \sigma_1)$ where $\epsilon > 0$ is an infinitesimal small number.

- The (discrete) Fourier transform and the inverse Fourier transform from the lattice to k-space for the single-particle states i.e. from Wannier functions $W_{\boldsymbol{R}_i a\sigma}(\boldsymbol{r})$ to Bloch-like functions $\psi_{\boldsymbol{k}a\sigma}(\boldsymbol{r})$ from is given by

$$\psi_{\boldsymbol{k}a\sigma}(\boldsymbol{r}) = \frac{1}{\sqrt{N}} \sum_{\boldsymbol{R}_i} e^{-i\boldsymbol{k}\cdot\boldsymbol{R}_i} W_{\boldsymbol{R}_i a\sigma}(\boldsymbol{r}), \tag{2.2}$$

$$W_{\boldsymbol{R}_i a\sigma}(\boldsymbol{r}) = \frac{1}{\sqrt{N}} \sum_{\boldsymbol{k}} e^{i\boldsymbol{k}\cdot\boldsymbol{R}_i} \psi_{\boldsymbol{k}a\sigma}(\boldsymbol{r}). \tag{2.3}$$

- The Fourier transform and the inverse Fourier transform from imaginary times to Matsubara frequencies of the Matsubara Green's function is given by

$$G^{ab}_{\sigma\sigma'}(i\omega_n, \boldsymbol{k}) = \int_0^\beta d\tau e^{i\omega_n \tau} G^{ab}_{\sigma\sigma'}(\tau, \boldsymbol{k}), \tag{2.4}$$

$$G^{ab}_{\sigma\sigma'}(\tau, \boldsymbol{k}) = T \sum_{\omega_n} e^{-i\omega_n \tau} G^{ab}_{\sigma\sigma'}(i\omega_n, \boldsymbol{k}). \tag{2.5}$$

2.2 Definition of the Hubbard model

The Hubbard model was introduced simultaneously by Hubbard, Kanamori and Gutzwiller in 1963 [7–9]. A recent review can be found in Ref. [10]. The Hubbard model is a model to describe interacting electrons on a lattice. The Hubbard model for a single orbital in the unit cell is defined as

$$H = \sum_{ij\sigma\sigma'} t_{i\sigma j\sigma'} c^\dagger_{i\sigma} c_{j\sigma'} + U \sum_i n_{i\uparrow} n_{i\downarrow}. \tag{2.6}$$

The creation and annihilation operators create or annihilate an electron in a state located in unitcell i with lattice vector $\boldsymbol{R}_i$ and spin index σ. These state are periodically placed, localized and orthonormal and can be regarded as corresponding to Wannier functions. The hopping matrix elements $t_{i\sigma j\sigma'}$ describe the hopping from one orbital to another one. The interaction term with the interaction strength U is local. The model is often used to describe cuprate high-temperature superconductors. Electrons in a material also interact via the coulomb interactions with electrons in other orbitals but this effect is reduced due to screening and hence often neglected. Placing multiple orbitals in the unit cell the model becomes

$$H = \sum_{ijab\sigma\sigma'} t_{ia\sigma jb\sigma'} c^\dagger_{ia\sigma} c_{jb\sigma'} + U \sum_{ia} n_{ia\uparrow} n_{ia\downarrow}, \tag{2.7}$$

where the indices a and b label the orbitals. The model can be further extended to also include interorbital interactions U' and Hunds coupling J. In the noninteracting case $U = 0$ the model can be solved analytically via the discrete Fourier transformation

$$c^\dagger_{ia\sigma} = \frac{1}{\sqrt{N}} \sum_{\boldsymbol{k}} e^{i\boldsymbol{k}\cdot\boldsymbol{R}_i} c^\dagger_{\boldsymbol{k}a\sigma}, \tag{2.8}$$

$$c_{ia\sigma} = \frac{1}{\sqrt{N}} \sum_{\boldsymbol{k}} e^{-i\boldsymbol{k}\cdot\boldsymbol{R}_i} c_{\boldsymbol{k}a\sigma}. \tag{2.9}$$

The inverse transformation is given by

$$c^\dagger_{\boldsymbol{k}a\sigma} = \frac{1}{\sqrt{N}} \sum_{j} e^{-i\boldsymbol{k}\cdot\boldsymbol{R}_j} c^\dagger_{ja\sigma}, \tag{2.10}$$

$$c_{\boldsymbol{k}a\sigma} = \frac{1}{\sqrt{N}} \sum_{j} e^{i\boldsymbol{k}\cdot\boldsymbol{R}_j} c_{ja\sigma}. \tag{2.11}$$

$c^\dagger_{\boldsymbol{k}a\sigma}$ ($c_{\boldsymbol{k}a\sigma}$) creates (annihilates) an electron in a Bloch-like basis state. With this transformation the model becomes diagonal in $\boldsymbol{k}$

$$H_0 = \sum_{\boldsymbol{k}} H_0^{\boldsymbol{k}} = \sum_{\boldsymbol{k}} \sum_{ab\sigma\sigma'} c^\dagger_{\boldsymbol{k}a\sigma} \big(\mathcal{H}(\boldsymbol{k})\big)_{a\sigma b\sigma'} c_{\boldsymbol{k}b\sigma'}, \tag{2.12}$$

where $\mathcal{H}(\boldsymbol{k})$ is the Bloch-Hamiltonian matrix whose matrix elements are given by

$$\mathcal{H}_{a\sigma,b\sigma'}(\boldsymbol{k}) = \sum_{\boldsymbol{R}_{ij}} t_{ia\sigma jb\sigma'} \exp\left(-i\boldsymbol{k}\cdot\boldsymbol{R}_{ij}\right). \tag{2.13}$$

where $\boldsymbol{R}_{ij} = \boldsymbol{R}_i - \boldsymbol{R}_j$. $\mathcal{H}(\boldsymbol{k})$ needs to be diagonalized to obtain the band energies $\epsilon_n(\boldsymbol{k})$. In the case of a single (spinless) band one directly obtains the band energy $\epsilon(\boldsymbol{k})$. For a square lattice with unit cell length a and only nearest neighbor hopping t one obtains

$$\epsilon(\boldsymbol{k}) = 2t\left(\cos(k_x a) + \cos(k_y a)\right). \tag{2.14}$$

2.3 The Green's function

In a solid with of the order 10^{23} electrons a wave function often becomes an unfeasible concept to do numerical calculations. The reason is that the many-body wave function of such a system depends on all the electron position coordinates as an argument. Hence, the wave function requires too much memory to store on a computer.

A feasible approach to describe such systems instead is to use correlation functions that measure how electrons propagate through the system. Many physical observables can be expressed through these correlation functions. One example of such a correlation function is the single-particle Green's function which we will discuss in the following. This section is based on Refs. [100–103] that offer a good introductions into the Green's functions formalism.

2.3.1 Definition

The retarded one-particle Green's function for fermions on a lattice is defined as

$$G^{\mathrm{R}ab}_{\sigma\sigma'}(t,t',\boldsymbol{R}_i,\boldsymbol{R}_j) = -i\left\langle\left\{c_{ia\sigma}(t), c^\dagger_{jb\sigma'}(t')\right\}\right\rangle\Theta(t-t') \tag{2.15}$$

where $\{A,B\}$ is the anticommutator of two operators. The expectation value is with respect to the equilibrium density matrix in the grand canonical ensemble

$$\langle O\rangle = \frac{\mathrm{Tr}(e^{-\beta(H-\mu\hat{N})}O)}{\mathrm{Tr}(e^{-\beta(H-\mu\hat{N})})}. \tag{2.16}$$

where here $\hat{N}$ is the particle number operator. The creation and annihilation operators are written in the Heisenberg picture

$$c_{ia\sigma}(t) = e^{i(H-\mu\hat{N})t} c_{ia\sigma} e^{-i(H-\mu\hat{N})t}, \tag{2.17}$$

$$c^\dagger_{ia\sigma}(t) = e^{i(H-\mu\hat{N})t} c^\dagger_{ia\sigma} e^{-i(H-\mu\hat{N})t}. \tag{2.18}$$

The single particle Green's function can be interpreted as measuring how a single electron or hole propagates trough the system. The situation is sketched if Fig. 2.1. Note the Green's function we defined above is not necessarily a Green's function in the mathematical sense i.e. that they solve a differential equation, which in our case would be the Schrödinger equation. Although, in the case without interactions both coincide.

Later, we will encounter special cases of higher order correlation functions, such as the spin and the charge susceptibility.

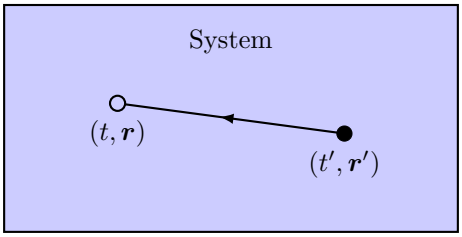

Figure 2.1: Sketch of the physical interpretation of the Green's function. The Green's function, here depicted as a line with an arrow, is a correlation function that measures how an electron or hole enters the system at $(t', \boldsymbol{r}')$ and then leaves the system at $(t, \boldsymbol{r})$. This way the properties of the system are probed by letting electrons or holes propagate through it.

2.3.2 Fourier transforms

In a system in which the Hamiltonian does not explicitly depend on time, the Green's function only depends on one time argument. Also, in a periodic system the Green's function only depends on the distance between the lattice sites. Both are true for the Hubbard model Eq. 2.7 we are interested in. Hence, we can simply write

$$G^{\mathrm{R}}(t-t', \boldsymbol{R}_i - \boldsymbol{R}_j) = G^{\mathrm{R}}(t-t', 0, \boldsymbol{R}_i - \boldsymbol{R}_j, 0) = G^{\mathrm{R}}(t, t', \boldsymbol{R}_i, \boldsymbol{R}_j) \tag{2.19}$$

Taking advantage of the periodicity we can define the retarded one-particle Green's function in k-space as

$$G^{\mathrm{R}ab}_{\sigma\sigma'}(t, \boldsymbol{k}) = -i \left\langle \left\{ c_{\boldsymbol{k}a\sigma}(t), c^{\dagger}_{\boldsymbol{k}b\sigma'}(t') \right\} \right\rangle \Theta(t-t') \tag{2.20}$$

The basis transformation is done via a discrete Fourier transformation

$$G^{\mathrm{R}ab}_{\sigma\sigma'}(t, \boldsymbol{k}) = \frac{1}{N} \sum_{\boldsymbol{R}} e^{i\boldsymbol{k}\cdot\boldsymbol{R}} G^{\mathrm{R}ab}_{\sigma\sigma'}(t, \boldsymbol{R}) \tag{2.21}$$

With a Fourier transform in time we can go to real frequencies. To obtain a well defined expression we insert an infinitisimal damping part $e^{-\eta t}$ with $\eta > 0$ an infinitesimal real number, to make the integral convergent

$$G^{\mathrm{R}}(\omega, \boldsymbol{k}) = \int_{-\infty}^{\infty} dt e^{i\omega t} e^{-\eta t} G^{\mathrm{R}}(t, \boldsymbol{k}). \tag{2.22}$$

2.3.3 Example: Single-band without interactions

In a noninteracting (spinless) system with one band with energies $\epsilon(\boldsymbol{k})$ we can easily calculate the time dependence of the annihilatation operator in the Heisenberg picture

$$-i\partial_t c_{\boldsymbol{k}}(t) = \left[H - \mu\hat{N}, c_{\boldsymbol{k}}(t) \right] = -(\epsilon(\boldsymbol{k}) - \mu) c_{\boldsymbol{k}}(t). \tag{2.23}$$

Hence, we get

$$c_{\boldsymbol{k}}(t) = e^{-i(\epsilon(\boldsymbol{k})-\mu)t} c_{\boldsymbol{k}} \tag{2.24}$$

The Green's function is then given by

$$G^{\mathrm{R}}_0(t, \boldsymbol{k}) = -ie^{-i\epsilon(\boldsymbol{k})t} \left\langle \left\{ c_{\boldsymbol{k}}, c^{\dagger}_{\boldsymbol{k}} \right\} \right\rangle \Theta(t) = -ie^{-i\epsilon(\boldsymbol{k})t} \Theta(t). \tag{2.25}$$

Going to frequency space we get

$$G_0^{\mathrm{R}}(\boldsymbol{k},\omega) = \int_{-\infty}^{\infty} dt e^{i\omega t} e^{-\eta t}(-i) e^{-i(\epsilon(\boldsymbol{k})-\mu)t}\Theta(t) = \frac{1}{\omega + i\eta - \epsilon(\boldsymbol{k}) + \mu}. \tag{2.26}$$

In the case for several bands this expression generalizes to

$$G_0^{\mathrm{R}}(\boldsymbol{k},\omega) = \left((\omega + i\eta)\mathbb{1} - \mathcal{H}(\boldsymbol{k}) + \mu\mathbb{1}\right)^{-1}, \tag{2.27}$$

where $\mathbb{1}$ is the unit matrix, so that the Green's function now becomes a matrix.

2.3.4 Spectral representation

In this section we want to derive the Lehmann representation or spectral representation of the retarded Green's function

$$G^{\mathrm{R}ab}_{\sigma\sigma'}(\omega,\boldsymbol{k}) = \int_{-\infty}^{\infty} \mathrm{d}\omega' \frac{A^{ab}_{\sigma\sigma'}(\omega',\boldsymbol{k})}{\omega + i\eta - \omega'}. \tag{2.28}$$

with the spectral function given by

$$\begin{aligned} A^{ab}_{\sigma\sigma'}(\omega,\boldsymbol{k}) = \frac{1}{Z}\sum_{m,n} e^{-\beta(E_n-\mu N_n)}\Big(&\langle n|c_{\boldsymbol{k}a\sigma}|m\rangle \langle m|c^\dagger_{\boldsymbol{k}b\sigma'}|n\rangle \,\delta\big(\omega - (E_m - E_n - \mu)\big) \\ &+ \langle n|c^\dagger_{\boldsymbol{k}b\sigma'}|m\rangle \langle m|c_{\boldsymbol{k}a\sigma}|n\rangle \,\delta\big(\omega - (E_n - E_m - \mu)\big)\Big), \end{aligned} \tag{2.29}$$

where $Z = \mathrm{Tr}\left(e^{-\beta(H-\mu N)}\right)$, $\{|n\rangle\}$ is a complete set of the many-body eigenstates of $H - \mu\hat{N}$, N_n is the number of particles in state $|n\rangle$ and E_n its energy. The trace of the spectral function is a observable and can be observed in angle-resolved photon emission spectroscopy (APRES) experiments.

The spectral representation can be derived from

$$G^{\mathrm{R}ab}_{\sigma\sigma'}(\omega,\boldsymbol{k}) = \int_{-\infty}^{\infty} dt e^{i\omega t} G^{\mathrm{R}}(t,\boldsymbol{k}) \tag{2.30}$$

$$= -i\int_0^{\infty} dt e^{i\omega t} e^{-\eta t} \left\langle \left\{ c_{\boldsymbol{k}a\sigma}(t), c^\dagger_{\boldsymbol{k}b\sigma'}(0)\right\}\right\rangle. \tag{2.31}$$

We now rewrite the anticommutator by inserting a complete set of the many-body eigenstates of $H - \mu\hat{N}$

$$\begin{aligned} \left\langle \left\{ c_{\boldsymbol{k}a\sigma}(t), c^\dagger_{\boldsymbol{k}b\sigma'}\right\}\right\rangle = \frac{1}{Z}\sum_{m,n}\Big(&\langle n|e^{-\beta(H-\mu\hat{N})} e^{i(H-\mu\hat{N})t} c_{\boldsymbol{k}a\sigma} e^{-i(H-\mu\hat{N})t}|m\rangle \langle m|c^\dagger_{\boldsymbol{k}b\sigma'}|n\rangle \\ &+ \langle n|e^{-\beta(H-\mu\hat{N})} c^\dagger_{\boldsymbol{k}b\sigma'}|m\rangle \langle m|e^{i(H-\mu\hat{N})t} c_{\boldsymbol{k}a\sigma} e^{-i(H-\mu\hat{N})t}|n\rangle \Big). \end{aligned} \tag{2.32}$$

We now use $e^{-i(H-\mu\hat{N})t}|n\rangle = e^{-i(E_n-N_n)t}|n\rangle$. In the first term $|n\rangle$ has one less particle than $|m\rangle$. In the second term it is the other way around. So we get $(E_m - \mu N_m) - (E_n - \mu N_n) = E_m - E_n - \mu$ for the first term and $(E_n - \mu N_n) - (E_m - \mu N_m) = E_n - E_m - \mu$ in the second term. We get

$$\begin{aligned} \left\langle \left\{ c_{\boldsymbol{k}a\sigma}(t), c^\dagger_{\boldsymbol{k}b\sigma'}\right\}\right\rangle = \frac{1}{Z}\sum_{m,n}\Big(&e^{-\beta(E_n-\mu N_n)} e^{-i(E_m-E_n-\mu)t} \langle n|c_{\boldsymbol{k}a\sigma}|m\rangle \langle m|c^\dagger_{\boldsymbol{k}b\sigma'}|n\rangle \\ &+ e^{-\beta(E_n-\mu N_n)} e^{-i(E_n-E_m-\mu)t} \langle n|c^\dagger_{\boldsymbol{k}b\sigma'}|m\rangle \langle m|c_{\boldsymbol{k}a\sigma}|n\rangle \Big). \end{aligned} \tag{2.33}$$

Plugging the expression into Eq. 2.31 and performing the integral, we obtain

$$G^{\mathrm{R}}(\omega,\boldsymbol{k}) = \frac{1}{Z}\sum_{m,n}\Big(e^{-\beta(E_n-\mu N_n)}\frac{1}{\omega+i\eta-(E_m-E_n-\mu)}\,\langle n|c_{\boldsymbol{k}a\sigma}|m\rangle\,\langle m|c^{\dagger}_{\boldsymbol{k}b\sigma'}|n\rangle + e^{-\beta(E_n-\mu N_n)}\frac{1}{\omega+i\eta-(E_n-E_m-\mu)}\,\langle n|c^{\dagger}_{\boldsymbol{k}b\sigma'}|m\rangle\,\langle m|c_{\boldsymbol{k}a\sigma}|n\rangle\Big) \tag{2.34}$$

Comparing with Eq. 2.28 we can identify the spectral function Eq. 2.29.

The spectral function can easily be recovered from the retarded Green's function. Using the Sokhatsky–Weierstrass theorem

$$\lim_{\eta\to 0^+}\frac{1}{\omega+i\eta} = \mathcal{P}\frac{1}{\omega} - i\pi\delta(\omega), \tag{2.35}$$

where $\mathcal{P}$ is the principal part, one can show that the spectral function is obtained from the antihermitian part of the Green's function

$$A^{ab}_{\sigma\sigma'}(\omega,\boldsymbol{k}) = -\frac{1}{2\pi i}\left(G^{\mathrm{R}ab}_{\sigma\sigma'}(\omega,\boldsymbol{k}) - \big(G^{\mathrm{R}ba}_{\sigma'\sigma}(\omega,\boldsymbol{k})\big)^*\right), \tag{2.36}$$

where * denotes complex conjugation. In the case of a (spinless) noninteractiong system with a single band we get for the spectral function

$$A(\boldsymbol{k},\omega) = -\frac{1}{\pi}\mathrm{Im}\big(G^{\mathrm{R}}(\omega,\boldsymbol{k})\big) = \delta(\omega-(\epsilon(\boldsymbol{k})-\mu)). \tag{2.37}$$

This expression coincides with the k-point resolved density of states.

2.3.5 Self-energy

In an interacting system it is very difficult to calculate the exact Green's function. This is only possible for a limited number of cases. Hence, one often tries to find approximate expressions for the Green's function. The self-energy can be defined via the Dyson equation

$$\Sigma^{\mathrm{R}}(\omega,\boldsymbol{k}) = G^{\mathrm{R}}_0(\omega,\boldsymbol{k})^{-1} - G^{\mathrm{R}}(\omega,\boldsymbol{k})^{-1}. \tag{2.38}$$

The self-energy can be understand as a correction to the noninteracting Green's function on how electrons propagate through the interacting system. Reordering the last equation we can write the interacting Green's function in terms of the self-energy as

$$G^{\mathrm{R}}(\omega,\boldsymbol{k}) = \big(\omega+i\eta-\mathcal{H}(\boldsymbol{k})+\mu-\Sigma^{\mathrm{R}}(\omega,\boldsymbol{k})\big)^{-1}. \tag{2.39}$$

Numerous many-body methods are concerned with calculating an approximate expression for the self-energy. In DMFT the self-energy is assumed to be constant in k-space and obtained by calculating the self-energy by mapping the lattice problem to an auxiliary system, the Anderson impurity model. In TPSC a frequency and k-dependent self-energy is calculated from spin and charge fluctuations. An approximate expression for the self-energy can also be obtained via perturbation theory or a number of other approximations, mentioned in the introduction.

2.4 The Matsubara Green's function

2.4.1 Definition

The Matsubara Green's function for fermions on a lattice is defined as

$$\begin{aligned} G^{ab}_{\sigma\sigma'}(\tau,\boldsymbol{R}_i-\boldsymbol{R}_j) &= -\langle\mathcal{T}_\tau c_{ia\sigma}(\tau)c^{\dagger}_{jb\sigma'}\rangle \\ &= -\langle c_{ia\sigma}(\tau)c^{\dagger}_{jb\sigma'}\rangle + \langle c^{\dagger}_{jb\sigma'}c_{ia\sigma}(\tau)\rangle \end{aligned} \tag{2.40}$$

where $\tau \in [-\beta, \beta]$ with $\beta = \frac{1}{T}$ is imaginary time, and $\mathcal{T}_\tau$ is time ordering in imaginary time. In this definition we again took advantage of periodicity in real space and time translation invariance due to the Hamiltonian being time-independent. Time evolution in imaginary time is defined as

$$c_{ia\sigma}(\tau) = e^{(H-\mu\hat{N})\tau} c_{ia\sigma} e^{-(H-\mu\hat{N})\tau}, \tag{2.41}$$

$$c^\dagger_{ia\sigma}(\tau) = e^{(H-\mu\hat{N})\tau} c^\dagger_{ia\sigma} e^{-(H-\mu\hat{N})\tau}. \tag{2.42}$$

A discrete Fourier transform yields the Matsubara Green's function in k-space

$$G^{ab}_{\sigma\sigma'}(\tau, \boldsymbol{k}) = -\left\langle \mathcal{T}_\tau c_{\boldsymbol{k}a\sigma}(\tau) c^\dagger_{\boldsymbol{k}b\sigma'} \right\rangle. \tag{2.43}$$

It can be shown that the Matsubara Green's function is antiperiodic in imaginary time i.e. for $T \in [-\beta, 0]$ it holds

$$G^{ab}_{\sigma\sigma'}(\tau, \boldsymbol{k}) = -G^{ab}_{\sigma\sigma'}(\tau + \beta, \boldsymbol{k}). \tag{2.44}$$

Proof. Let $\tau \in [-\beta, 0]$. From the cyclic property of the trace we get

$$\begin{aligned} G^{ab}_{\sigma\sigma'}(\tau, \boldsymbol{k}) &= \frac{1}{Z} \mathrm{Tr}\left(e^{-\beta(H-\mu\hat{N})} c^\dagger_{\boldsymbol{k}b\sigma'} c_{\boldsymbol{k}a\sigma}(\tau) \right) \\ &= \frac{1}{Z} \mathrm{Tr}\left(e^{-\beta(H-\mu\hat{N})} e^{\beta(H-\mu\hat{N})}) e^{(H-\mu\hat{N})\tau} c_{\boldsymbol{k}a\sigma} e^{-(H-\mu\hat{N})\tau} e^{-\beta(H-\mu\hat{N})} c^\dagger_{\boldsymbol{k}b\sigma'} \right) \\ &= \langle c_{\boldsymbol{k}a\sigma}(\tau + \beta) c^\dagger_{\boldsymbol{k}b\sigma'} \rangle \\ &= -G^{ab}_{\sigma\sigma'}(\tau + \beta, \boldsymbol{k}). \end{aligned} \tag{2.45}$$

□

By a Fourier transform we can go to Matsubara frequencies. Taking advantage of the antiperiodicity we can write

$$G^{ab}_{\sigma\sigma'}(i\omega_n, \boldsymbol{k}) = \int_0^\beta d\tau e^{i\omega_n \tau} G^{ab}_{\sigma\sigma'}(\tau, \boldsymbol{k}), \tag{2.46}$$

where the fermionic Matsubara frequencies are defined as

$$\omega_n = (2n+1)\pi T. \tag{2.47}$$

The inverse transformation is given by

$$G^{ab}_{\sigma\sigma'}(\tau, \boldsymbol{k}) = \frac{1}{\beta} \sum_{\omega_n} e^{i\omega_n \tau} G^{ab}_{\sigma\sigma'}(i\omega_n, \boldsymbol{k}). \tag{2.48}$$

Analogous to the case for the retarded Green's function one can obtain with the Heisenberg equation of motion for the noninteracting case of a single (spinless) band

$$G^{ab}_{0\sigma\sigma'}(\tau, \boldsymbol{k}) = -e^{-(\epsilon(\boldsymbol{k})-\mu)\tau} \left((1 - f_T(\epsilon(\boldsymbol{k}))) \, \Theta(\tau) - f_T(\epsilon(\boldsymbol{k})) \Theta(-\tau) \right) \tag{2.49}$$

where $f_T(\epsilon)$ is the Fermi-Dirac distribution

$$f_T(\epsilon) = \frac{1}{1 + e^{\beta\epsilon}}. \tag{2.50}$$

In Matsubara frequencies this equation becomes

$$G_0(i\omega_n, \boldsymbol{k}) = \frac{1}{i\omega_n - \epsilon(\boldsymbol{k}) + \mu}. \tag{2.51}$$

For multiple orbitals in the unit cell the last equation generalizes to

$$G_0(i\omega_n, \boldsymbol{k}) = \left(i\omega_n \mathbb{1} - \mathcal{H}(\boldsymbol{k}) + \mu \mathbb{1}\right)^{-1}, \tag{2.52}$$

where $\mathbb{1}$ is the unit matrix.

2.4.2 Spectral representation and analytic continuation

Similarly to the retarded Green's function the Matsubara Green's function has a spectral representation. A similar calculation yields

$$G^{ab}_{\sigma\sigma'}(i\omega_n, \boldsymbol{k}) = \int_{-\infty}^{\infty} \mathrm{d}\omega' \frac{A^{ab}_{\sigma\sigma'}(\omega', \boldsymbol{k})}{i\omega_n - \omega'}. \tag{2.53}$$

with the spectral function $A(\omega, \boldsymbol{k})$ given by Eq. 2.29. The spectral representation can also be used to define a function $G(z, \boldsymbol{k})$ with $z \in \mathbb{C}$ that is holomorphic everywhere except the real axis where it has poles. In the limit of an infinite size lattice the poles merge and form a branch cut. It is apparent from that expression the retarded Green's function can be obtained from the Matsubara Green's function by analytic continuation $i\omega_n \to \omega + i\eta$ i.e.

$$G(i\omega_n, \boldsymbol{k}) \overset{i\omega_n \to \omega + i\eta}{\to} G^{\mathrm{R}}(\omega, \boldsymbol{k}). \tag{2.54}$$

2.5 Correlation functions from functional derivatives

In the following we present a source field formalism developed by Martin and Schwinger with which one can obtain correlation functions as functional derivatives of a generating functional [104, 105]. With this formalism we can also find an expression for the self-energy. The obtained expressions will be used later in Chap. 4 to derive the TPSC self-consistency equations.

2.5.1 Generating functional

We define a partition function $Z[\phi]$ with a source field ϕ

$$Z[\phi] = \left\langle \mathcal{T}_\tau \exp\left(-c^\dagger(\bar{1})\phi(\bar{1}, \bar{2})c(\bar{2})\right)\right\rangle. \tag{2.55}$$

The thermal expectation value is again given by Eq. 2.16. In the above expression one has to think of the exponential function as being defined through its Taylor series. We used the shorthand notation

$$(1) = (\tau_1, \boldsymbol{R}_{i_1}, a_1, \sigma_1). \tag{2.56}$$

The overbar indicates summation over indices and integration over complex time. Explicitly one has

$$c^\dagger(\bar{1})\phi(\bar{1}, \bar{2})c(\bar{2}) = \sum_{\boldsymbol{R}_{i_1}\boldsymbol{R}_{i_2}} \sum_{a_1 a_2} \sum_{\sigma_1\sigma_2} \int_0^\beta d\tau_1 \int_0^\beta d\tau_2 c^\dagger_{\boldsymbol{R}_{i_1} a_1 \sigma_1}(\tau_1)\phi_{\boldsymbol{R}_{i_1} a_1 \sigma_1, \boldsymbol{R}_{i_2} a_2 \sigma_2}(\tau_1, \tau_2) c_{\boldsymbol{R}_{i_2} a_2 \sigma_2}(\tau_2) \tag{2.57}$$

Defining

$$S[\phi] = \exp\left(-c^\dagger(\bar{1})\phi(\bar{1}, \bar{2})c(\bar{2})\right) \tag{2.58}$$

the Matsubara Greens function in the presence of a source field can now be obtained as a functional derivative of the generating functional $\ln(Z[\phi])$

$$G(1,2)_\phi = -\frac{\delta \ln Z[\phi]}{\delta\phi(2,1)} = -\frac{\langle \mathcal{T}_\tau S[\phi]\, c(1)c^\dagger(2)\rangle}{\langle \mathcal{T}_\tau S[\phi]\rangle} = -\left\langle \mathcal{T}_\tau c(1)c^\dagger(2)\right\rangle_\phi. \tag{2.59}$$

Setting $\phi = 0$ one obtains the original expression for the Matsubara Green's function

$$G(1,2) = G(1,2)_{\phi=0}. \tag{2.60}$$

Note that it holds

$$\frac{\delta\phi(1,2)}{\delta\phi(3,4)} = \delta(1-3)\delta(2-4). \tag{2.61}$$

Higher order correlation functions can be obtained by taking further functional derivatives. We define the generalized susceptibility as

$$\begin{aligned}\chi(1,2;3,4)_\phi &= -\frac{\delta G(1,2)_\phi}{\delta\phi(3,4)} \\ &= \frac{\delta}{\delta\phi(3,4)} \frac{\langle \mathcal{T}_\tau S[\phi]\, c(1)c^\dagger(2)\rangle}{\langle \mathcal{T}_\tau S[\phi]\rangle} \\ &= -\langle \mathcal{T}_\tau c(1)c^\dagger(2)c^\dagger(3)c(4)\rangle_\phi - G(1,2)_\phi G(4,3)_\phi. \end{aligned} \tag{2.62}$$

The first term in this expression is a four point correlation function. As special cases we obtain the occupation number correlation functions defined by

$$\chi(1,2) = \chi(1,1^+;2^+,2) = \langle \mathcal{T}_\tau n(1)n(2)\rangle - \langle n(1)\rangle \langle n(2)\rangle. \tag{2.63}$$

Similar to the Matsubara Green's function we can take advantage of time translation invariance and periodicity of the system to show that the function only depends on the differences $\tau = \tau_1 - \tau_2$ and $\boldsymbol{R} = \boldsymbol{R}_{i_1} - \boldsymbol{R}_{i_2}$. Further, one can prove that for $\tau \in [-\beta, 0]$ it holds $\chi(\tau, \boldsymbol{R}) = \chi(\tau + \beta, \boldsymbol{R})$. With that we can define the Fourier transforms as

$$\int_0^\beta d\tau e^{iq_m\tau} \sum_{\boldsymbol{R}} e^{-i\boldsymbol{q}\cdot\boldsymbol{R}} \chi^{a_1a_2}_{\sigma_1\sigma_2}(\tau, \boldsymbol{R}) = \chi^{a_1a_2}_{\sigma_1\sigma_2}(iq_m, \boldsymbol{q}), \tag{2.64}$$

with the Bosonic Matsubara frequencies defined by

$$q_m = 2m\pi T. \tag{2.65}$$

From these expressions spin susceptibilities for the spin z-direction and charge susceptibilities can be constructed (see also Chap. 4).

2.5.2 Self-energy in the Hubbard model

In this section we derive an expression for the self-energy in the Hubbard model given by Eq. 2.6. We will do so by deriving the equation of motion for the Green's function, from which we can identify the self-energy. The Heisenberg equation of motion in imaginary time for the annihilation operator is

$$\partial_\tau c_{ia\sigma}(\tau) = \left[H - \mu \sum_{ia} n_{ia}, c_{ia\sigma}(\tau) \right]. \tag{2.66}$$

where $n_{ia} = n_{ia\uparrow} + n_{ia\downarrow}$. We can use the following identity to evaluate the commutator

$$[AB, C] = A\{B, C\} - \{A, C\}B. \tag{2.67}$$

From this identity we get an expression that will be helpful in the following, namely

$$\left[c^\dagger_{ia\sigma} c_{jb\sigma'}, c_{ld\sigma''} \right] = -\delta_{ad}\delta_{\sigma\sigma''}\delta_{il} c_{jb\sigma'}. \tag{2.68}$$

With the help of this expression one can calculate the above commutator for the individual terms of the Hamiltonian in Eq. 2.6. We get

$$\left[\sum_{ijab\sigma\sigma'} t_{ia\sigma jb\sigma'} c^\dagger_{ia\sigma} c_{jb\sigma'}, c_{ld\sigma''}\right] = -\sum_{jb\sigma'} t_{ld\sigma'' jb\sigma'} c_{jb\sigma'} \tag{2.69}$$

$$\left[U\sum_{ia} n_{ia\uparrow} n_{ia\downarrow}, c_{ld\sigma''}\right] = -U n_{ld-\sigma''} c_{ld\sigma''} \tag{2.70}$$

$$\left[-\mu\sum_{ia} n_{ia}, c_{ld\sigma''}\right] = \mu c_{ld\sigma''} \tag{2.71}$$

Taking these terms together we obtain

$$\partial_\tau c_{ld\sigma''}(\tau) = -\sum_{jb\sigma'} t_{ld\sigma'' jb\sigma'} c_{jb\sigma'}(\tau) - U n_{ld-\sigma''}(\tau) c_{ld\sigma''}(\tau) + \mu c_{ld\sigma''}(\tau) \tag{2.72}$$

Taking the time-derivative of the first time argument of the Green's function the derivative acts on the annihilation operator. Hence, we get

$$\begin{aligned}\partial_{\tau_1} G^{a_1 a_2}_{\sigma_1\sigma_2}(\tau_1, \boldsymbol{R}_{i_1}, \tau_2, \boldsymbol{R}_{i_2})_\phi = {} & \delta_{a_1 a_2}\delta_{\sigma_1\sigma_2}\delta_{i_1 i_2}\delta(\tau_1-\tau_2) - t_{i_1 a_1 \sigma_1 \bar{i}_3 \bar{a}_3 \bar{\sigma}_3} G^{\bar{a}_3 a_2}_{\bar{\sigma}_3\sigma_2}(\tau_1, \boldsymbol{R}_{\bar{i}_3}, \tau_2, \boldsymbol{R}_{i_2})_\phi \\ & - \phi^{a_1\bar{a}_3}_{\sigma_1\bar{\sigma}_3}(\tau_1, \boldsymbol{R}_{i_1}, \bar{\tau}_3, \boldsymbol{R}_{\bar{i}_3}) G^{\bar{a}_3 a_2}_{\bar{\sigma}_3\sigma_2}(\bar{\tau}_3, \boldsymbol{R}_{\bar{i}_3}, \tau_2, \boldsymbol{R}_{i_2})_\phi \\ & + \mu G^{a_1 a_2}_{\sigma_1\sigma_2}(\tau_1, \boldsymbol{R}_{i_1}, \tau_2, \boldsymbol{R}_{i_2})_\phi \\ & - U \left\langle \mathcal{T}_\tau c^\dagger_{i_1 a_1 -\sigma_1}(\tau_1) c_{i_1 a_1 -\sigma_1}(\tau_1) c_{i_1 a_1 \sigma_1}(\tau_1) c^\dagger_{i_2 a_2 \sigma_2}(\tau_2)\right\rangle_\phi .\end{aligned} \tag{2.73}$$

The delta distribution is obtained from the time derivative of the time ordering. The ϕ is obtained by differentiating the time ordered product in the exponential in $\langle\cdot\rangle_\phi$. One can identify the non-interacting Green's function as

$$G_0(1,\bar{2})^{-1} = -\left(\delta_{\sigma_1\bar{\sigma}_2}\delta_{a_1\bar{a}_2}\delta_{i_1\bar{i}_2}\partial_{\tau_1} + t_{i_1 a_1 \sigma_1 \bar{i}_2 \bar{a}_2 \bar{\sigma}_2} - \mu\delta_{\sigma_1\bar{\sigma}_2}\delta_{a_1\bar{a}_2}\delta_{i_1\bar{i}_2}\right)\delta(\tau_1 - \bar{\tau}_2) \tag{2.74}$$

Note that the $^{-1}$ is with respect to convolution. Hence, Eq. 2.73 can be written as

$$\begin{aligned}G_0(1,\bar{3})^{-1} G(\bar{3},2)_\phi = {} & \delta_{a_1 a_2}\delta_{\sigma_1\sigma_2}\delta_{i_1 i_2}\delta(\tau_1-\tau_2) + \phi^{a_1\bar{a}_3}_{\sigma_1\bar{\sigma}_3}(\tau_1, \boldsymbol{R}_{i_1}, \bar{\tau}_3, \boldsymbol{R}_{\bar{i}_3}) G^{\bar{a}_3 a_2}_{\bar{\sigma}_3\sigma_2}(\bar{\tau}_3, \boldsymbol{R}_{\bar{i}_3}, \tau_2, \boldsymbol{R}_{i_2})_\phi \\ & + U \left\langle \mathcal{T}_\tau c^\dagger_{i_1 a_1 -\sigma_1}(\tau_1) c_{i_1 a_1 -\sigma_1}(\tau_1) c_{i_1 a_1 \sigma_1}(\tau_1) c^\dagger_{i_2 a_2 \sigma_2}(\tau_2)\right\rangle_\phi .\end{aligned} \tag{2.75}$$

Comparing to the Dyson equation we can identify

$$\Sigma(1,\bar{3})_\phi G(\bar{3},2)_\phi = U \left\langle \mathcal{T}_\tau c^\dagger_{i_1 a_1 -\sigma_1}(\tau_1) c_{i_1 a_1 -\sigma_1}(\tau_1) c_{i_1 a_1 \sigma_1}(\tau_1) c^\dagger_{i_2 a_2 \sigma_2}(\tau_2)\right\rangle_\phi . \tag{2.76}$$

Solving this expression explicitly for the self-energy we get

$$\Sigma(1,2)_\phi = U \left\langle \mathcal{T}_\tau c^\dagger_{i_1 a_1 -\sigma_1}(\tau_1) c_{i_1 a_1 -\sigma_1}(\tau_1) c_{i_1 a_1 \sigma_1}(\tau_1) c^\dagger_{\bar{i}_3 \bar{a}_3 \bar{\sigma}_3}(\bar{\tau}_3)\right\rangle_\phi (G^{-1})^{\bar{a}_3 a_2}_{\bar{\sigma}_3\sigma_2}(\bar{\tau}_3, \boldsymbol{R}_{\bar{i}_3}, \tau_2, \boldsymbol{R}_{i_2})_\phi . \tag{2.77}$$

With the self-energy the Green's function can be written as

$$G(1,2)^{-1}_\phi = G_0(1,2)^{-1} - \phi(1,2) - \Sigma(1,2)_\phi . \tag{2.78}$$

2.5.3 Bethe-Salpeter equation for the susceptibilities

In the following we derive an integral equation for the generalized susceptibilities, namely the Bethe-Salpeter equation expanded in one of the two particle-hole channels. From functionally differentiating the identity

$$G(1,\bar{3})_\phi G^{-1}(\bar{3},2)_\phi = \delta(1-2) \tag{2.79}$$

we get the following expression

$$\frac{\delta G(1,2)_\phi}{\delta\phi(3,4)} = -G(1,\bar{5})_\phi \frac{\delta G^{-1}(\bar{5},\bar{6})_\phi}{\delta\phi(3,4)} G(\bar{6},2)_\phi. \tag{2.80}$$

Inserting Eq. 2.78 one obtains

$$\begin{aligned}
\chi_\phi(1,2;3,4) &= -\frac{\delta G(1,2)_\phi}{\delta\phi(3,4)} \\
&= -G(1,\bar{5})_\phi \delta(3-\bar{5})\delta(4-\bar{6}) G(\bar{6},2)_\phi - G(1,\bar{5})_\phi \frac{\delta\Sigma(\bar{5},\bar{6})_\phi}{\delta\phi(3,4)} G(\bar{6},2)_\phi \\
&= -G(1,3)_\phi G(4,2)_\phi - G(1,\bar{5})_\phi \frac{\delta\Sigma(\bar{5},\bar{6})_\phi}{\delta\phi(3,4)} G(\bar{6},2)_\phi.
\end{aligned} \tag{2.81}$$

The last equation shows that Σ only depends on ϕ via the Green's function and does not have an explicit dependence on ϕ. Hence we can use the chain rule

$$\chi_\phi(1,2;3,4) = -G(1,3)_\phi G(4,2)_\phi - G(1,\bar{5})_\phi \frac{\delta\Sigma(\bar{5},\bar{6})_\phi}{\delta G(\bar{7},\bar{8})_\phi} \frac{\delta G(\bar{7},\bar{8})_\phi}{\delta\phi(3,4)} G(\bar{6},2)_\phi. \tag{2.82}$$

We can again identify the functional derivative of G with minus the generalized susceptibility. Further, we define the vertex function as

$$\Gamma(5,6;7,8)_\phi = \frac{\delta\Sigma(5,6)_\phi}{\delta G(7,8)_\phi}. \tag{2.83}$$

This function is irreducible in a particle hole-channel. That means diagrams contributing to it cannot be cut in two by cutting two Green's function lines that go in opposite directions. The irreducible vertex function describes the interaction between two particles. Further, setting $\phi = 0$ the Bethe-Salpeter equation (in one of the two particle-hole channels) can be written as

$$\chi(1,2;3,4) = -G(1,3)G(4,2) + G(1,\bar{5})\Gamma(\bar{5},\bar{6};\bar{7},\bar{8})\chi(\bar{7},\bar{8};3,4)G(\bar{6},2). \tag{2.84}$$

This equation includes both the longitudinal and the transversal particle-hole channel. Since we also do not assume spin rotation symmetry here the longitudinal and the transversal channel can be coupled. In fact spin-orbit coupling breaks spin rotation symmetry.

Chapter 3

Elementary band representations for the Matsubara Green's function

In this chapter we discuss the applicability of elementary band representations (EBRs) to diagnose spatial- and time-reversal-symmetry protected topological phases in interacting insulators in terms of their single-particle Matsubara Green's functions. We do so by considering an auxiliary non-interacting system $H_{\mathrm{T}}(\mathbf{k}) = -G^{-1}(0, \mathbf{k})$, known as the topological Hamiltonian, whose bands can, as for any non-interacting periodic system, be labeled by EBRs. We restrict ourselves to zero temperature and assume that the groundstate of the considered system is non-degenerate. We find that the labeling of the bands of the topological Hamiltonian by EBRs cannot change under continous variations of the parameters of the Hamiltonian if neither (i) the gap in the spectral function at zero frequency closes, (ii) the Green's function has a zero eigenvalue at zero frequency or (iii) the Green's function breaks a protecting symmetry. We demonstrate the use of EBRs applied to the Green's function on the one-dimensional Su-Schrieffer-Heeger model with Hubbard interactions (SSH+U model), which we solve by exact diagonalization for a finite number of unit cells. The use of EBRs for the Green's function to diagnose so-called symmetry protected topological (SPT) phases is discussed, but remains an open question.

This chapter is organized as follows. In Sec. 3.1 we give an overview over the topological classification of solids without interactions and with interactions. We also discuss the relation to physical observables. In this context we also discuss the protection of topological invariants due to symmetries including spatial symmetries. In Sec. 3.3 we establish the conditions that $G(i\omega, \boldsymbol{k})$ needs to fulfill to define topological invariants in terms of $G(i\omega, \boldsymbol{k})$ and, we review the concept of a topological Hamiltonian. This analysis sets the framework for the EBR classification of Green's functions. In Sec. 3.4 we show how Bloch-like wave functions and the corresponding creation and annihilation operators transform under spatial symmetries. In Sec. 3.5 we give a brief introduction on EBRs and how they can be used to diagnose if a system is topological. In Sec. 3.6 we investigate the implications that the spatial symmetries of the many-body Hamiltonian have on $G(i\omega, \boldsymbol{k})$. In Sec. 3.7 we discuss the EBR-based classification of the topological Hamiltonian and discuss its use and limitations. In Sec. 3.8 we analyze the interacting Green's function of the one-dimensional Su-Schrieffer-Heeger model [106] with Hubbard interactions (SSH+U) within the framework of TQC, diagnosing its topological phases by making use of the spatial inversion symmetry present in the model. In Sec. 3.9 we summarize our findings. Unless stated otherwise this chapter is based on Ref. [1]. Additional sections are added to make the discussion self-contained. The ED solver to calculate the exact eigenstates of the SSH+U model was written by Steve Winter.

3.1 Introduction on the topological classification of solids

Non-interacting topological insulators are well understood in terms of band topology [40–44]. An insulator is called topologically trivial if it is possible to continuously deform its band structure and corresponding eigenstates to those of an atomic insulator without closing the energy gap or breaking

a symmetry. If such a continuous deformation is not possible the system is called nontrivial or topological. Topological phases can be characterized by topological invariants that indicate an obstruction to such a continuous deformation to an atomic insulator, if the invariant has a nontrivial value. The Chern number, first proposed for the integer quantum Hall effect, is the most common example for a topological invariant [45]. Other notable examples for physical observables and phenomena that are directly related to topological characterization of the bands are the electric polarization [46, 47], the quantum spin Hall effect [48, 49] and the orbital magnetization [50, 51].

Another important concept is the protection of topological phases due to symmetries. Actually, all non-interacting topological phases protected by combinations of time reversal symmetry (TR), particle-hole symmetry (PH) and chiral symmetry (CS), i.e. which belong to one of the ten Cartan-Altland-Zirnbauer (CAZ) symmetry classes [52], have been classified by K-theory [53, 54].

Another important class of topological insulators are topological crystalline insulators which are protected by spatial symmetries [55]. In three dimensions non-interacting topological crystalline insulators have been systematically investigated in all 230 space groups, with and without TR present, in the formalism of topological quantum chemistry (TQC) [56, 57] in terms of elementary band representations (EBRs) [58–60] or equivalently in the formalism of symmetry indicators [61, 62] or the algorithm in Ref. [63]. These formalisms are based on the fact that Bloch wave functions at high symmetry k-points can be classified by irreducible representations (irreps) of the little group of these k-points. In this way spatial symmetries place constraints on the connectivity of the bands in the Brillouin zone, which can be used to identify those band structures that are compatible with an atomic insulator.

The topological classification and the extension to the above concepts of interacting systems is much more involved compared to noninteracting ones. In principle, non-interacting insulators have a very simple structure. Their ground state wave function is given by a Slater determinant of all single-particle states below the Fermi level. Thus, the gap in the single-particle spectrum makes the ground state wave function unique. To decide if two non-interacting insulators are topologically equivalent is the same as investigating whether the corresponding Hamiltonians can be smoothly connected while maintaining symmetries and maintaining the gap. The gap manifests in terms of (i) the many-body ground state staying gapped, or (ii) the presence of a gap in the single-particle excitations. Both features are equivalent in the absence of interactions. Hence it is sufficient to analyze the topological properties of the map $\boldsymbol{k} \mapsto \mathcal{H}(\boldsymbol{k})$, where $\boldsymbol{k}$ is a reciprocal wavevector in the Brilloun zone (a d-torus, where d is the dimension) and $\mathcal{H}(\boldsymbol{k})$ is the Bloch Hamiltonian. Hence it is equivalent for noninteracting systems to investigate the topological properties of the (zero temperature) single-particle Matsubara Green's function $G(i\omega, \boldsymbol{k})$, which for the non-interacting case is given as:

$$G_0(i\omega, \boldsymbol{k}) = \big(i\omega - \mathcal{H}(\boldsymbol{k})\big)^{-1} \tag{3.1}$$

where $i\omega$ denotes the Matsubara frequency, which at zero temperature becomes continuous. In the presence of interactions investigating the adiabatic connectivity of Hamiltonians while the ground state stays gapped and investigating the Green's function is a priori not equivalent anymore.

In a more general context, the concept of symmetry protected topological (SPT) phases [66–72] has been introduced to investigate the smooth connectivity of gapped, short range entangled phases while maintaining symmetries. Alternatively, the topological characterization of the full interacting single-particle Matsubara Green's function $G(i\omega, \boldsymbol{k})$ was put forward in efs. [73–80]. For the CAZ symmetry classes it was shown that one obtains the same topological classification for the Green's function as for non-interacting Hamiltonians i.e. $\mathbb{Z}$, $\mathbb{Z}_2$ or 0 [76]. A similar Green's functions-based framework for identifying spatial-symmetry-protected topological phases in interacting systems is investigated in Ref. [1], on which this chapter is based on. Topological invariants of the Green's function can in some cases related to physical observables. One example is the Hall conductivity which can be written as [107]

$$\sigma^H_{\alpha\beta}(T=0) = -\frac{e^2}{h}\frac{\epsilon_{\rho\eta\zeta}}{24\pi^2}\int dk \mathrm{Tr}\Big(\partial_\rho G^{-1}(k)G(k)\partial_\eta G^{-1}(k)G(k)\partial_\zeta G^{-1}(k)G(k)\Big), \tag{3.2}$$

where $\rho\eta\zeta$ are summed over and stand for $i\omega_n, k_\alpha, k_\beta$. $\epsilon_{\rho\eta\zeta}$ is the fully antisymmetric tensor. For a derivation and why this expression is a topological invariant of the Green's function see chap. 5. The same holds for the spin Hall conductivity.

3.2 Analytical properties of the Matsubara Green's Function

In this section we investigate analytic properties of the Green's function, necessary to apply EBRs to interacting systems in terms of the Green's function. For completeness and to avoid misunderstandings we again give the definition of the zero-temperature Matsubara Green's function and specify the basis we work with in this chapter. We then define the conditions the Matsubara Green's functions has to fulfill to define topological invariants. We then proof that, for a Green's function fulfilling the first two GNSC-conditions, the corresponding topological Hamiltonian is Hermitian with finite eigenvalues whose absolute value is bounded from below.

We consider a lattice model defined on a basis of exponentially localized, orthonormal Wannier functions $W_{ia}(\boldsymbol{r})$ consistent with the symmetries of our system, where the index i labels the unit cell with lattice vector $\boldsymbol{R}_i$ to which $W_{ia}(\boldsymbol{r})$ belongs to. The Wannier function in that cell is specified by the index a which here can also include spin. From the Wannier functions $W_{ia}(\boldsymbol{r})$ one can construct Bloch-like wave functions $\psi_{\boldsymbol{k}a}(\boldsymbol{r})$ by a Fourier transform. In the basis of Bloch-like wave functions the single-particle Matsubara Green's function in the zero-temperature limit is defined as

$$G_{ab}(\tau, \boldsymbol{k}) = -\langle 0| \mathcal{T} c_{\boldsymbol{k}a}(\tau) c^\dagger_{\boldsymbol{k}b} |0\rangle , \tag{3.3}$$

where $c^\dagger_{\boldsymbol{k}a}$ ($c_{\boldsymbol{k}a}$) creates (annihilates) an electron in the Bloch-like state with crystal momentum $\boldsymbol{k}$ and orbital index a. The time evolution is in imaginary time τ. $\mathcal{T}$ denotes time ordering in imaginary time and $|0\rangle$ denotes the ground state, which in the following we assume to be non-degenerate. We include the chemical potential μ in the Hamiltonian. Note that naively the chemical potential in an interacting insulator can be placed anywhere inside the gap of the spectral function at zero temperature. This may lead to ambiguities in the topological classification of G near phase boundaries where the single-particle gap does not close and the change instead happens through an eigenvalue being zero. However the chemical potential in the zero temperature limit $\mu(T \to 0)$ is unique and can be calculated by ensuring fixed particle density as a function of T and then taking the zero temperature limit. See also the discussion in Ref. [108]. With a Fourier transform one can go to imaginary frequencies $i\omega$, where here in the zero temperature limit the discrete Matsubara frequencies $i\omega_n$ become continuous $i\omega_n \to i\omega$. The Lehmann representation of the zero temperature Matsubara Green's function is

$$G_{ab}(i\omega, \boldsymbol{k}) = \sum_m \left[\frac{\langle 0| c_{\boldsymbol{k}a} |m\rangle \langle m| c^\dagger_{\boldsymbol{k}b} |0\rangle}{i\omega - (E_m - E_0)} + \frac{\langle m| c_{\boldsymbol{k}a} |0\rangle \langle 0| c^\dagger_{\boldsymbol{k}b} |m\rangle}{i\omega + (E_m - E_0)} \right]. \tag{3.4}$$

For the ground state having N particles the sum runs over the exact eigenstates $|m\rangle$ of the many-body Hamiltonian with $N+1$ and $N-1$ particles. The E_m are the corresponding exact energy eigenvalues. E_0 is the ground state energy. For the special case of a non-interacting Hamiltonian the Matsubara Green's function can be simply written in terms of the corresponding Bloch Hamiltonian, see Eq. (3.1).

The Matsubara Green's function $G(i\omega, \boldsymbol{k})$ has an analytical extension from the imaginary axis to the whole complex plane except the real axis, i.e. $G(z, \boldsymbol{k})$ with $z \in \mathbb{C} \setminus \mathbb{R}$. The spectral representation of $G(z, \boldsymbol{k})$ is

$$G(z, \boldsymbol{k}) = \int_{-\infty}^{\infty} \frac{\mathrm{d}\omega'}{2\pi} \frac{A(\omega', \boldsymbol{k})}{z - \omega'} \tag{3.5}$$

with the matrix elements $A_{ab}(\omega, \boldsymbol{k})$ of the spectral function given by

$$\begin{aligned} A_{ab}(\omega, \boldsymbol{k}) = &\sum_n \langle 0| c_{\boldsymbol{k}a} |n\rangle \langle n| c^\dagger_{\boldsymbol{k}b} |0\rangle 2\pi\delta\big(\omega - (E_n - E_0)\big) \\ &+ \sum_n \langle n| c_{\boldsymbol{k}a} |0\rangle \langle 0| c^\dagger_{\boldsymbol{k}b} |n\rangle 2\pi\delta\big(\omega - (E_0 - E_n)\big), \end{aligned} \tag{3.6}$$

where $\omega \in \mathbb{R}$. Inserting Eq. (3.6) into Eq. (3.5) reproduces the Lehmann representation in Eq. (3.4). From Eq. 3.5 one can directly see that $G(z, \boldsymbol{k})$ has poles on the real axis. For the case of an infinite crystal the poles of $G(z, \boldsymbol{k})$ become dense and form a branch cut [109]. It can be shown from its definition that the spectral function is Hermitian and positive semi-definite for all $\boldsymbol{k}$ and ω. For a vector $\boldsymbol{v}$ with the same dimension as the spectral function and $||\boldsymbol{v}|| = 1$ we have

$$
\begin{aligned}
&\sum_{a,b} v_a^* A_{a,b}(\omega,\boldsymbol{k}) v_b \\
&= \sum_{ab}\left(\sum_n v_a^* \langle 0| c_{\boldsymbol{k}a} |n\rangle \langle n| c_{\boldsymbol{k}b}^\dagger |0\rangle v_b 2\pi\delta\big(\omega-(E_n-E_0)\big)\right) \\
&\quad + \sum_{ab}\left(\sum_n v_a^* \langle n| c_{\boldsymbol{k}a} |0\rangle \langle 0| c_{\boldsymbol{k}b}^\dagger |n\rangle v_b 2\pi\delta\big(\omega-(E_0-E_n)\big)\right) \\
&= \sum_n |\langle n|\left(\sum_b v_b c_{\boldsymbol{k}b}^\dagger\right)|0\rangle|^2 2\pi\delta\big(\omega-(E_n-E_0)\big) + \sum_n |\langle 0|\left(\sum_b v_b c_{\boldsymbol{k}b}^\dagger\right)|n\rangle|^2 2\pi\delta\big(\omega-(E_0-E_n)\big) \\
&\geq 0. \qquad (3.7)
\end{aligned}
$$

where * denotes complex conjugation. Further, taking again a vector $\boldsymbol{v}$ with the same dimension as the spectral function and $||\boldsymbol{v}|| = 1$ the spectral function is normalized in the following sense

$$
\begin{aligned}
&\int_{-\infty}^{\infty} \frac{\mathrm{d}\omega}{2\pi} \sum_{a,b} v_a^* A_{a,b}(\omega,\boldsymbol{k}) v_b \\
&= \sum_{ab} v_a^* \langle 0| \{c_{\boldsymbol{k}a}, c_{\boldsymbol{k}b}^\dagger\} |0\rangle v_b \\
&= \sum_{a,b} v_a^* v_b \delta_{ab} \\
&= 1, \qquad (3.8)
\end{aligned}
$$

Every complex matrix can be decomposed into a Hermitian and an antihermitian part. Since $A(\omega,\boldsymbol{k})$ is Hermitian and with $z = x + iy$ with $x, y \in \mathbb{R}$ we can write the Green's function as

$$
G(z,\boldsymbol{k}) = \int_{-\infty}^{\infty} \frac{d\omega'}{2\pi} A(\omega',\boldsymbol{k}) \frac{(x-\omega')}{(x-\omega')^2+y^2} - i\int_{-\infty}^{\infty} \frac{d\omega'}{2\pi} A(\omega',\boldsymbol{k}) \frac{y}{(x-\omega')^2+y^2}, \qquad (3.9)
$$

which defines a decomposition into an Hermitian and an antihermitian part $G = G_1 + iG_2$ with both G_1 and G_2 being Hermitian. Evaluating the limit of z approaching the real axis we must distinguish between taking the limit coming from the upper or the lower complex plane. For $\eta > 0$ and $\omega \in \mathbb{R}$ one obtains

$$
\lim_{\eta\to 0} G(\omega \pm i\eta, \boldsymbol{k}) = \mathcal{P}\int_{-\infty}^{\infty} \frac{d\omega'}{2\pi} \frac{A(\omega',\boldsymbol{k})}{(\omega-\omega')} \mp \frac{i}{2} A(\omega,\boldsymbol{k}), \qquad (3.10)
$$

where $\mathcal{P}$ denotes the Cauchy principal value.

For the analysis of symmetry-protected topological invariants in terms of the zero temperature Matsubara Green's function [73–80] it is assumed that the exact ground state of the many-body Hamiltonian is unique and the chemical potential is included in the many-body Hamiltonian. In this case, the topological invariants are well defined and cannot change under continuous changes of the Green's function as long as the GNSC-conditions (gapped, non-singular, symmetries preserved, continuously differentiable) which we define below, are fulfilled.

***Definition* 1.** *A Matsubara Green's function $G(i\omega,\boldsymbol{k})$ with associated spectral function $A(\omega,\boldsymbol{k})$ together with a set of protecting symmetries fulfills the GNSC-conditions if all following conditions hold:*

1. *There is a non-zero gap in $A(\omega,\boldsymbol{k})$ at zero frequency, i.e. there exists an $\epsilon > 0$ such that $A(\omega,\boldsymbol{k}) = 0$ for all $\omega \in [-\epsilon,\epsilon]$ for all $\boldsymbol{k}$.*
2. *$G(0,\boldsymbol{k})$ is non-singular for all $\boldsymbol{k}$.*

3. G does not break a symmetry contained in the set of protecting symmetries.

4. $G(i\omega, \boldsymbol{k})$ is continuously differentiable in $\boldsymbol{k}$ for all $i\omega$.

$G(0, \boldsymbol{k})$ being nonsingular implies that all eigenvalues are non-zero for all $\boldsymbol{k}$. The intuition between such a continuous deformation is to continuously change the parameters of the many-body Hamiltonian. The Green's function then also changes continuously if there is no phase transition. It may be noted that G does not break a spatial symmetry means that $G(i\omega, \boldsymbol{k})$ commutes with the band representation matrices as we will discussed in Sec. 3.6. For the implications of TR, PH and CS on G, see Ref. [76].

We now focus on the case where the spectral function has a non-zero gap at zero frequency for every k-point, i.e. the first condition in *Definition* 1. This causes both limits $\lim_{\eta\to 0} G(\omega \pm i\eta, \boldsymbol{k})$ to coincide within the gap and as a consequence $G(i\omega, \boldsymbol{k})$ is analytic in $i\omega$. Further in this case $G(0, \boldsymbol{k})$ is Hermitian, because the antihermitian part $iG_2(0, \boldsymbol{k})$ is directly proportional to the spectral function $A(0, \boldsymbol{k})$ and hence vanishes, as can be seen from Eq. (3.10).

We now show that for a gapped spectral function the absolute values of the eigenvalues of $G(0, \boldsymbol{k})$ are bounded from above. To our knowledge this has not been shown before Ref. [1]. Since the gap is non-zero, there exists an $\epsilon > 0$ such that the interval $[-\epsilon, \epsilon]$ lies inside the gap. For a vector $\boldsymbol{v}$ with the same number of elements as G has rows (or columns) and $||\boldsymbol{v}|| = 1$ we can make the following estimate

$$
\begin{aligned}
&|\sum_{ab} v_a^* G_{ab}(0, \boldsymbol{k}) v_b| \\
&\leq \sum_{ab} \int_{-\infty}^{\infty} \frac{d\omega'}{2\pi} v_a^* A_{ab}(\omega', \boldsymbol{k}) v_b \frac{1}{|\omega'|} \\
&= \sum_{ab} \int_{\mathbb{R}\setminus[-\epsilon,\epsilon]} \frac{d\omega'}{2\pi} v_a^* A_{ab}(\omega', \boldsymbol{k}) v_b \frac{1}{|\omega'|} \\
&\leq \frac{1}{\epsilon} \sum_{ab} \int_{\mathbb{R}\setminus[-\epsilon,\epsilon]} \frac{d\omega'}{2\pi} v_a^* A_{ab}(\omega', \boldsymbol{k}) v_b \\
&= \frac{1}{\epsilon}.
\end{aligned} \tag{3.11}
$$

Going from the first to the second line we have used that the spectral function $A(\omega, \boldsymbol{k})$ is positive semi-definite. Using these properties it follows that the eigenvalues of $G(0, \boldsymbol{k})$ are real and and their absolute value is bounded from above.

3.3 Topological Hamiltonian

In Ref. [79] it was shown that it is sufficient to focus on the Green's function at zero frequency to obtain the topological invariants for the CAZ symmetry classes. Equivalently it is possible to define an auxiliary non-interacting Hamiltonian [80] – the topological Hamiltonian – which has the same topological invariants as the full interacting single-particle Green's function

$$\mathcal{H}_{\mathrm{T}}(\mathbf{k}) = -G^{-1}(0, \mathbf{k}). \tag{3.12}$$

In Sec. 3.2 we showed that for a gap in the spectral weight around zero frequency the eigenvalues of $G(0, \boldsymbol{k})$ are real and and their absolute value is bounded from above. It follows that the topological Hamiltonian, which for $G(0, \boldsymbol{k})$ non-singular (i.e. $\det\big(G(0, \boldsymbol{k})\big) \neq 0$) can be defined by Eq. (3.12), is a Hermitian matrix and has real eigenvalues with their absolute value being bounded from below for all k-points.

The analysis of topological invariants in terms of the Green's function has been applied to a variety of model systems in which the topology is protected by symmetries in the CAZ symmetry classes [110–119] and it has been shown that, if at least one of the GNSC-conditions is violated, the respective CAZ invariant is not well defined anymore [76, 110].

3.4 Spatial symmetry representations

In this section we show how Bloch-like wave functions and the corresponding creation and annihilation operators transform under spatial symmetries. Generally a crystal is a periodic arrangement of atoms in a certain dimension. Additionally, a crystal can have spatial symmetries. These spatial symmetries form a group. In three dimensions all possibilities are enumareted in the 230 space groups.

The Matsubara Green's function $G(i\omega_n, \boldsymbol{k})$ is expressed in the basis of Bloch-like states $\psi_{\boldsymbol{k}a}(\boldsymbol{r})$ that are the Fourier transforms of Wannier functions $W_{ia}(\boldsymbol{r})$, where $\boldsymbol{R}$ is the lattice vector or the unit cell i and a the orbital index. To see how the Matsubara Green's function transforms under spatial symmetries we need to see first how Bloch-like basis functions transform.

In Sec. 3.4.1 we give some background on representation theory of groups. In Sec. 3.4.2 we discuss the distinction between reducible and irreducible representations of a group. In Sec. 3.4.3 we derive representations for spatial symmetries under which Bloch-like wavefunctions transform. In Sec. 3.4.4 we show how the corresponding creation and annihilation operators transform.

3.4.1 Group representations

Generally, if we consider an n-dimensional vector space V that is spanned by the basis functions $\{\psi_1, .., \psi_n\}$, then a representation is a homomorphism $\rho : \mathcal{G} \to GL(V)$. The action of a group element $h \in \mathcal{G}$ in this basis can be represented by $n \times n$-dimensional matrices $\rho_{\mathcal{G}}$

$$\rho_{\mathcal{G}}(h) = \begin{pmatrix} \rho_{\mathcal{G}}(h)_{11} & \rho_{\mathcal{G}}(h)_{12} & \cdots & \rho_{\mathcal{G}}(h)_{1n} \\ \rho_{\mathcal{G}}(h)_{21} & \rho_{\mathcal{G}}(h)_{22} & \cdots & \rho_{\mathcal{G}}(h)_{2n} \\ \vdots & \vdots & \ddots & \vdots \\ \rho_{\mathcal{G}}(h)_{n1} & \rho_{\mathcal{G}}(h)_{n2} & \cdots & \rho_{\mathcal{G}}(h)_{nn} \end{pmatrix} \tag{3.13}$$

Acting h on $\psi \in V$ translates to a matrix multiplication $\rho_{\mathcal{G}}(h)\psi$. The group product of two elements $g, h \in \mathcal{G}$ is translated into a matrix multiplication

$$\rho_{\mathcal{G}}(gh) = \rho_{\mathcal{G}}(g)\rho_{\mathcal{G}}(h). \tag{3.14}$$

3.4.2 Reducible and irreducible representations

A representation is called reducible if there is a subspace $W \subset V$ that is invariant under each $h \in G$. That means $\forall h \in \mathcal{G}$ and $\phi \in W$ it holds

$$\rho_{\mathcal{G}}(h)\phi \in W. \tag{3.15}$$

If a representation is not reducible it is called irreducible representation (irrep).

In our context we will deal with an orthonormal basis and symmetry operations that have unitary representation matrices i.e.

$$\rho_{\mathcal{G}}(g^{-1}) = \rho^{\dagger}_{\mathcal{G}}(g), \tag{3.16}$$

where here † denotes the adjoint of a matrix. In this case each reducible representation can be brought into block diagonal form via a unitary basis transformation U that is the same for every $h \in \mathcal{G}$

$$\rho_{\mathcal{G}}(h) = U\rho_{\mathcal{G}}(gh)U^{\dagger} = \begin{pmatrix} \rho^{(1)}_{\mathcal{G}}(h) & 0 & \cdots & 0 \\ 0 & \rho^{(2)}_{\mathcal{G}}(h) & \cdots & 0 \\ \vdots & \vdots & \ddots & \vdots \\ 0 & 0 & \cdots & \rho^{(m)}_{\mathcal{G}}(h) \end{pmatrix} = \rho^{(1)}_{\mathcal{G}}(h) \oplus \rho^{(2)}_{\mathcal{G}}(h) \oplus \cdots \oplus \rho^{(n)}_{\mathcal{G}}(h) \tag{3.17}$$

where each block corresponds to a irreducible representation with the dimension of the respective invariant subspace.

Proof. Let $\psi \in W$ and $\phi \in W^\perp$ with W invariant under any symmetry transformation $h \in \mathcal{G}$. By construction ϕ and ψ are orthogonal i.e. $\langle\phi|\psi\rangle = 0$ and $\rho_\mathcal{G}(h)\psi \in \mathcal{G}$. We have for all $h \in \mathcal{G}$

$$0 = \langle\phi|\rho_\mathcal{G}(h)\psi\rangle = \langle\rho_\mathcal{G}^\dagger(h)\phi|\psi\rangle = \langle\rho_\mathcal{G}(h^{-1})\phi|\psi\rangle\,. \tag{3.18}$$

Since h runs over all elements in $\mathcal{G}$ it holds

$$\langle\psi|\rho_\mathcal{G}(h)\phi\rangle = 0 \tag{3.19}$$

Hence, $\rho_\mathcal{G}(h)\phi \in W^\perp$ and the offdiagonal matrix elements of $\rho_\mathcal{G}(h)$ between the subspaces W and $W^\perp$ must vanish. Repeating the argument for all invariant subspaces yields that $\rho_\mathcal{G}(h)$ must be blockdiagonal. □

3.4.3 Spatial symmetry representation for Bloch-like functions

In the following we show how the Bloch-like basis states transform under spatial symmetries. We consider Bloch like-wave functions that are constructed from Wannier functions that are consistent with the symmetries of the respective spacegroup of the crystal. First, we show how Wannier functions transform under spatial symmetries. This section is based on Refs. [56, 57], although to be consistent with the rest of this thesis the notation differs.

In a given space group $\mathcal{G}$ the spatial symmetries $h \in \mathcal{G}$ can be denoted as $h = \{R|\mathbf{v}\} \in \mathcal{G}$ acting in real space as $\boldsymbol{r} \to R\boldsymbol{r}+\mathbf{v}$. Here, $\mathbf{v}$ is a shift and R is the part of h that leaves at least one point invariant, i.e. R is a rotation, reflection, inversion or a combination of those. Here and in the following we set $\boldsymbol{k}' \equiv R\boldsymbol{k}$, with $\boldsymbol{k}'$ being the corresponding k-point in the first Brillouin zone. A crystal can be thought of as a collection of periodically placed Wannier functions that are consistent with the symmetries of the space group the crystal belongs to. Under the symmetry operations these Wannier functions have to transform into each other. The action of a spatial symmetry $h = \{R|\mathbf{v}\} \in \mathcal{G}$ is given by

$$\begin{aligned}
\rho_\mathcal{G}(\{R|\mathbf{v}\})W_{ia}(\boldsymbol{r}) &= \rho_\mathcal{G}(\{R|0\})\rho_\mathcal{G}(\{E|\mathbf{v}\})W_{ia}(\boldsymbol{r}) \\
&= \rho_\mathcal{G}(\{E|R\mathbf{v}\})\rho_\mathcal{G}(\{R|0\})W_{ia}(\boldsymbol{r}) \\
&= \rho_\mathcal{G}(\{E|R\mathbf{v}\})W_{ia}(R^{-1}\boldsymbol{r}) \\
&= W_{ia}(R^{-1}\boldsymbol{r} - R\mathbf{v}),
\end{aligned} \tag{3.20}$$

where here E is the identity. It is possible to express the transformed Wannier function on the right side through the basis of the original Wannier functions. This will give us the explicit form of the symmetry representations $\rho_\mathcal{G}(h)$.

To do so we decompose the orbital index a into two indices $a = (r_a, q_a)$, where r_a is the site in the unit cell and which belongs to a Wyckoff position and q_a labels the orbital.

For simplicity we consider a set of Wannier functions in a single Wyckoff position of some multiplicity. In this case r_a just labels the sites in one Wyckoff position. The site symmetry group $\mathcal{G}_{r_a}$ of a site at $\boldsymbol{r}_a$ is defined by those symmetry operations that leave that site invariant

$$\mathcal{G}_{r_a} = \{g \in \mathcal{G} | g\boldsymbol{r}_{r_a} = \boldsymbol{r}_{r_a}\} \tag{3.21}$$

This group is isomorphic to a crystallographic point group. If $h \in \mathcal{G}_1$, then the Wannier functions transform under some representation

$$\rho_\mathcal{G}(h)W_{01q_a}(\boldsymbol{r}) = \sum_{q_b} D(h)_{q_b q_a} W_{01q_b}(\boldsymbol{r}). \tag{3.22}$$

Different sites in a unitcell in the same Wyckoff position are related by symmetry operations $g_{r_a} \in \mathcal{G}$

$$g_{r_a}\boldsymbol{r}_1 = \boldsymbol{r}_{r_a}. \tag{3.23}$$

If $h \in \mathcal{G}_{r_a}$, then

$$g = g_{r_a}^{-1} h g_{r_a} \in \mathcal{G}_1. \tag{3.24}$$

This means the $\mathcal{G}_{r_a}$ for the same Wyckoff position are isomorphic. Hence, we get

$$\begin{aligned}
\rho_{\mathcal{G}}(h) W_{0 r_a q_a}(\boldsymbol{r}) &= \rho_{\mathcal{G}}(g_{r_a} g g_{r_a}^{-1}) W_{0 r_a q_a}(\boldsymbol{r}) \\
&= \rho_{\mathcal{G}}(g_{r_a}) \rho_{\mathcal{G}}(g) \rho_{\mathcal{G}}(g_{r_a}^{-1}) W_{0 r_a q_a}(\boldsymbol{r}) \\
&= \rho_{\mathcal{G}}(g_{r_a}) \rho_{\mathcal{G}}(g) W_{01 q_a}(\boldsymbol{r}) \\
&= \rho_{\mathcal{G}}(g_{r_a}) \sum_{q_b} D(g)_{q_b q_a} W_{01 q_b}(\boldsymbol{r}) \\
&= \sum_{q_b} D(g)_{q_b q_a} W_{0 r_a q_b}(\boldsymbol{r}).
\end{aligned} \tag{3.25}$$

So, Wannier functions in the same unit cell in the same Wyckoff position transform under the same representations.

Now in a next step we consider $h \in \mathcal{G}$ that takes a site at $\boldsymbol{r}_{r_a}$ to a site at $\boldsymbol{r}_{r_b} + \boldsymbol{R}_{ab}$ in a different unitcell, where $\boldsymbol{R}_{ab}$ is a lattice vector

$$h \boldsymbol{r}_{r_a} = \boldsymbol{r}_{r_b} + \boldsymbol{R}_{ab}. \tag{3.26}$$

It follows that

$$\{E| - \boldsymbol{R}_{ab}\} h g_{r_a} \boldsymbol{r}_1 = g_{r_b} \boldsymbol{r}_1. \tag{3.27}$$

and consequently

$$g_{r_a r_b} = g_{r_b}^{-1} \{E| - \boldsymbol{R}_{ab}\} h g_{r_a} \in \mathcal{G}_1. \tag{3.28}$$

Since $g_{r_a r_b} \in \mathcal{G}_1$ we know its representation namely $D(g_{r_a r_b})$. We can write this last equation as

$$h = \{E|\boldsymbol{R}_{ab}\} g_{r_b} g_{r_a r_b} g_{r_a}^{-1}. \tag{3.29}$$

With that we get the representation for any Wannier function $W_{i r_a q_a}(\boldsymbol{r})$ for $h = \{R|\mathbf{v}\} \in \mathcal{G}$

$$\begin{aligned}
\rho_{\mathcal{G}}(h) W_{i r_a q_a}(\boldsymbol{r}) &= \rho_{\mathcal{G}}(h) \rho_{\mathcal{G}}(\{E|\mathbf{R_i}\}) W_{0 r_a q_a}(\boldsymbol{r}) \\
&= \rho_{\mathcal{G}}(\{E|R\mathbf{R_i}\}) \rho_{\mathcal{G}}(h) W_{0 r_a q_a}(\boldsymbol{r}) \\
&= \rho_{\mathcal{G}}(\{E|R\mathbf{R_i}\}) \rho_{\mathcal{G}}(\{E|\boldsymbol{R}_{ab}\}) \rho_{\mathcal{G}}(g_{r_b}) \rho_{\mathcal{G}}(g_{r_a r_b}) \rho_{\mathcal{G}}(g_{r_a}^{-1}) W_{i r_a q_a}(\boldsymbol{r}) \\
&= \rho_{\mathcal{G}}(\{E|R\mathbf{R_i} + \boldsymbol{R}_{ab}\}) \rho_{\mathcal{G}}(g_{r_b}) \rho_{\mathcal{G}}(g_{r_a r_b}) \rho_{\mathcal{G}}(g_{r_a}^{-1}) \rho_{\mathcal{G}}(g_{r_a}) W_{i 1 q_a}(\boldsymbol{r}) \\
&= \rho_{\mathcal{G}}(\{E|R\mathbf{R_i} + \boldsymbol{R}_{ab}\}) \sum_{q_b} D(g_{r_a r_b})_{q_b q_a} W_{0 r_b q_b}(\boldsymbol{r}) \\
&= \sum_{q_b} D(g_{r_a r_b})_{q_b q_a} W_{0 r_b q_b}(\boldsymbol{r} - R\mathbf{R_i} - \boldsymbol{R}_{ab}).
\end{aligned} \tag{3.30}$$

Note that for a given $h \in \mathcal{G}$ the corresponding $\boldsymbol{R}_{ab}$ is uniquely defined by Eq. 3.26.

From the representation for the Wannier functions Eq. 3.30 we can get the representations for the Bloch-like functions

$$\begin{aligned}\rho^{\boldsymbol{k}}_{\mathcal{G}}(h)\psi_{\boldsymbol{k}r_aq_a}(\boldsymbol{r}) &= \rho^{\boldsymbol{k}}_{\mathcal{G}}(h)\sum_{\boldsymbol{R}_i} e^{i\boldsymbol{k}\cdot\boldsymbol{R}_i} W_{ir_aq_a}(\boldsymbol{r}) \\ &= \sum_{\boldsymbol{R}_i} e^{i\boldsymbol{k}\cdot\boldsymbol{R}_i}\sum_{q_b} D(g_{r_ar_b})_{q_bq_a} W_{0r_bq_b}(\boldsymbol{r} - R\mathbf{R_i} - \boldsymbol{R}_{ab}) \\ &= \sum_{q_b} e^{-i(R\boldsymbol{k})\cdot\boldsymbol{R}_{ab}} D(g_{r_ar_b})_{q_bq_a}\sum_{\boldsymbol{R}_i} e^{i(R\boldsymbol{k})\cdot(R\boldsymbol{R}_i+\boldsymbol{R}_{ab})} W_{0r_bq_b}(\boldsymbol{r} - R\mathbf{R_i} - \boldsymbol{R}_{ab}) \\ &= \sum_{q_b} e^{-i(R\boldsymbol{k})\cdot\boldsymbol{R}_{ab}} D(g_{r_ar_b})_{q_bq_a}\psi_{(R\boldsymbol{k})r_bq_b}(\boldsymbol{r}). \end{aligned} \tag{3.31}$$

Going from the second to the third line we have used that R is orthogonal. So the Bloch-like wave functions transform with the band-representations that are given by

$$\left(\rho^{\boldsymbol{k}}_{\mathcal{G}}(h)\right)_{r_bq_b,r_aq_a} = e^{-i(R\boldsymbol{k})\cdot\boldsymbol{R}_{ab}} D(g_{r_ar_b})_{q_bq_a}. \tag{3.32}$$

Writing the index for the site and the orbital index as one combined orbital index we can simply write

$$\rho_{\mathcal{G}}(h)\psi_{\boldsymbol{k}a} = \sum_b \rho^{\boldsymbol{k}}_{\mathcal{G}}(h)_{ba}\psi_{\boldsymbol{k}'a}. \tag{3.33}$$

where $\boldsymbol{k}'$ is the corresponding k-point in the first Brillouin zone i.e. $\boldsymbol{k}' = R\boldsymbol{k}+\boldsymbol{K}$ with a reciprocal lattice vector $\boldsymbol{K}$. For sets of Wannier functions in other Wyckoff positions one can construct the corresponding band representations in similar fashion and then take the direct sum and the form of Eq. 3.33 stays unchanged. The band representations $\rho^{\boldsymbol{k}}_{\mathcal{G}}(h)$ are sets of unitary matrices with the dimension given by the number of orbitals in the unit cell (including spin).

3.4.4 Spatial symmetry operations for creation and annihilation operators

Now we want to see how the spatial symmetries act on creation and annihilation operators. In this way we see can see later how the Bloch Hamiltonian transforms under spatial symmetries and it will also become important later on when we investigate how the Matsubara Green's function transforms. We associate a unitary operator U_h with the spatial symmetry operation $h \in \mathcal{G}$. From the transformation of the Bloch-like single particle states Eq. 3.33 it follows that U_h acts on creation and annihilation operators as

$$U_h c^\dagger_{\boldsymbol{k}a} U_h^\dagger = \sum_b \rho^{\boldsymbol{k}}_{\mathcal{G}}(h)_{ba} c^\dagger_{\boldsymbol{k}'b}, \tag{3.34}$$

$$U_h c_{\boldsymbol{k}a} U_h^\dagger = \sum_b \left(\rho^{\boldsymbol{k}}_{\mathcal{G}}(h)^\dagger\right)_{ab} c_{\boldsymbol{k}'b}, \tag{3.35}$$

where $(^\dagger)$ denotes the conjugate transpose of a matrix. a and b again labels the orbital indices that here can include spin and $\boldsymbol{k}' = R\boldsymbol{k} + \boldsymbol{K}$, with a reciprocal lattice vector $\boldsymbol{K}$ such that $\boldsymbol{k}'$ lies in the first Brillouin zone. So creation and annihilation operators for the Bloch like basis states also transform with the band representations.

To conclude this section we have seen that a Bloch-like function $\psi_{a\boldsymbol{k}}$ and the associated creation and annihilation operatores $c^\dagger_{\boldsymbol{k}a}$ and $c_{\boldsymbol{k}a}$ in a crystal with space group $\mathcal{G}$ for $h \in \mathcal{G}$ transform under the so called band representations $\rho^{\boldsymbol{k}}_{\mathcal{G}}(h)$ by Eq. 3.33, 3.34 and 3.35.

3.5 Elementary Band representations

In this section we will see which consequences spatial symmetries have for the Bloch Hamiltonian. We will see that the bands at high symmetry k-points can be labeled by irrpes of the respective little group. This labeling implies certain compatibility relations on how the bands connect in k-space. These

relations can be used to construct EBRs. EBRs can then be used to identify non-trivial topology in a system. A large parts of this section is based on Refs. [56, 57] and is a brief summary of the central ideas of these works.

A general Hamilton operator H is invariant under the action of $h \in \mathcal{G}$ if it commutes with the associated operator U_h or equivalently

$$H = U_h^\dagger H U_h. \tag{3.36}$$

Now we investigate the implications of spatial symmetries for the Bloch Hamiltonian. A noninteracting Hamiltonian in a periodic system has the form

$$H_0 = \sum_{\boldsymbol{k}} H_0^{\boldsymbol{k}} = \sum_{\boldsymbol{k}} \sum_{ab} c_{\boldsymbol{k}a}^\dagger \big(\mathcal{H}(\boldsymbol{k})\big)_{ab} c_{\boldsymbol{k}b}. \tag{3.37}$$

where $\mathcal{H}(\boldsymbol{k})$ is the Bloch Hamiltonian matrix. The Hamiltonian transforms under symmetries as

$$\begin{aligned} H_0 &= U_h H_0 U_h^\dagger \\ &= \sum_{\boldsymbol{k}ab} U_h c_{\boldsymbol{k}a}^\dagger \big(\mathcal{H}(\boldsymbol{k})\big)_{ab} c_{\boldsymbol{k}b} U_h^\dagger \\ &= \sum_{\boldsymbol{k}abcd} c_{\boldsymbol{k}'c}^\dagger \rho_{\mathcal{G}}^{\boldsymbol{k}}(h)_{ca} \big(\mathcal{H}(\boldsymbol{k})\big)_{ab} \rho_{\mathcal{G}}^{\boldsymbol{k}}(h)_{bd}^\dagger c_{\boldsymbol{k}'d}, \end{aligned} \tag{3.38}$$

So for the Bloch Hamiltonian it holds

$$\big(\mathcal{H}(\boldsymbol{k}')\big)_{cd} = \sum_{ab} \rho_{\mathcal{G}}^{\boldsymbol{k}}(h)_{ca} \big(\mathcal{H}(\boldsymbol{k})\big)_{ab} \rho_{\mathcal{G}}^{\boldsymbol{k}}(h)_{bd}^\dagger. \tag{3.39}$$

where again $\boldsymbol{k}' = R\boldsymbol{k} + \boldsymbol{K}$ with a reciprocal lattice vector $\boldsymbol{K}$ such that $\boldsymbol{k}'$ is in the first Brillouin zone. The little group of a k-point $\boldsymbol{k}$ is defined as

$$\mathcal{G}_{\boldsymbol{k}} = \{h = \{R|\mathbf{v}\} \in \mathcal{G} | \boldsymbol{k} = \boldsymbol{k}'\}, \tag{3.40}$$

If H_0 is invariant under a spatial symmetry h, then from the above relation it follows that at all k-points with $h \in \mathcal{G}_{\boldsymbol{k}}$ the Bloch Hamiltonian matrix $\mathcal{H}(\boldsymbol{k})$ commutes with the band representation matrix $\rho_{\mathcal{G}}^{\boldsymbol{k}}(h)$. From this commutative property it follows that eigenstates of $\mathcal{H}(\boldsymbol{k})$ transform as irreps of $\mathcal{G}_{\boldsymbol{k}}$. Hence, at each $\boldsymbol{k}$ the bands that correspond to the eigenstates can be labeled by the irreps of the corresponding little group $\mathcal{G}_{\boldsymbol{k}}$.

Labeling bands at each k-point by irreps of the respective little group places conditions on how bands in the Brillouin zone are connected. In particular, if one considers a high-symmetry line starting from a high-symmetry point in k-space then, the little group of the line must be a subgroup of the little group of a point. So, each irrep at the high-symmetry point becomes a sum of irreps that appear on the line. The irreps along the line are completely determined by the irreps that appear at the point. The same applies to high symmetry lines and and planes. This decomposition of irrepes is called compatibility relations.

In Sec. 3.4.3 we have seen that placing a set of Wannier functions in a Wyckoff induces a band representation. Band representations can be decomposed into its elementary building blocks the so called elementary band representations (EBRs). A band representation, is elementary if and only if it can be induced from an irreducible representation of a maximal site-symmetry group and if it is not an exception (see Ref. [57] for a list of exceptions). A site-symmetry group $\mathcal{G}_{r_a}$ is non-maximal if there exists a finite group $\mathcal{G}' \neq \mathcal{G}_{r_a}$, such that $\mathcal{G}_{r_a} \subset \mathcal{G}' \subset \mathcal{G}$. A site-symmetry group that is not non-maximal is maximal. All possible EBRs for all space groups are tabulated on the Bilbao crystallographic Server [120, 121].

Now we will see how EBRs can help to decide if a set of bands is topological. A set of bands is in the atomic limit if they originate from a set of Wannier functions that are consistent with the symmetries of the crystal. Any set of bands that is in an atomic limit can be written as a direct sum of EBRs, because EBRs are constructed in such a way that they are the elementary building blocks of all band

structures that correspond to a symmetry preserving atomic limit. An isolated group of bands that stems not from such an atomic limit is topological. In this case the topological set of bands correspond to a so-called quasiband representation, i.e. any solution of the compatibility relations. This is the case if we have a disconnected EBR at the Fermi level with the chemical potential lying in the gap.

The reason why the occupied bands of such a disconnected EBR at the Fermi level must be topological is the following. The multiplicity of the irreps at high symmetry k-points of the occupied bands must be maintained under continuous deformations of the Hamiltonian as long as symmetries and the gap is maintained. It follows that if there is a disconnected EBR with the gap at zero energy then it has to stay disconnected under continuous changes while maintaining the gap. So one cannot continuously deform such a system into an atomic limit without closing the gap or breaking the symmetries. Hence the system is topological. Labeling bands by irreps at the high symmetry k-points and identifying the EBRs is hence a way to identify a topologically non-trivial system.

Note aslo the possibility of a so called obstructed atomic limit. Such a system is topologically trivial, but the position of the Wannier functions that induce the EBR does not coincide with the original atom position and it is not possible to continuously deform the system without breaking the symmetries into one where the position of the Wannier function coincides with original position of the atoms.

For more details such as how to identify the irreps of a given band, the inclusion of time reversal symmetry and examples, see Refs. [56, 57].

3.6 Spatial symmetries of the Matsubara Green's function

In this section, we recall the action of spatial symmetries on the Green's function and consequently the topological Hamiltonian $\mathcal{H}_{\mathrm{T}}(\boldsymbol{k})$. We show that these always transform in the same way as non-interacting Bloch Hamiltonians. We assume a non-degenerate many-body ground state $|0\rangle$. It directly follows that the ground state is an eigenstate of every U_h, elsewise H expressed in the basis of the exact eigenstates would not commute with the spatial symmetries. Since U_h is unitary the eigenvalues must have modulus one and we can write for $h \in \mathcal{G}$

$$U_h |0\rangle = e^{i\phi_h} |0\rangle , \tag{3.41}$$

with $\phi_h \in [0, 2\pi)$. For imaginary time $\tau > 0$ we have

$$\begin{aligned}
G_{ab}(\tau, \boldsymbol{k}) &= - \langle 0| \, c_{\boldsymbol{k}a}(\tau) c^\dagger_{\boldsymbol{k}b} \, |0\rangle \\
&= - \langle 0| \, e^{H\tau} c_{\boldsymbol{k}a} e^{-H\tau} c^\dagger_{\boldsymbol{k}b} \, |0\rangle \\
&= - \langle 0| \, e^{U_h^\dagger H U_h \tau} c_{\boldsymbol{k}a} e^{-U_h^\dagger H U_h \tau} c^\dagger_{\boldsymbol{k}b} \, |0\rangle \\
&= - \langle 0| \, U_h^\dagger e^{H\tau} U_h c_{\boldsymbol{k}a} U_h^\dagger e^{-H\tau} U_h c^\dagger_{\boldsymbol{k}b} U_h^\dagger U_h \, |0\rangle \\
&= - \sum_{cd} \rho^{\boldsymbol{k}}_{\mathcal{G}}(h)^\dagger_{ac} \, \langle 0| \, c_{\boldsymbol{k}'c}(\tau) c^\dagger_{\boldsymbol{k}'d} \, |0\rangle \, \rho^{\boldsymbol{k}}_{\mathcal{G}}(h)_{db} \\
&= \sum_{cd} \rho^{\boldsymbol{k}}_{\mathcal{G}}(h)^\dagger_{ac} G_{cd}(\tau, \boldsymbol{k}') \rho^{\boldsymbol{k}}_{\mathcal{G}}(h)_{db}.
\end{aligned} \tag{3.42}$$

A similar calculation holds for $\tau < 0$. Fourier transforming to go to Matsubara frequencies i.e. $G(i\omega, \boldsymbol{k})$ yields the same result for each value of $i\omega$. The above result shows, that for a unique many-body ground state the Green's function transforms under the band representations in the same way as a (non-interacting) Bloch Hamiltonian. This makes sense because we express the Green's function in the same basis states as the Bloch Hamiltian.

Note that for a degenerate ground state the physical system at $T = 0$ has a freedom in the choice of the ground state. This freedom can result in the spontaneous breaking of a symmetry of the Hamiltonian. In this case there is also an ambiguity in the Green's function in Eq. (3.3). This can lead to the Green's function not fulfilling the above symmetry relations. For non-spatial symmetries this possibility was already observed in Ref. [110]. However, taking the zero-temperature limit from the finite temperature Matsubara Green's function in the case of a degenerate ground state, the only remaining states are the

degenerate groundstates. The resulting Green's function turns out to be an average over orthonormal basis states spanning the degenerate ground state space. Since the symmetry operators U_h are unitary, the space of ground states is invariant under their action. Hence, when taking the zero temperature limit, the Matsubara Green's function still commutes with the band representations of the spatial symmetries even for a degenerate ground state.

Similarly, provided the GNSC-conditions are fulfilled, a topological Hamiltonian $\mathcal{H}_{\mathrm{T}}(\boldsymbol{k})$ may be defined according to $\mathcal{H}_{\mathrm{T}}(\boldsymbol{k}) = -G^{-1}(0,\boldsymbol{k})$. From Eq. 3.42 it follows that the topological Hamiltonian transforms in the same way as the Green's function

$$\big(\mathcal{H}_{\mathrm{T}}(\boldsymbol{k})\big)_{ab} = \sum_{cd} \rho^{\boldsymbol{k}}_{\mathcal{G}}(h)^{\dagger}_{ac} \big(\mathcal{H}_{\mathrm{T}}(\boldsymbol{k}')\big)_{cd} \rho^{\boldsymbol{k}}_{\mathcal{G}}(h)_{db}. \tag{3.43}$$

Also, if $G(i\omega,\boldsymbol{k})$ is continuously differentiable in $\boldsymbol{k}$, $\mathcal{H}_{\mathrm{T}}(\boldsymbol{k})$ is also continuously differentiable in $\boldsymbol{k}$. It follows that the eigenvalues of $\mathcal{H}_{\mathrm{T}}(\boldsymbol{k})$ form continuous bands in k-space that can be labeled by irreps of the little group of the respective k-points. Analogous to the non-interacting case, compatibility relations yield restrictions on the connectivity of the bands. Again one can then write symmetry representations of bands as linear combinations of EBRs. Also in the case of TR present in the interacting system the resulting irreps of the little groups and EBRs have been classified and can be applied the same way as in the noninteracting case [56, 57]. One might have guessed from the beginning that the topological Hamiltonian as an effective non-interacting Hamiltonian transforms with the band representations. However, our detailed derivation also shows at which places subtleties regarding the zero temperature limit and possible degenerate groundstates, that are only possible with interactions in an insulator, come in. In the following we clarify the meaning of assigning EBRs to the bands of a topological Hamiltonian in an interacting system.

3.7 EBR-based analysis of the topological Hamiltonian: Use and limitations

In this section, we discuss the interpretation of EBR-based analysis of the topological Hamiltonian in the spirit of TQC. Analogous arguments hold for the application of a symmetry indicator analysis [61, 62] or the application of the algorithm described in Ref. [63]. For gapped non-interacting Hamiltonians, topological indices are invariant under unitary transformations of occupied (unoccupied) single-particle states. As a result, in terms of an EBR analysis we are concerned usually with the combined transformation properties of occupied single-particle states, independent of their energy ordering [56, 57]. To apply non-interacting classifications to $\mathcal{H}_{\mathrm{T}}(\boldsymbol{k})$, an equivalent distinction is required. Following Refs. [78, 79], for a Green's function fulfilling the GNSC-conditions, the eigenvalues of $\mathcal{H}_{\mathrm{T}}(\boldsymbol{k})$ can be classified as either an L-zero or an R-zero. Note that, originally the classification of R-zeros and L-zeros was used to discuss the eigenvalues of $G(0,\boldsymbol{k})$. This is equivalent to $\mathcal{H}_{\mathrm{T}}(\boldsymbol{k})$, because both share the same eigenvectors. An eigenvalue of the topological Hamiltonian $\mu_n(\boldsymbol{k})$ is called an R-zero if $\mu_n(\boldsymbol{k}) < 0$ and an L-zero if $\mu_n(\boldsymbol{k}) > 0$. Regarding the topological Hamiltonian as an effective noninteracting Hamiltonian these correspond to the occupied and the unoccupied single-particle states respectively if there is a gap at zero energy. Analogous to a non-interacting system the R-zeros and L-zeros can then each be written as a linear combination of EBRs with positive integer coefficients if they each correspond to a trivial set of bands or as a quasiband representation if they each correspond to a topological set of bands. In the case of a lattice model this means that there is a disconnected EBR with the gap at zero energy. For interacting systems, the eigenvalues can give some indication how the spectral weight is distributed on the real frequency axis. However there meaning will become clear now when we investigate what happens under continuous changes of the Green's function.

Let us consider continuously changing the parameters of the many-body Hamiltonian, while maintaining symmetries and the ground state staying non-degenerate. If the groundstate stays nondegenerate then $G(i\omega,\boldsymbol{k})$ and hence $G(0,\boldsymbol{k})$ also changes continuously on the path. As long as there are no zero eigenvalues of $G(0,\boldsymbol{k})$ the topological Hamiltonian is well defined and also changes continuously on the path. For each point on this continuous path we can label the eigenvalues of the topological Hamiltonian at high symmetry k-points by the respective little group irreps, see also Fig. 3.1. As long as the

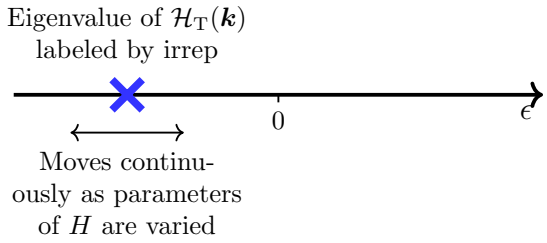

Figure 3.1: Eigenvalues of the topological Hamiltonian at high symmetry k-points can be labeled by irreps of the little group of the k-point. The gap in the spectral function at $\omega = 0$ causes the eigenvalues to be real. Depending on the sign of the eigenvalue it is either an R-zero or an L-zero. As the parameters in the many-body Hamiltonian are varied, the eigenvalues move on the real axis as long as the gap is maintained. The gap further prevents the eigenvalues from crossing zero. By assumption we excluded a zero eigenvalue of $G(0, \boldsymbol{k})$, so that all eigenvalues of the topological Hamiltonian are finite. If also the Green's function does not break a symmetry while the parameters of the many body Hamiltonian are varied, the multiplicity of irreps of R-zeros cannot change.

gap in the spectral function at zero frequency remains non-zero, as it must as long as the ground state is non-degenerate, then $G(0, \boldsymbol{k})$ remains Hermitian and the eigenvalues of the topological Hamiltonian move continuously on the real axis. Additionally, the eigenvalues cannot cross over zero, because their absolute value is bounded from below if the gap in the spectral function remains non-zero as we showed in Sec. 3.2. Further, with the condition that $G(0, \boldsymbol{k})$ never has a zero eigenvalue on the path makes the inverse of $G(0, \boldsymbol{k})$ well defined and finite. Hence the eigenvalues of the topological Hamiltonian also stay finite. Taking the above considerations together, at a high symmetry k-point the multiplicity of irreps of R-zeros (L-zeros) must be maintained under the above assumptions. The classification with respect to the EBR approach is therefore robust under continuous changes of the Green's function.

The above considerations provide an interpretation to the labeling of the bands of the topological Hamiltonian by irreps and EBRs. For any ground state of an interacting Hamiltonian that can be adiabatically connected to a non-interacting Hamiltonian without the corresponding Green's function violating the GNSC-conditions, topological invariants of the Green's function must match the non-interacting invariants obtained in the limit and can be diagnosed by an EBR analysis. Similarly, along any path on which the ground state is unique and whose endpoints are non-interacting models with ground states of different non-interacting topological indices, there must be at least one point where an L-zero becomes an R-zero and/or vice-versa. This requires at least one of the GNSC-conditions to be violated, which occur the scenarios which we again list in the following:

(i) A gap closing in the spectral function at $\omega = 0$, which corresponds to a zero-energy excitation with finite quasiparticle weight. This is analogous to a change of a topological invariant by a gap closing in the non-interacting limit. For fixed filling, the L-zero and R-zero of different irreps must exchange at $\omega = 0$ in this scenario.

(ii) A zero eigenvalue in $G(0, \boldsymbol{k})$, corresponds to a divergence in the self-energy $\Sigma(i\omega, \boldsymbol{k})$ at zero frequency, defined according to:

$$G(i\omega, \boldsymbol{k}) = \big(i\omega - \mathcal{H}(\boldsymbol{k}) - \Sigma(i\omega, \boldsymbol{k})\big)^{-1}. \tag{3.44}$$

This is only possible with interactions, as a non-interacting $G(0, \boldsymbol{k})$ cannot have zeros provided the energy spectrum is bounded. For the invariants defined previously in Refs. [73–80] the possibility of a change by a zero in the Green's function was recognized in Ref. [76] and is discussed in Refs. [110, 111, 122, 123]. In the present context, this corresponds to an L-zero and R-zero of different irreps exchanging at infinity.

(iii) A change in the symmetry of the many-body Hamiltonian or ground state. The latter case may occur via spontaneous symmetry breaking, which lowers the symmetry of both the ground state

and Green's function. As a result, any Green's function invariants associated with the broken symmetries become ill-defined. See also the discussion Ref. [110] for the case of a chiral symmetry. However, since the many-body Hamiltonian is invariant under the spontaneously broken symmetry this implies that the ground state must be degenerate. We have excluded the possibility of a degenerate ground state by assumption in our analysis.

At this point, we should note three caveats related to the above discussion and a possible correspondence of the Green's function invariants to SPT phases in the presence of interactions.

The first caveat, also discussed in Ref. [124], is that there exist uniquely interacting SPT phases, which cannot be adiabatically connected to non-interacting limits provided certain symmetries are preserved. Within these phases, Green's function invariants obtained from the topological Hamiltonian are not constrained by the requirement of non-interacting correspondence. A priori, they could take either any value when the GNSC-conditions are fulfilled, or they may not be well-defined. An example of the latter case was recently demonstrated in Ref. [4] for a 1D model exhibiting two gapped phases adiabatically connected to non-interacting limits, in addition to an interacting SPT phase. The latter was characterized by a divergence in the self-energy at zero frequency, i.e. a zero eigenvalue in $G(0, \boldsymbol{k})$ over the entire phase, so the topological Hamiltonian is ill defined in that phases.

The second caveat is that the Green's function only probes single-particle excitations. As a result, the spectrum of $\mathcal{H}_{\mathrm{T}}(\boldsymbol{k})$ may remain gapped with finite eigenvalues even as the spectrum of the many-body Hamiltonian becomes gapless with respect to a multi-particle excitation. This allows, in principle, for a transition between distinct SPT phases where the single-particle Green's function invariants do not change. On the other hand it is also possible that a transition with a gap closing of the spectral function gets replaced by a zero eigenvalue of $G(0, \boldsymbol{k})$ as discussed in Refs. [110, 123]. This then corresponds to the divergence of an eigenvalue of the toplogical Hamiltonian.

The third caveat is that the Green's function invariants may also change without a phase transition, i.e. while the ground state remains non-degenerate. This applies to cases where the topological classification breaks down upon including interactions, as explicitly demonstrated in Ref. [68] for the CAZ symmetry class BDI where the $\mathbb{Z}$ classification breaks down to a $\mathbb{Z}_4$ classification ($\mathbb{Z}_8$ without particle number conservation). For the model in Ref. [68] it was argued in Ref. [110] that the Green's function invariant changes by a zero eigenvalue in the Green's function. The same holds for an application of EBRs to the Green's function, in particular for cases where EBRs and invariants may be explicitly related. However the situation changes if the Green's function invariant is related to a physical observable as for example the Hall conductivity [107]. In this case the change of the invariant necessitates a quantum phase transition.

So we find that a precise statement in which cases there is a correspondence between SPT phases and an EBR analysis of the Green's function remains an open question. The main problem is the occurrence of zero eigenvalues in the Green's function, which is only possible with interactions.

In Ref. [110] shows that in a system with interactions in with non zero Green's function topological invariant there now can be edge zeros of the Green's function instead of the poles corresponding to gapless (single-particle) edgestates. Ref. [125] suggests an experimental protocol of revealing these boundary zeros that are elsewise invisible in experiments.

3.8 An example: EBRs for the Green's function in the SSH+U model

In this section we give a detailed demonstration of the above extension of EBRs for the Green's function on the SSH+U model. The model posses inversion symmetry which we use together with the topological Hamiltonian to determine the different topological phases in the system. The system also possesses time reversal (TR), particle-hole (PH) and chiral symmetries (CS) and thus it belongs to the CAZ symmetry class BDI with a $\mathbb{Z}$ classification for the Greens function [76]. As we will show the EBR classification determines if the corresponding topological invariant N_1 is twice an even or twice an odd integer. The factor of two is because of spin. Due to its simplicity the model is well suited to demonstrate the use of

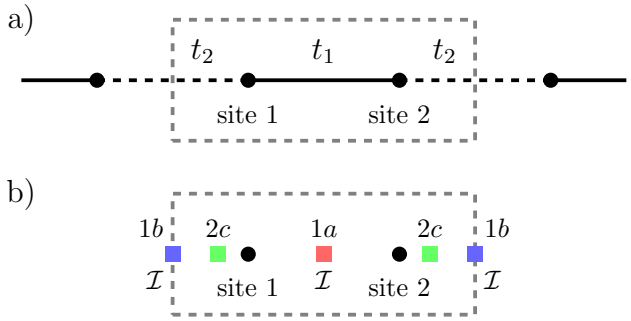

Figure 3.2: a) The SSH model with the unit cell, sites and hoppings shown, b) Unit cell of the SSH model with Wyckoff positions 1a,1b and 2c. The centers of the inversion symmetry $\mathcal{I}$ are located in 1a and 1b. See the text for the description of the model.

the formalism. Also, due to its simplicity, it is possible to solve the model numerically exactly with ED for a finite number of unitcells. We thus do not have to rely on approximations.

3.8.1 The SSH+U model

The SSH+U model is defined by

$$H = t_1 \sum_{j\sigma} (c^\dagger_{j2\sigma} c_{j1\sigma} + c^\dagger_{j1\sigma} c_{j2\sigma}) + t_2 \sum_{j\sigma} (c^\dagger_{j+1,1\sigma} c_{j2\sigma} + c^\dagger_{j2\sigma} c_{j+1,1\sigma}) + U \sum_{ja} (n_{ja\uparrow} - \frac{1}{2})(n_{ja\downarrow} - \frac{1}{2}). \tag{3.45}$$

where $c^\dagger_{ja\sigma}$ ($c_{ja\sigma}$) creates (annihilates) an electron in unit cell j, site $a \in \{1, 2\}$ and with spin σ. We consider the SSH+U model at half-filling. The form of the interaction term is such that the chemical potential is zero and thus can be regarded as being included in the Hamiltonian. Fig. 3.2 a) shows the unit cell with hopping parameters. Fig. 3.2 b) shows the Wyckoff positions and the centers of inversion symmetry.

The model belongs to the CAZ symmetry class BDI, which implies a $\mathbb{Z}$ classification for the Green's function, with the corresponding topological invariant N_1 [76]. A DMRG study on a finite system [110] investigated the case $t_1 + t_2 > 0$ and found the system to be trivial with $N_1 = 0$ for $t_1 - t_2 > 0$ while for $t_1 - t_2 < 0$ the system is in a topological phase with $N_1 = 2$ for all values of $U > 0$ [110]. At the transition at $t_1 = t_2$ the model reduces to the usual 1D Hubbard model. In this case for $U = 0$ the system is metallic and possesses band crossing at $k = \pi$. Then for any $U > 0$ the system becomes a Mott insulator with a charge gap and gapless spin excitations [21]. Collective excitations that are not single particle excitations, such as spin excitations, are not visible in the single-particle Green's function. Hence, the transition in the bulk Green's function topological invariant N_1 happens by a zero in the Green's function at $k = \pi$ [111]. In the following, we investigate how this transition at finite U is related to an EBR classification that makes use of inversion symmetry.

3.8.2 Symmetry analysis

The model possesses time reversal (TR), particle-hole (PH) and chiral symmetries (CS). We do not have to include spin in our discussion since the model possesses spin rotation symmetry. We thus suppressed the spin indices throughout the following. CS has the following representation for the Green's function in k-space [110]:

$$U_{\mathrm{CS}} = \begin{pmatrix} 1 & 0 \\ 0 & -1 \end{pmatrix} = \sigma_3. \tag{3.46}$$

Hence, CS places the following restriction on the topological Hamiltonian:

$$\mathcal{H}_{\mathrm{T}}(k) = -\sigma_3 \mathcal{H}_{\mathrm{T}}(k) \sigma_3. \tag{3.47}$$

We now expand the topological Hamiltonian into Pauli matrices. Because of Eq. (3.47) only terms proportional to σ_1 and σ_2 are allowed. We can hence write

$$\mathcal{H}_{\mathrm{T}}(k) = q_1(k)\sigma_1 + q_2(k)\sigma_2. \tag{3.48}$$

$q_1(k)$ and $q_2(k)$ are real, k-dependent coefficients. Setting $q(k) = q_1(k) + iq_2(k)$, the Green's function topological invariant N_1 can then be written in terms of the topological Hamiltonian as [76, 110]

$$\begin{aligned} N_1 &= 2 \ \mathrm{Tr} \int \frac{\mathrm{d}k}{4\pi i} U_{\mathrm{CS}} \mathcal{H}_{\mathrm{T}}(k) \partial_k \mathcal{H}_{\mathrm{T}}^{-1}(k) \\ &= 2 \int \frac{\mathrm{d}k}{2\pi i} q(k) \partial_k q^{-1}(k). \end{aligned} \tag{3.49}$$

The factor of two in front of the integral comes from the spin degeneracy in the model. The trace goes over the matrix indices of the topological Hamiltonian. The invariant just measures how often $q(k)$ winds around the origin in the complex plane.

We consider the inversion centered in the Wyckoff position 1a of the unit cell. The corresponding high-symmetry k-points are $\kappa = 0$ and $\kappa = \pi$, whose little groups contain inversion and the identity. For these k-points, the electron operators transform under inversion as

$$\mathcal{I} c^\dagger_{\kappa a \sigma} \mathcal{I}^\dagger = \sum_b \left(\rho^\kappa_{\mathcal{G}}(\mathcal{I})\right)_{ba} c^\dagger_{\kappa b \sigma} \tag{3.50}$$

with the band representation of the inversion operator $\rho^{\boldsymbol{k}}_{\mathcal{G}}(\mathcal{I})$ explicitly given by

$$\rho^{\boldsymbol{k}}_{\mathcal{G}}(\mathcal{I}) = \begin{pmatrix} 0 & 1 \\ 1 & 0 \end{pmatrix} = \sigma_1. \tag{3.51}$$

At these high-symmetry k-points, the eigenvectors of the topological Hamiltonian can be labeled by the eigenvalue of the inversion symmetry, i.e. $+1$ or -1. In this simple case working with the inversion eigenvalues is equivalent to work with irreps, because with only inversion symmetry there are only two irreps that can be distinguished by the eigenvalue of inversion. With only inversion symmetry there exist four possible EBRs each containing one band (actually two degenerate bands upon including the degeneracy in spin space). This provides four cases for the Green's function, defined by the EBR of the lower band. In the 1D group $P\bar{1}$, the EBRs are induced by either an s-like (even under inversion) or a p-like Wannier function (odd under inversion) in the 1a or the 1b Wyckoff position. We label the EBR by the orbital type in the respective Wyckoff position which induces the EBR.

We summarize these four cases in Tab. 3.1. Note that all these phases are topologically trivial in the sense that they can be adiabatically connected to an atomic limit. However they are topologically distinct in the sense that they are obstructed atomic limits that cannot be deformed into each other without closing the gap and breaking or breaking a symmetry.

In the SSH+U model both chiral and inversion symmetry are present at the same time. In Sec.3.8.3 whe show that the index N_1 can be directly related to the inversion eigenvalues at $k = 0, \pi$: $N_1 = 4n+2$ with $n \in \mathbb{Z}$ if both inversion eigenvalues have opposite sign and $N_1 = 4n$ if the signs are equal.

3.8.3 Relationship between Green's function topological invariants and EBRs for the SSH+U Model

As a consequence of inversion symmetry, we have get with Eq. (3.43)

$$\mathcal{H}_{\mathrm{T}}(k) = \sigma_1 \mathcal{H}_{\mathrm{T}}(-k) \sigma_1. \tag{3.52}$$

For the Pauli matrix expansion coefficients in Eq. (3.48) this equation implies

Table 3.1: Four possibilities to label the bands of the topological Hamiltonian by EBRs in the SSH+U model. The inversion eigenvalues at $k = 0$ and $k = \pi$ fully determine the irreps. The EBR is labeled by the orbital type which induces the EBR. The inversion eigenvalues are also indicated in the band structure sketches.

Lower irrep at $k = 0$	Lower irrep at $k = \pi$	Lower EBR	N_1	Band structure sketch
Γ_+	X_+	s_{1a}	0	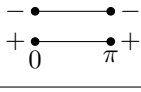
Γ_-	X_-	p_{1a}	0	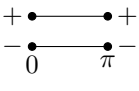
Γ_+	X_-	s_{1b}	2	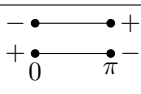
Γ_-	X_+	p_{1b}	2	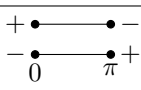

$$q_1(k) = q_1(-k), \tag{3.53}$$
$$q_2(k) = -q_2(-k). \tag{3.54}$$

So inversion symmetry further restricts the form of the topological Hamiltonian. The eigenvalues of the topological Hamiltonian can be expressed as

$$\mu_\pm(k) = \pm\sqrt{\big(q_1(k)\big)^2 + \big(q_2(k)\big)^2} \tag{3.55}$$

The eigenvectors of the lower and the upper band $v_-(k)$ and $v_+(k)$ are

$$v_-(k) = \frac{1}{\sqrt{2}} \begin{pmatrix} 1 \\ \frac{-q(k)}{|q(k)|} \end{pmatrix}, \tag{3.56}$$
$$v_+(k) = \frac{1}{\sqrt{2}} \begin{pmatrix} 1 \\ \frac{q(k)}{|q(k)|} \end{pmatrix}. \tag{3.57}$$

Of special interest are the high symmetry k-points $\kappa = 0, \pi$, where inversion symmetry i.e. Eq. 3.54 implies that $q_2(\kappa)$ must vanish, so that $q(\kappa) = q_1(\kappa)$. The inversion eigenvalues can simply be calculated by multiplying the representation of the inversion operator with the eigenvectors. We get for the upper and the lower band

$$\rho^\kappa_{\mathcal{G}}(\mathcal{I}) v_-(\kappa) = -\mathrm{sign}\big(q_1(\kappa)\big) v_-(\kappa), \tag{3.58}$$
$$\rho^\kappa_{\mathcal{G}}(\mathcal{I}) v_+(\kappa) = \mathrm{sign}\big(q_1(\kappa)\big) v_+(\kappa). \tag{3.59}$$

The evolution of the spectrum, the expansion coefficients q_1 and q_2 and inversion eigenvalues of the topological Hamiltonian for different parameters for the non-interacting limit $U = 0$ are shown in Fig. 3.3. If the inversion eigenvalues have the same sign at both $\kappa = 0$ and $\kappa = \pi$, it follows from Eq. (3.58) that $q(0)$ and $q(\pi)$ also have the same sign. From Eq. (3.53) and Eq. (3.54) we get that the $q(k)$ curve must be mirror symmetric with respect to the q_1 axis. Now it is easy to see that the winding

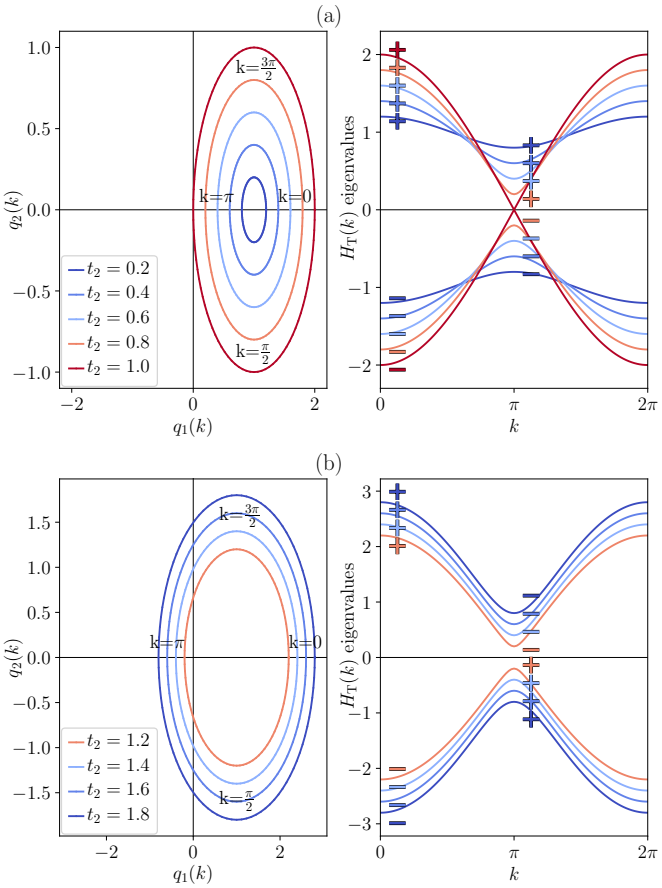

Figure 3.3: Illustration of the topological invariant N_1 for the (non-interacting) SSH model with $t_1 = 1$ fixed. The respective left plot shows the winding of the Pauli matrix expansion coefficients $q_1(k)$ and $q_2(k)$ around the origin when k sweeps the Brillouin zone (see Eq. (3.48)). The respective right plot shows the band structure with inversion eigenvalues of the eigenstates at the high-symmetry k-points, denoted by $+$ or $-$. The inversion eigenvalues fully determine the irreps. The value of N_1 can already be read of from looking at the inversion eigenvalues. In the $N_1 = 0$ phase the inversion values within the same band have the same sign, in the $N_1 = 2$ phase they have opposite signs. In Fig. (a) for $t_1 > t_2$ one finds $N_1 = 0$ except for the point of the transition at $t_1 = t_2 = 1$ where the gap closes. In Fig. (b) for $t_2 > t_1$ one finds $N_1 = 2$.

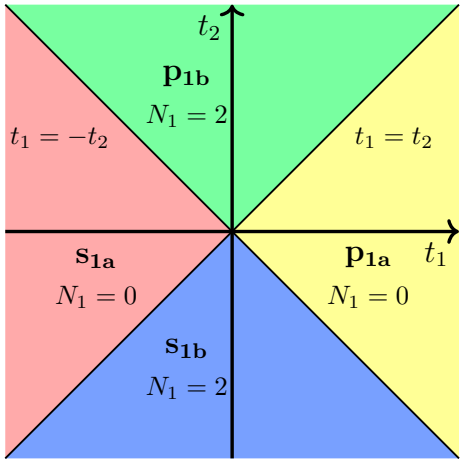

Figure 3.4: Phase diagram obtained from an EBR analysis for the Green's function of the SSH+U model. The phases are labeled by the EBR lowest in energy, derived from the inversion eigenvalues (see Table 3.1). The respective value of N_1 is also shown. We find the classification of the Green's function is independent of the value of the Hubbard interaction U, hence yielding the same phase diagram for any value of U.

number must be $2n$ in this case. Suppose the contrary would be true and we would wind $2n+1$ times around the origin. In this case in the interval $[0, \pi]$ $q(k)$ winds exactly an integer and a half times around the origin, because of $q_1(k) = q_1(-k)$ and $q_2(k) = -q_2(-k)$. The latter also implies $q_2(\pi) = 0$. One can imagine winding in the exact opposite direction while k goes backwards form 2π to π. However, this would mean $q_1(0)$ and $q_1(\pi)$ have different signs. Hence, the one must wind $2n$ times around the origin.

With the same symmetry arguments it follows that if at both high symmetry k-points the inversion eigenvalues have the opposite sign and hence the signs of $q_1(0)$ and $q_1(\pi)$ are opposite, then the winding number must be $2n+1$. Note, that if $q_2(k) = 0$ for all k and $q_1(0)$ and $q_1(\pi)$ have different signs then then there must be a k-point for which both q_1 and q_2 either vanish or become infinite at the same time. But this case is excluded by the assumptions that we have a gap in the spectral function and $G(0, \boldsymbol{k})$ being nonsingular. So we really have to wind $2n+1$ times around the origin and cannot circumvent the wind by going through the origin or infinity.

We can summarize our findings in the following way. If in the SSH+U model the inversion eigenvalues of the lower band at the high-symmetry k-points have the same sign, then $N_1 = 2n$ with $n \in \mathbb{Z}$. If they have opposite signs, then $N_1 = 2n+1$ with $n \in \mathbb{Z}$. Spin degeneracy gives a further factor of two. This means $N_1 = 4n+2$ if both inversion eigenvalues have opposite sign and $N_1 = 4n$ if the signs are equal.

3.8.4 Exact diagonalization results

To compute $\mathcal{H}_T(\boldsymbol{k})$ at finite U, we employ exact diagonalization (ED) calculations with six unit cells and periodic boundary conditions (PBC). A higher number of unitcells would be possible in principle, but is unnecessary for our demonstration of the formalism. In this context, a significant advantage of employing the irreps at high-symmetry k-points to characterize the topology of the Green's function is that they are well-defined in finite-size calculations without extrapolation as long as the high symmetry k-points are included in the k-point grid. Also, a previous DMRG study that considered systems consisting up to 125 unit cells also did not find any indication for a finite size effect for the invariant N_1 [110].

With ED we calculate the Green's function by evaluating the Lehmann representation Eq. (3.4). Therefore we calculate the exact ground state in the N particle sector (N corresponding to half-filling) and the $m_{\max}$ lowest in energy exact eigenstates in the $N+1$ and $N-1$ particle sector of the full many-body Hamiltonian with Lanczos method. The number $m_{\max}$ is determined such that we at least take into account 99% of the spectral function in the respective Green's function entry. Remember in this

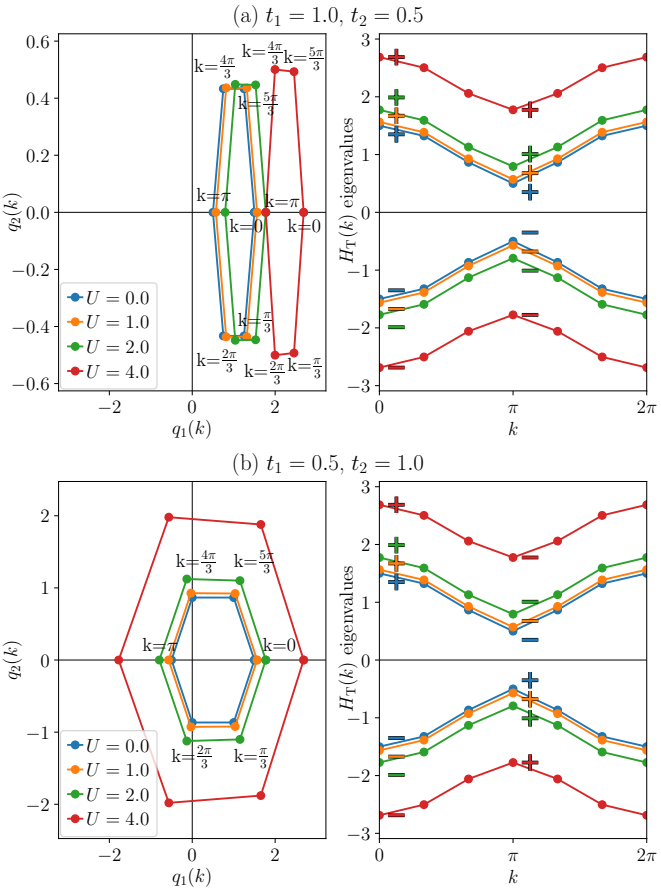

Figure 3.5: Exact diagonalization results for the topological Hamiltonian as a function of U. Each figure corresponds to a representative choice of the hopping parameters t_1 and t_2 for each phase. Labeled by the EBR of the lower band the phases shown are (a) $\mathrm{p_{1a}}$, (b) $\mathrm{p_{1b}}$. The respective left plot shows the winding around the origin of the Pauli matrix expansion coefficients $q_1(k)$ and $q_2(k)$ (see Eq. (3.48)) when k sweeps the Brillouin zone. The respective right plot shows the eigenvalues of the topological Hamiltonian together with the inversion eigenvalues of the respective eigenstates of the topological Hamiltonian at the high-symmetry k-points denoted by $+$ or $-$. The inversion eigenvalues fully determine the irreps. Increasing the Hubbard interaction U enlarges the expansion coefficients $q_1(k)$ and $q_2(k)$ without changing the topology.

context that the spectral function is normalized to one (see Eq. 3.8). We are interested only in $G(0, k)$ and in our case the Lehmann representation is a finite pole expansion, this small neglect of spectral function has no influence on the EBR classification in the present system. In principle it is possible to include all energy eigenvalues and states from the $N \pm 1$ particle sectors, but 99% of the spectral weight is sufficient for our purposes. From $G(0, k)$ the topological Hamiltonian is simply obtained by the definition of the topological Hamiltonian Eq. (3.12). The topological Hamiltonian is then analyzed in terms of EBRs and the invariant N_1. The latter can just be determined visually by plotting the expansion coefficients q_1 and q_2 as a function of k. The resulting phase diagram from this analysis is shown in Fig. 3.4. Depending on the choice of t_1 and t_2 all four cases listed in Tab. 3.1 can be realized. We find the classification of the Green's function is independent of the value of the Hubbard interaction U.

Let us focus on the cases where $t_1, t_2 > 0$, which yields two phases: $t_1 > t_2$ corresponds to a lower band with EBR p_{1a}, while $t_1 < t_2$ corresponds to a lower band with EBR p_{1b}. The topological Hamiltonian and its eigenvalues together with the inversion eigenvalues are shown in Fig. 3.5. For each phase we chose representative parameters t_1 and t_2, while increasing U. The ED results shown in Fig. 3.5 a) illustrate that a winding of the topological Hamiltonian in the q_1-q_2-plane around the

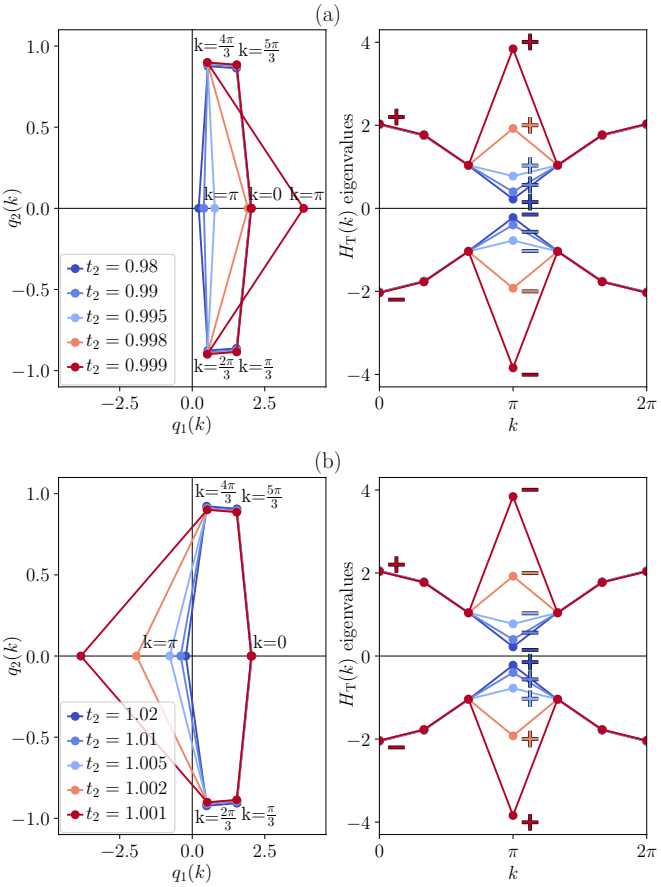

Figure 3.6: Exact diagonalization results for the topological Hamiltonian near the phase transition line $t_1 = t_2$ for a) $t_2 < 1$, b) $t_2 > 1$. In each case, $t_1 = 1$ and $U = 1$ are fixed. The respective left figure shows the winding around the origin of the Pauli matrix expansion coefficients $q_1(k)$ and $q_2(k)$ (see Eq. (3.48)) when k sweeps the Brillouin zone. The respective right plot shows the eigenvalues of the topological Hamiltonian together with the inversion eigenvalues of the respective eigenstates of the topological Hamiltonian at the high-symmetry k-points denoted by $+$ or $-$. The inversion eigenvalues fully determine the irreps. The results indicate that the transition happens by a swap over infinity of the eigenvalues of the topological Hamiltonian labeled by the inversion eigenvalues.

origin i.e. $N_1 = 2$ corresponds to the inversion eigenvalues of the lower band having opposite sign at $k = 0$ and $k = \pi$. Fig. 3.5 b) illustrates that if the eigenvalues of the lower band have the same sign then $N_1 = 0$. This is consistent with what we showed in Sec. 3.8.3 from symmetry considerations alone. Increasing U enlarges the matrix elements of the topological Hamiltonian and hence also its eigenvalues. Intuitively this occurs because enlarging U enlarges the gap in the spectral function. From the spectral representation, one expects that the matrix elements of $G(0, \boldsymbol{k})$ become smaller. In the present system U has no influence on the inversion eigenvalues or N_1, because enlarging the circle does not change the winding number N_1.

We now investigate what happens at the transition $t_1 = t_2$. In the noninteracting case i.e. $U = 0$, this transition occurs via gap closure at $k = \pi$. At this point in parameter space the eigenvalues labeled $+$ and $-$ swap by crossing over zero. At finite U this behavior changes as can be seen in Fig. 3.6. Approaching the phase transition line at $t_1 = t_2$, we find that the topological Hamiltonian and hence the self-energy at zero frequency starts to diverge at $k = \pi$. This implies that the Green's function at zero frequency becomes zero as we can confirm from our calculation.

At the transition the eigenvalues of the topological Hamiltonian labeled by $+$ and $-$ swap by crossing over infinity. Thus the Green's function EBR classification changes by violating the condition that

$G(0, \boldsymbol{k})$ must be non-singular i.e. condition two in *Definition* 1. This confirms that the simultaneous transition of N_1 at $t_1 = t_2$ happens by a divergence in $\Sigma(0, \pi)$ [111]. Note that one has to tune t_2 very close to the transition to observe the divergent behavior in the eigenvalues of the topological Hamiltonian. Initially, for not small enough t_2 it might look like the eigenvalues swap by crossing over zero, implying a gap closing in the spectral function at zero frequency (violating condition one in *Definition* 1) like in the corresponding non-interacting system.

3.9 Summary

In this chapter we investigated the applicability of elementary band representations in the spirit of TQC and symmetry indicators to diagnose spatial- and time-reversal-symmetry protected topological phases in interacting insulators in terms of their single-particle Green's functions.

Assuming that there exists only a unique ground state of the interacting system we illustrated that it is possible to define EBRs for the Matsubara Green's function in the zero temperature limit via the topological Hamiltonian in Eq. (3.12). This is analogous to previously defined Green's function invariants for the CAZ symmetry classes protected by TR, PH and CS [73–80]. We found that the Green's function EBR classification can only change by (i) a gap closing in the spectral function at zero frequency, (ii) the Green's function becoming singular at zero frequency (i.e. $\det\big(G(0, \boldsymbol{k})\big) = 0$ or equivalently $G(0, \boldsymbol{k})$ possesses a zero eigenvalue) or (iii) the Green's function breaking a protecting symmetry.

However, the question in which cases there is a strict correspondence between an EBR classification of Green's functions and SPT phases is left unanswered in the general case. However, in the case where the Green's function topological invariant corresponds to a physical observable, as for example the Hall conductivity (Eq. 3.2) the EBR analysis coincided with the SPT classification.

As an example, we demonstrated the use of the EBRs for Green's functions in one dimension on the SSH+U model which we solved via exact diagonalization on a finite number of sites. The SSH+U model is in the CAZ symmetry class BDI and has spatial inversion symmetry. The model posses topological invariant N_1 that including spin is related to the inversion eigenvalues at the high symmetry k-points $k = 0$ and $k = \pi$. We argued and demonstrated that $N_1 = 4n + 2$ if both inversion eigenvalues have opposite sign and $N_1 = 4n$ if the signs are equal.

In the case $U > 0$ this model features a transition where the Green's function becomes singular at zero frequency, which allows the eigenvalues of the topological Hamiltonian at high-symmetry k-points labeled by the inversion symmetry to swap by simultaneously becoming infinite. This is in contrast to the non-interacting system where the eigenvalues labeled by the inversion eigenvalues swap by becoming zero. Although we demonstrated the usage of EBRs for the Green's function only in one dimension, a similar analysis can also be applied in higher dimensions with respect to an arbitrary set of spatial symmetries.

For numerical calculations on interacting models and materials in which interaction effects are relevant, the EBR analysis can prove valuable as it requires only the calculation of irreps of the topological Hamiltonian at a few high-symmetry k-points. Thus this analysis does not require integration over k-space which often necessitates a much more dense k-point grid which for many methods is very costly in higher dimensions.

Chapter 4

Two-Particle Self-Consistent approach with spin-orbit coupling

In this chapter we present the extension of the Two-Particle Self-Consistent approach (TPSC) [28–30] to the case with spin-orbit coupling (SOC). We consider the multi-band case with multiple orbitals in the unit cell on which electrons interact via the Hubbard interaction. However, we restrict ourselves to the case where the orbitals within the unit cell are symmetry related. For a discussion on how to include the change of orbital occupations in TPSC when interactions are turned on in the case of orbitals that are not symmetry related see Ref. [6, 126]. The original formulation of TPSC does not allow for the inclusion of SOC, because spin rotation symmetry is assumed and subsequently used in many steps of the derivation of the TPSC self-consistency equations [30]. However, SOC explicitly breaks spin rotation symmetry. So the corresponding self-consistency equations including SOC need to be rederived. Instead of spin rotation symmetry we will take advantage of time reversal symmetry (TR) which is still preserved. TR is chosen instead of any other, for example spatial symmetry, because its preservation in the presence of SOC makes it the natural choice independent of the space group. We will see that the inclusion of SOC leads to new terms in the self-consistency equations and in the self-energy, which describe the coupling of spin and charge.

Many of our considerations, especially regarding time reversal symmetry are very general. We also expect them to be helpful including SOC in other diagrammatic methods at the two-particle level such as the dynamical vertex approximation (DΓA) [31] or the dual Fermion approach (DF) [32] which to our best knowledge has not been done yet.

This chapter is organized as follows. We begin with general consideration about SOC in Sec. 4.1. We also motivate when and why its inclusion becomes important in modeling correlated electronic systems and give examples for phenomena caused by SOC and the interplay with electronic correlation effects. In Sec. 4.2 we give an overview of the general ideas of TPSC and its strengths and weaknesses.

We then present a derivation of the TPSC self-consistency equations in the presence of SOC. The overall strategy will be the following. In Sec. 4.3 we give definitions for Green's functions and susceptibilities to clarify our notation. In Sec. 4.4 we find, assuming a vertex that is local in space, time and orbital, expressions from the Bethe-Salpeter equation for these susceptibilities. In Sec. 4.5 we then employ TR to reduce the number of independent vertex elements to four. In Sec. 4.6 we derive an ansatz equation to give a relation between double occupancies and one of the spin vertices. In Sec. 4.7 we derive sum rules for spin and charge susceptibilities to determine these vertex elements. In Sec. 4.8 we derive an expression for the self-energy. We do so by expanding the four-point function once in the longitudinal and once in the transversal channel and then taking the average of both results. We show that time reversal symmetry needs to explicitly be restored in the self-energy expression. In Sec. 4.9 we show that the $\mathrm{Tr}(G\Sigma)$ consistency check holds in the presence of SOC. In Sec. 4.10 we summarize all TPSC self-consistency equations and describe the algorithm. In Sec. 4.11 we show for consistency that the derived equations reduce to the usual TPSC self-consistency equations in the absence of SOC. In Sec. 4.12 we then build some intuition in the most simple case with SOC present, namely where

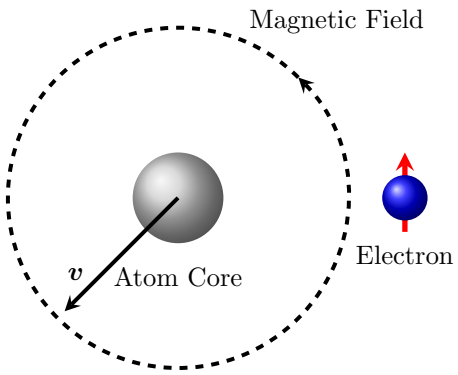

Figure 4.1: Sketch of the origin of spin-orbit coupling. In the rest frame of the electron the atom core moves around the electron. The resulting current produces a magnetic field to which the electrons magnetic dipole moment associated to the spin couples.

additionally S_z is conserved. We also give the TPSC algorithm for this case which is then implemented in a python code. In Sec. 4.13 we give details about our implementation.

In Sec. 4.14 we apply TPSC with SOC to the Kane-Mele-Hubbard model. We first introduce the Kane-Mele-Hubbard model and summarize previous findings. We then present obtained numerical results for the double occupancy, the renormalized TPSC spin and charge vertices, maxima of the spin, charge and mixed spin-charge susceptibilities, the Matsubara Green's function and the self-energy. Physical observables such as the spin-Hall conductivity, correlation lengths for antiferromagnetic spin fluctuations and the band renormalization are discussed separately in chapter 5.

4.1 Spin-orbit coupling

Spin-orbit coupling (SOC) is a relativistic effect that originates from the movement of an electron around the atom core. The SOC term can be derived from the Dirac equation. However, in a simplified picture one can imagine that in the rest frame of the electron the atom core moves around the electron. The resulting current produces a magnetic field to which the electrons magnetic dipole moment associated to the spin couples. A sketch can be seen in Fig. 4.1.

For an electron moving around an atom core the resulting spin-orbit potential in an atom can be written as

$$H_{SOC} = \zeta_{SOC}(r)\boldsymbol{L}\cdot\boldsymbol{S}, \tag{4.1}$$

where $\zeta_{SOC}(r)$ is a function that only depends on the radius, $\boldsymbol{L}$ is the angular momentum operator of the electron and $\boldsymbol{S}$ the spin operator of the electron. In the case of a single electron moving around the atom core the SOC scales as $\sim Z^4$, where Z is the atomic number. So, SOC becomes more important for heavier elements where as for lighter elements it can often be neglected. In a crystal environment the situation is more complicated, however, one can still imagine that from the perspective of the rest frame of the electron the surrounding ions move. The resulting current then again couples to the electrons magnetic dipole moment. Tab. 4.1 gives the size of the (effective) SOC in several commonly studied materials.

We again see that in systems with heavy elements SOC becomes more important. Spin-orbit coupling can lead to a number of interesting phenomena in materials. The interplay with electronic correlations can also become important. In the following we name a few examples.

SOC can lead to so called spin textures in cuprates [81, 82]. The SOC can be thought of a magnetic field in momentum space along which spins can align. The resulting spin texture can be measured with spin- and angle-resolved photoemission spectroscopy as done so in Bi2212 [81]. Cuprates are materials that are also well known for having strong electronic correlations.

Material	Size of the (effective) SOC
Graphene	42.2 μeV [127] (exp.)
Germanene	$23,9$ meV [128, 129] (theory)
Sr_2RuO_4	130 ± 30 meV [95] (exp.)
Sr_2IrO_4	~ 0.4 eV [130] (theory)
BiTeI	~ 0.4 eV (exp.) [131]

Table 4.1: Size of the (effective) SOC in several commonly studied materials.

SOC can have a large effect on the electronic structure of a material. A good example is the unconventional superconductor Sr_2RuO_4 [92–99] where SOC leads to splittings in the band structure and in the Fermi surface. The inclusion of SOC is thus necessary to describe the electronic structure and derived properties such as the superconducting order parameter in the material.

In the isostructural analogue Sr_2IrO_4 the SOC is even larger, because Ir is more heavy. The 5d orbitals are rather extended and one would expect them to lead to bands with a rather large band width where correlation effects do not play a large role. However, the SOC and crystal field splitting combined lead to a rather narrow (double degenerate) $j_{\text{eff}} = 1/2$ band. This narrow band is very susceptible to the Hubbard interaction [130, 132]. Sr_2IrO_4 was found to be insulating with small ferromagnetic moments [133, 134]. There are hopes of realizing exotic topological states in this or similar systems [135, 136].

In graphene it has been shown that an interplay of SOC of Rashba type and electron-electron interactions can lead to collective spin excitations [83–88]. Rashba SOC arises when there is a gradient in the electrical potential in the material, which from the rest frame of the electron looks like a magnetic field. This can be achieved by placing the material on a substrate or in hetero structures. This resonances can be measured in electron-spin resonance experiments [127].

The heavy-fermion superconductor $CeCoIn_5/YbCoIn_5$ is another example where both strong Rashba SOC as well as electron correlations exist [137, 138]. In this material the strength of the Rashba SOC can be tuned by varying the number of layers in the $YbCoIn_5$ blocks. Also, Rashba SOC can be tuned via the application of an electric field as demonstrated at $LaAlO_3/SrTiO_3$ interfaces. [139]

Another phenomenon caused by SOC is magnetic anisotropy (see e.g. Refs. [140–142]). The coupling of spin and orbital degrees of freedom leads to a preferred direction for the spins to align in momentum space causing them to be easier to be polarized in certain directions then in others.

Another prominent example is the so called spin Hall effect, first proposed in 1971 by Dyakonov and Perel [89], in which electrons travel perpendicular to an applied electric field, but in opposite directions depending on their spin. The spin Hall effect has been realized in a variety of systems, including the semiconductors GaAs and InGaAs where the phenomenon is driven by spin orbit coupling [143, 144]. In the quantum spin Hall (QSH) effect the spin Hall conductivity is quantized. The QSH was originally proposed by Kane and Mele [48, 49] for a single layer of graphene, where the intrinsic spin-orbit coupling (SOC) opens a band gap and causes a band inversion making the bands topological [49]. An observable QSH was first successfully predicted and measured in HgTe quantum wells [90, 91]. The spin Hall is discussed in more detail in chap. 5.

Further, it was suggested that with the gapless edgestates at the surface of a topological insulator it is possible to realize a p-wave superconductor [145, 146] or Majorana fermions [145] via proximity effects.

Hence, we see that understanding the interplay of SOC and electronic correlation lead to many interesting phenomena that are not fully understood yet. Studying the Hubbard model in the presence of SOC has thus gained interest in the past [147–153].

In TPSC we will see that SOC leads to a coupling of spin and charge channels in the form of spin-charge correlation functions. This spin-charge correlation functions appear also in other contexts, see e.g. Ref. [86] or Ref. [154]. Also spin fluctuations for the different directions will in general be different.

A symmetry that will be crucial to include SOC in TPSC is time reversal symmetry (TR). Intuitively the preservation of TR in the presence of SOC can be understood in the atomic case i.e. Eq. 4.1. Here,

the scalar product of angular momentum and spin is left invariant under the action of TR

$$\boldsymbol{L} \cdot \boldsymbol{S} \overset{\mathrm{TR}}{\to} (-\boldsymbol{L}) \cdot (-\boldsymbol{S}) = \boldsymbol{L} \cdot \boldsymbol{S}. \tag{4.2}$$

In a material the electron can be thought of having an angular momentum and hence a SOC with respect to every ion. Hence, TR is a preserved symmetry in the presence of SOC. The most impotant consequence of TR for TPSC is that it will allow us to reduce the number of independent vertex elements in TPSC to 4 that can be found with the help of spin and charge sum rules.

4.2 The Two-Particle Self-Consistent approach

The Two-Particle Self-Consistent (TPSC) approach is a weak to intermediate coupling approach to the Hubbard model capable of calculating a frequency- and momentum-dependent self-energy from spin and charge fluctuations. TPSC is constructed such that it satisfies conservation laws for spin and charge, the Pauli principle and the Mermin-Wagner theorem. TPSC is computationally inexpensive making it possible to study a variety of different physical systems. Further, TPSC is conceptually simple, which often allows for a transparent understanding of the underlying physics of the studied phenomena. Originally, TPSC has been developed for the single-band Hubbard model [28–30]. For reviews see Ref. [30, 33, 34]. TPSC has been benchmarked against DiagMC [155] and Quantum Monte Carlo [28–30, 156–158]. There are a number of extensions of TPSC including combinations with DMFT [5, 159, 160], TPSC+ [155, 161], disorder [37], TPSC+GG [155, 162], multi-site case [163–166], mulit-orbital case (to include interorbital interaction U' and Hund's coupling J) [6, 167–169], non-equilibrium [160, 162] and nearest neighbor interaction [170–172]. Further, the attractive Hubbard model ($U < 0$) has been studied [158, 173]. TPSC has been used to study a variety of systems that can be described by the Hubbard model such as the antiferromagnetic pseudo gap in cuprates [30, 35], optical conductivity [36], ferromagnetism [174], the crossover of antiferromagnetic spin fluctuations from two to three dimensions [175], magnetic properties of the three-dimensional Hubbard model[176] adiabatic cooling in cold atoms [38], unconventional superconductivity [166, 177–180] and resilience of Fermi liquid quasiparticles on cold parts of the Fermi surface [37].

The main limitations of TPSC are that it is not valid in the strong coupling limit, except at very high temperature [38]. TPSC is also not valid deep in the renormalized classical regime, where the energy of the characteristic spin fluctuations becomes smaller than the temperature $k_B T$ and the spin correlation length grows exponentially [28, 30]. Further TPSC overestimates spin fluctuations at low temperatures, which also leads to deviations from benchmarks in other derived quantities such as the double occupancy and the self-energy [155, 159]. TPSC works well in two or more dimensions but not in one dimension [181].

The general idea of TPSC is the following. We consider the single-band Hubbard model. We consider RPA-like expressions for spin and charge susceptibilities i.e.

$$\chi_{sp}(q) = \frac{\chi^{(1)}(q)}{1 - \frac{1}{2} U_{sp} \chi^{(1)}(q)}, \tag{4.3}$$

$$\chi_{ch}(q) = \frac{\chi^{(1)}(q)}{1 + \frac{1}{2} U_{ch} \chi^{(1)}(q)}, \tag{4.4}$$

where $q = (iq_m, \boldsymbol{q})$ and $\chi^{(1)}(q)$ is an effective noninteracting susceptibility given by

$$\chi^{(1)}(q) = -2 \frac{T}{N} \sum_k G^{(1)}(k+q) G^{(1)}(k), \tag{4.5}$$

where in the single-band case $G^{(1)} = G_0$. The spin and charge vertices U_{sp} and U_{ch} are then determined such that spin and charge sum rules are fulfilled

$$\frac{T}{N}\sum_q \chi_{ch}(q) = \langle n\rangle + 2\langle n_\uparrow n_\downarrow\rangle - \langle n\rangle^2 , \tag{4.6}$$

$$\frac{T}{N}\sum_q \chi_{sp}(q) = \langle n\rangle - 2\langle n_\uparrow n_\downarrow\rangle . \tag{4.7}$$

In RPA one sets $U_{sp} = U_{ch} = U$ without any renormalization. Adding Eq. 4.96 and Eq. 4.97 together in RPA it is easy to see that RPA violates these sum rules and consequently violates the Pauli principle in the form $\langle n_\uparrow^2\rangle = \langle n_\uparrow\rangle$. The ansatz equation, derived from a Hartree-Fock decoupling, is used to relate the double occupancy to the spin vertex. For $\langle n\rangle \leq 1$ the ansatz equation is

$$U_{sp} = U\frac{\langle n_\uparrow n_\downarrow\rangle}{\langle n_\uparrow\rangle\langle n_\downarrow\rangle} = 4U\frac{\langle n_\uparrow n_\downarrow\rangle}{\langle n\rangle^2}. \tag{4.8}$$

For $\langle n\rangle > 1$ a particle-hole transformation has to be used to map it to the case $\langle n\rangle \leq 1$ [30]. So we have three equations for U_{sp}, U_{ch} and $\langle n_\uparrow n_\downarrow\rangle$ that need to be solved self-consistently.

In a second level approximation the self-energy is calculated by

$$\Sigma^{(2)}(k) = U\frac{\langle n\rangle}{2} + \frac{U}{8}\sum_q G^{(1)}(k+q)\left(3U_{sp}\chi_{sp}(q) + U_{ch}\chi_{ch}(q)\right). \tag{4.9}$$

This expression is obtained by expanding the four-point correlator in the Schwinger-Dyson equation once in the longitudinal and once in the transversal channel and then averaging both results [33, 157]. Note that TPSC is not conserving anymore at the second level and there is no correspondence to a Luttinger-Ward functional. From the Dyson the Green's function is calculated by

$$G^{(2)}(i\omega_n, \boldsymbol{k}) = \left(i\omega_n - \mathcal{H}(\boldsymbol{k}) + \mu - \Sigma^{(2)}(i\omega_n, \boldsymbol{k})\right)^{-1}. \tag{4.10}$$

The chemical potential needs to be adjusted here to match the given filling.

4.3 Definitions

In this section we give a number of definitions that are important for the following derivation of the TPSC self-consistency equations. We discuss the distinction between first and second level quantities in TPSC. Then we define the correlation functions we are searching expressions for in TPSC. Further, we give the form of the irreducible particle-hole vertex, which in TPSC is assumed local in time and space.

4.3.1 First and second level quantities

We distinguish between first level (1) and second level (2) quantities. First level quantities can be derived from a Luttinger-Ward functional [182–185] and are hence conserving. Second level quantities, such as $G^{(2)}$ and $\Sigma^{(2)}$ later on, are constructed from first level ones but are not conserving and they do not correspond to a Luttinger Ward functional. The first level Green's function is given by

$$G^{(1)ab}_{\sigma\sigma'}(i\omega_n, \boldsymbol{k}) = \left(\left(i\omega_n - H(\boldsymbol{k}) + \mu^{(1)} - \Sigma^{(1)}\right)^{-1}\right)^{ab}_{\sigma\sigma'}. \tag{4.11}$$

The first level self-energy $\Sigma^{(1)}$ in TPSC is a frequency and k-independent constant (matrix) that is diagonal in orbital space. So $G^{(1)}$ is an effective non-interacting Green's function. If all orbitals in the unit cell are identical i.e. when they are mapped into each other by symmetry (as for example in the KMH model), the self-energy can just be absorbed in the chemical potential. With that one has in fact $G^{(1)} = G_0$. The first level susceptibility (an effective non-interacting susceptibility) is given by

$$\chi^{(1)a_1a_2}_{\sigma_1\sigma_2,\sigma_3\sigma_4}(q) = -\frac{T}{N}\sum_k G^{(1)a_1a_2}_{\sigma_2\sigma_3}(k+q)G^{(1)a_2a_1}_{\sigma_4\sigma_1}(k). \tag{4.12}$$

So for symmetry related orbitals again it holds $\chi^{(1)} = \chi^{(0)}$.

4.3.2 Susceptibilities

Now let us look at the interacting susceptibilities. We are interested in correlation functions of the density and spin operators that are given by

$$n_{ia} = c^\dagger_{ia\uparrow}c_{ia\uparrow} + c^\dagger_{ia\downarrow}c_{ia\downarrow} = n_{ia\uparrow} + n_{ia\downarrow}, \tag{4.13}$$
$$S^z_{ia} = c^\dagger_{ia\uparrow}c_{ia\uparrow} - c^\dagger_{ia\downarrow}c_{ia\downarrow} = n_{ia\uparrow} - n_{ia\downarrow}, \tag{4.14}$$
$$S^x_{ia} = c^\dagger_{ia\uparrow}c_{ia\downarrow} + c^\dagger_{ia\downarrow}c_{ia\uparrow} = S^+_{ia} + S^-_{ia}, \tag{4.15}$$
$$S^y_{ia} = -ic^\dagger_{ia\uparrow}c_{ia\downarrow} + ic^\dagger_{ia\downarrow}c_{ia\uparrow} = -iS^+_{ia} + iS^-_{ia}. \tag{4.16}$$

The inverse transformation is

$$S^+_{ia} = \frac{1}{2}(S^x_{ia} + iS^y_{ia}), \tag{4.17}$$
$$S^-_{ia} = \frac{1}{2}(S^x_{ia} - iS^y_{ia}), \tag{4.18}$$
$$n_{ia\uparrow} = \frac{1}{2}(n_{ia} + S^z_{ia}), \tag{4.19}$$
$$n_{ia\downarrow} = \frac{1}{2}(n_{ia} - S^z_{ia}). \tag{4.20}$$

Note that $(S^+_{ia})^\dagger = S^-_{ia}$. In the case of general SOC there is no conserved spin direction. Hence, transversal and longitudinal spin fluctuations can couple to each other. We now investigate all possible spin and charge susceptibilities, because they will show up in the self-energy. Susceptibilities have the general form

$$\chi^{ab}_{\alpha\beta}(\tau, \boldsymbol{R}_i - \boldsymbol{R}_j) = \langle \mathcal{T}_\tau O^\alpha_{ia}(\tau) O^\beta_{jb}(0)\rangle - \langle O^\alpha_{ia}\rangle \langle O^\beta_{jb}\rangle, \tag{4.21}$$

where the operators O^α can either be S^x, S^y, S^z or n corresponding to the labels x, y, z or c. Alternatively, one can go to the original basis and use the original operators i.e. O^α being $n_\uparrow$, $n_\downarrow$, S^+ or S^- corresponding to the labels $\uparrow$, $\downarrow$, $+$ or $-$. $\boldsymbol{R}_i$ is the lattice vector to the unit cell with the index i and a and b are site indices labeling the sites in the unit cell. With Fourier transform one can go to frequency momentum space $q = (iq_m, \boldsymbol{q})$. Note that with TR symmetry it always holds $\langle S^\alpha_a\rangle = 0$ as we will show later. For example the spin correlation function for two spins in x-direction is given by

$$\chi^{ab}_{xx}(\tau, \boldsymbol{R}_i - \boldsymbol{R}_j) = \langle \mathcal{T}_\tau S^x_{ia}(\tau) S^x_{jb}(0)\rangle. \tag{4.22}$$

This correlation function can be expressed in the original basis by the following linear combination

$$\chi_{xx} = \chi_{++} + \chi_{+-} + \chi_{-+} + \chi_{--}. \tag{4.23}$$

Appendix A gives a complete list of all spin correlation functions and their relation to each other. Conveniently we can define the matrices

$$\chi = \begin{pmatrix} \chi_{\uparrow\uparrow} & \chi_{\uparrow\downarrow} & \chi_{\uparrow+} & \chi_{\uparrow-} \\ \chi_{\downarrow\uparrow} & \chi_{\downarrow\downarrow} & \chi_{\downarrow+} & \chi_{\downarrow-} \\ \chi_{+\uparrow} & \chi_{+\downarrow} & \chi_{++} & \chi_{+-} \\ \chi_{-\uparrow} & \chi_{-\downarrow} & \chi_{-+} & \chi_{--} \end{pmatrix} \tag{4.24}$$

and

$$\chi' = \begin{pmatrix} \chi_{cc} & \chi_{cz} & \chi_{cx} & i\chi_{cy} \\ \chi_{zc} & \chi_{zz} & \chi_{zx} & i\chi_{zy} \\ \chi_{xc} & \chi_{xz} & \chi_{xx} & i\chi_{xy} \\ i\chi_{yc} & i\chi_{xz} & i\chi_{yx} & -\chi_{yy} \end{pmatrix}. \tag{4.25}$$

With the matrix M given by

$$M = \begin{pmatrix} 1 & 1 & 0 & 0 \\ 1 & -1 & 0 & 0 \\ 0 & 0 & 1 & 1 \\ 0 & 0 & 1 & -1 \end{pmatrix}, \tag{4.26}$$

one can relate χ and χ' by a simple basis transformation

$$\chi' = M\chi M. \tag{4.27}$$

Note that $\frac{1}{2}MM = \frac{1}{2}MM^{-1} = 1$.

4.3.3 Local irreducible two-particle vertex

Generally, the irreducible two-particle particle-hole vertex is defined as

$$\Gamma^{a_1a_2a_3a_4}_{\sigma_1\sigma_2\sigma_3\sigma_4}(1,2;3,4) = \frac{\delta\Sigma^{a_1a_2}_{\sigma_1\sigma_2}(1,2)}{\delta G^{a_3a_4}_{\sigma_3\sigma_4}(3,4)}. \tag{4.28}$$

In TPSC we assume a irreducible vertex that is local in space and time. Hence in frequency momentum space the irreducible vertex is a constant. It follows that in TPSC the local vertex takes the following form

$$\Gamma(1,2;3,4) = \delta_{\boldsymbol{R}_{i_1}\boldsymbol{R}_{i_2}}\delta_{\boldsymbol{R}_{i_1}\boldsymbol{R}_{i_3}}\delta_{\boldsymbol{R}_{i_1}\boldsymbol{R}_{i_4}}\delta_{a_1a_2}\delta_{a_1a_3}\delta_{a_1a_4}\delta(\tau_1-\tau_2^+)\delta(\tau_1-\tau_3^+)\delta(\tau_1-\tau_4)\Gamma^{a_1}_{\sigma_1\sigma_2\sigma_3\sigma_4}. \tag{4.29}$$

The elements of the local in space time and orbital vertex elements are defined by

$$\Gamma^{a_1}_{\sigma_1\sigma_2,\sigma_4\sigma_3} := \Gamma^{a_1}_{\sigma_1\sigma_2\sigma_3\sigma_4} = \frac{\delta\Sigma^{a_1a_1}_{\sigma_1\sigma_2}}{\delta G^{a_1a_1}_{\sigma_3\sigma_4}}. \tag{4.30}$$

The reason for the switch of the last two indices is that in this way we get a proper matrix notation in the Bethe-Salpeter-equation. To do so we introduce a combined spin index $\rho = (\sigma_1, \sigma_2)$. We combine the first two and the last two spin indices, that are separated by a comma, so that we can write $\Gamma_{\rho\eta}$, with ρ and η taking the values $\uparrow, \downarrow, +, -$.

At the level of the susceptibilities TPSC is conserving and one can derive the irreducible vertex from a Luttinger-Ward functional $\Phi[G]$. Hence we get the following symmetry for the TPSC vertex

$$\Gamma^{a}_{\sigma_1\sigma_2\sigma_3\sigma_4} = \frac{\delta\Sigma^{aa}_{\sigma_1\sigma_2}}{\delta G^{aa}_{\sigma_3\sigma_4}} = \frac{\delta\Phi[G]}{\delta G^{aa}_{\sigma_2\sigma_1}\delta G^{aa}_{\sigma_3\sigma_4}} = \frac{\delta\Sigma^{aa}_{\sigma_4\sigma_3}}{\delta G^{aa}_{\sigma_2\sigma_1}} = \Gamma^{a}_{\sigma_4\sigma_3\sigma_2\sigma_1}. \tag{4.31}$$

In matrix notation this equation reads

$$\Gamma_{\rho\zeta} = \Gamma_{\zeta\rho}. \tag{4.32}$$

Analogous to the susceptibility we can write the vertex as a matrix

$$\Gamma = \begin{pmatrix} \Gamma_{\uparrow\uparrow} & \Gamma_{\uparrow\downarrow} & \Gamma_{\uparrow+} & \Gamma_{\uparrow-} \\ \Gamma_{\downarrow\uparrow} & \Gamma_{\downarrow\downarrow} & \Gamma_{\downarrow+} & \Gamma_{\downarrow-} \\ \Gamma_{+\uparrow} & \Gamma_{+\downarrow} & \Gamma_{++} & \Gamma_{+-} \\ \Gamma_{-\uparrow} & \Gamma_{-\downarrow} & \Gamma_{-+} & \Gamma_{--} \end{pmatrix}. \tag{4.33}$$

Similarly to χ we can make a basis transformation for Γ. We define

$$\Gamma' = \frac{1}{2} M \Gamma M \tag{4.34}$$

Later on we will show that with TR symmetry Γ' has the following form

$$\Gamma' = \begin{pmatrix} \Gamma_{cc} & 0 & 0 & 0 \\ 0 & -\Gamma_{zz} & 0 & 0 \\ 0 & 0 & -\Gamma_{xx} & 0 \\ 0 & 0 & 0 & +\Gamma_{yy} \end{pmatrix}. \tag{4.35}$$

The rest of the matrix elements vanish with TR as we will show later. Hence in the end one is left with four independent constants, a charge vertex Γ_{cc} and three spin vertices $\Gamma_{xx}, \Gamma_{yy}, \Gamma_{zz}$, one for each spin direction, that now can be independent. Note that in RPA one would just have $\Gamma_{cc} = \Gamma_{\alpha\alpha} = U$.

4.4 Bethe-Salpeter equation

The goal of this section is to get something like the following equation for the susceptibilities

$$\chi' = \chi^{(1)\prime} - \frac{1}{2} \chi^{(1)\prime} \Gamma' \chi', \tag{4.36}$$

where we enforce TR symmetry on Γ' so that it only has four real independent matrix elements (see Eq. 4.35). More explicitly one can write this equation as

$$\begin{pmatrix} \chi_{cc} & \chi_{cz} & \chi_{cx} & i\chi_{cy} \\ \chi_{zc} & \chi_{zz} & \chi_{zx} & i\chi_{zy} \\ \chi_{xc} & \chi_{xz} & \chi_{xx} & i\chi_{xy} \\ i\chi_{yc} & i\chi_{xz} & i\chi_{yx} & -\chi_{yy} \end{pmatrix} = \begin{pmatrix} \chi^{(1)}_{cc} & \chi^{(1)}_{cz} & \chi^{(1)}_{cx} & i\chi^{(1)}_{cy} \\ \chi^{(1)}_{zc} & \chi^{(1)}_{zz} & \chi^{(1)}_{zx} & i\chi^{(1)}_{zy} \\ \chi^{(1)}_{xc} & \chi^{(1)}_{xz} & \chi^{(1)}_{xx} & i\chi^{(1)}_{xy} \\ i\chi^{(1)}_{yc} & i\chi^{(1)}_{xz} & i\chi^{(1)}_{yx} & -\chi^{(1)}_{yy} \end{pmatrix}$$
$$- \frac{1}{2} \begin{pmatrix} \chi^{(1)}_{cc} & \chi^{(1)}_{cz} & \chi^{(1)}_{cx} & i\chi^{(1)}_{cy} \\ \chi^{(1)}_{zc} & \chi^{(1)}_{zz} & \chi^{(1)}_{zx} & i\chi^{(1)}_{zy} \\ \chi^{(1)}_{xc} & \chi^{(1)}_{xz} & \chi^{(1)}_{xx} & i\chi^{(1)}_{xy} \\ i\chi^{(1)}_{yc} & i\chi^{(1)}_{xz} & i\chi^{(1)}_{yx} & -\chi^{(1)}_{yy} \end{pmatrix} \begin{pmatrix} \Gamma_{cc} & 0 & 0 & 0 \\ 0 & -\Gamma_{zz} & 0 & 0 \\ 0 & 0 & -\Gamma_{xx} & 0 \\ 0 & 0 & 0 & +\Gamma_{yy} \end{pmatrix} \begin{pmatrix} \chi_{cc} & \chi_{cz} & \chi_{cx} & i\chi_{cy} \\ \chi_{zc} & \chi_{zz} & \chi_{zx} & i\chi_{zy} \\ \chi_{xc} & \chi_{xz} & \chi_{xx} & i\chi_{xy} \\ i\chi_{yc} & i\chi_{xz} & i\chi_{yx} & -\chi_{yy}. \end{pmatrix} \tag{4.37}$$

We can bring the last equation in a more symmetrical form by getting rid of factors of i. We get

$$\begin{pmatrix} \chi_{cc} & \chi_{cz} & \chi_{cx} & \chi_{cy} \\ \chi_{zc} & \chi_{zz} & \chi_{zx} & \chi_{zy} \\ \chi_{xc} & \chi_{xz} & \chi_{xx} & \chi_{xy} \\ \chi_{yc} & \chi_{xz} & \chi_{yx} & \chi_{yy} \end{pmatrix} = \begin{pmatrix} \chi^{(1)}_{cc} & \chi^{(1)}_{cz} & \chi^{(1)}_{cx} & \chi^{(1)}_{cy} \\ \chi^{(1)}_{zc} & \chi^{(1)}_{zz} & \chi^{(1)}_{zx} & \chi^{(1)}_{zy} \\ \chi^{(1)}_{xc} & \chi^{(1)}_{xz} & \chi^{(1)}_{xx} & \chi^{(1)}_{xy} \\ \chi^{(1)}_{yc} & \chi^{(1)}_{xz} & \chi^{(1)}_{yx} & \chi^{(1)}_{yy} \end{pmatrix}$$
$$- \frac{1}{2} \begin{pmatrix} \chi^{(1)}_{cc} & \chi^{(1)}_{cz} & \chi^{(1)}_{cx} & \chi^{(1)}_{cy} \\ \chi^{(1)}_{zc} & \chi^{(1)}_{zz} & \chi^{(1)}_{zx} & \chi^{(1)}_{zy} \\ \chi^{(1)}_{xc} & \chi^{(1)}_{xz} & \chi^{(1)}_{xx} & \chi^{(1)}_{xy} \\ \chi^{(1)}_{yc} & \chi^{(1)}_{xz} & \chi^{(1)}_{yx} & \chi^{(1)}_{yy} \end{pmatrix} \begin{pmatrix} \Gamma_{cc} & 0 & 0 & 0 \\ 0 & -\Gamma_{zz} & 0 & 0 \\ 0 & 0 & -\Gamma_{xx} & 0 \\ 0 & 0 & 0 & -\Gamma_{yy} \end{pmatrix} \begin{pmatrix} \chi_{cc} & \chi_{cz} & \chi_{cx} & \chi_{cy} \\ \chi_{zc} & \chi_{zz} & \chi_{zx} & \chi_{zy} \\ \chi_{xc} & \chi_{xz} & \chi_{xx} & \chi_{xy} \\ \chi_{yc} & \chi_{xz} & \chi_{yx} & \chi_{yy} \end{pmatrix}. \tag{4.38}$$

This equation is the generalization of Eq. 4.3 and Eq. 4.4, only that now with SOC spin and charge are coupled.

To derive the above equation we start from the BSE expanded in one of the particle-hole channels Eq. 2.84

$$\chi(1,2;3,4) = -G(1,3)G(4,2) + G(1,\bar{5})\Gamma(\bar{5},\bar{6};\bar{7},\bar{8})\chi(\bar{7},\bar{8};3,4)G(\bar{6},2), \tag{4.39}$$

where $1 := (\tau_1, \boldsymbol{R}_{i_1}, a_1, \sigma_1)$. Restoring all orbital indices the equation reads

$$\begin{aligned}\chi^{a_1a_2a_3a_4}_{\sigma_1\sigma_2\sigma_3\sigma_4}(1,2;3,4) = &-G^{a_1a_3}_{\sigma_1\sigma_3}(1,3)G^{a_4a_2}_{\sigma_4\sigma_2}(4,2) \\ &+ G^{a_1\bar{a}_5}_{\sigma_1\bar{\sigma}_5}(1,\bar{5})\Gamma^{\bar{a}_5\bar{a}_6\bar{a}_7\bar{a}_8}_{\bar{\sigma}_5\bar{\sigma}_6\bar{\sigma}_7\bar{\sigma}_8}(\bar{5},\bar{6};\bar{7},\bar{8})\chi^{\bar{a}_7\bar{a}_8a_3a_4}_{\bar{\sigma}_7\bar{\sigma}_8\sigma_3\sigma_4}(\bar{7},\bar{8};3,4)G^{\bar{a}_6a_2}_{\bar{\sigma}_6\sigma_2}(\bar{6},2).\end{aligned} \tag{4.40}$$

Inserting the local TPSC vertex (Eq. 4.29) and setting $G \to G^{(1)}$ we get for the susceptibilities we are interested in

$$\begin{aligned}\chi^{a_1a_1a_2a_2}_{\sigma_1\sigma_2\sigma_3\sigma_4}(1,1^+;2^+,2) = &-G^{(1)a_1a_2}_{\sigma_1\sigma_3}(1,2^+)G^{(1)a_2a_1}_{\sigma_4\sigma_2}(2,1^+) \\ &+ G^{(1)a_1\bar{a}_6}_{\sigma_1\bar{\sigma}_5}(1,\bar{6}^+)\Gamma^{\bar{a}_6}_{\bar{\sigma}_5\bar{\sigma}_6\bar{\sigma}_7\bar{\sigma}_8}\chi^{\bar{a}_6\bar{a}_6a_3a_4}_{\bar{\sigma}_7\bar{\sigma}_8\sigma_3\sigma_4}(\bar{6},\bar{6}^+;2^+,2)G^{(1)\bar{a}_6a_1}_{\bar{\sigma}_6\sigma_2}(\bar{6},1^+).\end{aligned} \tag{4.41}$$

Again using the combined spin index $\rho_1 = (\sigma_{11}, \sigma_{12})$, we define $\chi^{a_1a_2}_{\rho_1\rho_2}(1,2) := \chi^{a_1a_1a_2a_2}_{\sigma_{12}\sigma_{11}\sigma_{21}\sigma_{22}}(1,1^+;2^+,2)$. As before we have $\Gamma^a_{\sigma_{12}\sigma_{11}\sigma_{21}\sigma_{22}} = \Gamma^a_{\rho_1\rho_2}$. Further we can identify $G^{(1)}G^{(1)}$ as $\chi^{(1)}$ the susceptibility of an effective non-interacting system. With that we can write the BSE with matrix multiplications, i.e.

$$\chi^{a_1a_2}_{\rho_1\rho_2}(1,2) = \chi^{(1)a_1a_2}_{\rho_1\rho_2}(1,2) - \chi^{(1)a_1\bar{a}_5}_{\rho_1\bar{\rho}_5}(1,\bar{5})\Gamma^{\bar{\alpha}_5}_{\bar{\rho}_5\bar{\rho}_7}\chi^{\bar{a}_5a_2}_{\bar{\rho}_7\rho_2}(\bar{5},2). \tag{4.42}$$

Going to frequency momentum space one gets

$$\chi^{a_1a_2}_{\rho_1\rho_2}(q) = \chi^{(1)a_1a_2}_{\rho_1\rho_2}(q) - \chi^{(1)a_1\bar{a}_5}_{\rho_1\bar{\rho}_5}(q)\Gamma^{\bar{a}_5}_{\bar{\rho}_5\bar{\rho}_7}\chi^{\bar{a}_5a_2}_{\bar{\rho}_7\rho_2}(q). \tag{4.43}$$

In matrix notation we indeed get

$$\chi = \chi^{(1)} - \chi^{(1)}\Gamma\chi. \tag{4.44}$$

Doing the basis transformation and inserting $1 = \frac{1}{2}MM$ one can write

$$\chi' = \chi^{(1)\prime} - \frac{1}{2}\chi^{(1)\prime}\Gamma'\chi'. \tag{4.45}$$

So we arrive at the desired result. What is now left to do is, that we have to argue with TR symmetry that the vertex has the desired form with only four independent constants.

4.5 Time reversal symmetry

In this section we investigate the consequences of time reversal symmetry (TR). TR is used instead of spin rotation symmetry to simplify the equations and reduce the number of independent vertex elements. We start by explaining how TR symmetry is implemented in the second quantization formalism in terms of an antiunitary operator. Note, that the antiunitarity of TR makes it more involved to deal with TR compared to unitary symmetries. Then, we investigate the consequences of TR symmetry for certain expectation values, susceptibilities, irreducible vertex, Green's function and self-energy. A list of implications following from TR is given in Appendix C.

4.5.1 Time reversal general definition

The time reversed single particle Schrödinger equation without spin takes the form

$$\left(\frac{\boldsymbol{p}^2}{2m} + V(\boldsymbol{r})\right)\psi(\boldsymbol{r},t) = i\frac{\partial\psi(\boldsymbol{r},t)}{\partial(-t)}. \tag{4.46}$$

where $V(\boldsymbol{r})$ is the crystal potential. If $\psi'(\boldsymbol{r},t)$ is a solution of the Schrödinger equation (without time reversal), then $\psi'^*(\boldsymbol{r},t)$ is a solution of the time reversed Schrödinger equation above. This means in

the single particle case without spin, time reversal is just given by complex conjugation $\mathcal{K}$. Spin, as any other angular momentum, changes sign under time reversal. Hence, time reversal in the spinfull case has a matrix representation namely $i\sigma_y\mathcal{K}$.

Within second quantization TR is implemented via a anti-unitary operator $\hat{U}_\mathrm{T}$. That means it is a unitary operator combined with complex conjugation $\mathcal{K}$. Since $\hat{U}_\mathrm{T}$ is anti-unitary it must act on a complex number by complex conjugation i.e. for $z \in \mathbb{C}$ we have

$$\hat{U}_\mathrm{T} z \hat{U}_\mathrm{T}^{-1} = z^*. \tag{4.47}$$

Note that due to the complex conjugation it is important that $\hat{U}_\mathrm{T}$ acts strictly to the right. $\hat{U}_\mathrm{T}$ acts directly on the space of the many-body states i.e. the Fock space. We do not need to write how $\hat{U}_\mathrm{T}$ looks explicitly. It is sufficient to specify how $\hat{U}_\mathrm{T}$ transforms creation and annihilation operators, which essentially specifies how it acts on the single particle basis. We assume that $c^\dagger_{ia\sigma}$ and $c_{ia\sigma}$ create and annihilate electrons in real and orthonormal orbitals on a lattice, where as usual i is the unit cell index, a the orbital index and σ the spin index. The transformation is

$$\hat{U}_\mathrm{T} c^\dagger_{ia\sigma} \hat{U}_\mathrm{T}^{-1} = \sum_{\sigma'} (i\sigma_y)_{\sigma\sigma'} c^\dagger_{ia\sigma'} = -\sigma c^\dagger_{ia-\sigma}, \tag{4.48}$$

$$\hat{U}_\mathrm{T} c_{ia\sigma} \hat{U}_\mathrm{T}^{-1} = \sum_{\sigma'} \left((i\sigma_y)^\dagger\right)_{\sigma'\sigma} c_{ia\sigma'} = -\sigma c_{ia-\sigma}, \tag{4.49}$$

where here by $A^\dagger$ with A a matrix we mean the adjoint of that matrix. The action on a many-body state $|\psi\rangle$, that corresponds to a Slater determinant, can always be obtained by

$$\hat{U}_\mathrm{T} |\psi\rangle = \hat{U}_\mathrm{T} \prod_j c^\dagger_j |0\rangle = \prod_j (\hat{U}_\mathrm{T} c^\dagger_j \hat{U}_\mathrm{T}^{-1}) \hat{U}_\mathrm{T} |0\rangle . \tag{4.50}$$

Here j can be any set of indices. The vacuum $|0\rangle$ is invariant under any symmetry. With linear combinations of Slater determinants the action on an arbitrary many-body state is determined. A many-body Hamiltonian in second quantization is invariant under TR if

$$\hat{U}_\mathrm{T} H \hat{U}_\mathrm{T}^{-1} = H. \tag{4.51}$$

Mathematical side note: Also for anti-unitary operators $\hat{U}$ it holds $\hat{U}^\dagger\hat{U} = \hat{U}\hat{U}^\dagger = 1$, because for anti-unitary operators the mathematical definition of the adjoint of an operator is changed to

$$\langle\phi|\hat{U}\psi\rangle = \left(\langle\hat{U}^\dagger\phi|\psi\rangle\right)^* \tag{4.52}$$

to compensate for the complex conjugation. As an example take $\hat{U}$ to be just the complex conjugation (on the Hilbert space L^2). $\hat{U}^\dagger$ is also anti-unitary and it holds $\hat{U}^\dagger = \hat{U}^{-1}$.

4.5.2 Time reversal symmetry for a non-interacting Hamiltonian

As an example for the implications of TR let us consider a non-interacting Hamiltonian that in second quantization is given by

$$H_0 = \sum_{ijab\sigma\sigma'} \mathcal{H}^{ab\sigma\sigma'}_{ij} c^\dagger_{ia\sigma} c_{jb\sigma'}. \tag{4.53}$$

TR symmetry implies

$$
\begin{aligned}
H &= \hat{U}_{\mathrm{T}} H \hat{U}_{\mathrm{T}}^{-1} \\
&= \sum_{ijab\sigma_1\sigma_2} \left(\mathcal{H}_{ij}^{ab\sigma_1\sigma_2}\right)^* \hat{U}_{\mathrm{T}} c_{ia\sigma_1}^\dagger \hat{U}_{\mathrm{T}}^{-1} \hat{U}_{\mathrm{T}} c_{jb\sigma_2} \hat{U}_{\mathrm{T}}^{-1} \\
&= \sum_{ijab\sigma_1\sigma_2} \sigma_1\sigma_2 \left(\mathcal{H}_{ij}^{ab\sigma_1\sigma_2}\right)^* c_{ia-\sigma_1}^\dagger c_{jb-\sigma_2} \\
&= \sum_{ijab\sigma_1\sigma_2} \sigma_1\sigma_2 \left(\mathcal{H}_{ij}^{ab-\sigma_1-\sigma_2}\right)^* c_{ia\sigma_1}^\dagger c_{jb\sigma_2}. \qquad (4.54)
\end{aligned}
$$

So the hopping elements of a TR invariant Hamiltonian must fulfill

$$
\mathcal{H}_{ij}^{ab\sigma_1\sigma_2} = \sigma_1\sigma_2 \left(\mathcal{H}_{ij}^{ab-\sigma_1-\sigma_2}\right)^*. \qquad (4.55)
$$

Going to k-space by a Fourier transform we see that TR has the following consequences for a Bloch Hamiltonian

$$
\begin{aligned}
\mathcal{H}^{ab\sigma_1\sigma_2}(\boldsymbol{k}) &= \sum_i e^{i\boldsymbol{k}\cdot\boldsymbol{R}_{ij}} \sigma_1\sigma_2 \mathcal{H}_{ij}^{ab\sigma_1\sigma_2} \\
&\overset{\mathrm{TR}}{=} \sum_i e^{i\boldsymbol{k}\cdot\boldsymbol{R}_{ij}} \sigma_1\sigma_2 \left(\mathcal{H}_{ij}^{ab-\sigma_1-\sigma_2}\right)^* \\
&= \left(\sum_i e^{-i\boldsymbol{k}\cdot\boldsymbol{R}_{ij}} \sigma_1\sigma_2 \mathcal{H}_{ij}^{ab-\sigma_1-\sigma_2}\right)^* \\
&= \sigma_1\sigma_2 \left(\mathcal{H}^{ab-\sigma_1-\sigma_2}(-\boldsymbol{k})\right)^*. \qquad (4.56)
\end{aligned}
$$

where $\boldsymbol{R}_{ij} = \boldsymbol{R}_i - \boldsymbol{R}_j$.

4.5.3 Time reversal symmetry implications for expectation values

Time reversal acts on the operators we are interested in as

$$
\begin{aligned}
\hat{U}_{\mathrm{T}} n_{ia\uparrow} \hat{U}_{\mathrm{T}}^{-1} &= n_{ia\downarrow}, && (4.57)\\
\hat{U}_{\mathrm{T}} n_{ia\downarrow} \hat{U}_{\mathrm{T}}^{-1} &= n_{ia\uparrow}, && (4.58)\\
\hat{U}_{\mathrm{T}} S_{ia}^{+} \hat{U}_{\mathrm{T}}^{-1} &= -S_{ia}^{-}, && (4.59)\\
\hat{U}_{\mathrm{T}} S_{ia}^{-} \hat{U}_{\mathrm{T}}^{-1} &= -S_{ia}^{+}. && (4.60)
\end{aligned}
$$

Hence one also has

$$
\begin{aligned}
\hat{U}_{\mathrm{T}} S_{ia}^{\alpha} \hat{U}_{\mathrm{T}}^{-1} &= -S_{ia}^{\alpha}, && (4.61)\\
\hat{U}_{\mathrm{T}} n_{ia} \hat{U}_{\mathrm{T}}^{-1} &= n_{ia}. && (4.62)
\end{aligned}
$$

From TR one can derive the following relations

$$
\begin{aligned}
\langle S_{ia}^{+} \rangle &= 0, && (4.63)\\
\langle S_{ia}^{-} \rangle &= 0, && (4.64)\\
\langle n_{ia\uparrow} \rangle &= \langle n_{ia\downarrow} \rangle. && (4.65)
\end{aligned}
$$

From these relations it directly follows that $\langle S_a^\alpha \rangle = 0$.

Proof. For the densities we get

$$\begin{aligned}
\langle n_{ia\sigma}\rangle &= \frac{1}{Z}\mathrm{Tr}\left(e^{-\beta H} n_{ia\sigma}\right) \\
&\overset{\mathrm{TR}}{=} \frac{1}{Z}\mathrm{Tr}\left(e^{-\beta \hat{U}_\mathrm{T}^{-1} H \hat{U}_\mathrm{T}} n_{ia\sigma}\right) \\
&= \frac{1}{Z}\sum_n \langle n|\hat{U}_\mathrm{T}^{-1} e^{-\beta H}\hat{U}_\mathrm{T} n_{ia\sigma}\hat{U}_\mathrm{T}^{-1}\hat{U}_\mathrm{T}|n\rangle \\
&= \frac{1}{Z}\sum_n \left(\langle \hat{U}_\mathrm{T} n|e^{-\beta H} n_{ia-\sigma}|\hat{U}_\mathrm{T} n\rangle\right)^* \\
&= \langle n_{ia-\sigma}\rangle\,.
\end{aligned} \tag{4.66}$$

Going from the third to the fourth line we use $\hat{U}_\mathrm{T}^{-1} = \hat{U}_\mathrm{T}^\dagger$ and the definition of the adjoint of an antiunitary operator Eq. 4.52. Further, for antiunitary operators $(\hat{U}_\mathrm{T}^\dagger)^\dagger = \hat{U}_\mathrm{T}$. Note that there is no cyclic property of the trace in case of an antiunitary operator. Going from the fourth to the fifth line the sum over all basis states stays invariant under TR. The complex conjugate has no effect because $\langle n_{ia\sigma}\rangle$ is real. This can be easily seen by just considering complex conjugation as the antiunitary operator.

For S_{ia}^+ one gets

$$\begin{aligned}
\langle S_{ia}^+\rangle &= \frac{1}{Z}\mathrm{Tr}\left(e^{-\beta H} c_{ia\uparrow}^\dagger c_{ia\downarrow}\right) \\
&\overset{\mathrm{TR}}{=} \frac{1}{Z}\mathrm{Tr}\left(e^{-\beta \hat{U}_\mathrm{T}^{-1} H \hat{U}_\mathrm{T}} c_{ia\uparrow}^\dagger c_{ia\downarrow}\right) \\
&= \frac{1}{Z}\sum_n \langle n|\hat{U}_\mathrm{T}^{-1} e^{-\beta H}\hat{U}_\mathrm{T} c_{ia\uparrow}^\dagger \hat{U}_\mathrm{T}^{-1}\hat{U}_\mathrm{T} c_{ia\downarrow}\hat{U}_\mathrm{T}^{-1}\hat{U}_\mathrm{T}|n\rangle \\
&= -\frac{1}{Z}\sum_n \left(\langle \hat{U}_\mathrm{T} n|e^{-\beta H} c_{ia\downarrow}^\dagger c_{ia\uparrow}|\hat{U}_\mathrm{T} n\rangle\right)^* \\
&= -\frac{1}{Z}\sum_n \langle n|\left(e^{-\beta H} c_{ia\downarrow}^\dagger c_{ia\uparrow}\right)^\dagger|n\rangle \\
&= -\frac{1}{Z}\sum_n \langle n|c_{ia\uparrow}^\dagger c_{ia\downarrow} e^{-\beta H}|n\rangle \\
&= -\langle S_{ia}^+\rangle\,.
\end{aligned} \tag{4.67}$$

Hence it must hold $\langle S_{ia}^+\rangle = 0$. Flipping spins it also follows $\langle S_{ia}^-\rangle = 0$.

□

4.5.4 Time reversal of the susceptibilities

We will now show that for the susceptibilities it holds

$$\chi_{\rho\zeta}^{ab}(iq_m, \boldsymbol{q}) = \eta_{\rho\zeta}\chi_{-\zeta-\rho}^{ba}(iq_m, -\boldsymbol{q}). \tag{4.68}$$

where $\eta_{\rho\zeta}$ gives a factor of -1 for each $+$ or $-$ in ρ and ζ. In matrix notation this equation reads

$$\chi(iq_m, \boldsymbol{q}) = W\chi^T(iq_m, -\boldsymbol{q})W. \tag{4.69}$$

where W is explicitly given by

$$W = \begin{pmatrix} 0 & 1 & 0 & 0 \\ 1 & 0 & 0 & 0 \\ 0 & 0 & 0 & -1 \\ 0 & 0 & -1 & 0 \end{pmatrix}. \tag{4.70}$$

So, W flips $\uparrow$ to $\downarrow$ and $+$ to $-$ and gives the minus signs for the appropriate indices.

Proof. As shown before it follows from TR that $\langle n_\uparrow \rangle = \langle n_\downarrow \rangle$ and $\langle S^+ \rangle = \langle S^- \rangle = 0$. So for the susceptibilities one only needs to focus on the first term. We calculate for $\tau > 0$ [1]

$$\begin{aligned}
\langle O_{ia\rho}(\tau) O_{jb\zeta} \rangle &= \frac{1}{Z} \mathrm{Tr} \left(e^{-\beta H} e^{H\tau} O_{ia\rho} e^{-H\tau} O_{jb\zeta} \right) \\
&\overset{\mathrm{TR}}{=} \frac{1}{Z} \mathrm{Tr} \left(e^{-\beta \hat{U}_\mathrm{T}^{-1} H \hat{U}_\mathrm{T}} e^{\hat{U}_\mathrm{T}^{-1} H \hat{U}_\mathrm{T} \tau} O_{ia\rho} e^{-\hat{U}_\mathrm{T}^{-1} H \hat{U}_\mathrm{T} \tau} O_{jb\zeta} \right) \\
&= \frac{1}{Z} \sum_m \langle m | \hat{U}_\mathrm{T}^{-1} e^{-\beta H} e^{H\tau} \hat{U}_\mathrm{T} O_{ia\rho} \hat{U}_\mathrm{T}^{-1} e^{-H\tau} \hat{U}_\mathrm{T} O_{jb\zeta} \hat{U}_\mathrm{T}^{-1} \hat{U}_\mathrm{T} | m \rangle \\
&= \eta_{\rho\zeta} \frac{1}{Z} \sum_m \left(\langle \hat{U}_\mathrm{T} m | e^{-\beta H} e^{H\tau} O_{ia-\rho} e^{-H\tau} O_{jb-\zeta} | \hat{U}_\mathrm{T} m \rangle \right)^* \\
&= \eta_{\rho\zeta} \frac{1}{Z} \sum_m \left(\langle m | e^{-\beta H} e^{H\tau} O_{ia-\rho} e^{-H\tau} O_{jb-\zeta} | m \rangle \right)^* \\
&= \eta_{\rho\zeta} \frac{1}{Z} \sum_m \langle m | \left(e^{-\beta H} e^{H\tau} O_{ia-\rho} e^{-H\tau} O_{jb-\zeta} \right)^\dagger | m \rangle \\
&= \eta_{\rho\zeta} \frac{1}{Z} \sum_m \langle m | O_{jb-\zeta} e^{-H\tau} O_{ia-\rho} e^{H\tau} e^{-\beta H} | m \rangle \\
&= \eta_{\rho\zeta} \frac{1}{Z} \sum_m \langle m | e^{-\beta H} e^{H\tau} O_{jb-\zeta} e^{-H\tau} O_{ia-\rho} | m \rangle \\
&= \eta_{\rho\zeta} \langle O_{jb-\zeta}(\tau) O_{ia-\rho} \rangle .
\end{aligned} \tag{4.71}$$

Similar for $\tau < 0$. So in the end we get

$$\chi^{ab}_{\rho\zeta}(\tau, -\boldsymbol{r}) = \eta_{\rho\zeta} \chi^{ba}_{-\zeta-\rho}(\tau, -\boldsymbol{r}). \tag{4.72}$$

Going to frequency momentum space we get the claimed identity.

□

4.5.5 Time reversal of the vertex

In the following we use TR to motivate the following identity for the TPSC vertex

$$\Gamma^a_{\rho\zeta} = \eta_{\rho\zeta} \Gamma^a_{-\zeta-\rho}. \tag{4.73}$$

This relation is analogous to the one for the susceptibility 4.68. We do so by enforcing TR on the BSE. Let us first iterate the BSE

$$\chi(iq_m, \boldsymbol{q}) = \chi^{(1)}(iq_m, \boldsymbol{q}) - \chi^{(1)}(iq_m, \boldsymbol{q}) \Gamma \chi^{(1)}(iq_m, \boldsymbol{q}) + \chi^{(1)}(iq_m, \boldsymbol{q}) \Gamma \chi^{(1)}(iq_m, \boldsymbol{q}) \Gamma \chi^{(1)}(iq_m, \boldsymbol{q}) - \dots \quad . \tag{4.74}$$

It must hold

$$\begin{aligned}
\chi(iq_m, \boldsymbol{q}) &\overset{\mathrm{TR}}{=} W \chi(iq_m, -\boldsymbol{q})^T W \\
&= W \chi^{(1)}(iq_m, -\boldsymbol{q})^T W - W \left(\chi^{(1)}(iq_m, -\boldsymbol{q}) \Gamma \chi^{(1)}(iq_m, -\boldsymbol{q}) W \right)^T + \dots \\
&= W \chi^{(1)}(iq_m, -\boldsymbol{q})^T W - W \chi^{(1)}(iq_m, -\boldsymbol{q})^T W W \Gamma^T W W \chi^{(1)}(iq_m, -\boldsymbol{q})^T W + \dots \\
&\overset{\mathrm{TR}}{=} \chi^{(1)}(iq_m, \boldsymbol{q}) - \chi^{(1)}(iq_m, \boldsymbol{q}) W \Gamma^T W \chi^{(1)}(iq_m, \boldsymbol{q}) + \dots
\end{aligned} \tag{4.75}$$

[1] Despite the name imaginary time the complex conjugate has no effect on τ. τ is considered as a real number in the interval $[-\beta, \beta]$.

Hence for the vertex it must hold

$$\Gamma = W\Gamma^T W. \tag{4.76}$$

Component wise one obtains the above identity.

4.5.6 Form of the TPSC vertex

We now motivate that in the presence of TR the TPSC vertex has only four independent elements out of the original 16. The independent elements are charge vertex Γ_{cc} and the three spin vertices Γ_{xx}, Γ_{yy} and Γ_{zz}.

Among other identities we get from Eq. 4.32 i.e. $\Gamma_{\rho\zeta} = \Gamma_{\zeta\rho}$ that

$$\Gamma_{\uparrow\downarrow} = \Gamma_{\downarrow\uparrow}, \tag{4.77}$$
$$\Gamma_{+-} = \Gamma_{-+}. \tag{4.78}$$

From TR one has the identity $\Gamma_{\rho\zeta} = \eta_{\rho\zeta}\Gamma_{-\zeta-\rho}$. Among other identities we get

$$\Gamma_{\uparrow\uparrow} = \Gamma_{\downarrow\downarrow}, \tag{4.79}$$
$$\Gamma_{++} = \Gamma_{--}. \tag{4.80}$$

Combining the above identities we see that (see the definitions in appendix A and B)

$$\Gamma_{cz} = \Gamma_{zc} = 0, \tag{4.81}$$
$$\Gamma_{xy} = \Gamma_{yx} = 0. \tag{4.82}$$

Note that this is analogous to $\chi^{aa}_{cz}(\tau = 0, \boldsymbol{r} = 0) = 0$ and $\chi^{aa}_{xy}(\tau = 0, \boldsymbol{r} = 0) = 0$ in the presence of time reversal symmetry as we will see for the sum rules. Since the choice of coordinate system is in principle arbitrary, this means that only the diagonal i.e. Γ_{ch}, Γ_{xx}, Γ_{yy} and Γ_{zz} survive. Also note that with that all elements of the vertex which flip one spin such as $\Gamma_{\uparrow+} = \Gamma_{\uparrow\uparrow,\uparrow\downarrow}$ are zero. This make sense because the Hubbard interaction also conserves spin. [2] So as claimed before there are only four independent vertices and with that the BSE reads

$$\chi' = \chi^{(1)\prime} - \frac{1}{2}\chi^{(1)\prime}\Gamma'\chi'. \tag{4.83}$$

4.5.7 Time reversal symmetry of the Green's function and the self-energy

We also need the implications of TR symmetry for the Green's function and the self-energy, because we want the corresponding TPSC expression to also fulfill TR. For the Green's function TR implies

$$G^{ab}_{\sigma\sigma'}(i\omega_n, \boldsymbol{k}) = \sigma\sigma' G^{ba}_{-\sigma'-\sigma}(i\omega_n, -\boldsymbol{k}), \tag{4.84}$$

Similarly for the self-energy one has

$$\Sigma^{ab}_{\sigma\sigma'}(i\omega_n, \boldsymbol{k}) = \sigma\sigma' \Sigma^{ba}_{-\sigma'-\sigma}(i\omega_n, -\boldsymbol{k}). \tag{4.85}$$

Proof. With time reversal invariance we get for the Matsubara Green's function for $\tau > 0$

[2] What about Γ^{++} that flips two spins and it can still be nonzero now in TPSC? The situation is similar to $\Gamma_{\uparrow\uparrow}$, which can be thought of in order having processes/diagrams involving $\Gamma_{\uparrow\downarrow}$ and $\Gamma_{\downarrow\uparrow}$. The situation is similar here with Γ_{+-} and Γ_{-+}. The same is not possible with flipping just one spin.

$$
\begin{aligned}
G^{ab}_{\sigma\sigma'}(\tau, \boldsymbol{R}_i - \boldsymbol{R}_j) &= -\frac{1}{Z}\mathrm{Tr}\left(e^{-\beta H}e^{H\tau}c_{ia\sigma}e^{-H\tau}c^\dagger_{jb\sigma'}\right) \\
&= -\frac{1}{Z}\mathrm{Tr}\left(e^{-\beta \hat{U}_\mathrm{T}^{-1}H\hat{U}_\mathrm{T}}e^{\hat{U}_\mathrm{T}^{-1}H\hat{U}_\mathrm{T}\tau}c_{ia\sigma}e^{-\hat{U}_\mathrm{T}^{-1}H\hat{U}_\mathrm{T}\tau}c^\dagger_{jb\sigma'}\right) \\
&= -\frac{1}{Z}\sum_n \langle n|\hat{U}_\mathrm{T}^{-1}e^{-\beta H}e^{H\tau}\hat{U}_\mathrm{T}c_{ia\sigma}\hat{U}_\mathrm{T}^{-1}e^{-H\tau}\hat{U}_\mathrm{T}c^\dagger_{jb\sigma'}\hat{U}_\mathrm{T}^{-1}\hat{U}_\mathrm{T}|n\rangle \\
&= -\frac{1}{Z}\sum_n \left(\langle \hat{U}_\mathrm{T}n|e^{-\beta H}e^{H\tau}\hat{U}_\mathrm{T}c_{ia\sigma}\hat{U}_\mathrm{T}^{-1}e^{-H\tau}\hat{U}_\mathrm{T}c^\dagger_{jb\sigma}\hat{U}_\mathrm{T}^{-1}|\hat{U}_\mathrm{T}n\rangle\right)^* \\
&= -\sigma\sigma'\frac{1}{Z}\sum_n \left(\langle n|e^{-\beta H}e^{H\tau}c_{ia-\sigma}e^{-H\tau}c^\dagger_{jb-\sigma}|n\rangle\right)^* \\
&= -\sigma\sigma'\frac{1}{Z}\sum_n \langle n|(e^{-\beta H}e^{H\tau}c_{ia}e^{-H\tau}c^\dagger_{jb})^\dagger|n\rangle \\
&= -\sigma\sigma'\frac{1}{Z}\sum_n \langle n|c_{jb}e^{-H\tau}c^\dagger_{ia}e^{H\tau}e^{-\beta H}|n\rangle \\
&= -\sigma\sigma'\frac{1}{Z}\sum_n \langle n|e^{-\beta H}e^{H\tau}c_{jb}e^{-H\tau}c^\dagger_{ia}|n\rangle \\
&= \sigma\sigma' G^{ba}_{-\sigma-\sigma'}\left(\tau, -(\boldsymbol{R}_i - \boldsymbol{R}_j)\right). \qquad (4.86)
\end{aligned}
$$

A similar calculation holds for $\tau < 0$. Going to Frequency momentum space yields Eq. 4.84.

For the self-energy the same relation must hold, because the self-energy can be written with the Dyson equation as a difference of two inverses of Green's functions

$$\Sigma^{ab}_{\sigma\sigma'}(i\omega_n, \boldsymbol{k}) = \left(G_0^{-1}(i\omega_n, \boldsymbol{k})\right)^{ab}_{\sigma\sigma'} - \left(G^{-1}(i\omega_n, \boldsymbol{k})\right)^{ab}_{\sigma\sigma'} \qquad (4.87)$$

Since a matrix inverse is unique the self-energy must obey the same relation as the Green's function and the above identity Eq. 4.85 holds.

□

4.6 Ansatz equation for the spin vertex

In the following we will derive a relation between one of the spin vertices and the double occupancy. This equation is commonly referred to as ansatz equation. The ansatz equation can be motivated from a Hartree-Fock decoupling. The presence of SOC complicates the derivation, but invoking TR symmetry yields the same result as without SOC. We start from the exact expression for the self-energy in Eq. 2.77 (here $1 := (\tau_1, \boldsymbol{R}_{i_1})$), which with just Hubbard interaction at each site reads

$$\Sigma^{a_1\bar{a}_4}_{\sigma_1\bar{\sigma}_4}(1, \bar{4})_\phi G^{\bar{a}_4 a_2}_{\bar{\sigma}_4\sigma_2}(\bar{4}, 2)_\phi = -U\left\langle \mathcal{T}_\tau c^\dagger_{a_1-\sigma_1}(1^{++})c_{a_1-\sigma_1}(1^+)c_{a_1\sigma_1}(1)c^\dagger_{a_2\sigma_2}(2)\right\rangle_\phi. \qquad (4.88)$$

At $2 = 1^+$, $a_1 = a_2$, $\sigma_1 = \sigma_2$ one has exactly

$$\Sigma^{a_1\bar{a}_4}_{\sigma_1\bar{\sigma}_4}(1, \bar{4})_\phi G^{\bar{a}_4 a_1}_{\bar{\sigma}_4\sigma_1}(\bar{4}, 1^+)_\phi = U\left\langle \mathcal{T}_\tau n_{a_1-\sigma_1}(1)n_{a_1\sigma_1}(1)\right\rangle_\phi. \qquad (4.89)$$

When the label 1 does not coincide with 2 it becomes more reasonable to do a Hartree-Fock factorization

$$
\begin{aligned}
\Sigma^{(1)a_1\bar{a}_4}_{\sigma_1\bar{\sigma}_4}(1, \bar{4})_\phi G^{(1)\bar{a}_4 a_2}_{\bar{\sigma}_4\sigma_2}(\bar{4}, 2)_\phi = A^{a_1}_\phi \Big(& G^{(1)a_1a_1}_{-\sigma_1-\sigma_1}(1^+, 1^{++})_\phi G^{(1)a_1a_2}_{\sigma_1\sigma_2}(1, 2)_\phi \\
&- G^{(1)a_1a_1}_{\sigma_1-\sigma_1}(1, 1^{++})_\phi G^{(1)a_1a_2}_{-\sigma_1\sigma_2}(1^+, 2)_\phi\Big), \qquad (4.90)
\end{aligned}
$$

where A^a_ϕ is a constant. The (1) superscript denotes that these are our first order expressions. Later we will find an improved expression for the self-energy $\Sigma^{(2)}$. Again setting $2 = 1^{++}$, $a_1 = a_2$, $\sigma_1 = \sigma_2$ we get

$$\Sigma^{(1)a_1\bar{a}_4}_{\sigma_1\bar{\sigma}_4}(1,\bar{4})_\phi G^{(1)\bar{a}_4 a_2}_{\bar{\sigma}_4\sigma_2}(\bar{4},1^{++})_\phi = A^{a_1}_\phi \Big(\langle n_{a_1-\sigma_1}\rangle_\phi \langle n_{a_1\sigma_1}\rangle_\phi - \langle c^\dagger_{a_1-\sigma_1} c_{a_1\sigma_1}\rangle_\phi \langle c^\dagger_{a_1\sigma_1} c_{a_1-\sigma_1}\rangle_\phi \Big). \quad (4.91)$$

Comparing the two results we get

$$A^{a_1}_\phi = U \frac{\langle n_{a_1-\sigma_1} n_{a_1\sigma_1}\rangle_\phi}{\langle n_{a_1-\sigma_1}\rangle_\phi \langle n_{a_1\sigma_1}\rangle_\phi - \langle c^\dagger_{a_1-\sigma_1} c_{a_1\sigma_1}\rangle_\phi \langle c^\dagger_{a_1\sigma_1} c_{a_1-\sigma_1}\rangle_\phi}. \quad (4.92)$$

If we multiply Eq. 4.90 from the right side with $G^{(1)\bar{a}_2 a_2}_{\bar{\sigma}_2\sigma_2}(\bar{2},2)^{-1}_\phi$, we get the first order expression for the self-energy

$$\begin{aligned}\Sigma^{(1)a_1a_2}_{\sigma_1\sigma_2}(1,2)_\phi = {} & A^{a_1}_\phi \langle n_{a_1-\sigma_1}\rangle_\phi \delta_{a_1a_2}\delta_{\sigma_1\sigma_2}\delta(1-2) \\ & - A^{a_1}_\phi \langle c^\dagger_{a_1-\sigma_1} c_{a_1\sigma_1}\rangle_\phi \delta_{a_1a_2}\delta_{-\sigma_1\sigma_2}\delta(1^+-2). \end{aligned} \quad (4.93)$$

From this expression one can calculate the spin vertex

$$\begin{aligned}\Gamma_{zz}(1,2;3,4)_\phi &= \frac{1}{2}\left(\frac{\delta\Sigma^{(1)a_1a_2}_{\uparrow\uparrow}(1,2)_\phi}{\delta G^{(1)a_3a_4}_{\downarrow\downarrow}(3,4)_\phi} + \frac{\delta\Sigma^{(1)a_1a_2}_{\downarrow\downarrow}(1,2)_\phi}{\delta G^{(1)a_3a_4}_{\uparrow\uparrow}(3,4)_\phi} - \frac{\delta\Sigma^{(1)a_1a_2}_{\uparrow\uparrow}(1,2)_\phi}{\delta G^{(1)a_3a_4}_{\uparrow\uparrow}(3,4)_\phi} - \frac{\delta\Sigma^{(1)a_1a_2}_{\downarrow\downarrow}(1,2)_\phi}{\delta G^{(1)a_3a_4}_{\downarrow\downarrow}(3,4)_\phi} \right) \\ &= A^{a_1}_\phi \delta_{a_1a_2}\delta_{a_1a_3}\delta_{a_1a_4}\delta(1-2)\delta(1-3)\delta(1^+-4). \end{aligned} \quad (4.94)$$

The functional derivatives of A_ϕ cancel each other. Setting ϕ to zero we see that $\Gamma^{a_1}_{zz} = A^{a_1}_{\phi=0}$. With that we get the ansatz equation for Γ_{zz}

$$\Gamma^{a_1}_{zz} = U \frac{\langle n_{a_1-\sigma_1} n_{a_1\sigma_1}\rangle}{\langle n_{a_1-\sigma_1}\rangle \langle n_{a_1\sigma_1}\rangle}. \quad (4.95)$$

Note that $\langle c^\dagger_{a_1\sigma_1} c_{a_1-\sigma_1}\rangle = 0$ due to time reversal symmetry (see Eq. 4.63).

Interestingly one can do the same calculation with the spin quantization axis along the x or y-axis. One would obtain $\Gamma^{a_1}_{xx} = U\frac{\langle n_{a_1\uparrow} n_{a_1\downarrow}\rangle}{\langle n_{a_1\uparrow}\rangle\langle n_{a_1\downarrow}\rangle}$ and $\Gamma^{a_1}_{yy} = U\frac{\langle n_{a_1\uparrow} n_{a_1\downarrow}\rangle}{\langle n_{a_1\uparrow}\rangle\langle n_{a_1\downarrow}\rangle}$ respectively. If one would use these ansatz equations in the respective spin sum rules one would arrive at an inconsistency, because one would get different double occupancies from the sum rules if the vertices have different values. Hence we suggest to use the ansatz equation in the channel where the spin fluctuations are strongest, to have feedback on the double occupations in that channel. In the KMH model this means to use the ansatz equation in the transversal channel i.e. for $\alpha = x$. This procedure is then also consistent with the $\mathrm{Tr}(G^{(1)}\Sigma^{(2)})$ check.

Note, that the above Hartree-Fock decoupling is only good at low filling where the electrons are less likely to see each other [159]. In the case of $\langle n_a\rangle > 1$ it is hence better to carry out a particle-hole transformation of the Hamiltonian so that $\langle n_a\rangle \to 1 - \langle n_a\rangle$ in the ansatz equation [36].

4.7 Sum rules for the susceptibilities

We can derive sum rules for the susceptibilities. Note that unlike the Green's function the susceptibilities are all continuous at $\tau = 0$, because either the commutators vanish or in the case of the mixed spin susceptibilities both the left side limit $\tau \to 0^+$ and the right side limit $\tau \to 0^-$ give zero as we show below. In the presence of TR the sum rules take the following form

$$\frac{T}{N}\sum_q \chi^{aa}_{cc}(q) = \langle n_a\rangle + 2\langle n_{a\uparrow} n_{a\downarrow}\rangle - \langle n_a\rangle^2, \quad (4.96)$$

$$\frac{T}{N}\sum_q \chi^{aa}_{\alpha\alpha}(q) = \langle n_a\rangle - 2\langle n_{a\uparrow} n_{a\downarrow}\rangle, \quad (4.97)$$

where $\alpha = x, y, z$. The sum over all other mixed susceptibilities are zero, because of TR symmetry. Hence, they can not be used to determine matrix elements of the TPSC vertices. In conclusion, invoking TR symmetry results in four sum rules for four vertex elements, which is consistent.

Proof. For the charge sum rule we get

$$\begin{aligned}\chi^{aa}_{cc}(\tau = 0, \boldsymbol{r} = 0) &= \langle n_{a\uparrow} n_{a\uparrow}\rangle + \langle n_{a\uparrow} n_{a\downarrow}\rangle + \langle n_{a\downarrow} n_{a\uparrow}\rangle + \langle n_{a\downarrow} n_{a\downarrow}\rangle - \langle n_a\rangle^2 \\ &= \langle n_a\rangle + 2\langle n_{a\uparrow} n_{a\downarrow}\rangle - \langle n_a\rangle^2\end{aligned} \tag{4.98}$$

For the spin sum rule for the z-direction we get (note that $\langle S^\alpha_a\rangle \overset{\text{TR}}{=} 0$):

$$\begin{aligned}\chi^{aa}_{zz}(\tau = 0, \boldsymbol{r} = 0) &\overset{\text{TR}}{=} \langle n_{a\uparrow} n_{a\uparrow}\rangle - \langle n_{a\uparrow} n_{a\downarrow}\rangle - \langle n_{a\downarrow} n_{a\uparrow}\rangle + \langle n_{a\downarrow} n_{a\downarrow}\rangle \\ &= \langle n_a\rangle - 2\langle n_{a\uparrow} n_{a\downarrow}\rangle .\end{aligned} \tag{4.99}$$

for the x direction one gets similarly

$$\begin{aligned}\chi^{aa}_{xx}(\tau = 0, \boldsymbol{r} = 0) &\overset{\text{TR}}{=} \langle (c^\dagger_{a\uparrow} c_{a\downarrow} + c^\dagger_{a\downarrow} c_{a\uparrow})(c^\dagger_{a\uparrow} c_{a\downarrow} + c^\dagger_{a\downarrow} c_{a\uparrow})\rangle \\ &= \langle c^\dagger_{a\downarrow} c_{a\uparrow} c^\dagger_{a\uparrow} c_{a\downarrow} + c^\dagger_{a\downarrow} c_{a\uparrow} c^\dagger_{a\uparrow} c_{a\downarrow}\rangle \\ &= \langle c^\dagger_{a\downarrow} c_{a\downarrow}(1 - c^\dagger_{a\uparrow} c_{a\uparrow}) + c^\dagger_{a\uparrow} c_{a\uparrow}(1 - c^\dagger_{a\downarrow} c_{a\downarrow})\rangle \\ &= \langle n_a\rangle - 2\langle n_{a\uparrow} n_{a\downarrow}\rangle .\end{aligned} \tag{4.100}$$

and for the y-direction

$$\begin{aligned}\chi^{aa}_{yy}(\tau = 0, \boldsymbol{r} = 0) &\overset{\text{TR}}{=} \langle (-ic^\dagger_{a\uparrow} c_{a\downarrow} + ic^\dagger_{a\downarrow} c_{a\uparrow})(-ic^\dagger_{a\uparrow} c_{a\downarrow} + ic^\dagger_{a\downarrow} c_{a\uparrow})\rangle \\ &= \langle (c^\dagger_{a\uparrow} c_{a\downarrow} - c^\dagger_{a\downarrow} c_{a\uparrow})(-c^\dagger_{a\uparrow} c_{a\downarrow} + c^\dagger_{a\downarrow} c_{a\uparrow})\rangle \\ &= \langle c^\dagger_{a\downarrow} c_{a\uparrow} c^\dagger_{a\uparrow} c_{a\downarrow} + c^\dagger_{a\uparrow} c_{a\downarrow} c^\dagger_{a\uparrow} c_{a\downarrow})\rangle \\ &= \langle n_a\rangle - 2\langle n_{a\uparrow} n_{a\downarrow}\rangle .\end{aligned} \tag{4.101}$$

As expected one gets the same result for all spin directions. Actually, this already follows from the arbitrariness of choice of coordinate system for the spin direction. For the sum rules of the mixed spin-charge susceptibilities χ_{cz} and χ_{zc} one has

$$\chi^{aa}_{cz}(\tau = 0, \boldsymbol{r} = 0) \overset{TR}{=} \langle n_{a\uparrow} n_{a\uparrow}\rangle - \langle n_{a\downarrow} n_{a\downarrow}\rangle - \langle n_{a\uparrow} n_{a\downarrow}\rangle + \langle n_{a\downarrow} n_{a\uparrow}\rangle \overset{TR}{=} 0 \tag{4.102}$$

$$\chi^{aa}_{zc}(\tau = 0, \boldsymbol{r} = 0) \overset{TR}{=} \langle n_{a\uparrow} n_{a\uparrow}\rangle - \langle n_{a\downarrow} n_{a\downarrow}\rangle + \langle n_{a\uparrow} n_{a\downarrow}\rangle - \langle n_{a\downarrow} n_{a\uparrow}\rangle \overset{TR}{=} 0 \tag{4.103}$$

Also, the mixed spin susceptibilities vanish in the presence of TR. For example one has

$$\begin{aligned}\chi^{aa}_{yx}(\tau = 0^-, \boldsymbol{r} = 0) &\overset{TR}{=} \langle (c^\dagger_{a\uparrow} c_{a\downarrow} + c^\dagger_{a\downarrow} c_{a\uparrow})(-ic^\dagger_{a\uparrow} c_{a\downarrow} + ic^\dagger_{a\downarrow} c_{a\uparrow})\rangle \\ &= -i\langle c^\dagger_{a\downarrow} c_{a\uparrow} c^\dagger_{a\uparrow} c_{a\downarrow} - c^\dagger_{a\uparrow} c_{a\downarrow} c^\dagger_{a\downarrow} c_{a\uparrow}\rangle \\ &= -i(\langle n_{a\downarrow}\rangle - \langle n_{a\uparrow}\rangle) \\ &\overset{TR}{=} 0.\end{aligned} \tag{4.104}$$

Since the choice of coordinate system is arbitrary the same must hold for all other $\chi_{\alpha\beta}$ with $\alpha \neq \beta$. Further, since $\chi^{aa}_{yx}(\tau = 0^-, \boldsymbol{r} = 0) = \chi^{aa}_{xy}(\tau = 0^+, \boldsymbol{r} = 0) = 0$ the above also means that the mixed spin susceptibilities are continuous at $\tau = 0$.

□

4.8 Self-energy

We now derive an expression for the self-energy in TPSC. The TPSC vertex is known to violate crossing symmetry[33, 157]. Hence to restore crossing symmetry in the self-energy expression one commonly expands the four-point correlation function once in the longitudinal and once in the transversal channel and then takes the average. We follow the same strategy here. Additionally, in the presence of spin-orbit coupling we also have to restore TR symmetry, which we do by averaging over the TPSC self-energy and its time reversed partner. We also explain that the necessity of this last step originates, from the fact that the position of the bare and the renormalized vertex in general cannot be interchanged anymore when they are matrices.

4.8.1 Self-energy expanded in the longitudinal channel

A local constant irreducible vertex violates crossing symmetry [33, 157]. Hence, our strategy is, following Refs. [33, 157], to expand the four-point correlator for the self-energy once in the longitudinal and once in the transversal channel and average both results.

We start from exact expression for the self-energy in the Hubbard model Eq. 2.77 which with the shorthand notation $U_{31} = U\delta(\tau_1 - \tau_3)\delta_{\boldsymbol{R}_{i_1}\boldsymbol{R}_{i_3}}\delta_{a_1a_3}\delta_{\sigma_1-\sigma_3}$ can be written as

$$\Sigma(1,2)_\phi = -U_{\bar{3}1}\left\langle \mathcal{T}_\tau c^\dagger(\bar{3}^{++})c(\bar{3}^+)c(1)c^\dagger(\bar{4})\right\rangle_\phi G^{-1}(\bar{4},2)_\phi. \tag{4.105}$$

The Four-point function we can get in the particle-hole channel from a functional derivative i.e.

$$\langle \mathcal{T}_\tau c(1)c^\dagger(2)c^\dagger(3)c(4)\rangle_\phi = \frac{\delta G(1,2)_\phi}{\delta\phi(3,4)} - G(1,2)_\phi G(4,3)_\phi, \tag{4.106}$$

where we recognize the generalized susceptibility, which we expand in the particle-hole channel yielding the Bethe-Saltpeter equation

$$\chi(1,2;3,4) = -\frac{\delta G(1,2)_\phi}{\delta\phi(3,4)}|_{\phi=0} = -G(1,3)G(4,2) + G(1,\bar{5})\Gamma(\bar{5},\bar{6};\bar{7},\bar{8})\chi(\bar{7},\bar{8};3,4)G(\bar{6},2). \tag{4.107}$$

In the longitudinal channel we have to set $3 \to \bar{3}^{++}$ and $4 \to 3^+$ so that in functional derivative has only two times a 3 as argument. Also, we set $1 \to 1$, $2 \to \bar{4}$ so that one cancels the G^{-1} in the end. We get no overall minus sign because the number of permutations is even. We get

$$\begin{aligned}
\Sigma^l(1,2)_\phi &= -U_{\bar{3}1}\left(\frac{\delta G(1,\bar{4})_\phi}{\delta\phi(\bar{3}^{++},\bar{3}^+)} - G(1,\bar{3}^{++})_\phi G(\bar{3}^+,\bar{4})_\phi\right)G^{-1}(\bar{4},2)_\phi \\
&= -U_{\bar{3}1}\Big(G(\bar{3}^+,\bar{3}^{++})G(1,\bar{4}) - G(1,\bar{5})\Gamma(\bar{5},\bar{6};\bar{7},\bar{8})\chi(\bar{7},\bar{8};\bar{3}^{++},\bar{3}^+)G(\bar{6},\bar{4}) \\
&\quad - G(1,\bar{3}^{++})_\phi G(\bar{3}^+,\bar{4})_\phi\Big)G^{-1}(\bar{4},2)_\phi \\
&= U_{\bar{3}1}\Big(G(\bar{3}^+,\bar{3}^{++})_\phi\delta(1,2) + G(1,\bar{5})\Gamma(\bar{5},2;\bar{7},\bar{8})\chi(\bar{7},\bar{8};\bar{3}^{++},\bar{3}^+) \\
&\quad - G(1,\bar{3}^{++})\delta(\bar{3}^+ - 2)\Big) \\
&= U_{\bar{3}1}G(1,\bar{3}^{++})_\phi\delta(1,2) - U_{21^+}G(1,2^+) + U_{\bar{3}1}G(1,\bar{5})\Gamma(\bar{5},2;\bar{7},\bar{8})\chi(\bar{7},\bar{8};\bar{3}^{++},\bar{3}^+).
\end{aligned} \tag{4.108}$$

Plugging in the Hubbard interaction, setting the source filed $\phi = 0$ and restoring spin and orbital indices we get

$$\begin{aligned}
\Sigma^{la_1a_2}_{\sigma_1\sigma_2}(1,2) &= UG^{a_1a_1}_{-\sigma_1-\sigma_1}(1,1^+)\delta(\tau_1-\tau_2)\delta_{\boldsymbol{R}_{i_1}\boldsymbol{R}_{i_2}}\delta_{a_1a_2}\delta_{\sigma_1\sigma_2} - U\delta(\tau_1-\tau_2)\delta_{\boldsymbol{R}_{i_1}\boldsymbol{R}_{i_2}}\delta_{a_1a_2}\delta_{\sigma_1-\sigma_2}G^{a_1a_1}_{\sigma_1-\sigma_1}(1,2^+) \\
&\quad + UG^{a_1\bar{a}_5}_{\sigma_1\bar{\sigma}_5}(1,\bar{5})\Gamma^{\bar{a}_5a_2\bar{a}_7\bar{a}_8}_{\bar{\sigma}_5\sigma_2\bar{\sigma}_7\bar{\sigma}_8}(\bar{5},2;\bar{7},\bar{8})\chi^{\bar{a}_7\bar{a}_8a_1a_1}_{\bar{\sigma}_7\bar{\sigma}_8-\sigma_1-\sigma_1}(\bar{7},\bar{8};1^+,1).
\end{aligned} \tag{4.109}$$

The first term is the Hartree term and the second term is the Fock term. As one can see, the delta function makes the Fock term proportional to $\langle S_a^+ \rangle$ or $\langle S_a^- \rangle$, which vanish in the presence of TR. We now insert the local TPSC vertex Eq. 4.29 in the above equation. We get

$$\begin{aligned}\Sigma^{la_1a_2}_{\sigma_1\sigma_2}(1,2) = & UG^{a_1a_1}_{-\sigma_1-\sigma_1}(1,1^+)\delta(\tau_1-\tau_2)\delta_{\boldsymbol{R}_{i_1}\boldsymbol{R}_{i_2}}\delta_{a_1a_2}\delta_{\sigma_1\sigma_2} \\ & + UG^{a_1a_2}_{\sigma_1\bar{\sigma}_4}(1,2^+)\Gamma^{a_2}_{\bar{\sigma}_4\sigma_2\bar{\sigma}_6\bar{\sigma}_7}\chi^{a_2a_1}_{\bar{\sigma}_6\bar{\sigma}_7-\sigma_1-\sigma_1}(2,2^+,1^+,1). \end{aligned} \tag{4.110}$$

Going to frequency momentum space, setting $G = G^{(1)}$ and using the matrix notation we get

$$\Sigma^{la_1a_2}_{\sigma_1\sigma_2}(k) = U\frac{\langle n\rangle}{2}\delta_{a_1a_2}\delta_{\sigma_1\sigma_2} + U\frac{T}{N}\sum_q G^{(1)a_1a_2}_{\sigma_1\bar{\sigma}_4}(k+q)\left(\Gamma\chi(q)\right)^{a_2a_1}_{\bar{\sigma}_4\sigma_2;-\sigma_1-\sigma_1}. \tag{4.111}$$

Note that Γ can be regarded as a diagonal matrix in the site space. Using the basis transformation M one can write the expression in terms of Γ' and χ'

$$\Sigma^{la_1a_2}_{\sigma_1\sigma_2}(k) = U\frac{\langle n\rangle}{2}\delta_{a_1a_2}\delta_{\sigma_1\sigma_2} + \frac{U}{4}\frac{T}{N}\sum_q G^{(1)a_1a_2}_{\sigma_1\bar{\sigma}_4}(k+q)\left(M\Gamma'\chi'(q)M\right)^{a_2a_1}_{\bar{\sigma}_4\sigma_2;-\sigma_1-\sigma_1}. \tag{4.112}$$

4.8.2 Self-energy expanded in the transversal channel

Now, we want to expand the four-point correlator in the expression for the self-energy in the transversal particle-hole channel. Again we start from the following exact expression for the self-energy in the Hubbard model (Eq. 4.105

$$\Sigma(1,2)_\phi = -U_{\bar{3}1}\left\langle \mathcal{T}_\tau c^\dagger(\bar{3}^{++})c(\bar{3}^+)c(1)c^\dagger(\bar{4})\right\rangle_\phi G^{-1}(\bar{4},2)_\phi. \tag{4.113}$$

Similar to the expansion in the longitudinal we express the four point correlation function in terms of a functional derivative i.e.

$$\left\langle \mathcal{T}_\tau c(1)c^\dagger(2)c^\dagger(3)c(4)\right\rangle_\phi = \frac{\delta G(1,2)_\phi}{\delta\phi(3,4)} - G(1,2)_\phi G(4,3)_\phi, \tag{4.114}$$

and then use the BSE in the particle-hole channel. Expanding in the transversal channel means that the four point correlator is generated by a functional derivative with a field that is offdiagonal in spin (because of the Hubbard interaction) i.e. here we have to set $3 \to \bar{3}^{++}$ and $4 \to 1$. Also, we set $1 \to 3^+$, $2 \to \bar{4}$. We obtain

$$\begin{aligned}\Sigma^t(1,2)_\phi &= -U_{\bar{3}1}\left(\frac{\delta G(\bar{3}^+,\bar{4})_\phi}{\delta\phi(\bar{3}^{++},1)} - G(\bar{3}^+,\bar{3}^{++})_\phi G(1,\bar{4})_\phi\right)G^{-1}(\bar{4},2)_\phi \\ &= -U_{\bar{3}1}\Big(G(1,\bar{3}^{++})G(\bar{3}^+,\bar{4}) - G(\bar{3}^+,\bar{5})\Gamma(\bar{5},\bar{6};\bar{7},\bar{8})\chi(\bar{7},\bar{8};\bar{3}^{++},1)G(\bar{6},\bar{4}) \\ &\quad - G(\bar{3}^+,\bar{3}^{++})_\phi G(1,\bar{4})_\phi\Big)G^{-1}(\bar{4},2)_\phi \\ &= -U_{\bar{3}1}\Big(G(1,\bar{3}^{++})_\phi\delta(\bar{3}^+-2) + G(\bar{3}^+,\bar{5})\Gamma(\bar{5},2;\bar{7},\bar{8})\chi(\bar{7},\bar{8};\bar{3}^{++},1) \\ &\quad - G(\bar{3}^+,\bar{3}^{++})\delta(1-2)\Big) \\ &= U_{\bar{3}1}G(\bar{3}^+,\bar{3}^{++})_\phi\delta(1,2) - U_{21^+}G(1,2^+) - U_{\bar{3}1}G(\bar{3}^+,\bar{5})\Gamma(\bar{5},2;\bar{7},\bar{8})\chi(\bar{7},\bar{8};\bar{3}^{++},1). \end{aligned} \tag{4.115}$$

Plugging in the Hubbard interaction, setting the source filed $\phi = 0$ and restoring spin and orbital indices we get

$$\begin{aligned}\Sigma^{ta_1a_2}_{\sigma_1\sigma_2}(1,2) = & UG^{a_1a_1}_{-\sigma_1-\sigma_1}(1,1^+)\delta(\tau_1-\tau_2)\delta_{\boldsymbol{R}_{i_1}\boldsymbol{R}_{i_2}}\delta_{a_1a_2}\delta_{\sigma_1\sigma_2} \\ & - UG^{a_1\bar{a}_5}_{-\sigma_1\bar{\sigma}_5}(1^+,\bar{5})\Gamma^{\bar{a}_5\bar{a}_2\bar{a}_7\bar{a}_8}_{\bar{\sigma}_5\sigma_2\bar{\sigma}_7\bar{\sigma}_8}(\bar{5},2;\bar{7},\bar{8})\chi^{\bar{a}_7\bar{a}_8a_1a_1}_{\bar{\sigma}_7\bar{\sigma}_8-\sigma_1\sigma_1}(\bar{7},\bar{8};1^{++},1). \end{aligned} \tag{4.116}$$

The Fock term vanishes due to TR. Plugging in the local TPSC vertex we get

$$\begin{aligned}\Sigma^{ta_1a_2}_{\sigma_1\sigma_2}(1,2) = U\delta(\tau_1-\tau_2)\delta_{\boldsymbol{R}_{i_1}\boldsymbol{R}_{i_2}}\delta_{a_1a_2}\delta_{\sigma_1\sigma_2}G^{a_1a_1}_{-\sigma_1-\sigma_1}(1,1^+)\\ - UG^{a_1a_2}_{-\sigma_1\bar{\sigma}_5}(1^+,2^-)\Gamma^{a_2}_{\bar{\sigma}_5\sigma_2\bar{\sigma}_7\bar{\sigma}_8}\chi^{a_2a_1}_{\bar{\sigma}_7\bar{\sigma}_8-\sigma_1\sigma_1}(2,2^+,1^+,1)\end{aligned} \tag{4.117}$$

Going to frequency momentum space, setting $G = G^{(1)}$ and using the matrix notation we get

$$\Sigma^{ta_1a_2}_{\sigma_1\sigma_2}(1,2) = U\frac{\langle n\rangle}{2}\delta_{a_1a_2}\delta_{\sigma_1\sigma_2} - U\frac{T}{N}\sum_q G^{(1)a_1a_2}_{-\sigma_1\bar{\sigma}_5}(k+q)\left(\Gamma\chi(q)\right)^{a_2a_1}_{\bar{\sigma}_5\sigma_2,-\sigma_1\sigma_1}. \tag{4.118}$$

Expressed by Γ' and χ' one gets

$$\Sigma^{ta_1a_2}_{\sigma_1\sigma_2}(1,2) = U\frac{\langle n\rangle}{2}\delta_{a_1a_2}\delta_{\sigma_1\sigma_2} - \frac{U}{4}\frac{T}{N}\sum_q G^{(1)a_1a_2}_{-\sigma_1\bar{\sigma}_5}(k+q)\left(M\Gamma'\chi'(q)M\right)^{a_2a_1}_{\bar{\sigma}_5\sigma_2,-\sigma_1\sigma_1}. \tag{4.119}$$

4.8.3 Time reversal of the TPSC self-energy

We now investigate time reversal symmetry in the TPSC expression for the self-energy derived above, first in the longitudinal channel, then in the transversal channel. As shown before, the exact self-energy must fulfill TR in the following form

$$\Sigma^{ab}_{\sigma\sigma'}(i\omega_n,\boldsymbol{k}) = \sigma\sigma'\Sigma^{ba}_{-\sigma'-\sigma}(i\omega_n,-\boldsymbol{k}). \tag{4.120}$$

Further, for Green's function, susceptibility and vertex it must hold

$$G^{ab}_{\sigma\sigma'}(i\omega_n,\boldsymbol{k}) = \sigma\sigma'G^{ba}_{-\sigma'-\sigma}(i\omega_n,-\boldsymbol{k}) \tag{4.121}$$

$$\chi^{ab}_{\rho\zeta}(iq_m,\boldsymbol{q}) = \eta_{\rho\zeta}\chi^{ba}_{-\zeta-\rho}(iq_m,-\boldsymbol{q}) \tag{4.122}$$

$$\Gamma^{a}_{\rho\zeta} = \eta_{\rho\zeta}\Gamma^{a}_{-\zeta-\rho}, \tag{4.123}$$

where $\eta_{\rho\zeta}$ gives a factor of -1 for each $+$ or $-$. The last two equations can also be written as

$$\Gamma^{a}_{\sigma_1\sigma_2,\sigma_3\sigma_4} = \sigma_1\sigma_2\sigma_3\sigma_4\Gamma^{a}_{-\sigma_3-\sigma_4,-\sigma_1-\sigma_2}, \tag{4.124}$$

$$\chi^{ab}_{\sigma_1\sigma_2,\sigma_3\sigma_4}(iq_m,\boldsymbol{q}) = \sigma_1\sigma_2\sigma_3\sigma_4\chi^{ba}_{-\sigma_3-\sigma_4,-\sigma_1-\sigma_2}(iq_m,-\boldsymbol{q}). \tag{4.125}$$

We repeat the TPSC self-energy in the longitudinal channel for convenience here

$$\Sigma^{la_1a_2}_{\sigma_1\sigma_2}(k) = U\frac{\langle n\rangle}{2}\delta_{a_1a_2}\delta_{\sigma_1\sigma_2} + U\frac{T}{N}\sum_q G^{(1)a_1a_2}_{\sigma_1\bar{\sigma}_4}(k+q)\left(\Gamma\chi(q)\right)^{a_2a_1}_{\bar{\sigma}_4\sigma_2,-\sigma_1-\sigma_1}. \tag{4.126}$$

We only focus on the part with the vertex, because it is trivial that the Hartree term fulfills TR. We calculate for the TPSC self-energy in the longitudinal channel

$$\begin{aligned}\sigma_1\sigma_2\Sigma^{la_2a_1}_{-\sigma_2-\sigma_1}(i\omega_n,-\boldsymbol{k}) &= U\frac{T}{N}\sum_{iq_m\boldsymbol{q}} G^{(1)a_2a_1}_{-\sigma_2\bar{\sigma}_4}(i\omega_n+iq_m,-\boldsymbol{k}+\boldsymbol{q})\left(\Gamma\chi(iq_m,\boldsymbol{q})\right)^{a_1a_2}_{\bar{\sigma}_4-\sigma_1,\sigma_2\sigma_2}\\ &= U\frac{T}{N}\sum_{iq_m\boldsymbol{q}} G^{(1)a_1a_2}_{-\bar{\sigma}_4\sigma_2}(i\omega_n+iq_m,\boldsymbol{k}+\boldsymbol{q})\Gamma^{a_1}_{\bar{\sigma}_4-\sigma_1,\bar{\sigma}_5\bar{\sigma}_6}\chi^{a_1a_2}_{\bar{\sigma}_5\bar{\sigma}_6,\sigma_2\sigma_2}(iq_m,-\boldsymbol{q})\\ &= U\frac{T}{N}\sum_{iq_m\boldsymbol{q}} G^{(1)a_1a_2}_{-\bar{\sigma}_4\sigma_2}(i\omega_n+iq_m,\boldsymbol{k}+\boldsymbol{q})\chi^{a_2a_1}_{-\sigma_2-\sigma_2,\bar{\sigma}_5\bar{\sigma}_6}(iq_m,\boldsymbol{q})\Gamma^{a_1}_{\bar{\sigma}_5\bar{\sigma}_6,-\bar{\sigma}_4\sigma_1}\\ &= U\frac{T}{N}\sum_{iq_m\boldsymbol{q}} G^{(1)a_1a_2}_{\bar{\sigma}_4\sigma_2}(i\omega_n+iq_m,\boldsymbol{k}+\boldsymbol{q})\left(\chi(iq_m,\boldsymbol{q})\Gamma\right)^{a_2a_1}_{-\sigma_2-\sigma_2,\bar{\sigma}_4\sigma_1}.\end{aligned} \tag{4.127}$$

Going from the first to the second row we used TR of the Green's function. Going from the second to the thrid row we used TR of χ and Γ.

In the transversal channel we can do a similar calculation. For the self-energy expanded in the transversal channel we found the following expression

$$\Sigma^{ta_1a_2}_{\sigma_1\sigma_2}(1,2) = U\frac{\langle n\rangle}{2}\delta_{a_1a_2}\delta_{\sigma_1\sigma_2} - U\frac{T}{N}\sum_q G^{(1)a_1a_2}_{-\sigma_1\bar{\sigma}_4}(k+q)\left(\Gamma\chi(q)\right)^{a_2a_1}_{\bar{\sigma}_4\sigma_2,-\sigma_1\sigma_1}. \tag{4.128}$$

Focussing again on the part with the vertex we get for the time reversed expression

$$\begin{aligned}
\sigma_1\sigma_2\Sigma^{ta_2a_1}_{-\sigma_2-\sigma_1}(i\omega_n,-\boldsymbol{k}) &= -U\frac{T}{N}\sum_{iq_m\boldsymbol{q}} G^{(1)a_2a_1}_{\bar{\sigma}_4\sigma_2}(i\omega_n+iq_m,-\boldsymbol{k}+\boldsymbol{q})\left(\Gamma\chi(iq_m,\boldsymbol{q})\right)^{a_1a_2}_{\bar{\sigma}_4-\sigma_1,\sigma_2-\sigma_2}\\
&= -U\frac{T}{N}\sum_{iq_m\boldsymbol{q}} G^{(1)a_1a_2}_{-\sigma_2-\bar{\sigma}_4}(i\omega_n+iq_m,\boldsymbol{k}+\boldsymbol{q})\left(\Gamma^{a_1}_{\bar{\sigma}_4-\sigma_1,\bar{\sigma}_5\bar{\sigma}_6}\chi^{a_1a_2}_{\bar{\sigma}_5\bar{\sigma}_6,\sigma_2-\sigma_2}(iq_m,-\boldsymbol{q})\right)\\
&= -U\frac{T}{N}\sum_{iq_m\boldsymbol{q}} G^{(1)a_1a_2}_{-\sigma_2-\bar{\sigma}_4}(i\omega_n+iq_m,\boldsymbol{k}+\boldsymbol{q})\chi^{a_2a_1}_{-\sigma_2\sigma_2,\bar{\sigma}_5\bar{\sigma}_6}(iq_m,\boldsymbol{q})\Gamma^{a_1}_{\bar{\sigma}_5\bar{\sigma}_6,-\bar{\sigma}_4\sigma_1}\\
&= -U\frac{T}{N}\sum_{iq_m\boldsymbol{q}} G^{(1)a_1a_2}_{-\sigma_2\bar{\sigma}_4}(i\omega_n+iq_m,\boldsymbol{k}+\boldsymbol{q})\left(\chi(iq_m,\boldsymbol{q})\Gamma\right)^{a_2a_1}_{-\sigma_2\sigma_2,\bar{\sigma}_4\sigma_1}
\end{aligned} \tag{4.129}$$

As we can see the above expressions do not fulfill TR symmetry, because the TPSC vertex switches from one side of the susceptibility to the other. Graphically the action of TR can be represented as follows for terms contributing to the self-energy

$\Sigma(1-2)\sim$ 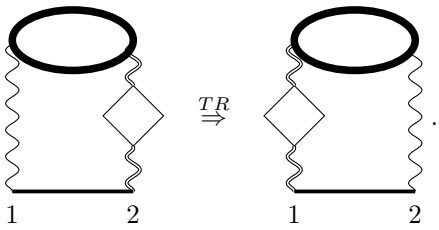 . (4.130)

The wiggled line represents the bare Hubbard interaction, the straight line the first level Green's function $G^{(1)}$, the ellipse one of the susceptibilities and the wiggled line with a square represents a renormalized vertex (spin or charge). Unlike to the single-band case with spin-rotation symmetry, where the TPSC vertices are just numbers, it does matter now on which site the bare vertex U and on which site the renormalized vertex Γ is placed, because Γ is a matrix now.

Note that it is possible to obtain the time reversed expressions also from the equation of motion for the Green's function $G(1,2)$, but then acting the time derivative ∂_τ on the second argument instead of the first one. Doing so one obtains the following starting point which then has to be expanded in the longitudinal or transversal channel

$$G(1,\bar{3})_\phi\Sigma(\bar{3},2)_\phi = -U_{2\bar{3}}\left\langle\mathcal{T}_\tau c(1)c^\dagger(\bar{3}^{++})c(\bar{3}^{+})c^\dagger(2)\right\rangle_\phi. \tag{4.131}$$

We conclude that, since TPSC is not an exact theory, it does matter how and which four-point correlation function we expand for the self-energy. The obtained result is linked to the breaking of symmetries, namely crossing symmetry and TR symmetry. We suggest to average the self-energy with its time reversed partner to restore TR symmetry.

4.8.4 Final expression for the self-energy

We now present the final self-energy expression in TPSC with SOC. We suggest averaging the self-energy expressions with its time reversed partners to restore time reversal symmetry. This is analogues

to averaging of the expression obtained by expanding in the transversal and in the longitudinal channel, which we also adopt [33, 157]. The final TPSC self-energy expression then reads:

$$\begin{aligned}\Sigma^{(2)a_1a_2}_{\sigma_1\sigma_2}(k) = U\delta_{a_1a_2}\delta_{\sigma_1\sigma_2}\frac{\langle n_a\rangle}{2} \\ + \frac{U}{16}\frac{T}{N}\sum_q \Big(G^{(1)a_1a_2}_{\sigma_1\bar{\sigma}_4}(k+q)\,(M\Gamma'\chi'(q)M)^{a_2a_1}_{\bar{\sigma}_4\sigma_2,-\sigma_1-\sigma_1} \\ + G^{(1)a_1a_2}_{\bar{\sigma}_4\sigma_2}(k+q)\,(M\chi'(q)\Gamma'M)^{a_2a_1}_{-\sigma_2-\sigma_2,\bar{\sigma}_4\sigma_1} \\ + G^{(1)a_1a_2}_{-\sigma_1\bar{\sigma}_4}(k+q)\,(M\Gamma'\chi'(q)M)^{a_2a_1}_{\bar{\sigma}_4\sigma_2,-\sigma_1\sigma_1} \\ + G^{(1)a_1a_2}_{-\sigma_2\bar{\sigma}_4}(k+q)\,(M\chi'(q)\Gamma'M)^{a_2a_1}_{-\sigma_2\sigma_2,\bar{\sigma}_4\sigma_1}\Big).\end{aligned} \tag{4.132}$$

The second level Green's function can be constructed from the Dyson equation

$$G^{(2)ab}_{\sigma\sigma'}(i\omega_n,\boldsymbol{k}) = \left(\left(i\omega_n - \mathcal{H}(\boldsymbol{k}) + \mu - \Sigma^{(2)}(i\omega_n,\boldsymbol{k})\right)^{-1}\right)^{ab}_{\sigma\sigma'}. \tag{4.133}$$

However, note that the chemical potential needs to be adjusted to match the initially given particle number.

4.9 $\mathrm{Tr}(\Sigma G)$ consistency check

In this section we want to prove the following equation

$$\frac{1}{2}\frac{T}{N}\sum_{\omega_n\boldsymbol{k}}\mathrm{Tr}\left(\Sigma^{(2)}(i\omega_n,\boldsymbol{k})G^{(1)}(i\omega_n,\boldsymbol{k})e^{-i\omega_n 0^-}\right) = U\sum_a \langle n_{a\uparrow}n_{a\downarrow}\rangle\,, \tag{4.134}$$

where the trace runs over spin and orbital indices. Using $G^{(2)}$ instead of $G^{(1)}$ the expression is not fulfilled exactly anymore, but it can be used as a consistency check between one-particle and two-particle quantities. This test gives a strong indication if TPSC is still valid in the parameter regime of interest, see also Ref. [159].

Proof. First, we consider the self-energy expanded in the longitudinal channel

$$\Sigma^{la_1a_2}_{\sigma_1\sigma_2}(k) = U\frac{\langle n\rangle}{2}\delta_{a_1a_2}\delta_{\sigma_1\sigma_2} + U\frac{T}{N}\sum_q G^{(1)a_1a_2}_{\sigma_1\bar{\sigma}_4}(k+q)\,(\Gamma\chi(q))^{a_2a_1}_{\bar{\sigma}_4\sigma_2,-\sigma_1-\sigma_1}\,. \tag{4.135}$$

Recall that the effective non-interacting susceptibility $\chi^{(1)}$ is defined as

$$\chi^{(1)a_1a_2}_{\sigma_1\sigma_2,\sigma_3\sigma_4}(q) = -\sum_k G^{(1)a_1a_2}_{\sigma_2\sigma_3}(k+q)G^{(1)a_2a_1}_{\sigma_4\sigma_1}(k). \tag{4.136}$$

For the Hartree part $\Sigma^{(2)Hab}$ we get

$$\frac{1}{2}\frac{T}{N}\sum_k\sum_{ab\sigma_1\sigma_2}\Sigma^{(2)Hab}_{\sigma_1\sigma_2}(k)G^{(1)ba}_{\sigma_2\sigma_1}(k)e^{-ik_n0^-} = \frac{1}{2}\sum_{a\sigma_1\sigma_2}U\frac{\langle n_a\rangle}{2}\langle n_{a\sigma_1}\rangle\,\delta_{\sigma_1\sigma_2} = \sum_a\frac{U}{4}\langle n_a\rangle^2\,. \tag{4.137}$$

Now we can check what happens to the vertex part Σ^{lV}

$$
\begin{aligned}
&\frac{1}{2}\frac{T}{N}\sum_{k}\sum_{a_1a_2\sigma_1\sigma_2}\Sigma^{(2)lVa_1a_2}_{\sigma_1\sigma_2}(k)G^{(1)a_2a_1}_{\sigma_2\sigma_1}(k)e^{-ik_n0^-}\\
&=\frac{U}{2}\left(\frac{T}{N}\right)^2\sum_{kq}\sum_{a_1a_2\sigma_1\sigma_2\sigma_4}G^{(1)a_1a_2}_{\sigma_1\sigma_4}(k+q)\left(\Gamma\chi(q)\right)^{a_2a_1}_{\sigma_4\sigma_2,-\sigma_1-\sigma_1}G^{(1)a_2a_1}_{\sigma_2\sigma_1}(k)\\
&=-\frac{U}{2}\frac{T}{N}\sum_{q}\sum_{a_1a_2\sigma_1\sigma_2\sigma_4}\chi^{(1)a_1a_2}_{\sigma_1\sigma_1,\sigma_4\sigma_2}(q)\left(\Gamma\chi(q)\right)^{a_2a_1}_{\sigma_4\sigma_2,-\sigma_1-\sigma_1}\\
&=\frac{U}{2}\frac{T}{N}\sum_{q}\sum_{a_1\sigma_1}\left(\chi^{a_1a_1}_{\sigma_1\sigma_1,-\sigma_1-\sigma_1}(q)-\chi^{(1)a_1a_1}_{\sigma_1\sigma_1,-\sigma_1-\sigma_1}(q)\right)\\
&=\frac{U}{4}\frac{T}{N}\sum_{q}\sum_{a_1}\left(\chi^{a_1a_1}_{cc}(q)-\chi^{a_1a_1}_{zz}(q)-\left(\chi^{(1)a_1a_1}_{cc}(q)-\chi^{(1)a_1a_1}_{zz}(q)\right)\right)\\
&\overset{\text{TR}}{=}\sum_{a_1}\left(-\frac{U}{4}\langle n_{a_1}\rangle^2+U\langle n_{\uparrow a_1}n_{\downarrow a_1}\rangle\right).
\end{aligned}
\tag{4.138}
$$

Note the minus sign in going from the second to the third row. The convergence factor can be dropped because of the $\sim\frac{1}{\omega_n^2}$ in the convolution. Going from the third to the fourth row we inserted the BSE. Going from the fourth to the fifth row we notice that the expression can be written as a difference between χ_{cc} and χ_{zz}. The sums over $\chi^{(1)aa}_{zz}(q)$ and $\chi^{(1)aa}_{cc}(q)$ cancel each other. This can be seen by making use of the sum rules in the corresponding non-interacting case, where one has

$$
\frac{T}{N}\sum_{q}\chi^{(1)aa}_{zz}(q)=\langle n_a\rangle_{(1)}-2\langle n_{a\uparrow}n_{a\downarrow}\rangle_{(1)}\overset{\text{TR}}{=}\langle n_a\rangle_{(1)}-2\langle n_{a\uparrow}\rangle_{(1)}\langle n_{a\downarrow}\rangle_{(1)}\overset{\text{TR}}{=}\langle n_a\rangle_{(1)}-\frac{\langle n_a\rangle^2_{(1)}}{2},
\tag{4.139}
$$

$$
\begin{aligned}
\frac{T}{N}\sum_{q}\chi^{(1)aa}_{ch}(q)&=\langle n_a\rangle_{(1)}+2\langle n_{a\uparrow}n_{a\downarrow}\rangle_{(1)}-\langle n_a\rangle^2_{(1)}\overset{\text{TR}}{=}\langle n_a\rangle_{(1)}+2\langle n_{a\uparrow}\rangle_{(1)}\langle n_{a\downarrow}\rangle_{(1)}-\langle n_a\rangle^2_{(1)}\\
&\overset{\text{TR}}{=}\langle n_a\rangle_{(1)}-\frac{\langle n_a\rangle^2_{(1)}}{2}.
\end{aligned}
\tag{4.140}
$$

We used that in a non-interacting system we can use Wick's theorem to do a decoupling of the double-occupancies. However, because of TR symmetry terms such as $\langle c^\dagger_{a\uparrow}c_{a\downarrow}\rangle$ vanish. Taking the results for the Hartree term and the vertex term together, one obtains the result claimed above.

A similar calculation can be done for the self-energy expanded in the transversal channel. The transversal channel self-energy reads

$$
\Sigma^{ta_1a_2}_{\sigma_1\sigma_2}(1,2)=U\frac{\langle n\rangle}{2}\delta_{a_1a_2}\delta_{\sigma_1\sigma_2}-U\frac{T}{N}\sum_{q}G^{(1)a_1a_2}_{-\sigma_1\bar{\sigma}_5}(k+q)\left(\Gamma\chi(q)\right)^{a_2a_1}_{\bar{\sigma}_5\sigma_2,-\sigma_1\sigma_1}.
\tag{4.141}
$$

We get for the vertex part Σ^{tV}

$$
\begin{aligned}
&\frac{1}{2}\frac{T}{N}\sum_{k}\sum_{a_1a_2\sigma_1\sigma_2}\Sigma^{(2)tV a_1a_2}_{\sigma_1\sigma_2}(k)G^{(1)a_2a_1}_{\sigma_2\sigma_1}(k)e^{-ik_n0^-}\\
&=-\frac{U}{2}\left(\frac{T}{N}\right)^2\sum_{kq}\sum_{a_1a_2\sigma_1\sigma_2\sigma_4}G^{(1)a_1a_2}_{-\sigma_1\bar{\sigma}_5}(k+q)\left(\Gamma\chi(q)\right)^{a_2a_1}_{\bar{\sigma}_5\sigma_2,-\sigma_1\sigma_1}G^{(1)a_2a_1}_{\sigma_2\sigma_1}(k)\\
&=\frac{U}{2}\frac{T}{N}\sum_{q}\sum_{a_1a_2\sigma_1\sigma_2\sigma_5}\chi^{(1)a_1a_2}_{\sigma_1-\sigma_1,\sigma_5\sigma_2}(q)\left(\Gamma\chi(q)\right)^{a_2a_1}_{\sigma_5\sigma_2,-\sigma_1\sigma_1}\\
&=-\frac{U}{2}\frac{T}{N}\sum_{q}\sum_{a_1\sigma_1}\left(\chi^{a_1a_1}_{\sigma_1-\sigma_1,-\sigma_1\sigma_1}(q)-\chi^{(1)a_1a_1}_{\sigma_1-\sigma_1,-\sigma_1\sigma_1}(q)\right)\\
&=-\frac{U}{4}\frac{T}{N}\sum_{q}\sum_{a_1}\left(\chi^{a_1a_1}_{xx}(q)+\chi^{a_1a_1}_{yy}(q)-\left(\chi^{(1)a_1a_1}_{xx}(q)+\chi^{(1)a_1a_1}_{yy}(q)\right)\right)\\
&\overset{\text{TR}}{=}\sum_{a_1}\left(-\frac{U}{4}\left\langle n_{a_1}\right\rangle^2+U\left\langle n_{\uparrow a_1}n_{\downarrow a_1}\right\rangle\right)
\end{aligned}
\tag{4.142}
$$

The calculations for the time reversed expressions work analogously. So with the averaging of the above expressions we get the claimed result. □

4.10 TPSC+SOC algorithm

We now summarize all necessary equations and then describe the algorithm for TPSC with SOC in the case of symmetry related orbitals. We define the following susceptibilities

$$
\chi^{ab}_{\alpha\beta}(\tau,\boldsymbol{R}_i-\boldsymbol{R}_j)=\left\langle\mathcal{T}_\tau O^\alpha_{ia}(\tau)O^\beta_{jb}(0)\right\rangle-\left\langle O^\alpha_{ia}\right\rangle\left\langle O^\beta_{jb}\right\rangle, \tag{4.143}
$$

where the operators O^α can either be S^x, S^y, S^z or n corresponding to the labels x, y, z or c or in a different basis $n_\uparrow$, $n_\downarrow$, S^+ or S^- represented by the labels $\uparrow$, $\downarrow$, $+$ or $-$. $\boldsymbol{R}_i$ is the lattice vector to the unit cell with the index i and a and b are site indices labeling the sites in the unit cell. With Fourier transform one can go to frequency momentum space $q=(iq_m,\boldsymbol{q})$. The susceptibilities can be written in a useful matrix notation

$$
\chi'=\begin{pmatrix}\chi_{cc}&\chi_{cz}&\chi_{cx}&i\chi_{cy}\\ \chi_{zc}&\chi_{zz}&\chi_{zx}&i\chi_{zy}\\ \chi_{xc}&\chi_{xz}&\chi_{xx}&i\chi_{xy}\\ i\chi_{yc}&i\chi_{xz}&i\chi_{yx}&-\chi_{yy}\end{pmatrix}, \tag{4.144}
$$

$$
\chi=\begin{pmatrix}\chi_{\uparrow\uparrow}&\chi_{\uparrow\downarrow}&\chi_{\uparrow+}&\chi_{\uparrow-}\\ \chi_{\downarrow\uparrow}&\chi_{\downarrow\downarrow}&\chi_{\downarrow+}&\chi_{\downarrow-}\\ \chi_{+\uparrow}&\chi_{+\downarrow}&\chi_{++}&\chi_{+-}\\ \chi_{-\uparrow}&\chi_{-\downarrow}&\chi_{-+}&\chi_{--}\end{pmatrix}. \tag{4.145}
$$

Both bases can be related by a basis transformation

$$
\chi'=M\chi M, \tag{4.146}
$$

where

$$
M=\begin{pmatrix}1&1&0&0\\ 1&-1&0&0\\ 0&0&1&1\\ 0&0&1&-1\end{pmatrix}. \tag{4.147}
$$

The first level susceptibility is defined as

$$\chi^{(1)a_1a_2}_{\sigma_1\sigma_2,\sigma_3\sigma_4}(q) = -\sum_k G^{(1)a_1a_2}_{\sigma_2\sigma_3}(k+q)G^{(1)a_2a_1}_{\sigma_4\sigma_1}(k), \tag{4.148}$$

where the first two and last two spin indices can be grouped together to the labels $\uparrow$, $\downarrow$, $+$ or $-$. $G^{(1)}$ is the Green's function of an effective noninteracting system. For symmetry related orbitals this Green's function is equivalent to the noninteraction one i.e $G^{(1)} = G_0$. Invoking time reversal symmetry the TPSC vertex takes the form

$$\Gamma' = \begin{pmatrix} \Gamma_{cc} & 0 & 0 & 0 \\ 0 & -\Gamma_{zz} & 0 & 0 \\ 0 & 0 & -\Gamma_{xx} & 0 \\ 0 & 0 & 0 & \Gamma_{yy} \end{pmatrix}. \tag{4.149}$$

The interacting expressions for the susceptibility obtained from the BSE is given by

$$\chi'(q) = \left(1 + \frac{1}{2}\Gamma'\chi'^{(1)}(q)\right)^{-1} \chi'^{(1)}(q). \tag{4.150}$$

The spin and charge sum rules are given by

$$\frac{T}{N}\sum_q \chi^{aa}_{cc}(q) = \langle n_a\rangle + 2\langle n_{a\uparrow}n_{a\downarrow}\rangle - \langle n_a\rangle^2, \tag{4.151}$$

$$\frac{T}{N}\sum_q \chi^{aa}_{\alpha\alpha}(q) = \langle n_a\rangle - 2\langle n_{a\uparrow}n_{a\downarrow}\rangle, \tag{4.152}$$

where $\alpha = x, y, z$. The ansatz equation, relating one vertex element to the double occupancies, is given by

$$\Gamma^a_{\alpha\alpha} = U\frac{\langle n_{a\uparrow}n_{a\downarrow}\rangle}{\langle n_{a\uparrow}\rangle\langle n_{a\downarrow}\rangle}. \tag{4.153}$$

We suggest using the ansatz equation in the spin direction that reaches an instability first. Sum rules and ansatz equation yield four equations for four unknown vertex elements (for symmetry related orbitals), that have to be found self-consistently. The second level self-energy is calculated via

$$\begin{aligned}\Sigma^{(2)a_1a_2}_{\sigma_1\sigma_2}(k) = {} & U\delta_{a_1a_2}\delta_{\sigma_1\sigma_2}\frac{\langle n_a\rangle}{2} \\ & + \frac{U}{16}\frac{T}{N}\sum_q \Big(G^{(1)a_1a_2}_{\sigma_1\bar{\sigma}_4}(k+q)\,(M\Gamma'\chi'(q)M)^{a_2a_1}_{\bar{\sigma}_4\sigma_2,-\sigma_1-\sigma_1} \\ & + G^{(1)a_1a_2}_{\bar{\sigma}_4\sigma_2}(k+q)\,(M\chi'(q)\Gamma'M)^{a_2a_1}_{-\sigma_2-\sigma_2,\bar{\sigma}_4\sigma_1} \\ & + G^{(1)a_1a_2}_{-\sigma_1\bar{\sigma}_4}(k+q)\,(M\Gamma'\chi'(q)M)^{a_2a_1}_{\bar{\sigma}_4\sigma_2,-\sigma_1\sigma_1} \\ & + G^{(1)a_1a_2}_{-\sigma_2\bar{\sigma}_4}(k+q)\,(M\chi'(q)\Gamma'M)^{a_2a_1}_{-\sigma_2\sigma_2,\bar{\sigma}_4\sigma_1}\Big).\end{aligned} \tag{4.154}$$

The Matsubara Green's $G^{(2)}$ function is calculated from the Dyson equation

$$G^{(2)a_1a_2}_{\sigma_1\sigma_2}(i\omega_n,\boldsymbol{k}) = \left(\left(i\omega_n - \mathcal{H}_\sigma(\boldsymbol{k}) + \mu - \Sigma^{(2)}_\sigma(i\omega_n,\boldsymbol{k})\right)^{-1}\right)^{(2)a_1a_2}_{\sigma_1\sigma_2}, \tag{4.155}$$

where the trace runs over spin and orbital indices. The chemical potential μ needs to adjusted here to match the given filling n, because the self-energy can cause differences from the chemical potential at the first level $\mu^{(1)}$. The $\mathrm{Tr}(G\Sigma)$ check can be used as a consistency check between first level and second level quantities

$$\frac{1}{2}\frac{T}{N}\sum_{i\omega_n \boldsymbol{k}} \mathrm{Tr}\left(\Sigma^{(2)}(i\omega_n,\boldsymbol{k})G^{(1)}(i\omega_n,\boldsymbol{k})e^{-i\omega_n 0^-}\right) = U\sum_a \langle n_{a\uparrow}n_{a\downarrow}\rangle\,. \tag{4.156}$$

The error with respect to replacing $G^{(1)}$ by $G^{(2)}$ gives a good indication if TPSC is still valid in the current parameter regime.

For given hopping parameters, Hubbard interaction, temperature and filling the TPSC algorithm now works as follows. First, the effective noninteracting Green's function $G^{(1)}$ and susceptibility $\chi^{(1)}$ (Eq. 4.148) are calculated. Then a basis rotation to the more physical $\chi'^{(1)}$ (Eq. 4.146) is carried out. The definition of the interacting susceptibilities in Eq. 4.150, the sum rules in Eq. 4.151 and Eq. 4.152 and the ansatz equation in Eq. 4.153 used for the spin direction, where the spin fluctuations are strongest, are a set of coupled equations for the four matrix elements of the TPSC vertex that need to be solved self-consistently. Numerically, the TPSC vertex is the solution of a multidimensional root-finding problem. A reasonable starting guess can be obtained by first solving the corresponding uncoupled problem i.e. the one where $\chi^{(1)}_{\alpha\beta} = 0$ for $\alpha \neq \beta$. The second level self-energy $\Sigma^{(2)}$ can be calculated by Eq. 4.154. Using the Dyson equation (Eq. 4.155) yields $G^{(2)}$. Generally, the chemical potential needs to be adjusted. The $\mathrm{Tr}(G\Sigma)$ check in Eq. 4.156 with $G^{(2)}$ instead of $G^{(1)}$ can be used as a consistency check. A relative error of $< 10\%$ we find to be acceptable.

4.11 Consistency check: Without spin-orbit coupling

We now show that the equations for TPSC with SOC, summarized in Sec. 4.10, reduce to the original TPSC equations, summarized in Sec. 4.2, in the case of a single band without SOC. Vanishing SOC corresponds to restoring spin rotation symmetry.

First note, that the self-energy as well as the Green's function become proportional to the unit matrix in spin space. That means we can write

$$G^{ab}_{\sigma\sigma'}(i\omega_n,\boldsymbol{k}) \to G(i\omega_n,\boldsymbol{k}) \tag{4.157}$$
$$\Sigma^{ab}_{\sigma\sigma'}(i\omega_n,\boldsymbol{k}) \to \Sigma(i\omega_n,\boldsymbol{k}) \tag{4.158}$$

The first level quantities such as $G^{(1)}$ are equal to the non-interacting ones in the single-band case i.e. $G^{(1)} = G_0$, because $\Sigma^{(1)}$ can always be absorbed in the chemical potential. For the susceptibility χ' all coupling terms such as χ_{cz} or χ_{xy} vanish. Further, one has with spin rotation symmetry

$$\chi_{xx} = \chi_{yy} = \chi_{zz} \to \chi_{sp}, \tag{4.159}$$
$$\Gamma_{xx} = \Gamma_{yy} = \Gamma_{zz} \to U_{sp}. \tag{4.160}$$

We also identify

$$\chi_{cc} \to \chi_{ch}, \tag{4.161}$$
$$\Gamma_{cc} \to U_{ch}. \tag{4.162}$$

As we can see, the TPSC vertices just become numbers. Further, at the first level (here equal to the non-interacting case) we get defining $\chi^{(1)} := 2\chi^{(1)}_{\uparrow\uparrow}$

$$\chi^{(1)}_{sp} = \chi^{(1)}_{ch} = \chi^{(1)} \tag{4.163}$$

With the vanishing of all mixed susceptibilities we simply get from the BSE

$$\chi_{sp}(q) = \frac{\chi^{(1)}(q)}{1 - \frac{1}{2}U_{sp}\chi^{(1)}(q)}, \tag{4.164}$$

$$\chi_{ch}(q) = \frac{\chi^{(1)}(q)}{1 + \frac{1}{2}U_{ch}\chi^{(1)}(q)}. \tag{4.165}$$

$$\tag{4.166}$$

The sum rules stay unchanged, because the spin sum rule is the same for any spin component in any case. The ansatz equation simply becomes

$$U_{sp} = U\frac{\langle n_\uparrow n_\downarrow\rangle}{\langle n_\uparrow\rangle\langle n_\downarrow\rangle} = 4U\frac{\langle n_\uparrow n_\downarrow\rangle}{\langle n\rangle^2}. \tag{4.167}$$

For the self-energy one retrieves the original expression

$$\Sigma^{(2)}(k) = U\frac{\langle n\rangle}{2} + \frac{U}{8}\sum_q G^{(1)}(k+q)\left(3U_{sp}\chi_{sp}(q) + U_{ch}\chi_{ch}(q)\right), \tag{4.168}$$

where as usual one obtains the terms proportional to $\frac{U}{4}\left(U_{ch}\chi_{ch} + U_{sp}\chi_{sp}\right)$ for the longitudinal channel and $\frac{U}{4}\left(2U_{sp}\chi_{sp}\right)$ for the transversal channel. The averaging to restore time reversal is not needed anymore, because the verices are just numbers. The Dyson equation remains unchanged. The $\mathrm{Tr}(G\Sigma)$ check becomes

$$\frac{T}{N}\sum_{i\omega_n \boldsymbol{k}} \Sigma^{(2)}(i\omega_n, \boldsymbol{k})G^{(1)}(i\omega_n, \boldsymbol{k})e^{-i\omega_n 0^-} = U\langle n_\uparrow n_\downarrow\rangle. \tag{4.169}$$

The factor of $\frac{1}{2}$ vanishes, because there is no sum over spin indices here.

4.12 Spin-orbit coupling simplest case: S^z conserved

We now study the simplest case of SOC, namely the case where the SOC is proportional to S^z. Concretely, we mean that $[S^z_{ia}, H] = 0$ at each site. Hence, there cannot be a term in the Hamiltonian that flips the spin. In this way we can build intuition what changes in the presence of SOC.

4.12.1 TPSC algorithm simplified through S^z conservation

The conservation of S^z_{ia} at each site, leads to the absence of terms that flip a spin from up to down or vice versa. Hence, Green's function and self-energy only depend of one spin index

$$G^{ab}_{\sigma\sigma'}(i\omega_n, \boldsymbol{k}) \to G^{ab}_{\sigma}(i\omega_n, \boldsymbol{k}) \tag{4.170}$$

$$\Sigma^{ab}_{\sigma\sigma'}(i\omega_n, \boldsymbol{k}) \to \Sigma^{ab}_{\sigma}(i\omega_n, \boldsymbol{k}) \tag{4.171}$$

$$\tag{4.172}$$

Also, all susceptibilities that involve one or even two spin flips must be zero. Hence, we are left with only six nonzero susceptibilities $\chi_{\uparrow\uparrow}$, $\chi_{\uparrow\downarrow}, \chi_{\downarrow\uparrow}, \chi_{\downarrow\downarrow}, \chi_{+-}$ and χ_{-+}. For the more physical spin, charge or mixed spin-charge susceptibilities this means, that only χ_{cc}, $\chi_{zc}, \chi_{cz}, \chi_{zz}, \chi_{xx}$ and χ_{yy} are nonzero. From $[S^z_{ia}, H] = 0$ it also follows that the system possesses a rotation symmetry around the z-axis. Hence, $\chi_{xx} = \chi_{yy}$ and also $\Gamma_{xx} = \Gamma_{yy}$. In the BSE we see that the longitudinal channel and the transversal channel decouple In the transversal channel one has

$$\chi_{xx}(q) = \left(1 - \frac{1}{2}\Gamma_{xx}\chi^{(1)}_{xx}(q)\right)^{-1} \chi^{(1)}_{xx}(q) \tag{4.173}$$

$$\chi_{yy}(q) = \left(1 - \frac{1}{2}\Gamma_{yy}\chi^{(1)}_{yy}(q)\right)^{-1} \chi^{(1)}_{yy}(q) \tag{4.174}$$

In the longitudinal channel one has four equations that can be written elegantly in terms of matrices

$$\begin{pmatrix} \chi_{cc} & \chi_{cz} \\ \chi_{zc} & \chi_{zz} \end{pmatrix} = \left(\begin{pmatrix} 1 & 0 \\ 0 & 1 \end{pmatrix} + \frac{1}{2} \begin{pmatrix} \chi^{(1)}_{cc} & \chi^{(1)}_{cz} \\ \chi^{(1)}_{zc} & \chi^{(1)}_{zz} \end{pmatrix} \begin{pmatrix} \Gamma_{cc} & 0 \\ 0 & -\Gamma_{zz} \end{pmatrix} \right)^{-1} \begin{pmatrix} \chi^{(1)}_{cc} & \chi^{(1)}_{cz} \\ \chi^{(1)}_{zc} & \chi^{(1)}_{zz} \end{pmatrix}. \tag{4.175}$$

Note that the basis transformation to the physical susceptibilities in the longitudinal channel is

$$\begin{pmatrix} \chi_{cc} & \chi_{cz} \\ \chi_{zc} & \chi_{zz} \end{pmatrix} = \begin{pmatrix} 1 & 1 \\ 1 & -1 \end{pmatrix} \begin{pmatrix} \chi_{\uparrow\uparrow} & \chi_{\uparrow\downarrow} \\ \chi_{\downarrow\uparrow} & \chi_{\downarrow\downarrow} \end{pmatrix} \begin{pmatrix} 1 & 1 \\ 1 & -1 \end{pmatrix}. \tag{4.176}$$

In matrix form we can also write

$$\chi^l(q) = \left(1 + \frac{1}{2}\Gamma^l \chi^{l(1)}(q)\right)^{-1} \chi^{l(1)}(q), \tag{4.177}$$

where we defined

$$\chi^l(q) = \begin{pmatrix} \chi_{cc}(q) & \chi_{cz}(q) \\ \chi_{zc}(q) & \chi_{zz}(q) \end{pmatrix}, \tag{4.178}$$

$$\Gamma^l = \begin{pmatrix} \Gamma_{cc} & 0 \\ 0 & -\Gamma_{zz} \end{pmatrix}. \tag{4.179}$$

The spin and charge sum rules

$$\frac{T}{N}\sum_q \chi^{aa}_{cc}(q) = \langle n_a \rangle + 2\langle n_{a\uparrow} n_{a\downarrow} \rangle - \langle n_a \rangle^2, \tag{4.180}$$

$$\frac{T}{N}\sum_q \chi^{aa}_{\alpha\alpha}(q) = \langle n_a \rangle - 2\langle n_{a\uparrow} n_{a\downarrow} \rangle, \tag{4.181}$$

where $\alpha = x, y, z$, stay unchanged. The ansatz equation stays unchanged and is used in the channel were the instability in the spin susceptibility is reached first i.e.

$$\Gamma^a_{\alpha\alpha} = U\frac{\langle n_{a\uparrow} n_{a\downarrow} \rangle}{\langle n_{a\uparrow} \rangle \langle n_{a\downarrow} \rangle} = 4U\frac{\langle n_{a\uparrow} n_{a\downarrow} \rangle}{\langle n_a \rangle^2}. \tag{4.182}$$

The expression for the self-energy simplifies to

$$\Sigma^{(2)ab}_\sigma(k) = U\delta_{ab}\langle n_{a-\sigma} \rangle + \frac{U}{8}\frac{T}{N}\sum_q G^{(1)ab}_\sigma(k+q)V^{ab}_{l\sigma}(q) + \frac{U}{8}\frac{T}{N}\sum_q G^{(1)ab}_{-\sigma}(k+q)V^{ab}_{t\sigma}(q) \tag{4.183}$$

with

$$V^{ab}_{l\sigma}(q) = \Gamma^b_{cc}\chi^{ba}_{cc}(q) + \Gamma^b_{zz}\chi^{ba}_{zz}(q) - \sigma\frac{1}{2}\big(\Gamma^b_{zz}\chi^{ba}_{zc}(q) + \Gamma^b_{ch}\chi^{ba}_{cz}(q) + \chi^{ba}_{zc}(q)\Gamma^a_{ch} + \chi^{ba}_{cz}(q)\Gamma^a_{zz}\big), \tag{4.184}$$

$$V^{ab}_{t\sigma}(q) = \Gamma^b_{xx}\chi^{ba}_{xx}(q) + \Gamma^b_{yy}\chi^{ba}_{yy}(q). \tag{4.185}$$

The Dyson equation stays unchanged. The $\mathrm{Tr}(G\Sigma)$ check also stays unchanged i.e.

$$\frac{1}{2}\frac{T}{N}\sum_{i\omega_n \boldsymbol{k}} \mathrm{Tr}\left(\Sigma^{(2)}(i\omega_n,\boldsymbol{k})G^{(1)}(i\omega_n,\boldsymbol{k})e^{-i\omega_n 0^-}\right) = U\sum_a \langle n_{a\uparrow}n_{a\downarrow}\rangle\,, \tag{4.186}$$

where the trace runs over orbital and spin indices. The algorithm essentially stays the same as for general SOC. The only difference is though that the vertices in the longitudinal and in the transversal channel can be found consecutively. Also note that since $\Gamma_{xx} = \Gamma_{yy}$ one only needs to solve one one-diminsional root-finding problem for Γ_{xx}.

4.12.2 Graphical representation for the Bethe-Salpeter-equation

The BSE equation in the longitudinal channel can be written as

$$\begin{pmatrix}\chi_{cc} & \chi_{cz}\\ \chi_{zc} & \chi_{zz}\end{pmatrix} = \begin{pmatrix}\chi^{(1)}_{cc} & \chi^{(1)}_{cz}\\ \chi^{(1)}_{zc} & \chi^{(1)}_{zz}\end{pmatrix} - \frac{1}{2}\begin{pmatrix}\chi^{(1)}_{cc} & \chi^{(1)}_{cz}\\ \chi^{(1)}_{zc} & \chi^{(1)}_{zz}\end{pmatrix}\begin{pmatrix}\Gamma_{cc} & 0\\ 0 & -\Gamma_{zz}\end{pmatrix}\begin{pmatrix}\chi_{cc} & \chi_{cz}\\ \chi_{zc} & \chi_{zz}\end{pmatrix}. \tag{4.187}$$

These four equations can be represented graphically in the following way

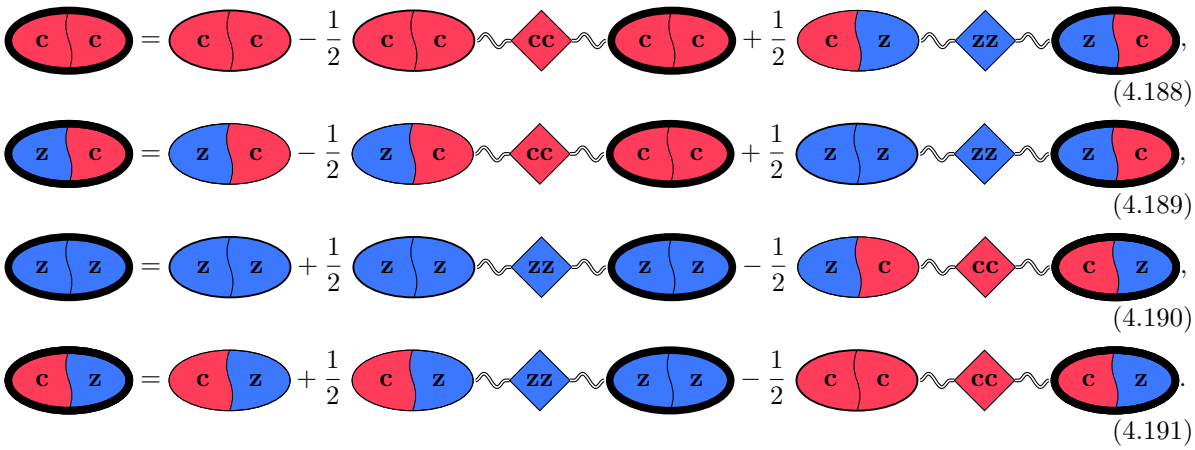

(4.188)

(4.189)

(4.190)

(4.191)

The susceptibilities are depicted as bubbles with label corresponding to the operators. Susceptibilities with a thick boundary correspond to the full interacting susceptibility $\chi_{\alpha\beta}$. Susceptibilities with a thin boundary correspond to the effective noninteracting ones $\chi^{(1)}_{\alpha\beta}$. The TPSC vertices are depicted as squares with double wiggled lines attached to them. The point of these diagrams is that spins always interact via the spin vertex and charges via the charge vertex. The new thing with SOC is that a coupling of S^z to S^z is now also possible via the charge vertex, because χ_{cz} and χ_{zc} are nonzero now. Without SOC the this mechanism is not possible anymore. One has to keep in mind though that each quantity is a matrix whose individual elements correspond to individual spins and charges that couple to each other. Also one has to keep in mind that each susceptibility carries a frequency and a momentum. One can plug this coupled equations into each other and iterate them. The factors of $\frac{1}{2}$ ensure convergence (for small enough product of vertex elements and maximum values of the susceptibilities) like in a geometric series. For example up to second order one gets the following diagrams for the S^z spin susceptibility

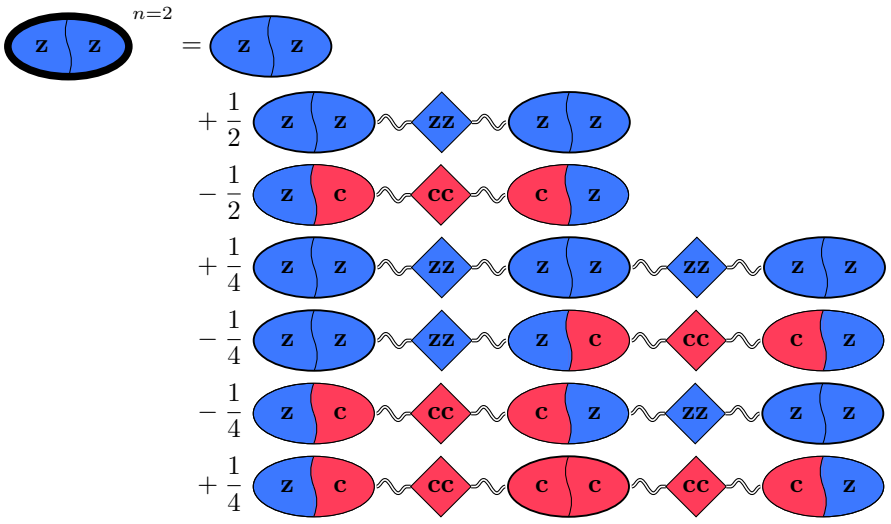

In the transversal channel we recover the ordinary expressions for χ_{xx} and χ_{yy}, where the coupling of the spin x-components is mediated by the vertex element Γ_{xx} and analogous for the y-components. This is similar to the original TPSC. Analogous consideration, apply to the general case SOC. There, longitudinal and transversal channel are coupled and all possible couplings involving susceptibilities with S_x, S_y, S_z and n are allowed, following the same logic outlined above.

4.12.3 Graphical representation for the self-energy

Contribution to the self-energy can graphically be represented as

$$\Sigma(1-2) = \qquad (4.192)$$

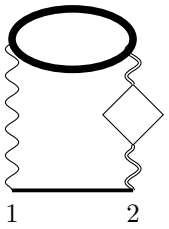

The wiggled line represents the bare Hubbard interaction, the straight line the first level Green's function $G^{(1)}$, the ellipse one of the susceptibilities and the wiggled line with a square represents a renormalized vertex (spin or charge). As can be seen from Eq. 4.183, 4.184 and 4.185, at one side of the interacting susceptibility there is always a renormalized TPSC vertex attached, namely the one corresponding to the operator at that side of the susceptibility.

4.13 Implementation of TPSC with SOC

We implemented TPSC with SOC in a Python code for the Kane-Mele-Hubbard model (KMH). The code is based on a TPSC code for the Hubbard model on a square lattice [161, 186], that in parts is based on the TPSC sparse-ir tutorial [187]. The implemented algorithm follows the one explained in Sec. 4.10. Since the KMH model possesses conservation of S^z the implemented equations simplify to those given in Sec. 4.12. The code assumes particle-hole symmetry for $n > 1$ (more than half filling). The code also assumes symmetry related orbitals so that the first level self-energy $\Sigma^{(1)}$ is a constant that can be absorbed in the chemical potential. We use the sparse-ir library [187–189] to represent Green's functions and susceptibilities in an efficient manner. The sparse-ir library also allows for efficient Fourier transforms between imaginary times and Matsubara frequencies, as well as an efficient calculation of the sum rules 4.180 and 4.181. Convolutions can be efficiently evaluated using

(a) (b)

Figure 4.2: (a) The Kane-Mele-Hubbard model with next neighbor hopping t, spin-orbit coupling λ and onsite Hubbard interaction U. The basis vectors are $\boldsymbol{a}_1 = (1, 0)a$ and $\boldsymbol{a}_2 = (1/2, \sqrt{3}/2)a$ with lattice constant a. (b) The hexagonal Brillouin zone of the model.

fast Fourier transforms, see appendix D. Green's functions, susceptibilities, self-energies are implemented as numpy arrays. The antiperiodicity of the Green's function in imaginary time is used so that only positive imaginary times need to be stored. The antiperiodicity of the Green's function is also used to simplify the calculation of the noninteracting susceptibility. The matrix notation in Eq. 4.177 allows for an efficient implementation. Since in the Kane-Mele-Hubbard model the spin fluctuations are stronger for the S^x and S^y spin components the ansatz equation is used in the transversal channel i.e. the spin x-direction. Eq. 4.177, 4.180 and 4.181 presents a multi-dimensional root-finding problem for Γ_{cc} and Γ_{zz}, that is solved using the scipy optimize root hybr function that uses MINPACK's hybrd and hybrj routines (modified Powell method). A good starting guess can be obtained by first neglecting the spin-charge coupling χ_{cz} and χ_{zc} and solving the resulting one dimensional root-finding problems. For the one-dimensional root-finding problems for the spin vertices it is possible to give a search interval to avoid numerical instabilities associated with the pole in the expression for the spin susceptibility e.g. in Eq. 4.173 (see appendix E).

The code would be easily generalizeabe to the case without particle-hole symmetry. Generalizing to the case of general SOC requires the implementation of the algorithm in Sec. 4.10. Generalization to the case where the sites are not symmetry related anymore i.e. $\langle n_a \rangle \neq \langle n_b \rangle$ requires more changes to the code and the input of the densities $\langle n_a \rangle$ from a different method (see Ref. [6]). The Bloch Hamiltonian can be adapted in the respective file.

4.14 Numerical results for the Kane-Mele Hubbard model

In the following we first introduce the Kane-Mele-Hubbard model, which will then serve as a test bed to demonstrate the TPSC method with SOC included. Our focus is to study the interplay of Hubbard interaction and spin-orbit coupling. We consider the weak to intermediate coupling regime, i.e. U values that are reasonable within TPSC. Further we only consider relatively small values of spin-orbit coupling, because usually it is a small effect. We only consider the half filled case. We put a special focus on low temperatures i.e. smaller than the band gap, where thermal excitation effects play a smaller role. We present numerical results for the double occupancy, renormalized TPSC spin and charge vertices, spin susceptibility, charge susceptibility mixed spin charge susceptibility, Green's function and self-energy. All calculations in this chapter are performed on a 120×120 k-point grid and at half filling. These calculations can be performed on a laptop.

4.14.1 The Kane-Mele-Hubbard model

In this section we describe the Kane-Mele-Hubbard model. Further results for the model can also be found in Chap. 5. The Kane-Mele model was originally proposed by Kane and Mele [48, 49] for a single layer of graphene, where the intrinsic spin-orbit coupling (SOC) opens a band gap and causes a

band inversion making the bands topological. The model host a so called quantum spin Hall (QSH) phase. The spin Hall effect is a physical phenomenon in which electrons move perpendicular to the direction of an applied electrical field, but in opposite directions depending on the spin orientation. In the QSH phase the corresponding spin Hall conductivity SHC is quantized, because it can be written as a Brillouin zone integral over the Berry curvature of the occupied bands. However, in graphene the size of the intrinsic SOC was found to be of the order of a few microelectronvolt, so that the QSH would only be observable at unrealistically low temperatures [127, 190–192]. Note, that the Kane-Mele model introduced in Ref. [48] can be thought of two time reversed copies of the Haldane model on top of each other [193].

Later on onsite Hubbard interactions where added to study the effect of interactions yielding the Kane-Mele-Hubbard model. So far, the KMH model has been investigated in Refs. [194–207] and reviewed in Refs. [208–210]. The Kane-Mele-Hubbard model is defined by the following Hamiltonian

$$H = -t \sum_{\langle i,j \rangle} c_i^\dagger c_j + i\lambda \sum_{\langle\langle i,j \rangle\rangle} \nu_{ij} c_i^\dagger \sigma_z c_j + U \sum_i n_{i\uparrow} n_{i\downarrow}. \tag{4.193}$$

The indices i and j run over all lattice sites of which there are two in the unit cell, $c_i^\dagger$ (c_i) is a row (column) vector of creation (annihilation) operators i.e. $(c_{i\uparrow}^\dagger, c_{i\downarrow}^\dagger)$ and $\nu_{ij} = \pm 1$ depending on if going from i to j is clockwise or counterclockwise. In the model t is a nearest neighbor hopping, U the strength of the Hubbard interaction and λ the strength of the SOC coupling that is consistent with the symmetries of graphene [48, 49]. The SOC term breaks spin rotation symmetry, but time reversal symmetry and the conservation of the spin z-components S^z are preserved. The model and the reciprocal space are depicted in Fig. 4.2. We consider the model at half-filling.

We now describe our concrete choice of lattice parameters and orbital positions that are also necessary for the implementation. We take the lattice of our model to be

$$\boldsymbol{a}_1 = \begin{pmatrix} 1 \\ 0 \end{pmatrix} a, \quad \boldsymbol{a}_2 = \begin{pmatrix} \frac{1}{2} \\ \frac{\sqrt{3}}{2} \end{pmatrix} a. \tag{4.194}$$

The volume of the elementary cell is

$$V_{ez} = \frac{\sqrt{3}}{2} a^2. \tag{4.195}$$

For simplicity we set $a = 1$. The positions of the orbitals are at

$$\boldsymbol{r}_1 = 0 \cdot \boldsymbol{a}_1 + 0 \cdot \boldsymbol{a}_2 \tag{4.196}$$

$$\boldsymbol{r}_2 = \frac{1}{3} \cdot \boldsymbol{a}_1 + \frac{1}{3} \cdot \boldsymbol{a}_2 \tag{4.197}$$

The lattice vectors in the reciprocal space are

$$\boldsymbol{K}_1 = \frac{2\pi}{a} \begin{pmatrix} 1 \\ -\frac{1}{\sqrt{3}} \end{pmatrix}, \quad \boldsymbol{K}_2 = \frac{2\pi}{a} \begin{pmatrix} 0 \\ \frac{2}{\sqrt{3}}. \end{pmatrix} \tag{4.198}$$

I holds $\boldsymbol{K}_i \cdot \boldsymbol{a}_j = 2\pi\delta_{ij}$. With this basis we can write every k-point $\boldsymbol{k}$ in reduced units as

$$\boldsymbol{k} = k_1 \boldsymbol{K}_1 + k_2 \boldsymbol{K}_2, \tag{4.199}$$

where $k_1, k_2 \in [0, 1]$. Reduced units allow us to effectively map the model on a square lattice simplifying the implementation. The spin indices can be included in the orbital indices to simplify the implementation. Here and in the following we use the convention that each 2×2 block describes the spin indices. In the periodic gauge (the orbital positions are not included in the Fourier transform) the Hamiltonian is given by

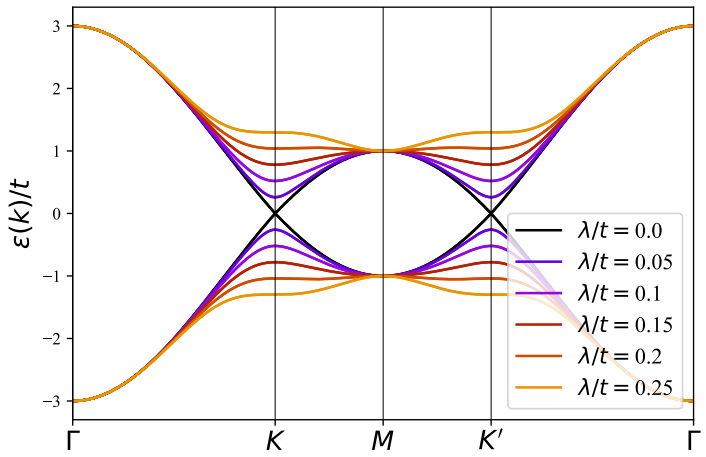

Figure 4.3: Band structure of the Kane-Mele model for different values of spin orbit coupling. At zero spin-orbit coupling the model possesses Dirac cones at $\boldsymbol{K}$ and $\boldsymbol{K}'$. Turning on spin-orbit coupling the Dirac cones are gaped out. Spin up and spin down bands are degenerate due to time reversal symmetry.

$$\mathcal{H}(\boldsymbol{k}) = \begin{pmatrix} \mathcal{H}^{11}_{\uparrow\uparrow}(\boldsymbol{k}) & \mathcal{H}^{11}_{\uparrow\downarrow}(\boldsymbol{k}) & \mathcal{H}^{12}_{\uparrow\uparrow}(\boldsymbol{k}) & \mathcal{H}^{12}_{\uparrow\downarrow}(\boldsymbol{k}) \\ \mathcal{H}^{11}_{\downarrow\uparrow}(\boldsymbol{k}) & \mathcal{H}^{11}_{\downarrow\downarrow}(\boldsymbol{k}) & \mathcal{H}^{12}_{\downarrow\uparrow}(\boldsymbol{k}) & \mathcal{H}^{12}_{\downarrow\downarrow}(\boldsymbol{k}) \\ \mathcal{H}^{21}_{\uparrow\uparrow}(\boldsymbol{k}) & \mathcal{H}^{21}_{\uparrow\downarrow}(\boldsymbol{k}) & \mathcal{H}^{22}_{\uparrow\uparrow}(\boldsymbol{k}) & \mathcal{H}^{22}_{\uparrow\downarrow}(\boldsymbol{k}) \\ \mathcal{H}^{21}_{\downarrow\uparrow}(\boldsymbol{k}) & \mathcal{H}^{21}_{\downarrow\downarrow}(\boldsymbol{k}) & \mathcal{H}^{22}_{\downarrow\uparrow}(\boldsymbol{k}) & \mathcal{H}^{22}_{\downarrow\downarrow}(\boldsymbol{k}) \end{pmatrix} = \begin{pmatrix} \gamma(\boldsymbol{k}) & 0 & h(\boldsymbol{k}) & 0 \\ 0 & -\gamma(\boldsymbol{k}) & 0 & h(\boldsymbol{k}) \\ h^*(\boldsymbol{k}) & 0 & -\gamma(\boldsymbol{k}) & 0 \\ 0 & h^*(\boldsymbol{k}) & 0 & \gamma(\boldsymbol{k}) \end{pmatrix} \tag{4.200}$$

with

$$h(\boldsymbol{k}) = -t\left(1 + \exp(i\boldsymbol{k}\cdot\boldsymbol{a}_1) + \exp(i\boldsymbol{k}\cdot\boldsymbol{a}_2)\right), \tag{4.201}$$
$$\gamma(\boldsymbol{k}) = 2\lambda\left(\sin(\boldsymbol{k}\cdot\boldsymbol{a}_1) - \sin(\boldsymbol{k}\cdot\boldsymbol{a}_2) + \sin(\boldsymbol{k}\cdot(-\boldsymbol{a}_1+\boldsymbol{a}_2))\right) \tag{4.202}$$

or in reduced units (using Eq. 4.199)

$$h(\boldsymbol{k}) = -t\left(1 + \exp(2\pi i k_1) + \exp(2\pi i k_2)\right), \tag{4.203}$$
$$\gamma(\boldsymbol{k}) = 2\lambda\left(\sin(2\pi k_1) - \sin(2\pi k_2) + \sin(2\pi(-k_1+k_2))\right). \tag{4.204}$$

For small SOC the band gap is the smallest at the k-points $\boldsymbol{K} = (2/3, 1/3)$ and $\boldsymbol{K}' = (1/3, 2/3)$ in reduced units, the location of the Dirac points in the absence of SOC. Note that the orbitals in the unitcell are related to each other by inversion symmetry. Hence, their the expectation values for the orbital resolved fillings are identical i.e. $\langle n_1\rangle = \langle n_2\rangle = \frac{\langle n\rangle}{2}$ where $\langle n\rangle$ is the total filling. This will later allow us to simplify the TPSC self-consistency equations. Most impotently the TPSC two-particle irreducible vertex will be identical for both orbitals and the orbital resolved fillings in the sum rules are simply given by $\frac{\langle n\rangle}{2}$.

A plot of the band structure for different values of SOC can be seen in Fig. 4.3. In the noninteracting case the SOC gaps out the Dirac cones at $\boldsymbol{K}$ and $\boldsymbol{K}'$. The band gap at $\boldsymbol{K}$ and $\boldsymbol{K}'$ is $\Delta = 6\sqrt{3}\lambda$. Spin up and spin down bands are degenerate due to time reversal symmetry. In the gapped phase at zero temperature the spin Hall conductivity takes the quntized value of $\sigma_{\mathrm{SH}} = -2\frac{e^2}{h}$. The quantization is due to the Chern theorem which can be independently applied to spin-up and spin-down subspaces [48, 49]. At $T = 0$ the SOC-U-phase diagram consists of a QSH insulating phase at small U values and a XY antiferromagnet at larger U values. An intermediate spin liquid phase suggested in Refs. [194, 197, 198, 201] could not be found by large scale QMC simulations [11]. The X-Y antiferromagnet at high U values

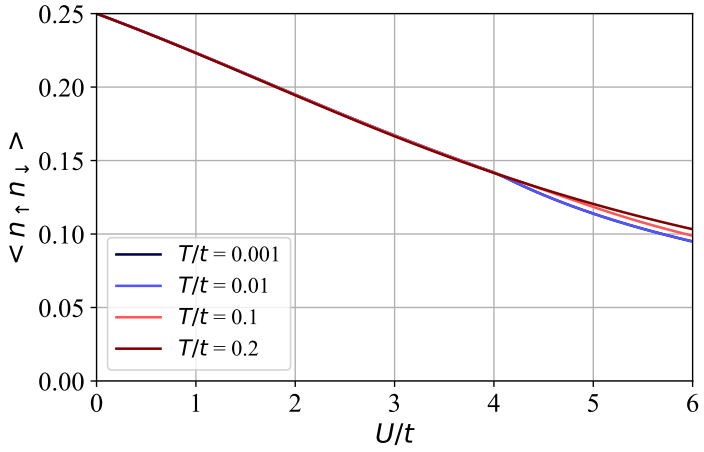

Figure 4.4: $\langle n_\uparrow n_\downarrow \rangle$ as a function of the SOC strength λ for different values of U for $T/t = 0.01$.

occurs because the SOC proportional to σ_z makes the x-y-plane the easy plane for the spins. This can be seen in the strong coupling limit where the Hamiltonian becomes [199]:

$$H_{U\to\infty} = \frac{4t^2}{U} \sum_{\langle i,j \rangle} \boldsymbol{S}_i \cdot \boldsymbol{S}_j + \frac{4\lambda^2}{U} \sum_{\langle\langle i,j \rangle\rangle} (S_i^z S_j^z - S_i^x S_j^x - S_i^y S_j^y) \tag{4.205}$$

Metallic edge states were found numerically to be gapped out by large enough interactions [211, 212] or spontaneously break time reversal symmetry and acquire magnetic order [202].

4.14.2 Double occupancy

Since both sites in the unit cell are related by inversion symmetry one has for the double occupancy $\langle n_{1\uparrow} n_{1\downarrow} \rangle = \langle n_{2\uparrow} n_{2\downarrow} \rangle$ which we define as $\langle n_\uparrow n_\downarrow \rangle$. Fig. 4.4 shows $\langle n_\uparrow n_\downarrow \rangle$ as a function of U for different temperatures and SOC of $\lambda/t = 0.01$. For $U = 0$ the double occupancy factors into the product of the noninteracting densities $\langle n_\uparrow n_\downarrow \rangle = \langle n_\uparrow \rangle \langle n_\downarrow \rangle = 0.25$. Increasing the interaction strength makes it energetically more costly for two electrons to occupy the same orbital so the double occupancy decreases. Note that after the transition to the XY antiferromagnet at $U/t \approx 4$ TPSC looses its validity, because it is a weak to intermediate coupling approach. The temperature dependence is very small. This behavior was already observed in on the honeycomb lattice without SOC [163].

In Fig. 4.5 shows $\langle n_\uparrow n_\downarrow \rangle$ as a function of the SOC strength λ for different values of U for $T/t = 0.01$. We see that for all values of $U \neq 0$ the double occupancy increases with increasing SOC. The reason is that SOC lowers the spin fluctuations in $\chi^{(1)}$ i.e. in the non-interacting case (see Sec. 4.14.5). Lower spin fluctuations lead to a less strongly renormalized spin vertex. Through the ansatz equation, that we choose to use in the transversal channel, the spin vertex in the transversal channel i.e. Γ^a_{xx} is proportional to the double occupancies, which are then increased.

4.14.3 Spin vertices

Fig. 4.6 shows the spin vertices Γ^a_{xx} (solid) and Γ^a_{zz} (dashed) as a function of U for different temperatures and SOC of $\lambda/t = 0.01$. Note that again, because of inversion symmetry, one has $\Gamma^1_{\alpha\alpha} = \Gamma^2_{\alpha\alpha}$, hence we neglect the orbital label.

Spin rotation symmetry around the spin z-axis leads to $\Gamma_{xx} = \Gamma_{yy}$. Γ_{xx} and Γ_{zz} increase with increasing U for all temperatures. The spin vertex in the longitudinal channel i.e. Γ_{zz} is always larger than Γ_{xx}, because the x-y plane is the easy plane for the spins (see also Sec.4.14.5). Consequently, the spin fluctuations in that plane are stronger leading to a stronger renormalization for Γ_{xx}. At low values of U, Γ_{xx} and Γ_{zz} are almost equal to U, showing that in the low U limit TPSC recovers RPA. With

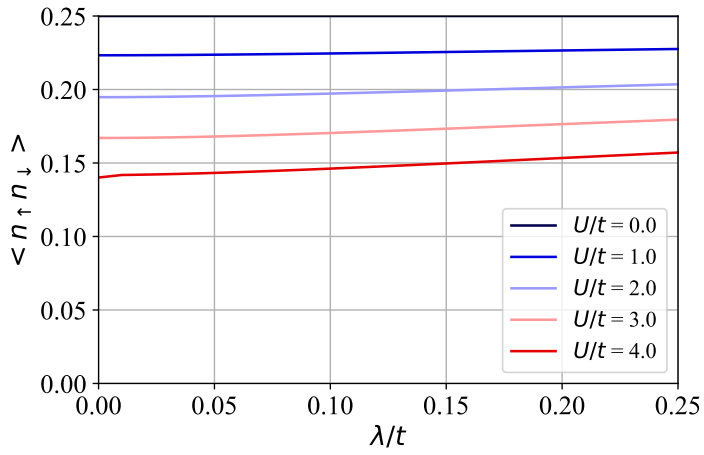

Figure 4.5: $\langle n_\uparrow n_\downarrow \rangle$ as a function of the SOC strength λ for different values of U for $T/t = 0.01$.

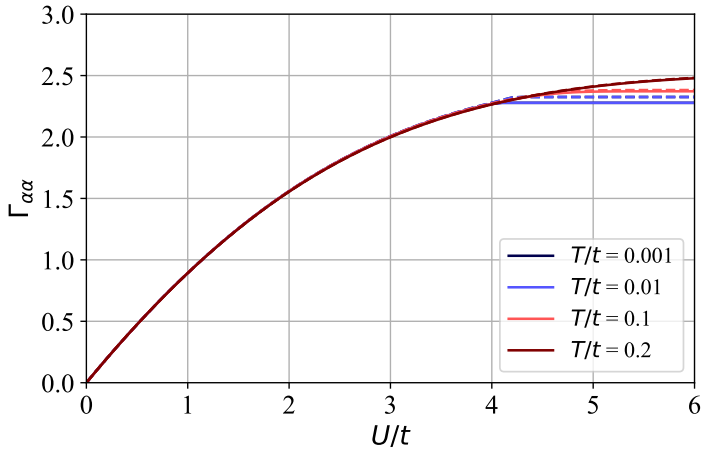

Figure 4.6: Spin vertices Γ_{xx} (solid) and Γ_{zz} (dashed) as a function of U for different temperatures and SOC of $\lambda/t = 0.01$.

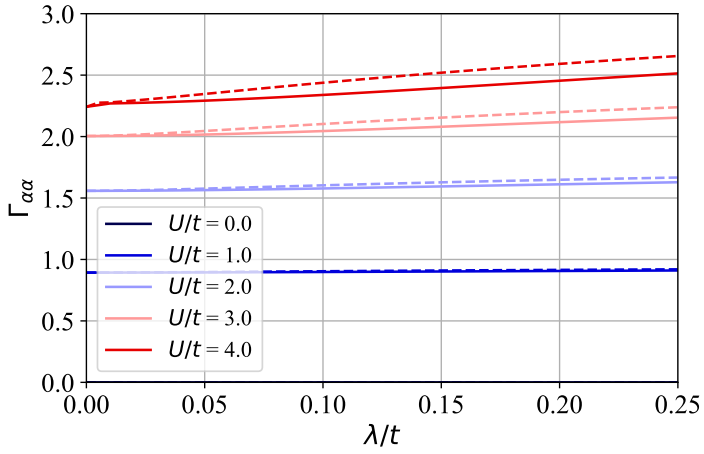

Figure 4.7: Spin vertices Γ_{xx} (solid) and Γ_{zz} (dashed) as a function of the SOC strength λ for different values of U for $T/t = 0.01$.

increasing U the vertices have the tendency to saturate. This reflects the physics of Kanamori-Brückner screening included in the ansatz equation [8, 28, 30]. When increasing U the two-body wave function becomes smaller when two electrons are on the same site. Thereby the effective interaction between electrons is reduced. The maximum energy this can cost is the bandwidth. Hence, the spin vertex saturates to a value of the order of the bandwidth. [30] Around $U/t = 4$ the transversal spin vertex Γ_{xx} converges to the critical value of $2/\chi_{xx}^{(1)n_{\max}}$, where $\chi_{xx}^{(1)n_{\max}}$ is the maximum eigenvalue of $\chi_{xx}^{(1)}(q)$. Increasing Γ_{xx} further would lead to a pole in the spin susceptibility χ_{xx} i.e. an instability to the XY antiferromagnet. The start of this plateau thus marks the transition to the XY antiferromagnet. TPSC is not valid anymore after reaching the plateau. This confirms that TPSC is a weak to intermediate coupling approach that cannot be used to investigate the strong coupling physics after the phase transition. We find the temperature dependence of the spin vertices to be very small, as already observed in on the honneycomb lattice without SOC [163].

In Fig. 4.7 shows the spin vertices Γ_{xx} (solid) and Γ_{zz} (dashed) as a function of the SOC strength λ for different values of U for $T/t = 0.01$. We see that both Γ_{xx} and Γ_{zz} increase slightly as a function of SOC strength. The reason is that SOC lowers the spin fluctuations in $\chi^{(1)}$ (see Sec. 4.14.5). Lower spin fluctuations lead to a less strongly renormalized spin vertex. Again we see that the longitudinal spin vertex Γ_{zz} is always larger then the transversal one Γ_{xx}. The difference is larger at higher U where spin fluctuations are larger.

4.14.4 Charge vertex

Fig. 4.8 shows the charge vertices Γ_{cc} as a function of U for different temperatures and SOC of $\lambda/t = 0.01$. Again we neglect the orbital label, because the orbitals are related by inversion symmetry. At low values of U the charge vertex Γ_{cc} is almost equal to U, showing that in the low U limit TPSC recovers RPA. At high values of U the charge vertex Γ_{cc} increases rapidly. The charge vertex thus suppresses the charge fluctuations compared to their non-interacting values and charge correlation legths become small and ill defined [163]. Note that after the transition to the XY antiferromagnet at $U/t \approx 4$ TPSC looses its validity. Below $U/t = 4$ the charge vertex is almost temperature independent.

In Fig.4.9 shows the charge vertices Γ_{cc} as a function of the SOC strength λ for different values of U for $T/t = 0.01$. We see that Γ_{cc} with the strength of SOC. This behavior is similar to the one observed for the spin vertex in the sense that increasing SOC lowers the fluctuations in the system thus making it less strongly renormalized. Since the renormalization for the charge vertex leads to a higher value, increasing SOC leads to a smaller charge vertex.

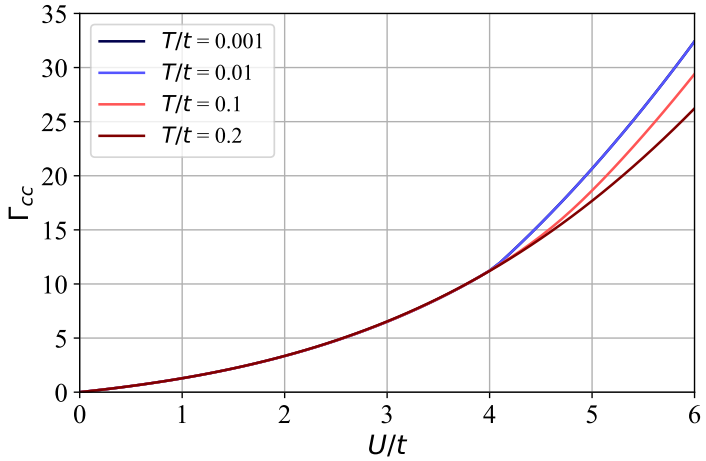

Figure 4.8: Charge vertices Γ_{cc} as a function of U for different temperatures and SOC of $\lambda/t = 0.01$.

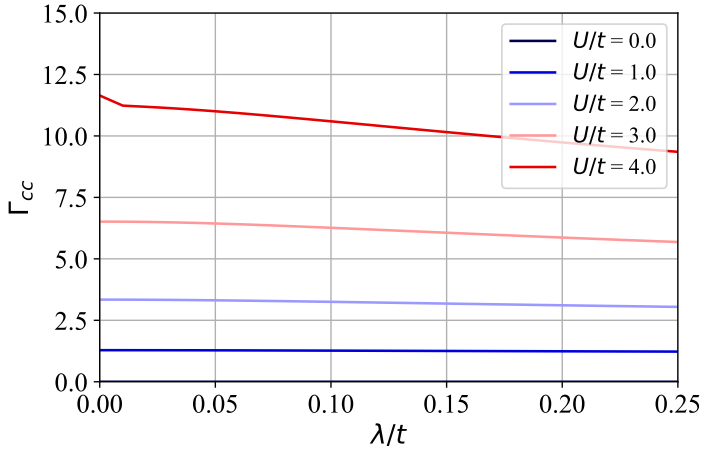

Figure 4.9: Charge vertices Γ_{cc} as a function of the SOC strength λ for different values of U for $T/t = 0.01$.

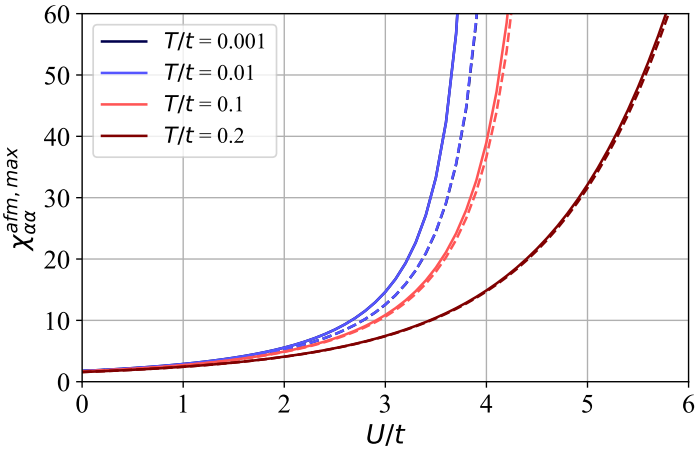

Figure 4.10: Maximum of the antiferromagnetic spin susceptibilities for spins aligned in the x direction and spins aligned in the z-direction i.e. χ_{xx} (solid) and χ_{zz} (dashed) as a function of U for different temperatures and SOC of $\lambda/t = 0.01$.

4.14.5 Maxima of antiferromagnetic and ferromagnetic spin susceptibilities

We define the antiferromagnetic and the ferromagnetic spin susceptibility for spins aligned in direction α as

$$\chi^{\mathrm{afm}}_{\alpha\alpha}(q) = \chi^{11}_{\alpha\alpha}(q) - \chi^{12}_{\alpha\alpha}(q) - \chi^{21}_{\alpha\alpha}(q) + \chi^{22}_{\alpha\alpha}(q), \tag{4.206}$$

$$\chi^{\mathrm{fm}}_{\alpha\alpha}(q) = \chi^{11}_{\alpha\alpha}(q) + \chi^{12}_{\alpha\alpha}(q) + \chi^{21}_{\alpha\alpha}(q) + \chi^{22}_{\alpha\alpha}(q), \tag{4.207}$$

where $\alpha = x, y, z$. Note that $\chi_{xx} = \chi_{yy}$ in the Kane-Mele-Hubbard model due to rotation symmetry around the spin z-axis. Fig. 4.10 shows the maximum of the antiferromagnetic spin susceptibilities for spins aligned in the x direction and spins aligned in the z-direction i.e. χ_{xx} (solid) and χ_{zz} (dashed) as a function of U for different temperatures and SOC of $\lambda/t = 0.01$. The maxima are located it $iq_m = 0$ and $\boldsymbol{q} = (0, 0)$. Note that contrary to the single-band Hubbard model the maximum at $\boldsymbol{q} = (0, 0)$ still corresponds to antiferromagnetic spin fluctuations, because there are two orbitals in the unit cell. With increasing U the maxima of the spin susceptibilities increase and diverge. For lower temperatures the divergence is at lower value of U. The curves for the maximum of χ_{xx} always lie above the curves for χ_{zz}, although the difference gets smaller for higher temperatures. At low temperatures the maximum of the spin susceptibility is independent of temperature. The reason is that at temperatures that are small compared to the gap $\Delta = 6\sqrt{3}\lambda$ thermal excitation effects play a vanishing role. Note that the two curves with the lowest temperatures overlap. We conclude that the divergence of the maximum of χ_{xx} marks the transition to the XY antiferromagnetic phase.

Fig. 4.11 shows the maximum of the antiferromagnetic spin susceptibilities for spins aligned in the x direction and spins aligned in the z-direction i.e. χ_{xx} (solid) and χ_{zz} (dashed) as a function of SOC for different values of U and $T/t = 0.01$. Increasing SOC leads to a decrease of the maxima of χ_{xx} and χ_{zz} for all values of U. At finite U this property is inherited from $\chi^{(1)}$ i.e. in the non-interacting case. Except at vanishing SOC the curves for χ_{xx} lie above the curves for χ_{zz}. Increasing SOC decreases the strength of spin fluctuations. This indicates that at higher values of SOC the critical U value for the transition to the XY antiferromagnet increases.

Fig. 4.12 shows the maximum of the ferromagnetic spin susceptibilities for spins aligned in the x direction and spins aligned in the z-direction i.e. χ_{xx} (solid) and χ_{zz} (dashed) as a function of U for different temperatures and SOC of $\lambda/t = 0.01$. With increasing U ferromagnetic spin fluctuations increase. For low temperatures they reach a plateau. Note that the curves for the two lowest temperatures lie on top of each other. Transversal ferromagnetic spin fluctuations are smaller then the longitudinal

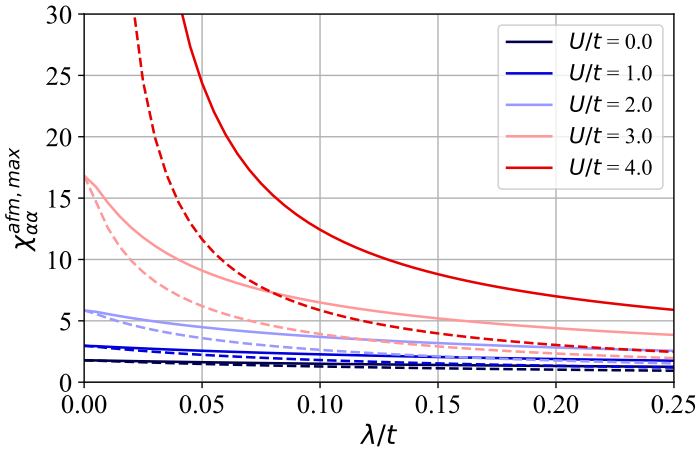

Figure 4.11: Maximum of the antiferromagnetic spin susceptibilities for spins aligned in the x direction and spins aligned in the z-direction i.e. χ_{xx} (solid) and χ_{zz} (dashed) as a function of SOC for different values of U and $T/t = 0.01$.

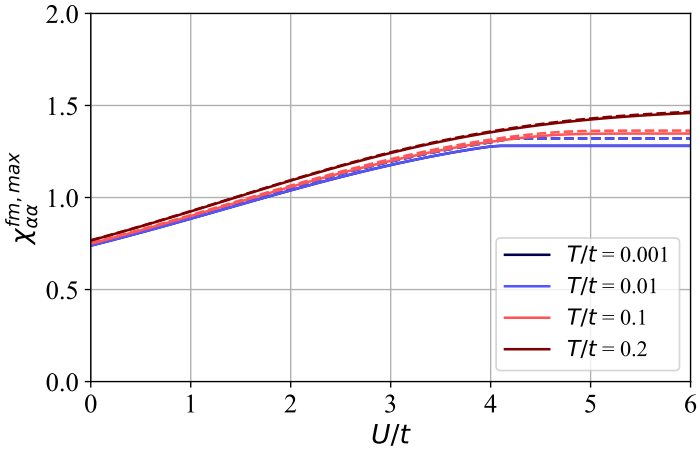

Figure 4.12: Maximum of the ferromagnetic spin susceptibilities for spins aligned in the x direction and spins aligned in the z-direction i.e. χ_{xx} (solid) and χ_{zz} (dashed) as a function of U for different temperatures and SOC of $\lambda/t = 0.01$.

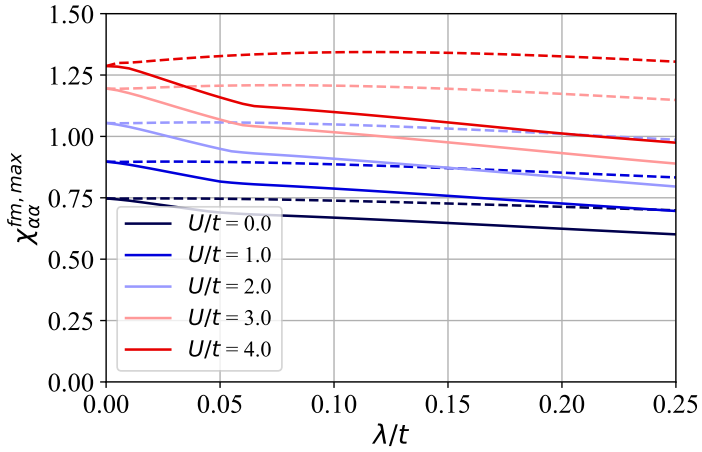

Figure 4.13: Maximum of the antiferromagnetic spin susceptibilities for spins aligned in the x direction and spins aligned in the z-direction i.e. χ_{xx} (solid) and χ_{zz} (dashed) as a function of U for different temperatures and SOC of $\lambda/t = 0.01$.

ferromagnetic ones at low temperature. The ferromagnetic spin fluctuations are generally much smaller then the antiferromagnetic ones, so antiferromagnetic spin fluctuations dominate.

Fig. 4.13 shows the maximum of the ferromagnetic spin susceptibilities for spins aligned in the x direction and spins aligned in the z-direction i.e. χ_{xx} (solid) and χ_{zz} (dashed) as a function of U for different temperatures and SOC of $\lambda/t = 0.01$. With increasing SOC the transversal ferromagnetic fluctuations decrease while for the longitudinal ones there is no clear trend. The longitudinal curves lie lie above the transversal curves for non-vanishing SOC.

We conclude this section with that the maximum for ferromagnetic spin fluctuation is very small compared to the antiferromagentic ones. So antiferromagnetic spin fluctuations dominate in the model. Comparing the maxima of χ_{xx} and χ_{zz}, we see that the spin fluctuation are stronger in the x-y plane. This is consistent with the Hamiltonian in the strong coupling limit Eq. 4.205 whose ground state is a XY antiferromagnet.

We conclude that antiferromagnetic spin fluctuations dominate over ferromagnetic ones. They increase with higher U and decrease with higher SOC. Transversal spin fluctuations are larger then longitudinal ones at finite SOC. The x-y plane is hence the easy plane for the spins and at zero temperature the system becomes an XY antiferromagnet at sufficiently high U.

4.14.6 Maxima of antiferromagnetic and ferromagnetic charge susceptibilities

Analogous the spin susceptibilities we define the antiferromagnetic and the ferromagnetic charge susceptibility as

$$\chi^{\mathrm{afm}}_{cc}(q) = \chi^{11}_{\alpha\alpha}(q) - \chi^{12}_{cc}(q) - \chi^{21}_{cc}(q) + \chi^{22}_{cc}(q), \tag{4.208}$$

$$\chi^{\mathrm{fm}}_{cc}(q) = \chi^{11}_{cc}(q) + \chi^{12}_{cc}(q) + \chi^{21}_{cc}(q) + \chi^{22}_{cc}(q). \tag{4.209}$$

Fig. 4.14 shows the maximum of the antiferromagnetic (solid) and ferromagnetic (dashed) charge susceptibilities as a function of U for different temperatures and SOC of $\lambda/t = 0.01$. The maxima for the antiferromagnetic charge fluctuations are located it $iq_m = 0$ and $\boldsymbol{q} = (0, 0)$ for the ferromagnetic ones they are located at $\boldsymbol{q} = (1/3, 2/3)$ and $\boldsymbol{q} = (2/3, 1/3)$ in reduced units. With increasing U the maxima decrease. So increasing U leads to a damping of charge fluctuations. The maxima only weakly depend on temperature. Antiferromagnetic spin fluctuations are larger then ferromagnetic ones although the

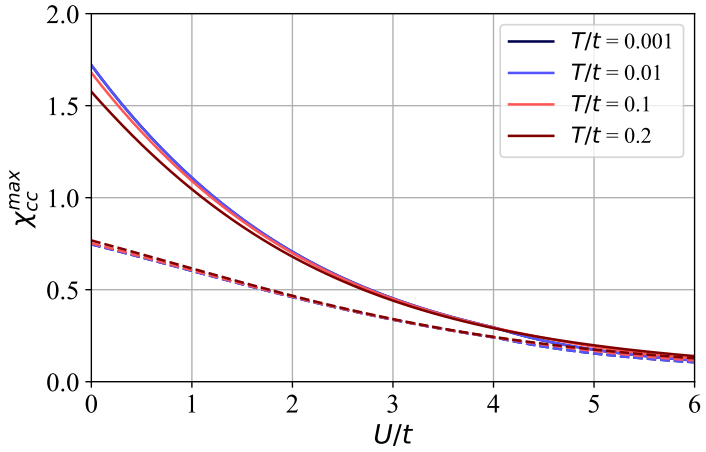

Figure 4.14: Maximum of the antiferromagnetic (solid) and ferromagnetic charge susceptibilities as a function of U for different temperatures and SOC of $\lambda/t = 0.01$.

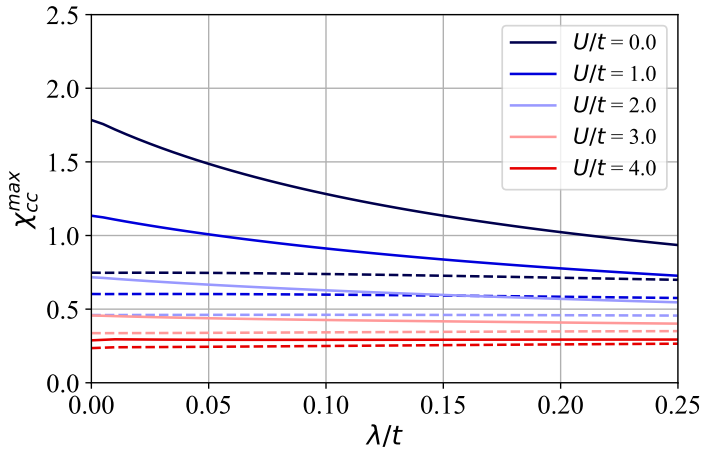

Figure 4.15: Maximum of the antiferromagnetic (solid) and ferromagnetic (dashed) charge susceptibilities as a function of the SOC strength λ for different values of U for $T/t = 0.01$.

difference almost vanishes for higher U values. Charge fluctuations are also much smaller then the antiferromagnetic spin fluctuations.

Fig. 4.15 shows the maximum of the antiferromagnetic (solid) and ferromagnetic (dashed) charge susceptibilities as a function of the SOC strength λ for different values of U for $T/t = 0.01$. At low U values increasing SOC leads to a decrease of the antiferromagnetic charge fluctuations. Similar to the spin fluctuations this behavior stems from $\chi^{(1)}$. At higher U values they stay almost constant. Ferromagnetic charge fluctuations are almost independent of SOC. We conclude this section with that charge fluctuations are small and are dominated by antiferromagnetic spin fluctuations.

4.14.7 Spin-charge susceptibility

The spin-charge susceptibilities describe the coupling of spin and charge. With spin rotation they must vanish. However SOC breaks spin rotation symmetry so they can be non-zero. In the Kane-Mele-Hubbard model the only non-vanishing spin-charge susceptibilities are χ_{cz} and χ_{zc}. All other mixed susceptibilities (including between different spin directions) vanish due to the conservation of spin in the z-direction. Because of TR symmetry (Eq. 4.68) it holds $\chi_{cz}^{ab}(iq_m, \boldsymbol{q}) = -\chi_{zc}^{ba}(iq_m, -\boldsymbol{q})$. Further, in

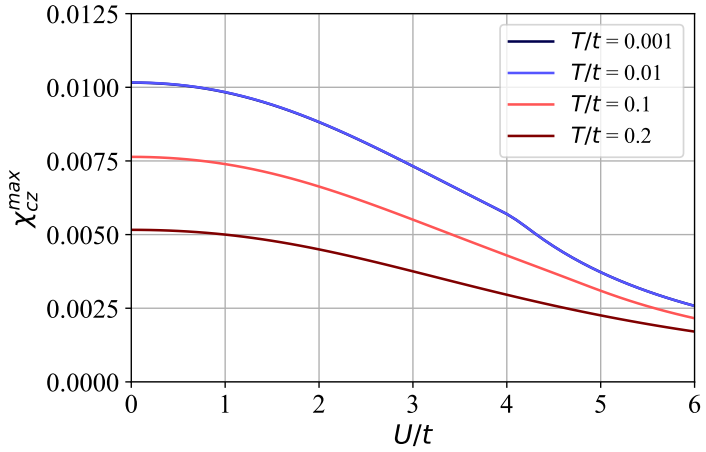

Figure 4.16: Maximal modulus of the eigenvalues of χ_{cz} (regarded as a matrix in orbital space) as a function of U for different temperatures and $\lambda/t = 0.01$.

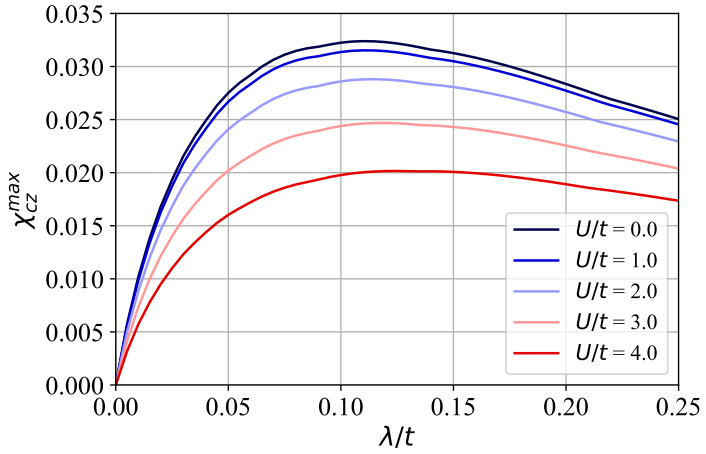

Figure 4.17: Maximal modulus of the eigenvalues of χ_{cz} as a function of the SOC strength λ for different values of U for $T/t = 0.01$.

TPSC we find $\chi_{cz}(0, \boldsymbol{q}) = 0$.

Fig. 4.16 shows the maximal modulus of the eigenvalues of χ_{zc} (regarded as a matrix in orbital space) as a function of U for different temperatures and SOC of $\lambda/t = 0.01$. The maxima of the eigenvalues of the spin charge susceptibility we find to be at $\boldsymbol{q} = (1/3, 2/3)$ and $\boldsymbol{q} = (2/3, 1/3)$ in reduced units. This is the location of the Dirac cones that are gaped out by the SOC. We see that the spin-charge susceptibility is much smaller as the spin susceptibilities and the charge susceptibility. With increasing U the maximum modulus of the χ_{cz} eigenvalue decreases. Lower temperatures lead to an increase until convergence at low enough temperatures. Note, that the curves with the two lowest temperatures lie on top of each other.

Fig. 4.15 shows the maximal modulus of the eigenvalues of χ_{cz} as a function of the SOC strength λ for different values of U for $T/t = 0.01$. Increasing the SOC the modulus of the maximum eigenvalue of χ_{cz} increases up to a maximum around $\lambda/t = 0.11$ after which it decreases again at all U values. At vanishing SOC χ_{cz} vanishes. The occurrence of a maximum is in so far surprising, that one could expect that mixed spin charge fluctuations would increase the larger the term is that explicitly breaks spin rotation symmetry. For all values of SOC higher U leads to a decrease of the maximal eigenvalue. However, we find mixed spin charge fluctuation to be much lower then spin or charge fluctuations in

the KMH model. However, it is not clear if this is a general property of every model with SOC.

4.14.8 Self-energy

Fig. 4.18 shows the dispersion of the TPSC self-energy in momentum space at the lowest Matsubara frequency $i\omega_0$ for $U/t = 4$, $T/t = 0.01$ and for $\lambda/t = 0.01$ as a typical self-energy plot. The Hartree part is not included, because it can be absorbed in the chemical potential. For these choices of parameters the system is close to the transition to the XY AFM, so antiferromagnetic spin fluctuations are strong. The top 2×2 plots show the real part of all orbital index combinations and the bottom 2×2 plots show the imaginary part. Only $\Sigma^{(2)}_{\uparrow}$ is shown, because of TR symmetry implies $\Sigma^{ab}_{\sigma}(i\omega_n, \boldsymbol{k}) = \Sigma^{ba}_{-\sigma}(i\omega_n, -\boldsymbol{k})$. The self-energy shows dispersion in momentum space, for diagonal and offdiagonal elements. Especially note the sharp features on the diagonals around $\boldsymbol{q} = (1/3, 2/3)$ and $\boldsymbol{q} = (2/3, 1/3)$ (reduced units).

Fig. 4.19 shows the imaginary part of the self-energy $\Sigma^{(2)11}_{\uparrow}(i\omega_n, \boldsymbol{k})$ as a function of $i\omega_n$ at high symmetry k-points for $T/t = 0.01$, $\lambda/t = 0.01$ and $U/t = 4$ in a) and $\lambda/t = 0.1$ and $U/t = 5.7$ in b). We find that the imaginary part of the offdiagonal elements of the self-energy vanishes at the high symmetry k-points. Both parameter choices are in the vicinity of the phase transition (compare Sec. 5.4.2). The self-energy at $\boldsymbol{k} = K$ is most negative. The effect is strongest at low frequencies. Also note the difference in the slope at low frequencies. This indicates, that correlation effects are strongest where the band gap is smallest. At higher frequencies the self-energies at different k-points converge to each other and show the same $\sim 1/\omega_n$ tail. Higher U values cause the modulus of the self-energy to increase.

In Fig. 4.20 the real part of the TPSC self-energy as a function of $i\omega_n$ at high symmetry k-points for $T/t = 0.01$, $\lambda/t = 0.01$ and $U/t = 4$, a) $\Sigma^{(2)11}_{\uparrow}(i\omega_n, \boldsymbol{k})$ without the Hartree part, b) $\Sigma^{(2)12}_{\uparrow}(i\omega_n, \boldsymbol{k})$. The diagonal parts of the real part are very small. Only the curve at $\boldsymbol{k} = K$ is nonzero. However the curve converges to zero for large Matsubara frequencies relatively quickly. The real parts of the offdiagonal self-energy are relatively large except at $\boldsymbol{k} = K$ where it vanishes. They also converge to zero for large frequencies. The imaginary parts of the offdiagonals at the high symmetry k-points are found to be zero. This also means, that at $\boldsymbol{k} = K$ the self-energy diagonal and purely imaginary.

Generally we find that dispersion and sharp features become stronger the closer the system is to the phase transition to the XY antiferromagnet. This is reasonable since in TPSC the largest contribution to the self-energy come from antiferromagnetic spin fluctuations.

4.14.9 Matsubara Green's function

Fig. 4.21 shows the imaginary part of the Green's function $G^{11}_{\uparrow}(i\omega_n, \boldsymbol{k})$ as a function of $i\omega_n$ at high symmetry k-points for $T/t = 0.01$, $\lambda/t = 0.01$ and $U/t = 4$ in a) and $\lambda/t = 0.1$ and $U/t = 5.7$ in b). For the Green's function time reversal symmetry implies $G^{ab}_{\sigma}(i\omega_n, \boldsymbol{k}) = G^{ba}_{-\sigma}(i\omega_n, -\boldsymbol{k})$. At low frequencies there is a large difference between the high-symmetry k-points. However, all curves converge to a $1/\omega_n$ behavior at high frequencies. For small SOC in a) the Green's function at $\boldsymbol{k} = K$ seems to diverge, but in fact the band gap is very small, so that the Green's function is large, but does not have a pole. The behavior becomes more clear in b) where SOC and hence also the gap is larger. The self-energy enters in the denominator of the self-energy. If the denominator is very small, as is the case for a small band gap, even small changes in the self-energy can have a large effect on the Green's function.

4.14.10 $\mathrm{Tr}(G\Sigma)$ consistency check

For the TPSC self-energy $\Sigma^{(2)}$ it must hold exactly (Eq. 4.156)

$$\begin{aligned}\frac{1}{2}Tr\left(\Sigma^{(2)}G^{(1)}\right) &= \frac{1}{2}\frac{T}{N}\sum_{kab\sigma}\Sigma^{(2)ab}_{\sigma}(k)G^{(1)ba}_{\sigma}(k)e^{-i\omega_n 0^-} \\ &= \sum_a U\left\langle n_{a\uparrow}n_{a\downarrow}\right\rangle, \end{aligned} \tag{4.210}$$

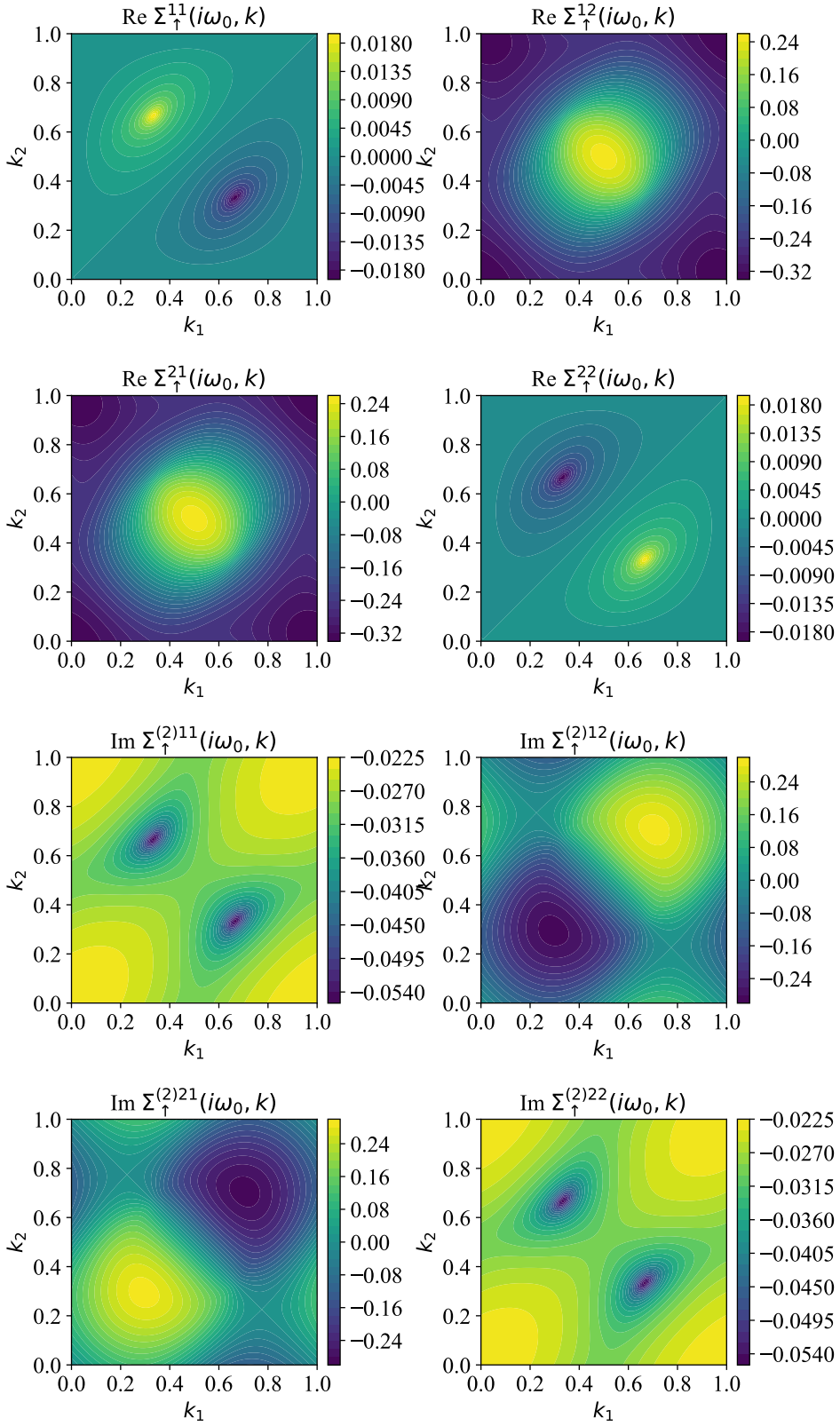

Figure 4.18: Dispersion of the TPSC self-energy $\Sigma_\uparrow^{(2)}(i\omega_0, \boldsymbol{k})$ in momentum space at the lowest Matsubara frequency for $U/t = 4$, $T/t = 0.01$ and for $\lambda/t = 0.01$. Real and imaginary part are shown. The Hartree part is not included.

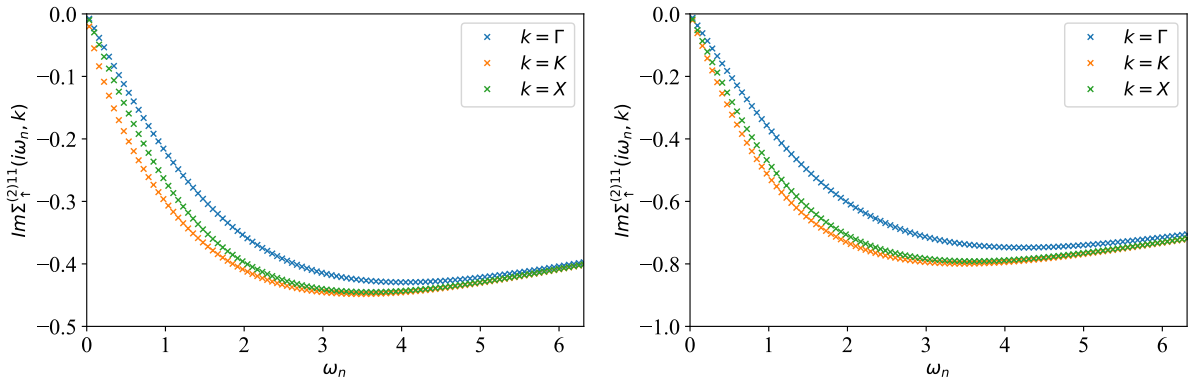

(a) (b)

Figure 4.19: Imaginary part of the TPSC self-energy $\Sigma^{(2)11}_{\uparrow}(i\omega_n, \boldsymbol{k})$ as a function of $i\omega_n$ at high symmetry k-points for $T/t = 0.01$. a) $\lambda/t = 0.01$ and $U/t = 4$, b) $\lambda/t = 0.1$ and $U/t = 5.7$.

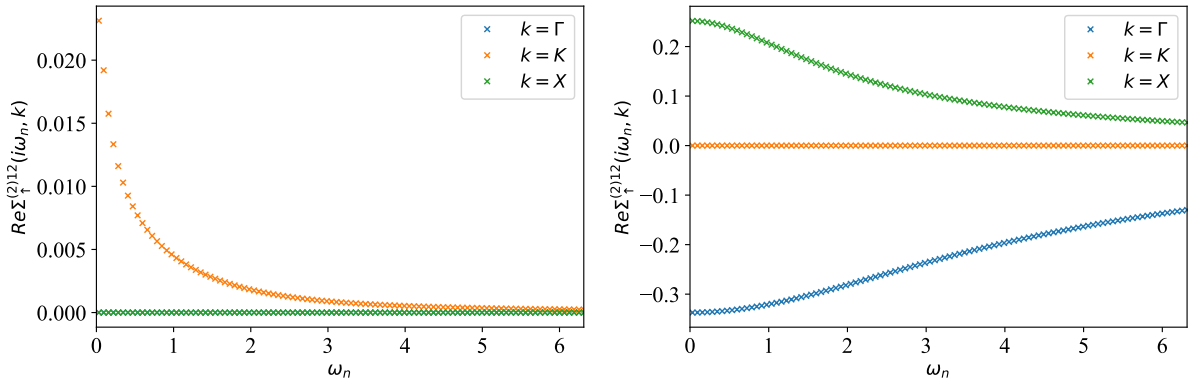

(a) (b)

Figure 4.20: Real part of the TPSC self-energy as a function of $i\omega_n$ at high symmetry k-points for $T/t = 0.01$, $\lambda/t = 0.01$ and $U/t = 4$, a) $\Sigma^{(2)11}_{\uparrow}(i\omega_n, \boldsymbol{k})$ without the Hartree part, b) $\Sigma^{(2)12}_{\uparrow}(i\omega_n, \boldsymbol{k})$.

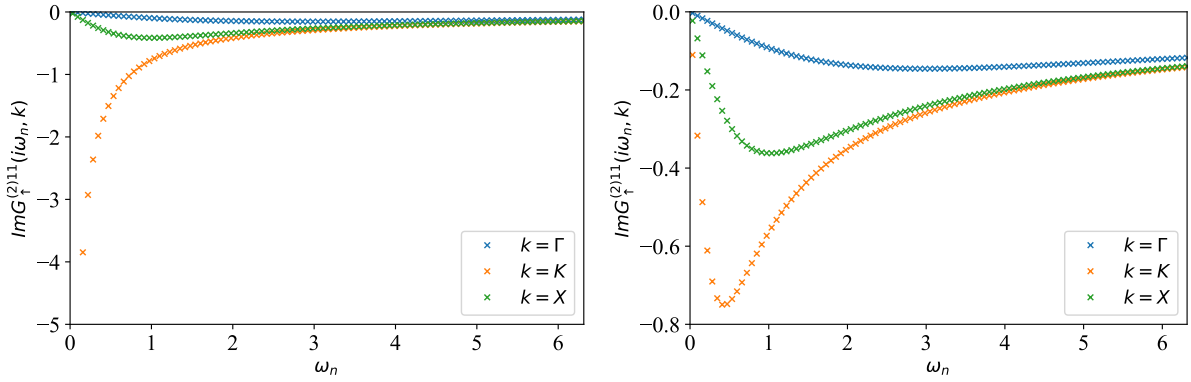

(a) (b)

Figure 4.21: Imaginary part of the Matsubara Green's function $G^{(2)11}_{\uparrow}(i\omega_n, \boldsymbol{k})$ as a function of $i\omega_n$ at high symmetry k-points for $T/t = 0.01$. a) $\lambda/t = 0.01$ and $U/t = 4$, b) $\lambda/t = 0.1$ and $U/t = 5.7$.

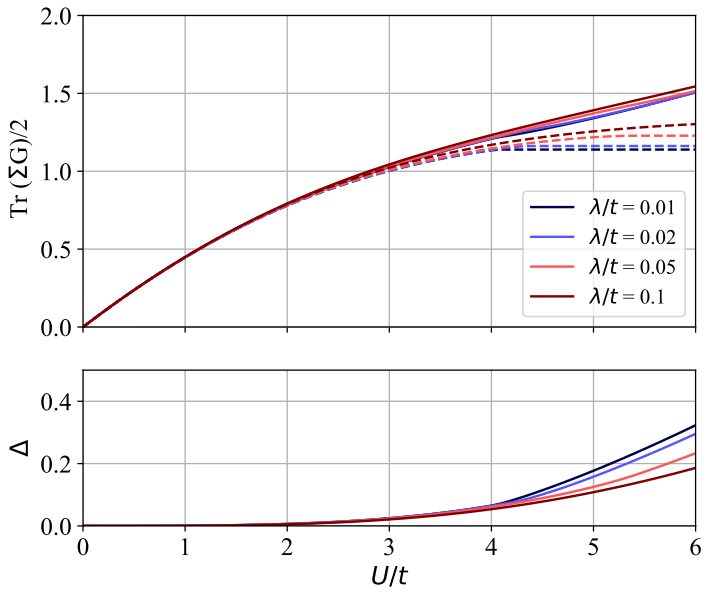

Figure 4.22: $\mathrm{Tr}\,(\Sigma G)$ consistency check as a function of U/t for different values of SOC and $T/t = 0.001$. Solid lines are the interacting Green's function $G = G^{(2)}$ and dashed lines the noninteracting one $G = G^{(1)}$. Upper panel: Absolute values of $\frac{1}{2}\mathrm{Tr}\,(\Sigma G)$. Lower panel: Relative error Δ (see Eq. 4.211). The deviation is modest up to the phase transition or $U/t \approx 5$ where TPSC starts losing its validity.

where here the trace runs over orbital and spin indices. Using $G^{(2)}$ instead of $G^{(1)}$ the relation can be used as a consistency test between one-particle and two-particle quantities. In Fig. 4.22 we show this test for different values of SOC. In the upper panel the absolute values and in the lower panel the relative derivation

$$\Delta = \frac{\mathrm{Tr}\left(\Sigma^{(2)}G^{(2)}\right) - \mathrm{Tr}\left(\Sigma^{(2)}G^{(1)}\right)}{\mathrm{Tr}\left(\Sigma^{(2)}G^{(1)}\right)} \tag{4.211}$$

can be seen. The error in general gets worse for higher values of U. For low SOC the deviation is relatively small up to the phase transition, then it starts to diverge rapidly. For larger values of SOC where the phase transition is at higher U values, the error can already be large at the point of the phase transition. This indicates that TPSC not valid anymore after the phase transition or high enough U values in general. The reason is that TPSC is a weak to intermediate coupling method that cannot describe strong coupling physics. The plateau in the dashed curves involving $G^{(1)}$ corresponds to the vertex Γ_{xx} converging to a value, where the spin susceptibility elsewise would have a pole if Γ_{xx} would become larger. This is another indication that TPSC is not valid anymore beyond the phase transition.

4.15 Summary

In this chapter we extended the TPSC approach to include SOC. Therefore, we derived new TPSC self-consistency equations including SOC. SOC breaks spin rotation symmetry which leads to a coupling of spin and charge sectors. However, SOC preserves time reversal symmetry. We introduced an efficient matrix notation for susceptibilities and vertices. Invoking time reversal symmetry we showed that a local and constant two-particle vertex in the particle-hole channel consists of three spin vertices and one charge vertex. The vertices can be determined with the help of spin and charge sum rules and an ansatz equation that relates the double occupancy to one of the vertices. The derived self-consistency equations constitute a multidimensional root-finding problem for the vertices that needs to be solved numerically. The self-energy is constructed from spin, charge and mixed spin-charge susceptibilities. Time reversal symmetry has to be explicitly restored in the self-energy, whenever the renormalized vertex is a matrix,

as is the case in the presence of SOC. If SOC is absent, we recover the orginal TPSC self-consistency equations from the self-consistency equations we derived.

As a test case we study the Kane-Mele-Hubbard model in which the SOC is proportional to the spin z-component. With TPSC we confirm that in the Kane-Mele-Hubbard model antiferromagnetic spin fluctuations dominate of ferromagnetic spin fluctuations and charge fluctuations. Mixed spin charge fluctuations are found to be very small compared to spin and charge fluctuations. Spin fluctuations in the x-y plane are stronger than in z direction and diverge first as Hubbard U is increased. This confirms that the Kane-Mele-Hubbard model is a XY antiferromagnet at zero temperature. The transversal spin vertices are more strongly renormalized then the longitudinal spin vertex. Higher SOC leads to a decrease of antiferromagnetic spin fluctuations, so that the phase transition is shifted to higher U values. The self-energy shows dispersion and sharp features in momentum space that become especially large close to the phase transition. The $\mathrm{Tr}(G\Sigma)$ check show that TPSC loses validity at the phase transition or if U gets to high.

Chapter 5

Spin Hall conductivity in the Kane-Mele Hubbard model at finite temperature

In this chapter we apply the TPSC method which we extended to include SOC in Chap. 4 to study the spin Hall conductivity in the Kane-Mele-Hubbard model at finite temperature. However, to make this chapter more self-contained we start by giving some background on the spin Hall effect and how to calculate conductivities in a tight binding mdoel.

In Sec. 5.1 we give a brief overview over the spin Hall effect and its history. In Sec. 5.2 we explain how to include a vector potential in a tight-binding model. We give an expression for the current and the current operator in a tight binding model and define the conductivity tensor and subsequently the Hall conductivity. In Sec. 5.3 we derive an expression for the spin Hall conductivity in terms of the Matsubara Green's function that is valid in the presence of interactions at finite temperature. We also show that this expression is topological invariant of the Matsubara Green's function. In Sec. 5.4 we present results obtained with TPSC for antiferromagnetic spin correlation lengths, spin Hall conductivity, phase diagram and band renormalization in the Kane-Mele-Hubbard model.

In this chapter we restore physical units. The results presented in this chapter are published in Ref. [2].

5.1 The spin Hall effect

The spin Hall effect is a physical phenomenon in which particles experience forces perpendicular to their flow direction, but of opposite directions depending on the spin orientation. The spin Hall effect was first proposed in 1971 [89]. Since its proposal, the spin Hall effect has been realized in a variety of systems, including the semiconductors GaAs and InGaAs where the phenomenon is driven by spin-orbit coupling [143, 144], in laser light traversing dielectric junctions [213] or in cold atom systems in optical lattices [214, 215]. A large spin Hall effect due to spin-orbit coupling has also been observed in AB-stacked $MoTe_2/WSe_2$ moiré bilayers (see Fig. 5.1) [216].

Likewise, the quantum spin Hall effect (QSH) is a spin selective version of the quantum Hall effect and describes a time reversal invariant electronic state with a bulk electronic band gap which hosts a quantized spin Hall conductivity. The state was originally proposed by Kane and Mele [48, 49] for a single layer of graphene, where the intrinsic spin-orbit coupling (SOC) opens a band gap and causes a band inversion making the bands topological [49]. The Kane-Mele model introduced in Ref. [48] can be thought of two time reversed copies of the Haldane model [193]. The Kane-Mele model introduced in Ref. [48] resembles graphene and consists of a honeycomb lattice with nearest neighbor hopping and SOC. The spin Hall conductivity in this case is quantized at zero temperature since it corresponds to a Brillouin zone integral over the Berry curvature of the occupied bands. However, in graphene the size

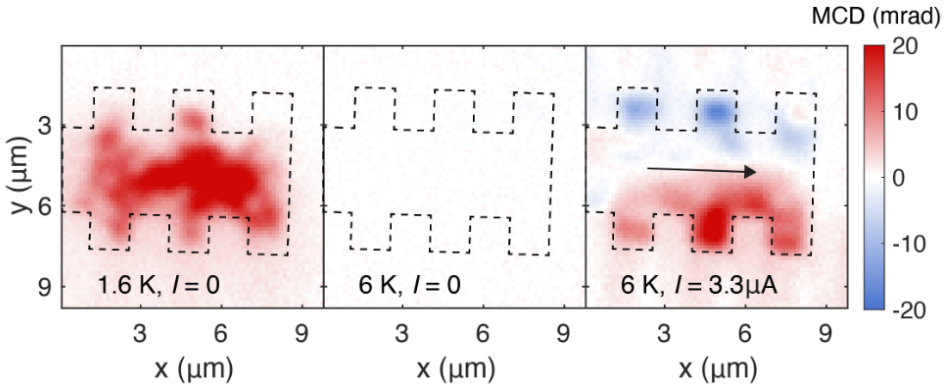

Figure 5.1: Accumulation of opposite sign spins at the edges of $MoTe_2/WSe_2$ due to a large spin Hall effect measured via magnetic circular dichroism (MCD) imaging for $1.6K$ with zero bias current (left panel), $6K$ with zero bias current (middle panel) and $6K$ with bias current equals $3.3\mu A$. Black dashed lines mark the sample boundaries and arrows show the bias current direction. The figure is reprinted from Ref. [216].

of the intrinsic SOC was found to be of the order of a few microelectronvolt, so that the QSH would only be observable at unrealistically low temperatures [127, 190–192]. An observable QSH was first successfully predicted and measured in HgTe quantum wells (see Fig. 5.2) [90, 91].

The observation in other systems followed [129, 217–227], notably, for example, in recent measurements in the graphene analog germanene [129]. Other possible avenues to observe this effect have been pursued by tuning the SOC through proximity effects to engineer topological phases [224].

5.2 Currents and conductivities

In this section we discuss currents and conductivities in the context of a tight binding model with a vector potential. First, we derive a general expression for the current and the current operator in the presence of a vector potential. Then we explain how a vector potential is included in a tight-binding model. We then give an expression for the current and the current operator in a tight-binding model with a vector potential. We work in imaginary time and frequency space, because this is simpler. Then we perform analytic continuation to real frequencies to obtain an expression for the conductivity tensor. In the end we are interested in the DC limit $\nu \to 0$. The Hall conductivity can be obtained as the antisymmetric part of the conductivity tensor. The whole discussion is semi-classical, i.e. we assume a vector potential with many photons, so that one photon more or less does not matter. This section follows Refs. [100, 228].

5.2.1 Current operator and coupling to the vector potential

We now derive a general expression for the current operator in the presence of a vector potential. We describe an uniform electric field by a position independent vector potential in imaginary time $\boldsymbol{A}(\tau)$. The electric field in imaginary time is obtained by

$$\boldsymbol{E}(\tau) = -\partial_\tau \boldsymbol{A}(\tau) \tag{5.1}$$

In real time one has $\boldsymbol{E}(t) = -\partial_t \boldsymbol{A}(t)$. Going to imaginary frequencies $i\nu_n$ we have

$$\boldsymbol{E}(iq_m) = iq_m \boldsymbol{A}(iq_m) \tag{5.2}$$

Classically, the vector potential enters the Hamilton function H in the following way

$$H^{\boldsymbol{A}} = \sum_n \frac{(\boldsymbol{p}_n + e\boldsymbol{A})^2}{2m} - e\phi, \tag{5.3}$$

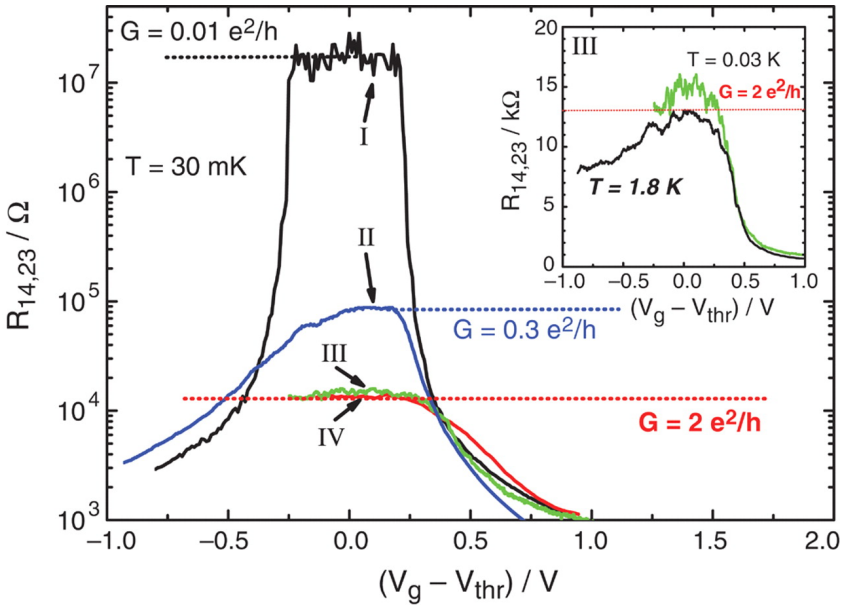

Figure 5.2: The longitudinal four-terminal resistance in HgTe quantum well structures of different sample sizes measured as a function of the gate voltage. For sample III and IV the measured value is close to the predicted quantized value of the longitudinal conductivity of $2\frac{e^2}{h}$ due to the gapless edge states that must be present in a QSH insulator. The figure is reprinted from Ref. [90].

where n is the particle index of the electrons. In quantum mechanics the replacement $\boldsymbol{p} \to p - e\boldsymbol{A}$ is called Peierls substitution. We now choose a gauge where ϕ is zero. This is always possible. Classically, the current is obtained by the expression

$$J_\alpha^{\boldsymbol{A}} = -\left(\frac{\partial H}{\partial A_\alpha}\right)_{p,r}, \tag{5.4}$$

where $J_\alpha^{\boldsymbol{A}}$ is the total current in direction α in the presence of a vector potential and H the Hamilton function. The current operator can be obtained from the correspondence principle. In quantum mechanics both $\boldsymbol{j}$ and H become operators. The current density is given by a functional derivatives

$$j_\alpha^{\boldsymbol{A}}(\tau, \boldsymbol{r}) = -\frac{\delta H^{\boldsymbol{A}(\tau)}}{\delta A_\alpha(\tau, \boldsymbol{r})}. \tag{5.5}$$

Here, the functional derivative is only with respect to the spacial coordinates, but not with respect to time. Note, that despite the time dependence $j_a^{\boldsymbol{A}}$ is in the Schrödinger representation. In a gauge with $\phi = 0$ the Hamiltonian becomes

$$H^{\boldsymbol{A}(\tau)} = \sum_n \frac{\boldsymbol{p}_n^2}{2m} - \frac{e}{2m}(\boldsymbol{p}_n \boldsymbol{A}(\tau, \boldsymbol{r}_n) + \boldsymbol{A}(\tau, \boldsymbol{r}_n)\boldsymbol{p}_n) + \frac{e^2}{2m}\boldsymbol{A}(\tau, \boldsymbol{r}_n)^2. \tag{5.6}$$

So with Eq. 5.5 we get for the current operator

$$j_\alpha^{\boldsymbol{A}}(\tau, \boldsymbol{r}) = \sum_n \frac{e}{2m}(\boldsymbol{p}_n \delta(\boldsymbol{r} - \boldsymbol{r}_n) + \delta(\boldsymbol{r} - \boldsymbol{r}_n)\boldsymbol{p}_n) - \frac{e^2}{m}\boldsymbol{A}(\tau', \boldsymbol{r}_n)\delta(\boldsymbol{r} - \boldsymbol{r}_n). \tag{5.7}$$

Up to linear order in $\boldsymbol{A}$ the coupling between the system and the vector potential is

$$H^{\Delta \boldsymbol{A}(\tau)} = -\int d\boldsymbol{r} j_\alpha^{\boldsymbol{A}=0}(\tau, \boldsymbol{r})\boldsymbol{A}(\tau, \boldsymbol{r}), \tag{5.8}$$

where $j_\alpha^{\boldsymbol{A}=0}$ is the first term in Eq. 5.7. Note the equivalence of a source field $\phi(1,2)$ and the vector potential $\boldsymbol{A}$ when one expresses the current operator with creation and annihilation operators. However, the vector potential has only one position and one time argument and there is no integration over τ. Integrating Eq. 5.7 over $\boldsymbol{r}$ we get for the total current

$$J_\alpha^{\boldsymbol{A}}(\tau) = \sum_n e\frac{\boldsymbol{p}_n}{m} - \frac{e^2}{m}\boldsymbol{A}(\tau, \boldsymbol{r}_n). \tag{5.9}$$

Note that the integration over a derivative of a delta distribution yields zero in a periodic system.

5.2.2 Vector potential in a tight-binding model

In this section we explain how to incorporate a vector potential in a tight binding model. We then also show that partial derivatives of the Bloch Hamiltonian $\mathcal{H}(\boldsymbol{k})$ by the vector potential can be replaced by partial derivatives with respect to $\boldsymbol{k}$. The Hamiltonian we consider is given by as a sum of a noninteracting Hamiltonian and the Hubbard interaction

$$H^A = H_0^A + H^U. \tag{5.10}$$

In a non-interacting periodic tight-binding model the vector potential can be included in the Hamiltonian in the following way. For each hopping element

$$t^{ab}_{\boldsymbol{R}_j+\boldsymbol{r}_a,\boldsymbol{R}_i+\boldsymbol{r}_b} = \langle w_{\boldsymbol{R}_j+\boldsymbol{r}_a,a}|H|w_{\boldsymbol{R}_i+\boldsymbol{r}_b,b}\rangle = \langle w_{\boldsymbol{R}_j-\boldsymbol{R}_i+\boldsymbol{r}_a,a}|H|w_{0+\boldsymbol{r}_b,b}\rangle = \mathcal{H}_{ab}(\boldsymbol{R}_j - \boldsymbol{R}_i), \tag{5.11}$$

where $w_{\boldsymbol{R}_i+\boldsymbol{r}_b,b}$ is a Wannier function localized at $\boldsymbol{R}_i + \boldsymbol{r}_b$, where $\boldsymbol{R}_i$ is the lattice vector for the unit cell, $\boldsymbol{r}_b$ the position in the unit cell and b a site/orbital index that also includes spin. $\mathcal{H}_{ab}(\boldsymbol{R}_j - \boldsymbol{R}_i)$ are the matrix elements of the Bloch Hamiltonian in real space, that are essentially given by the hopping elements. Including a vector potential each hopping term in the Hamiltonian becomes

$$t^{ab}_{\boldsymbol{R}_j+\boldsymbol{r}_a,\boldsymbol{R}_i+\boldsymbol{r}_b} c^\dagger_{\boldsymbol{R}_j+\boldsymbol{r}_a a} c_{\boldsymbol{R}_i+\boldsymbol{r}_b b} \to t^{ab}_{\boldsymbol{R}_j+\boldsymbol{r}_a,\boldsymbol{R}_i+\boldsymbol{r}_b} \exp\left(-i\frac{e}{\hbar}\int_{\boldsymbol{R}_i+\boldsymbol{r}_b}^{\boldsymbol{R}_j+\boldsymbol{r}_a} \boldsymbol{A}(\tau,\boldsymbol{r})\cdot d\boldsymbol{r}\right) c^\dagger_{\boldsymbol{R}_j+\boldsymbol{r}_a a} c_{\boldsymbol{R}_i+\boldsymbol{r}_b b}. \tag{5.12}$$

Only in this way expectation values of H are invariant under gauge transformations of the vector potential $\boldsymbol{A}(\tau,\boldsymbol{r}) \to \boldsymbol{A}(\tau,\boldsymbol{r}) + \nabla_{\boldsymbol{r}}\Lambda(\boldsymbol{r})$, because under such a gauge transformation creation (and similar annihilation) operators transform as

$$c^\dagger_{\boldsymbol{R}_j+\boldsymbol{r}_a a}(\tau) \to \exp\left(-i\frac{e}{\hbar}\Lambda(\tau, \boldsymbol{R}_j + \boldsymbol{r}_a)\right) c^\dagger_{\boldsymbol{R}_j+\boldsymbol{r}_a a}(\tau). \tag{5.13}$$

This is the lattice version of the change of a wave function under a gauge transformation

$$\psi(\tau,\boldsymbol{r}) \to \exp\left(-i\frac{e}{\hbar}\Lambda(\tau,\boldsymbol{r})\right)\psi(\tau,\boldsymbol{r}), \tag{5.14}$$

as follows from the Schrödinger equation with vector potential. Note that here e is the elementary charge. Assuming an uniform vector potential, Eq. 5.12 becomes

$$t^{ab}_{\boldsymbol{R}_j+\boldsymbol{r}_a,\boldsymbol{R}_i+\boldsymbol{r}_b} c^\dagger_{\boldsymbol{R}_j+\boldsymbol{r}_a a} c_{\boldsymbol{R}_i+\boldsymbol{r}_b b} \to t^{ab}_{\boldsymbol{R}_j+\boldsymbol{r}_a,\boldsymbol{R}_i+\boldsymbol{r}_b} \exp\left(-i\frac{e}{\hbar}\boldsymbol{A}(\tau)\cdot(\boldsymbol{R}_j - \boldsymbol{R}_i + \boldsymbol{r}_a - \boldsymbol{r}_b)\right) c^\dagger_{\boldsymbol{R}_j+\boldsymbol{r}_a} c_{\boldsymbol{R}_i+\boldsymbol{r}_b}. \tag{5.15}$$

The Hubbard interaction consists of creation-annihilation operator pairs and hence the gauge factors acquired through the vector potential cancel. Hence, the Hubbard part stays unchanged.

The Bloch Hamiltonian can be obtained by the following discrete Fourier transformation. We include the orbital positions in the Fourier transform. This corresponds to a specific gauge choice. We get

$$\begin{aligned}\mathcal{H}^{\boldsymbol{A}}_{ab}(\boldsymbol{k}) &= \sum_{\boldsymbol{R}} \mathcal{H}^{\boldsymbol{A}}_{ab}(\boldsymbol{R}) \exp\left(-i\boldsymbol{k}\cdot(\boldsymbol{R}+\boldsymbol{r}_a-\boldsymbol{r}_b)\right) \\ &= \sum_{\boldsymbol{R}} \mathcal{H}^{\boldsymbol{A}=0}_{ab}(\boldsymbol{R}) \exp\left(-i\boldsymbol{k}\cdot(\boldsymbol{R}+\boldsymbol{r}_a-\boldsymbol{r}_b)\right) \exp-\left(i\frac{e}{\hbar}\boldsymbol{A}(\tau)\cdot(\boldsymbol{R}+\boldsymbol{r}_a-\boldsymbol{r}_b)\right) \\ &= \sum_{\boldsymbol{R}} \mathcal{H}^{\boldsymbol{A}=0}_{ab}(\boldsymbol{R}) \exp\left(-i(\boldsymbol{k}+\frac{e}{\hbar}\boldsymbol{A}(\tau))\cdot(\boldsymbol{R}+\boldsymbol{r}_a-\boldsymbol{r}_b)\right) \\ &= \mathcal{H}^{\boldsymbol{A}=0}_{ab}(\boldsymbol{k}+\frac{e}{\hbar}\boldsymbol{A}(\tau)). \end{aligned} \tag{5.16}$$

The Fourier transformation for the annihilation (and respectively creation) operators is

$$c_{\boldsymbol{R}_i+\boldsymbol{r}_b b} = \frac{1}{N}\sum_{\boldsymbol{k}} \exp\left(i\boldsymbol{k}\cdot(\boldsymbol{R}_i+\boldsymbol{r}_b)\right) c_{\boldsymbol{k}b}. \tag{5.17}$$

This corresponds to a gauge choice, which is not periodic in k-space. This gauge choice is important, when there are multiple sites in the unit cell, so that one can replace derivatives by $\boldsymbol{A}$ at $\boldsymbol{A}=0$ by a derivative by $\boldsymbol{k}$. Explicitly, we have

$$\partial_{A_\alpha(\tau)} \mathcal{H}^{\boldsymbol{A}(\tau)}_{ab}(\boldsymbol{k})|_{\boldsymbol{A}=0} = \frac{e}{\hbar}\partial_{k_\alpha}\mathcal{H}^{\boldsymbol{A}=0}_{ab}(\boldsymbol{k}). \tag{5.18}$$

Note, that in the case of a uniform vector potential, i.e. zero magnetic field, $\boldsymbol{k}$ is still a good quantum number.

5.2.3 Current and current operator in a tight-binding model

In this section we give an expression for the current and the current operator in a vector potential. We follow Ref. [228]. Writing the Hamiltonian in a basis of Bloch-like basis functions we have (including spin in the orbital indices)

$$H^{\boldsymbol{A}(\tau)} = \sum_{\boldsymbol{k}ab} \mathcal{H}^{\boldsymbol{A}(\tau)}_{ab}(\boldsymbol{k}) c^\dagger_{\boldsymbol{k}a} c_{\boldsymbol{k}b} + H^U \tag{5.19}$$

Now we show that the total current operator in the presence of a uniform vector potential $\boldsymbol{A}$ is given by

$$J^{\boldsymbol{A}}_\alpha(\tau) = -\frac{\partial H^{\boldsymbol{A}(\tau)}}{\partial A_\alpha(\tau)}. \tag{5.20}$$

We start from Eq. 5.5. On a lattice the functional derivative with respect to the $\boldsymbol{r}$ dependence of $\boldsymbol{A}$ becomes a sum of partial derivatives at the orbital positions $\boldsymbol{R}_i+\boldsymbol{r}_a$. For the total current operator we have sum over all unit cells i and site/orbital indices a. Hence the current on a lattice is given by

$$J^{\boldsymbol{A}}_\alpha(\tau) = -\sum_{ia} \frac{\partial H^{\boldsymbol{A}(\tau)}}{\partial A_\alpha(\tau, \boldsymbol{R}_i+\boldsymbol{r}_a)}. \tag{5.21}$$

Formally, for uniform field $\boldsymbol{A}(\tau, \boldsymbol{R}_i+\boldsymbol{r}_a) = \boldsymbol{A}(\tau)$ for all i, a we can write with the chain rule

$$\begin{aligned} J^{\boldsymbol{A}}_\alpha(\tau) &= -\sum_{ia} \frac{\partial H^{\boldsymbol{A}(\tau)}}{\partial A_\alpha(\tau, \boldsymbol{R}_i+\boldsymbol{r}_a)} \\ &= -\sum_{ia} \frac{\partial H^{\boldsymbol{A}(\tau)}}{\partial A_\alpha(\tau, \boldsymbol{R}_i+\boldsymbol{r}_a)} \frac{\partial A_\alpha(\tau, \boldsymbol{R}_i+\boldsymbol{r}_a)}{\partial A_\alpha(\tau)} \\ &= -\frac{\partial H^{\boldsymbol{A}(\tau)}}{\partial A_\alpha(\tau)} \end{aligned} \tag{5.22}$$

Hence, one can replace the functional derivative by just one partial derivative. So in the Bloch basis one has for the current operator in the Schrödinger picture

$$J_\alpha^{\boldsymbol{A}}(\tau) = -\sum_{\boldsymbol{k}ab} \frac{\partial \mathcal{H}_{ab}^{\boldsymbol{A}(\tau)}(\boldsymbol{k})}{\partial A_\alpha(\tau)} c_{\boldsymbol{k}a}^\dagger c_{\boldsymbol{k}b}. \tag{5.23}$$

To obtain the current density one has do devide by the volume of the system. The time-dependent expectation value of this operator can be expressed by a single-particle non-equilibrium Green's function

$$\langle J_{H,\alpha}^{\boldsymbol{A}}(\tau)\rangle_{\boldsymbol{A}} = -\sum_{\boldsymbol{k}ab} \frac{\partial \mathcal{H}_{ab}^{\boldsymbol{A}(\tau)}(\boldsymbol{k})}{\partial A_\alpha(\tau)} G_{ba}^{\boldsymbol{A}}(\tau, \tau^+, \boldsymbol{k}). \tag{5.24}$$

where here $\langle\cdot\rangle_{\boldsymbol{A}} = \mathrm{Tr}(\rho^{\boldsymbol{A}}\cdot)$ and $\rho^{\boldsymbol{A}}$ is the non-equilibrium density matrix of the system with the states in the Heisenberg representation. The subscript H of J indicates that the operator is now also in the (imaginary time) Heisenberg picture to get a time dependent expectation value. The time-ordered non-equilibrium Matsubara Green's function is given by

$$G_{ab}^{\boldsymbol{A}}(\tau_1, \tau_2, \boldsymbol{k}) = -\langle T_\tau c_{\boldsymbol{k}a}(\tau_1) c_{\boldsymbol{k}b}^\dagger(\tau_2)\rangle_{\boldsymbol{A}}. \tag{5.25}$$

Later, we expand up to linear order in the vector potential to obtain the conductivity. The result will be expressed in terms of equilibrium quantities. Hence, we do not need to specify here how the non-equilibrium time evolution and density matrix looks like in detail. The total current can also be seen as the $\boldsymbol{q} = 0$ current density.

5.2.4 Definition of the conductivity

To linear order the current density in Matsubara frequency space is given by

$$j_\alpha^{\boldsymbol{A}}(iq_m) = \sum_\beta \left(\Pi_{\alpha\beta}(iq_m) - \frac{1}{V}\sum_{\boldsymbol{k}ab} \frac{e^2}{\hbar^2} \frac{\partial^2 \mathcal{H}_{ab}^{\boldsymbol{A}=0}(\boldsymbol{k})}{\partial k_\alpha \partial k_\beta} \langle c_{\boldsymbol{k}b}^\dagger c_{\boldsymbol{k}a}\rangle_{\boldsymbol{A}=0} \right) A_\beta(iq_m) + \mathcal{O}(\boldsymbol{A}^2), \tag{5.26}$$

where V is the volume of the system. The linear coefficient Π in the first term is called polarization. The second term is the diamagnetic term in a lattice model. The second derivative of the Bloch Hamiltonian with prefactor $\frac{1}{\hbar^2}$ is the generalization of the inverse mass in a lattice model. $\langle c_{\boldsymbol{k}b}^\dagger c_{\boldsymbol{k}a}\rangle_{\boldsymbol{A}=0}$ is in some sense the generalization of the density, that now depends on $\boldsymbol{k}$ and orbital indices. We can now perform analytic continuation on $\Pi_{\alpha\beta}(iq_m)$ to infinitesimally over the real frequency axis i.e. $iq_m \to \nu + i\eta$ to obtain the retarded polarization $\Pi_{\alpha\beta}^R(\nu) = \Pi_{\alpha\beta}(\nu + i\eta)$. In an alternative derivation the polarization can be derived from the current-current correlation function. The current-current correlation function has a spectral representation. Hence, there is a unique analytical continuation from Matsubara frequencies to real frequencies as usual for correlation functions. In real frequencies we have

$$j_\alpha^{\boldsymbol{A}}(\nu) = \sum_\beta \left(\Pi_{\alpha\beta}(\nu + i\eta) - \frac{1}{V}\sum_{\boldsymbol{k}a} \frac{e^2}{\hbar^2} \frac{\partial^2 \mathcal{H}_{aa}^{\boldsymbol{A}=0}(\boldsymbol{k})}{\partial k_\alpha \partial k_\beta} \langle c_{\boldsymbol{k}a}^\dagger c_{\boldsymbol{k}a}\rangle_{\boldsymbol{A}=0} \right) A_\beta(\nu) + \mathcal{O}(\boldsymbol{A}^2). \tag{5.27}$$

From $\boldsymbol{E}(t) = -\partial_t \boldsymbol{A}(t)$ we get

$$\boldsymbol{E}(\nu + i\eta) = i(\nu + i\eta)\boldsymbol{A}(\nu + i\eta). \tag{5.28}$$

So that we can identify the optical conductivity from Eq. 5.27 to be

$$\sigma_{\alpha\beta}(\nu) = \frac{\Pi_{\alpha\beta}(\nu + i\eta)}{i(\nu + i\eta)}. \tag{5.29}$$

Gauge invariance implies that one cannot have a response of a time and space independent vector potential, because in this case the electric and magnetic field are zero. Hence, one must have

$$\Pi_{\alpha\beta}(0+i\eta)) = \frac{1}{V}\sum_{\boldsymbol{k}a}\frac{e^2}{\hbar^2}\frac{\partial^2\mathcal{H}^{\boldsymbol{A}=0}_{aa}(\boldsymbol{k})}{\partial k_\alpha \partial k_\beta}\left\langle c^\dagger_{\boldsymbol{k}a}c_{\boldsymbol{k}a}\right\rangle_{\boldsymbol{A}=0}. \tag{5.30}$$

In the DC limit we must calculate

$$\begin{aligned}\sigma^{\mathrm{DC}}_{\alpha\beta} &= \lim_{\nu\to 0}\frac{\Pi_{\alpha\beta}(\nu+i\eta)-\Pi_{\alpha\beta}(0+i\eta)}{i\nu}\\ &= \lim_{\nu\to 0}\frac{\Pi_{\alpha\beta}(\nu+i\eta)-\Pi_{\alpha\beta}(0+i\eta)}{i(\nu+i\eta)-i(0+i\eta)}\\ &= -i\lim_{\nu\to 0}\partial_\nu\Pi_{\alpha\beta}(\nu+i\eta).\end{aligned} \tag{5.31}$$

We are interested in the real part of the DC conductivity i.e.

$$\mathrm{Re}\sigma^{\mathrm{DC}}_{\alpha\beta} = \lim_{\nu\to 0}\partial_\nu \mathrm{Im}\Pi_{\alpha\beta}(\nu+i\eta). \tag{5.32}$$

If we want to work with Matsubara frequencies, we can take advantage of analytic continuation. The Cauchy-Riemann equations for a complex differentiable function $f(z) = u(x,y)+iv(x,y)$ with $z = x+iy$, where u, v are real functions, are given by $\partial_x u = \partial_y v$ and $\partial_y u = -\partial_x v$. We get

$$\mathrm{Re}(\sigma^{\mathrm{DC}}_{\alpha\beta}) = \lim_{\nu\to 0}\partial_\nu \mathrm{Im}\left(\Pi_{\alpha\beta}(\nu+i\eta)\right) = -\lim_{q_m\to 0}\partial_{q_m}\mathrm{Re}\left(\Pi_{\alpha\beta}(iq_m)\right) = \lim_{iq_m\to 0}\partial_{iq_m}\mathrm{Im}\left(\Pi_{\alpha\beta}(iq_m)\right). \tag{5.33}$$

The small imaginary part $i\eta$ causes the function to be analytical, so the Cauchy-Riemann equations can be applied. The DC dissipationless intrinsic (in the absence of a magnetic field) Hall conductivity is given by the anti-symmetric part. We get

$$\sigma^{\mathrm{H}}_{\alpha\beta} = \frac{1}{2}(\sigma^{\mathrm{DC}}_{\alpha\beta} - \sigma^{\mathrm{DC}}_{\beta\alpha}). \tag{5.34}$$

5.3 Spin Hall conductivity expression for the interacting case

If there is a difference between Hall conductivity for up electrons and for down electrons, then there is a net spin Hall current in the system. The corresponding spin Hall conductivity (SHC) is defined as

$$\sigma^{\mathrm{SH}}_{xy} = \sigma^{\mathrm{H}\uparrow}_{xy} - \sigma^{\mathrm{H}\downarrow}_{yx} = \frac{1}{2}(\sigma^{\mathrm{DC}\uparrow}_{xy} - \sigma^{\mathrm{DC}\uparrow}_{yx}) - \frac{1}{2}(\sigma^{\mathrm{DC}\downarrow}_{xy} - \sigma^{\mathrm{DC}\downarrow}_{yx}). \tag{5.35}$$

In the following we will consider a system in which the spin z-component is conserved. In Sec. 5.3.1 We first derive an expression for the interacting spin Hall conductivity in terms of Matsubara Green's functions. In Sec. 5.3.2 we show that in the non-interacting case the Green's function expression reduces to a Brillouin zone integral over a Berry curvature. In Sec. 5.3.3 then we will show that at zero temperature the expression is a topological invariant in terms of the Matsubara Green's function. It follows that at zero temperature the SHC must be quantized to integer multiples of $2\frac{e^2}{h}$ also in the presence of interactions. In Sec. 5.3.4 we discuss vertex corrections for the interacting case and how they can be calculated within TPSC. In Sec. 5.3.5 we give some details about our implementation.

5.3.1 Derivation of the spin Hall conductivity at finite temperature

In the following we derive an expression for the spin Hall conductivity at finite temperature in terms of the Matsubara Green's function in two dimensions that is valid in the presence of interactions. Ref. [107] gives a derivation for the zero temperature Hall conductivity starting from the current current correlator. Here, we derive the Hall conductivity from a linear expansion in the vector potential of the current density expectation value. Our strategy will be the following. For simplicity we consider spinless electrons, so that in fact we derive an expression for the Hall conductivity. The spin Hall conductivity for

a system, where the z components of the electrons are conserved, can be obtained by adding spin indices and then taking the difference of conductivities for spin up and down. To obtain the Hall conductivity we write the expectation value of the current density in terms of a non-equilibrium Green's function. We then expand linearly in terms of the vector potential. The linear coefficient (minus the diamagnetic term) can be identified as the polarization and from its frequency derivative the conductivity. The obtained expression for the Hall conductivity only depends on equilibrium quantities, because expanding linearly implies that in the linear coefficient one sets $\boldsymbol{A} = 0$ after doing the functional derivative with respect to the vector potential. We finally discuss the zero-temperature limit and bring the expression for the Hall conductivity in a more symmetrical form. Throughout this section we work in a gauge where the orbital positions in the unit cell are included in the Fourier transform as in Eq. 5.16. The derivation presented in this section is based on Ref. [229].

Previously we found, that the expectation value for the current can be written in terms of a Green's functions as (Eq. 5.24)

$$\langle J^{\boldsymbol{A}}_{H,\alpha}(\tau)\rangle_{\boldsymbol{A}} = -\sum_{\boldsymbol{k}ab} \frac{\partial \mathcal{H}^{\boldsymbol{A}(\tau)}_{ab}(\boldsymbol{k})}{\partial A_\alpha(\tau)} G^{\boldsymbol{A}}_{ba}(\tau,\tau^+,\boldsymbol{k}). \tag{5.36}$$

Now we want to expand to linear order in the vector potential. For simplicity we will not write momentum and use a matrix notation for orbital indices. As discussed in Sec. 5.2.3 the functional derivative with respect to the vector potential on a lattice becomes a partial derivative with respect to the vector potential. The Green's function depends on the vector potential at different times, hence we need a functional derivative with respect to the vector potential in imaginary time. Expanding the current up to linear order in the vector potential we get

$$\begin{aligned} j^{\boldsymbol{A}}_\alpha = &-\frac{1}{V}\sum_\beta \int d\tau' \mathrm{Tr}\left(\frac{\partial \mathcal{H}^{\boldsymbol{A}(\tau)}}{\partial A_\alpha(\tau)} \frac{\delta G^{\boldsymbol{A}}(\tau,\tau^+)}{\delta A_\beta(\tau')}\right)_{\boldsymbol{A}=0} A_\beta(\tau') \\ &-\frac{1}{V}\sum_\beta \int d\tau' \mathrm{Tr}\left(\frac{\partial \mathcal{H}^{\boldsymbol{A}(\tau)}}{\partial A_\alpha(\tau)\partial A_\beta(\tau')}\delta(\tau-\tau') G^{\boldsymbol{A}}(\tau,\tau^+)\right)_{\boldsymbol{A}=0} A_\beta(\tau') + \mathcal{O}(\boldsymbol{A}^2). \end{aligned} \tag{5.37}$$

Here the trace also includes the sum over k-points. The dependence of the interacting Green's function on the vector potential is nontrivial. One can think of the interacting Green's function in terms of a perturbation series written in terms of the non-interacting Green's function. Each non-interacting Green's function now couples to the vector potential. For example whenever there is a process in which a particle-hole pair is created and destroyed after, both the hole and the electron couple to the external vector potential. Differentiating the identity $G^{\boldsymbol{A}} G^{\boldsymbol{A}-1} = 1$ we get the identity

$$\frac{\delta G^{\boldsymbol{A}}(\tau,\tau^+)}{\delta A_\beta(\tau')} = -G^{\boldsymbol{A}}(\tau,\bar{\tau}_1)\frac{\delta (G^{\boldsymbol{A}})^{-1}(\bar{\tau}_1,\bar{\tau}_2)}{\delta A_\beta(\tau')} G^{\boldsymbol{A}}(\bar{\tau}_2,\tau^+). \tag{5.38}$$

The first term in Eq. 5.37 corresponds to the polarization, which we can write as

$$\Pi_{\alpha\beta}(\tau-\tau') = \frac{1}{V}\mathrm{Tr}\left(\frac{\partial \mathcal{H}^{\boldsymbol{A}(\tau)}}{\partial A_\alpha(\tau)} G^{\boldsymbol{A}}(\tau,\bar{\tau}_1)\frac{\delta (G^{\boldsymbol{A}})^{-1}(\bar{\tau}_1,\bar{\tau}_2)}{\delta A_\beta(\tau')} G^{\boldsymbol{A}}(\bar{\tau}_2,\tau^+)\right)_{\boldsymbol{A}=0}. \tag{5.39}$$

The polarization only depends on one time argument, because of time translation invariance. The second term is the diamagnetic term

It is symmetric with respect to the exchange of α and β, so the term does not contribute to the Hall conductivity. Hence, we neglect the second term. The first term contains is a functional derivative of an inverse Green's function i.e. a renormalized vertex. The renormalized vertex can be written as a sum of a bare vertex and a vertex correction. In Matsubara frequencies one has the expressions

$$\Lambda_\beta(iq_m; i\omega_n, \boldsymbol{k}) = \left(\frac{\partial (G^{\boldsymbol{A}}(i\omega_n,\boldsymbol{k}))^{-1}}{\partial A_\beta(iq_m)}\right)_{\boldsymbol{A}=0} = \left(\frac{\partial (G^{\boldsymbol{A}}_0(i\omega_n,\boldsymbol{k}))^{-1}}{\partial A_\beta(iq_m)}\right)_{\boldsymbol{A}=0} - \left(\frac{\partial (\Sigma^{\boldsymbol{A}}(i\omega_n,\boldsymbol{k}))^{-1}}{\partial A_\beta(iq_m)}\right)_{\boldsymbol{A}=0}. \tag{5.40}$$

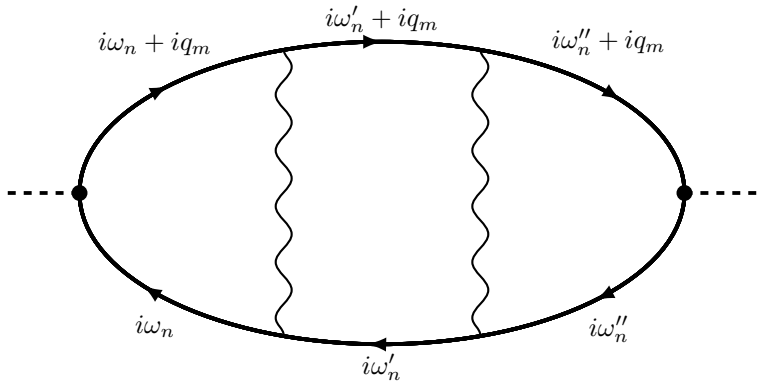

Figure 5.3: Diagram with vertex corrections contributing to the polarization. Thick lines represent Green's functions, wiggled lines represent vertex corrections, dots with dashed line attached represent the bare current vertices. We do not write momenta or orbital and spin indices. The vertex corrections stem from the right vertex. The frequency derivative with respect to iq_m acts everywhere a Green's function depends on iq_m. Vertex corrections on left side of the derivative can be absorbed in the left vertex that now becomes dressed.

The bare vertex is defined as

$$\lambda_\alpha(iq_m; i\omega_n, \boldsymbol{k}) = \left(\frac{\partial (G_0^{\boldsymbol{A}}(i\omega_n, \boldsymbol{k}))^{-1}}{\partial A_\beta(iq_m)}\right)_{\boldsymbol{A}=0} = -\left(\frac{\partial \mathcal{H}^{\boldsymbol{A}}(\boldsymbol{k})}{\partial A_\beta(iq_m)}\right)_{\boldsymbol{A}=0} = -\frac{e}{\hbar}\partial_{k_\alpha}\mathcal{H}_{ab}(\boldsymbol{k}). \tag{5.41}$$

The last equality only holds, because we work in the gauge where the orbital position is included in the Fourier transform (see Eq. 5.16). Note that the bare vertex does not explicitly depend on iq_m and $i\omega_n$ and hence it is constant in frequency. Writing the polarization in frequency- and momentum-space we get

$$\Pi_{\alpha\beta}(iq_m) = \frac{T}{V}\sum_{\omega_n \boldsymbol{k}} \mathrm{Tr}\left(\lambda_\alpha(iq_m; i\omega_n, \boldsymbol{k}) G(i\omega_n + iq_m, \boldsymbol{k}) \Lambda_\beta(iq_m; i\omega_n, \boldsymbol{k}) G(i\omega_n, \boldsymbol{k})\right), \tag{5.42}$$

where the trace runs over orbital indices and the multiplications are matrix multiplications. To obtain the DC conductivity one needs to do a frequency derivative (Eq. 5.33). The frequency derivative acts on two places in G and in Λ. Graphically, this can be seen in Fig. 5.3. The frequency derivative causes the bare vertex to become dressed. The reason is, that inserting the frequency derivative between vertex corrections in the dressed vertex allows to absorb the vertex corrections into the vertex at the respective side of the insertion point of the derivative. We get

$$\begin{aligned}\frac{\partial \Pi_{\alpha\beta}(iq_m)}{\partial iq_m} &= \frac{T}{V}\sum_{\omega_n \boldsymbol{k}} \mathrm{Tr}\left(\Lambda_\alpha(iq_m; i\omega_n, \boldsymbol{k}) \frac{\partial G(i\omega_n + iq_m, \boldsymbol{k})}{\partial iq_m} \Lambda_\beta(iq_m; i\omega_n, \boldsymbol{k}) G(i\omega_n, \boldsymbol{k})\right) \\ &= -\frac{T}{V}\sum_{\omega_n \boldsymbol{k}} \mathrm{Tr}\Big(\Lambda_\alpha(iq_m; i\omega_n, \boldsymbol{k}) G(i\omega_n + iq_m, \boldsymbol{k}) \frac{\partial G^{-1}(i\omega_n + iq_m, \boldsymbol{k})}{\partial iq_m} G(i\omega_n + iq_m, \boldsymbol{k}) \\ &\quad \times \Lambda_\beta(iq_m; i\omega_n, \boldsymbol{k}) G(i\omega_n, \boldsymbol{k})\Big).\end{aligned} \tag{5.43}$$

For the Hall conductivity we take the zero frequency limit of the imaginary part and antisymmetrize over α and β

$$\begin{aligned}\sigma^H_{\alpha\beta} &= \lim_{iq_m\to 0}\mathrm{Im}\frac{\partial\Pi_{\alpha\beta}(iq_m)}{\partial iq_m}\\ &= -\mathrm{Im}\frac{T}{2V}\sum_{\omega_n\boldsymbol{k}}\mathrm{Tr}\Big(\Lambda_\alpha(0;i\omega_n,\boldsymbol{k})G(i\omega_n,\boldsymbol{k})\frac{\partial G^{-1}(i\omega_n,\boldsymbol{k})}{\partial i\omega_n}G(i\omega_n,\boldsymbol{k})\Lambda_\beta(0;i\omega_n,\boldsymbol{k})G(i\omega_n,\boldsymbol{k})\\ &\quad-\Lambda_\beta(0;i\omega_n,\boldsymbol{k})G(i\omega_n,\boldsymbol{k})\frac{\partial G^{-1}(i\omega_n,\boldsymbol{k})}{\partial i\omega_n}G(i\omega_n,\boldsymbol{k})\Lambda_\alpha(0;i\omega_n,\boldsymbol{k})G(i\omega_n,\boldsymbol{k})\Big).\end{aligned} \tag{5.44}$$

There are two types of vertex corrections. Expanding the Self-energy $\Sigma^{\boldsymbol{A}}$ in terms of a perturbation series in terms of the noninteracting Green's function $G^{0,\boldsymbol{A}}$ we see that the vector potential enters Green's functions that depend on the outer momentum as well as Green's function that only depend on inner momenta that are integrated over. The second type of diagrams cancel, because of the antisymmetry of the Hall conductivity expression when exchanging α and β. The reason is that in the corresponding diagrams the vector potentials are attached to two different momentum loops that are integrated over. Hence, it is always possible possible to switch the integration variable for the momenta and find the corresponding diagram with $\alpha \leftrightarrow \beta$ that cancels it. This means that only diagrams of the first type survive and because of Eq. 5.18 we can replace the dressed vertices by derivatives of the Green's function

$$\Lambda_\alpha(0;i\omega_n,\boldsymbol{k}) \to -\frac{e}{\hbar}\partial_{k_\alpha}G^{-1}(i\omega_n,\boldsymbol{k}). \tag{5.45}$$

Alternatively, this identity can be justified from the Ward identity [107]. Note, that this can only be done for the Hall conductivity and not for the longitudinal conductivity. Hence, we get the following expression

$$\begin{aligned}\sigma^H_{\alpha\beta} = -\frac{e^2}{\hbar^2}\frac{T}{2V}\mathrm{Im}\sum_{\omega_n\boldsymbol{k}}\mathrm{Tr}\Big(&\frac{\partial G^{-1}(i\omega_n,\boldsymbol{k})}{\partial k_\alpha}G(i\omega_n,\boldsymbol{k})\frac{\partial G^{-1}(i\omega_n,\boldsymbol{k})}{\partial i\omega_n}G(i\omega_n,\boldsymbol{k})\frac{\partial G^{-1}(i\omega_n,\boldsymbol{k})}{\partial k_\beta}G(i\omega_n,\boldsymbol{k})\\ &-\frac{\partial G^{-1}(i\omega_n,\boldsymbol{k})}{\partial k_\beta}G(i\omega_n,\boldsymbol{k})\frac{\partial G^{-1}(i\omega_n,\boldsymbol{k})}{\partial i\omega_n}G(i\omega_n,\boldsymbol{k})\frac{\partial G^{-1}(i\omega_n,\boldsymbol{k})}{\partial k_\alpha}G(i\omega_n,\boldsymbol{k})\Big).\end{aligned} \tag{5.46}$$

We can now rewrite this expression into a more symmetrical form in which it is easier to see later that it becomes a topological invariant in terms of the Green's function at zero temperature. Taking advantage of the cyclic property of the trace and with the totally antisymmetric tensor $\epsilon_{\rho\eta\zeta}$ we can write

$$\sigma^H_{\alpha\beta} = \frac{e^2}{\hbar^2}\frac{T}{6V}\epsilon_{\rho\eta\zeta}\mathrm{Im}\sum_{\omega_n\boldsymbol{k}}\mathrm{Tr}\Big(\partial_\rho G^{-1}(i\omega_n,\boldsymbol{k})G(i\omega_n,\boldsymbol{k})\partial_\eta G^{-1}(i\omega_n,\boldsymbol{k})G(i\omega_n,\boldsymbol{k})\partial_\zeta G^{-1}(i\omega_n,\boldsymbol{k})G(i\omega_n,\boldsymbol{k})\Big). \tag{5.47}$$

where $\rho,\ \eta,\ \zeta$ are summed over and stand for $i\omega_n, k_\alpha, k_\beta$. In the continuum limit the sum over k-points is replaced by an integral

$$\begin{aligned}\sigma^H_{\alpha\beta} = \frac{e^2}{\hbar^2}\frac{T}{24\pi^2}\epsilon_{\rho\eta\zeta}\mathrm{Im}\int d\boldsymbol{k}\sum_{\omega_n}\mathrm{Tr}\Big(&\partial_\rho G^{-1}(i\omega_n,\boldsymbol{k})G(i\omega_n,\boldsymbol{k})\partial_\eta G^{-1}(i\omega_n,\boldsymbol{k})\\ &\times G(i\omega_n,\boldsymbol{k})\partial_\zeta G^{-1}(i\omega_n,\boldsymbol{k})G(i\omega_n,\boldsymbol{k})\Big).\end{aligned} \tag{5.48}$$

In the zero-temperature limit the Matsubara frequencies become continuous $i\omega_n \to i\omega$. Hence, the sum over Matsubara frequencies becomes an integral [1]

[1] The transition from the discrete sum to the integral can be shown in the following way. We have $\Delta\omega_n = \frac{2\pi T}{\hbar} = \frac{2\pi T}{\hbar}\Delta n$ with $\Delta n = 1$. With that we get $T\sum_{\omega_n} f(\omega_n)\Delta n = \frac{\hbar}{2\pi}\sum_{\omega_n} f(\omega_n)\Delta\omega_n \overset{T\to 0}{\to} \frac{\hbar}{2\pi}\int d\omega$.

$$\sigma^H_{\alpha\beta} = -\frac{e^2}{\hbar}\frac{\epsilon_{\rho\eta\zeta}}{48\pi^3}\mathrm{Im}i\int d\boldsymbol{k}\int_{-\infty}^{\infty} di\omega \mathrm{Tr}\Big(\partial_\rho G^{-1}(i\omega,\boldsymbol{k})G(i\omega,\boldsymbol{k})\partial_\eta G^{-1}(i\omega,\boldsymbol{k})G(i\omega,\boldsymbol{k})\partial_\zeta G^{-1}(i\omega,\boldsymbol{k})G(i\omega,\boldsymbol{k})\Big)$$
$$= -\frac{e^2}{h}\frac{\epsilon_{\rho\eta\zeta}}{24\pi^2}\mathrm{Re}\int d\boldsymbol{k}\int_{-\infty}^{\infty} di\omega \mathrm{Tr}\Big(\partial_\rho G^{-1}(i\omega,\boldsymbol{k})G(i\omega,\boldsymbol{k})\partial_\eta G^{-1}(i\omega,\boldsymbol{k})G(i\omega,\boldsymbol{k})\partial_\zeta G^{-1}(i\omega,\boldsymbol{k})G(i\omega,\boldsymbol{k})\Big). \tag{5.49}$$

Note that the expression is only well defined when G and G^{-1} are not singular, that means their determinant is non-zero. Also note, that the chemical potential for fixed filling goes to its zero temperature limit $\mu(T\to 0)$. Doing this limit is crucial in an insulator, where naively the chemical potential could be placed anywhere inside the gap. Later, we will show that the real part is unnecessary, because the integral is real. Making use of the short form notation $k = (i\omega, \boldsymbol{k})$ the Hall conductivity at zero temperature can be written as

$$\sigma^H_{\alpha\beta}(T=0) = -\frac{e^2}{h}\frac{\epsilon_{\rho\eta\zeta}}{24\pi^2}\int dk \mathrm{Tr}\Big(\partial_\rho G^{-1}(k)G(k)\partial_\eta G^{-1}(k)G(k)\partial_\zeta G^{-1}(k)G(k)\Big). \tag{5.50}$$

This expression coincides with the one derived in Ref. [107] and it corresponds to the Adler-Bell-Jackiw anomaly of the coefficient of the current correlator [230]. For the spin Hall conductivity for the case where S^z is conserved i.e. for the case σ is a good quantum number one has to take the difference between between spin up and spin down. At finite temperature one obtains

$$\sigma^{SH}_{\alpha\beta}(T) = \frac{e^2}{\hbar^2}\frac{T\epsilon_{\rho\eta\zeta}}{24\pi^2}\mathrm{Im}\int d\boldsymbol{k}\sum_{\omega_n\sigma}\mathrm{sign}(\sigma)\mathrm{Tr}\Big(\partial_\rho G^{-1}_\sigma(i\omega_n,\boldsymbol{k})G_\sigma(i\omega_n,\boldsymbol{k})\partial_\eta G^{-1}_\sigma(i\omega_n,\boldsymbol{k})$$
$$\times G_\sigma(i\omega_n,\boldsymbol{k})\partial_\zeta G^{-1}_\sigma(i\omega_n,\boldsymbol{k})G_\sigma(i\omega_n,\boldsymbol{k})\Big). \tag{5.51}$$

At zero temperature one obtains

$$\sigma^{SH}_{\alpha\beta}(T=0) = -\frac{e^2}{h}\frac{\epsilon_{\rho\eta\zeta}}{24\pi^2}\sum_\sigma\int dk\ \mathrm{sign}(\sigma)\mathrm{Tr}\Big(\partial_\rho G^{-1}_\sigma(k)G_\sigma(k)\partial_\eta G^{-1}_\sigma(k)G_\sigma(k)\partial_\zeta G^{-1}_\sigma(k)G_\sigma(k)\Big). \tag{5.52}$$

Note that all the above expression are in a gauge where the orbital positions in the unit cell are included in the Fourier transform (see Sec. 5.3.5).

5.3.2 Spin Hall conductivity in the non-interacting case

In this section we show that the expression for the Hall conductivity in the non-interacting case in an insulator at zero temperature reduces to the well know expression in terms of an Brillouin zone integral over the Berry curvature. The same must hold for the spin Hall conductivity when S^z is conserved. We start with the non-zero temperature expression for the Hall conductivity in Eq. 5.46, which we repeat here for convenience

$$\sigma^H_{\alpha\beta} = -\frac{e^2}{\hbar^2}\frac{T}{2V}\mathrm{Im}\sum_{\omega_n\boldsymbol{k}}\mathrm{Tr}\Big(\frac{\partial G^{-1}(i\omega_n,\boldsymbol{k})}{\partial k_\alpha}G(i\omega_n,\boldsymbol{k})\frac{\partial G^{-1}(i\omega_n,\boldsymbol{k})}{\partial i\omega_n}G(i\omega_n,\boldsymbol{k})\frac{\partial G^{-1}(i\omega_n,\boldsymbol{k})}{\partial_{k_\beta}}G(i\omega_n,\boldsymbol{k})$$
$$-\frac{\partial G^{-1}(i\omega_n,\boldsymbol{k})}{\partial k_\beta}G(i\omega_n,\boldsymbol{k})\frac{\partial G^{-1}(i\omega_n,\boldsymbol{k})}{\partial i\omega_n}G(i\omega_n,\boldsymbol{k})\frac{\partial G^{-1}(i\omega_n,\boldsymbol{k})}{\partial k_\alpha}G(i\omega_n,\boldsymbol{k})\Big). \tag{5.53}$$

Later we will perform the zero temperature limit. Note that the Bloch Hamiltonian $\mathcal{H}(\boldsymbol{k})$ and hence the Green's function are expressed in a gauge where the orbital positions in the unit cell are included in the Fourier transform (see e.g. Eq. 5.16). For the derivatives of the inverse Green's functions one has

$$\frac{\partial (G_0)^{-1}(i\omega_n, \boldsymbol{k})}{\partial i\omega_n} = \hbar, \tag{5.54}$$

$$\frac{\partial (G_0)^{-1}(i\omega_n, \boldsymbol{k})}{\partial k_\alpha} = -\frac{\partial \mathcal{H}(\boldsymbol{k})}{\partial k_\alpha}. \tag{5.55}$$

Eq. 5.53 can be evaluated in the eigenbasis of the $\mathcal{H}(\boldsymbol{k})$ i.e. $|n\boldsymbol{k}\rangle$, where n is a band index. Here, the ket denotes a vector in the orbital basis. We have in that basis

$$(G_0)'_{n_1 n_2}(i\omega_n, \boldsymbol{k}) = \frac{1}{(i\hbar\omega_n - \epsilon_{n_1}(\boldsymbol{k}) + \mu)} \delta_{n_1 n_2}, \tag{5.56}$$

$$(\partial_{k_\alpha} \mathcal{H}(\boldsymbol{k}))'_{n_1 n_2} = \sum_{ab} \langle n_1 \boldsymbol{k}|a\boldsymbol{k}\rangle \left(\partial_{k_\alpha} \mathcal{H}_{ab}(\boldsymbol{k})\right) \langle b\boldsymbol{k}|n_2\boldsymbol{k}\rangle . \tag{5.57}$$

Here the prime indicates that we are in the eigenbasis of $\mathcal{H}(\boldsymbol{k})$. $\epsilon_n(\boldsymbol{k})$ are the band energies. Inserting the above expressions one obtains

$$\begin{aligned}\sigma^H_{\alpha\beta} = -\frac{e^2}{\hbar}\frac{T}{2V}\mathrm{Im}\sum_{\omega_n \boldsymbol{k}}\sum_{n_1 n_2}\Big(&(\partial_{k_\alpha}\mathcal{H}(\boldsymbol{k}))'_{n_1 n_2}\frac{1}{(i\hbar\omega_n - \epsilon_{n_2}(\boldsymbol{k}) + \mu)^2}\left(\partial_{k_\beta}\mathcal{H}(\boldsymbol{k})\right)'_{n_2 n_1}\frac{1}{(i\hbar\omega_n - \epsilon_{n_1}(\boldsymbol{k}) + \mu)} \\ &- \left(\partial_{k_\beta}\mathcal{H}(\boldsymbol{k})\right)'_{n_1 n_2}\frac{1}{(i\hbar\omega_n - \epsilon_{n_2}(\boldsymbol{k}) + \mu)^2}(\partial_{k_\alpha}\mathcal{H}(\boldsymbol{k}))'_{n_2 n_1}\frac{1}{(i\hbar\omega_n - \epsilon_{n_1}(\boldsymbol{k}) + \mu)}\Big).\end{aligned} \tag{5.58}$$

For the nominators we can make a partial fraction decomposition. The chemical potential μ can be included in the band energies. Terms with $\epsilon_{n_1}(\boldsymbol{k}) = \epsilon_{n_2}(\boldsymbol{k})$ give no contribution, because in that case the first and the second term cancel each other. For $\epsilon_{n_1} \neq \epsilon_{n_2}$ one has

$$\begin{aligned}
&T\sum_{\omega_m}\frac{1}{(i\hbar\omega_m - \epsilon_{n_2}(\boldsymbol{k}))^2}\frac{1}{i\hbar\omega_m - \epsilon_{n_1}(\boldsymbol{k})} \\
&= T\sum_{\omega_m}\frac{1}{(i\hbar\omega_m - \epsilon_{n_2}(\boldsymbol{k}))^2}\frac{e^{-i\omega_m 0^-}}{i\hbar\omega_m - \epsilon_{n_1}(\boldsymbol{k})} \\
&= T\sum_{\omega_m}\frac{1}{i\hbar\omega_m - \epsilon_{n_2}(\boldsymbol{k})}\left(\frac{e^{-i\omega_m 0^-}}{i\hbar\omega_m - \epsilon_{n_1}(\boldsymbol{k})} - \frac{e^{-i\omega_m 0^-}}{i\hbar\omega_m - \epsilon_{n_2}(\boldsymbol{k})}\right)\frac{1}{\epsilon_{n_1}(\boldsymbol{k}) - \epsilon_{n_2}(\boldsymbol{k})} \\
&= T\sum_{\omega_m}\left(\frac{e^{-i\omega_m 0^-}}{i\hbar\omega_m - \epsilon_{n_1}(\boldsymbol{k})} - \frac{e^{-i\omega_m 0^-}}{i\hbar\omega_m - \epsilon_{n_2}(\boldsymbol{k})}\right)\frac{1}{(\epsilon_{n_1}(\boldsymbol{k}) - \epsilon_{n_2}(\boldsymbol{k}))^2} - \frac{e^{-i\omega_m 0^-}}{(i\hbar\omega_m - \epsilon_{n_2}(\boldsymbol{k}))^2}\frac{1}{\epsilon_{n_1}(\boldsymbol{k}) - \epsilon_{n_2}(\boldsymbol{k})} \\
&= \frac{f_T(\epsilon_{n_1}(\boldsymbol{k})) - f_T(\epsilon_{n_2}(\boldsymbol{k}))}{(\epsilon_{n_1}(\boldsymbol{k}) - \epsilon_{n_2}(\boldsymbol{k}))^2} + T\sum_{\omega_m}\frac{1}{\epsilon_{n_1}(\boldsymbol{k}) - \epsilon_{n_2}(\boldsymbol{k})}\frac{\partial}{\partial\epsilon_{n_2}(\boldsymbol{k})}\frac{e^{-i\omega_m 0^-}}{(i\hbar\omega_m - \epsilon_{n_2}(\boldsymbol{k}))} \\
&= \frac{f_T(\epsilon_{n_1}(\boldsymbol{k})) - f_T(\epsilon_{n_2}(\boldsymbol{k}))}{(\epsilon_{n_1}(\boldsymbol{k}) - \epsilon_{n_2}(\boldsymbol{k}))^2} + \frac{1}{\epsilon_{n_1}(\boldsymbol{k}) - \epsilon_{n_2}(\boldsymbol{k})}\frac{\partial f_T(\epsilon_{n_2}(\boldsymbol{k}))}{\partial\epsilon_{n_2}(\boldsymbol{k})}.
\end{aligned} \tag{5.59}$$

where f_T is the Fermi-Dirac distribution

$$f_T(\epsilon) = \frac{1}{1 + \exp(\frac{\epsilon}{k_B T})}. \tag{5.60}$$

In the zero temperature limit the Fermi-Dirac distributions become a heavyside functions $\Theta(-\epsilon)$ and its derivative a delta distribution

$$\lim_{T\to 0}\left(\frac{f_T(\epsilon_{n_1}(\boldsymbol{k}))-f_T(\epsilon_{n_2}(\boldsymbol{k}))}{\left(\epsilon_{n_1}(\boldsymbol{k})-\epsilon_{n_2}(\boldsymbol{k})\right)^2}+\frac{1}{\epsilon_{n_1}(\boldsymbol{k})-\epsilon_{n_2}(\boldsymbol{k})}\frac{\partial f_T(\epsilon_{n_2}(\boldsymbol{k}))}{\partial\epsilon_{n_2}(\boldsymbol{k})}\right)$$
$$=\frac{\Theta(-\epsilon_{n_1}(\boldsymbol{k}))-\Theta(-\epsilon_{n_2}(\boldsymbol{k}))}{\left(\epsilon_{n_1}(\boldsymbol{k})-\epsilon_{n_2}(\boldsymbol{k})\right)^2}-\frac{\delta(\epsilon_{n_2}(\boldsymbol{k}))}{\epsilon_{n_1}(\boldsymbol{k})-\epsilon_{n_2}(\boldsymbol{k})}. \tag{5.61}$$

The second term gives no contribution to the Hall conductivity in an insulator, because there are no single-particle states at zero energy. The expression for the Hall conductivity becomes

$$\sigma^H_{\alpha\beta}=-\frac{e^2}{\hbar}\frac{1}{2V}\mathrm{Im}\sum_{\boldsymbol{k}}\sum_{n_1n_2}\left(\frac{\left(\partial_{k_\alpha}\mathcal{H}(\boldsymbol{k})\right)'_{n_1n_2}\left(\partial_{k_\beta}\mathcal{H}(\boldsymbol{k})\right)'_{n_2n_1}}{\left(\epsilon_{n_1}(\boldsymbol{k})-\epsilon_{n_2}(\boldsymbol{k})\right)^2}-\frac{\left(\partial_{k_\alpha}\mathcal{H}(\boldsymbol{k})\right)'_{n_2n_1}\left(\partial_{k_\beta}\mathcal{H}(\boldsymbol{k})\right)'_{n_1n_2}}{\left(\epsilon_{n_2}(\boldsymbol{k})-\epsilon_{n_1}(\boldsymbol{k})\right)^2}\right)$$
$$\times\left(\Theta(-\epsilon_{n_1}(\boldsymbol{k}))-\Theta(-\epsilon_{n_2}(\boldsymbol{k}))\right). \tag{5.62}$$

The first bracket is antisymmetric under the exchange of summation indices n_1 and n_2. Hence we can write

$$\sigma^H_{\alpha\beta}=-\frac{e^2}{\hbar}\frac{1}{V}\mathrm{Im}\sum_{\boldsymbol{k}n_1n_2}\left(\frac{\left(\partial_{k_\alpha}\mathcal{H}(\boldsymbol{k})\right)'_{n_1n_2}\left(\partial_{k_\beta}\mathcal{H}(\boldsymbol{k})\right)'_{n_2n_1}}{\left(\epsilon_{n_1}(\boldsymbol{k})-\epsilon_{n_2}(\boldsymbol{k})\right)^2}-\frac{\left(\partial_{k_\alpha}\mathcal{H}(\boldsymbol{k})\right)'_{n_2n_1}\left(\partial_{k_\beta}\mathcal{H}(\boldsymbol{k})\right)'_{n_1n_2}}{\left(\epsilon_{n_2}(\boldsymbol{k})-\epsilon_{n_1}(\boldsymbol{k})\right)^2}\right)\Theta(-\epsilon_{n_1}(\boldsymbol{k})). \tag{5.63}$$

Using that the $\left(\partial_{k_\alpha}\mathcal{H}(\boldsymbol{k})\right)'_{n_1n_2}$ are hermitian we can write

$$\sigma^H_{\alpha\beta}=-\frac{e^2}{\hbar}\frac{1}{V}\sum_{\boldsymbol{k}}\sum_{n_1n_2}\left(\frac{2\mathrm{Im}\left(\partial_{k_\alpha}\mathcal{H}(\boldsymbol{k})\right)'_{n_1n_2}\left(\partial_{k_\beta}\mathcal{H}(\boldsymbol{k})\right)'_{n_2n_1}}{\left(\epsilon_{n_1}(\boldsymbol{k})-\epsilon_{n_2}(\boldsymbol{k})\right)^2}\right)\Theta(-\epsilon_{n_1}(\boldsymbol{k})). \tag{5.64}$$

In the continuum limit one obtains

$$\sigma^H_{\alpha\beta}=-\frac{e^2}{2\pi h}\int d\boldsymbol{k}\sum_{n_1n_2}\left(\frac{2\mathrm{Im}\left(\partial_{k_\alpha}\mathcal{H}(\boldsymbol{k})\right)'_{n_1n_2}\left(\partial_{k_\beta}\mathcal{H}(\boldsymbol{k})\right)'_{n_2n_1}}{\left(\epsilon_{n_1}(\boldsymbol{k})-\epsilon_{n_2}(\boldsymbol{k})\right)^2}\right)\Theta(-\epsilon_{n_1}(\boldsymbol{k})). \tag{5.65}$$

We now make it more explicit that this expression is an integral over the Berry curvature. To avoid subtleties about the parameterization of the bands when there is a crossing we assume isolated bands for simplicity here. For the more general case with band crossings see Ref. [231]. Terms with $n_1=n_2$ give a zero contribution as discussed above. For $n_1\neq n_2$ we have

$$\epsilon_{n_1}(\boldsymbol{k})\langle n_2\boldsymbol{k}|\partial_{k_\alpha}|n_1\boldsymbol{k}\rangle=\langle n_2\boldsymbol{k}|(\partial_{k_\alpha}\mathcal{H}(\boldsymbol{k})|n_1\boldsymbol{k}\rangle)=\langle n_2\boldsymbol{k}|(\partial_{k_\alpha}\mathcal{H}(\boldsymbol{k}))|n_1\boldsymbol{k}\rangle+\langle n_2\boldsymbol{k}|\epsilon_{n_2}(\boldsymbol{k})\partial_{k_\alpha}|n_1\boldsymbol{k}\rangle\,, \tag{5.66}$$

where we used $\langle n_1\boldsymbol{k}|(\partial_{k_\alpha}\epsilon_{n_2}(\boldsymbol{k}))|n_2\boldsymbol{k}\rangle=0$. So we get

$$\langle n_2\boldsymbol{k}|\partial_{k_\alpha}n_1\boldsymbol{k}\rangle=\frac{(\partial_{k_\alpha}\mathcal{H}(\boldsymbol{k}))_{n_2n_1}}{\epsilon_{n_1}(\boldsymbol{k})-\epsilon_{n_2}(\boldsymbol{k})}. \tag{5.67}$$

Complex conjugating gives

$$\langle\partial_{k_\alpha}n_1\boldsymbol{k}|n_2\boldsymbol{k}\rangle=\frac{(\partial_{k_\alpha}\mathcal{H}(\boldsymbol{k}))_{n_1n_2}}{\epsilon_{n_1}(\boldsymbol{k})-\epsilon_{n_2}(\boldsymbol{k})}. \tag{5.68}$$

So that we have

$$\sigma^H_{\alpha\beta} = \frac{e^2}{2\pi h} \sum_{n_1 n_2} \int d\boldsymbol{k} 2\mathrm{Im}\left(\langle \partial_{k_\alpha} n_1 \boldsymbol{k} | n_2 \boldsymbol{k}\rangle \langle n_2 \boldsymbol{k} | \partial_{k_\beta} n_1 \boldsymbol{k}\rangle\right) \Theta(-\epsilon_{n_1}(\boldsymbol{k})). \tag{5.69}$$

Since the sum over n_2 is the identity at that k-point we can write

$$\sigma^H_{\alpha\beta} = \frac{e^2}{2\pi h} \sum_{n_1 \mathrm{occ}} \int d\boldsymbol{k} 2\mathrm{Im}\left(\langle \partial_{k_\alpha} n_1 \boldsymbol{k} | \partial_{k_\beta} n_1 \boldsymbol{k}\rangle\right), \tag{5.70}$$

where we can identify the Berry curvature of band n_1

$$\Omega_{n_1,\alpha\beta}(\boldsymbol{k}) = 2\mathrm{Im}\left(\langle \partial_{k_\alpha} n_1 \boldsymbol{k} | \partial_{k_\beta} n_1 \boldsymbol{k}\rangle\right). \tag{5.71}$$

So the Hall conductivity can be written as a Brillouin zone integral over the Berry curvature over all occupied bands. According to the Chern theorem [232] the integral over the Berry curvature over a closed manifold (the Brillouin zone is a torus) must be equal to 2π times an integer, i.e.

$$\int d\boldsymbol{k} \Omega_{\alpha\beta}(\boldsymbol{k}) = 2\pi n, \quad n \in \mathbb{Z}, \tag{5.72}$$

Here, n is the Chern index. For a simplified proof of the Chern theorem see Ref. [231]. At zero temperature the Dirac distribution becomes a step function so that the Hall conductivity is quantized

$$\sigma^H_{\alpha\beta} = \frac{e^2}{h} n, \quad n \in \mathbb{Z}. \tag{5.73}$$

For a time reversal invariant system where the z-direction of the spins is conserved the Hall conductivities for spin up and spin down have opposite signs. Hence, the spin Hall conductivity in such a noninteracting system is quantized to

$$\sigma^{SH}_{\alpha\beta} = 2\frac{e^2}{h} n, \quad n \in \mathbb{Z}. \tag{5.74}$$

5.3.3 The spin Hall conductivity at zero temperature as a topological invariant

In this section we will show that the interacting expression at zero temperature for the Hall conductivity in Eq. 5.50 and consequently for the spin Hall conductivity in Eq. 5.52 can be regarded as a topological invariant expressed in terms of the Matsubara Green's function. To do so, we introduce a parameter γ that parameterizes a continuous deformation of the Matsubara Green's function $G \to G_\gamma$. During this deformation G and G^{-1} remain nonsingular (no poles and no zeros) and differentiable so that the expression for the Hall conductivity stays well defined. The physical picture behind this deformation is to continuously changes the parameters of the Hamiltonian without the system undergoing a phase transition. To show that the Hall conductivity is a topological invariant we then need to show that

$$\partial_\gamma \sigma^H(T = 0, \gamma) = 0. \tag{5.75}$$

Proof. Previously we found the following expression for the Hall conductivity at zero temperature

$$\sigma^H_{\alpha\beta}(T = 0) = -\frac{e^2}{h} \frac{\epsilon_{\rho\eta\zeta}}{24\pi^2} \int dk \mathrm{Tr}\Big(\partial_\rho G^{-1}(k) G(k) \partial_\eta G^{-1}(k) G(k) \partial_\zeta G^{-1}(k) G(k)\Big), \tag{5.76}$$

where $\rho\eta\zeta$ are summed over and stand for $i\omega_n, k_\alpha, k_\beta$. Letting G depend on a parameter i.e. $G \to G_\gamma$ the partial derivative with respect of this parameter can be pulled inside the integral. The expression under the integral becomes, not writing the argument of the Green's function

$$
\begin{aligned}
&\partial_\gamma \epsilon_{\rho\eta\zeta} \mathrm{Tr}\Big(\partial_\rho G_\gamma^{-1} G_\gamma \partial_\eta G_\gamma^{-1} G_\gamma \partial_\zeta G_\gamma^{-1} G_\gamma\Big) \\
&= 3\epsilon_{\rho\eta\zeta} \mathrm{Tr}\Big(\partial_\gamma \partial_\rho G_\gamma^{-1} G_\gamma \partial_\eta G_\gamma^{-1} G_\gamma \partial_\zeta G_\gamma^{-1} G_\gamma\Big) + 3\epsilon_{\rho\eta\zeta} \mathrm{Tr}\Big(\partial_\rho G_\gamma^{-1} \partial_\gamma G_\gamma \partial_\eta G_\gamma^{-1} G_\gamma \partial_\zeta G_\gamma^{-1} G_\gamma\Big) \\
&= 3\epsilon_{\rho\eta\zeta} \mathrm{Tr}\Big(\partial_\gamma \partial_\rho G_\gamma^{-1} G_\gamma \partial_\eta G_\gamma^{-1} G_\gamma \partial_\zeta G_\gamma^{-1} G_\gamma\Big) - 3\epsilon_{\rho\eta\zeta} \mathrm{Tr}\Big(\partial_\rho G_\gamma^{-1} G_\gamma \partial_\gamma G_\gamma^{-1} G_\gamma \partial_\eta G_\gamma^{-1} G_\gamma \partial_\zeta G_\gamma^{-1} G_\gamma\Big) \\
&= 3\epsilon_{\rho\eta\zeta} \mathrm{Tr}\Big(G_\gamma \partial_\gamma \partial_\rho G_\gamma^{-1} G_\gamma \partial_\eta G_\gamma^{-1} G_\gamma \partial_\zeta G_\gamma^{-1}\Big) + 3\epsilon_{\rho\eta\zeta} \mathrm{Tr}\Big(\partial_\rho G_\gamma \partial_\gamma G_\gamma^{-1} G_\gamma \partial_\eta G_\gamma^{-1} G_\gamma \partial_\zeta G_\gamma^{-1}\Big) \\
&= 3\partial_\rho \epsilon_{\rho\eta\zeta} \mathrm{Tr}\Big(G_\gamma \partial_\gamma G_\gamma^{-1} G_\gamma \partial_\eta G_\gamma^{-1} G_\gamma \partial_\zeta G_\gamma^{-1}\Big) - 3\epsilon_{\rho\eta\zeta} \mathrm{Tr}\Big(G_\gamma \partial_\gamma G_\gamma^{-1} \partial_\rho \left(G_\gamma \partial_\eta G_\gamma^{-1} G_\gamma \partial_\zeta G_\gamma^{-1}\right)\Big). \qquad (5.77)
\end{aligned}
$$

where made use of the cyclic property of the trace going from line 3 to 4 and for partial derivatives we used the identity

$$\partial_\xi G_\gamma = -G_\gamma \partial_\xi G_\gamma^{-1} G_\gamma, \qquad (5.78)$$

when going from line two to three and in going from line three to four for ∂_ρ. Going from line four to five we use the product rule backwards. The integral over the first term in the last row of Eq. 5.77 vanishes, because the integral over a total derivative over frequency momentum space vanishes. In the second term the terms with $\partial_\rho \partial_\eta G_\gamma^{-1}$ and $\partial_\rho \partial_\zeta G_\gamma^{-1}$ vanish because of $\epsilon_{\rho\eta\zeta}$ and the theorem of Schwarz. One is left with the terms

$$
\begin{aligned}
&- 3\epsilon_{\rho\eta\zeta} \mathrm{Tr}\Big(G_\gamma \partial_\gamma G_\gamma^{-1} \left(\partial_\rho G_\gamma \partial_\eta G_\gamma^{-1} G_\gamma \partial_\zeta G_\gamma^{-1}\right)\Big) - 3\epsilon_{\rho\eta\zeta} \mathrm{Tr}\Big(G_\gamma \partial_\gamma G_\gamma^{-1} \left(G_\gamma \partial_\eta G_\gamma^{-1} \partial_\rho G_\gamma \partial_\zeta G_\gamma^{-1}\right)\Big) \\
&= +3\epsilon_{\rho\eta\zeta} \mathrm{Tr}\Big(G_\gamma \partial_\gamma G_\gamma^{-1} \left(G_\gamma \partial_\rho G_\gamma^{-1} G_\gamma \partial_\eta G_\gamma^{-1} G_\gamma \partial_\zeta G_\gamma^{-1}\right)\Big) \\
&\quad + 3\epsilon_{\rho\eta\zeta} \mathrm{Tr}\Big(G_\gamma \partial_\gamma G_\gamma^{-1} \left(G_\gamma \partial_\eta G_\gamma^{-1} G_\gamma \partial_\rho G_\gamma^{-1} G_\gamma \partial_\zeta G_\gamma^{-1}\right)\Big) \\
&= 0. \qquad (5.79)
\end{aligned}
$$

Taking everything together we have indeed shown that the frequency momentum integral over Eq. 5.77 vanishes. With that it follows

$$\partial_\gamma \sigma^H(T = 0, \gamma) = 0. \qquad (5.80)$$

Hence, the Hall conductivity at zero temperature is proportional to a topological invariant of the Green's function.

□

The same calculations holds for the spin Hall conductivity in the case of time reversal symmetry and conservation of S^z, because when S_z is conserved each Green's function just acquires a spin label that is summed over with the corresponding sign (see Eq. 5.52). During the deformation the symmetries need to be preserved.

It follows that even with interactions the Hall conductivity as well as the spin Hall conductivity are quantized as long as one can adiabatically connect to the noninteracting system i.e. continuously changing the parameters of the Hamiltonian without the system undergoing a phase transition. In case of the spin Hall conductivity additionally time reversal symmetry and conservation of S^z need to be conserved during the adiabatic evolution. During this process the Green's function is deformed continuously and as shown above the topological invariant cannot change. Since we have shown that in the noninteracting case the Hall and the spin Hall conductivities are quantized (see Sec. 5.3.2) it follows they remain quantized during an adiabatic evolution.

Note that at zero temperature there is a simplified way of calculating the above topological invariant via the so called topological Hamiltonian [233] which is defined as

$$\mathrm{T}(\boldsymbol{k}) = -G^{-1}(0, \boldsymbol{k}). \qquad (5.81)$$

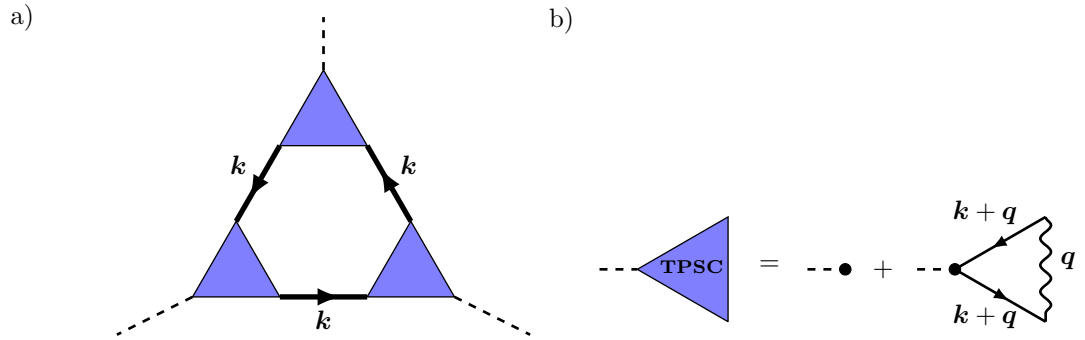

Figure 5.4: a) Graphical representation of the expression for the spin Hall conductivity. The thick lines represent the interacting Green's function, which in TPSC is $G^{(2)}$ given in Eq. 5.87. The triangles with attached dashed lines represent the renormalized vertices $\partial_\mu G^{-1}(k)$ with μ standing for either $i\omega_n$, k_x or k_y. b) TPSC expression for the renormalized vertex. The thin lines here represent the (here noninteracting) Green's function $G^{(1)}$. A dot with attached dashed line represents a bare vertex $\partial_\mu G^{(1)-1}(k)$. The wiggled line represents either a spin, a charge or a mixed spin-charge excitation.

$\mathrm{T}(\boldsymbol{k})$ is an effective non-interacting Hamiltonian whose Chern index of the corresponding eigenstates can be calculated via its Berry curvature. The reason is the following. Above we showed that the invariant stays unchanged under continuous changes of G as long as there is no phase transition where the invariant changes via a zero or a pole of the Green's function. Defining $G_{\mathrm{T}}(i\omega, \boldsymbol{k}) = (i\omega - \mathcal{H}_{\mathrm{T}}(\boldsymbol{k}))^{-1}$, one can do the deformation $G_\gamma = (1-\gamma)G + \gamma G_{\mathrm{T}}$ with $\gamma \in [0,1]$ during which, as shown in Ref. [233], G_γ has neither poles nor zeros. Hence the topological invariant stays unchanged during the deformation and the (spin) Hall conductivity can just be calculated from $\mathcal{H}_{\mathrm{T}}(\boldsymbol{k})$.

5.3.4 Vertex corrections to the spin Hall conductivity in TPSC

The vertex corrections to the electrical conductivity in TPSC correspond to the analogues of the Maki-Thompson and Aslamasov–Larkin contributions [36]. However, for the (spin) Hall conductivity the Aslamasov–Larkin contributions cancel, because of the antisymmetrization in $x \leftrightarrow y$. A graphical representation of the expression to calculate σ_{xy}^{SH} is shown in Fig. 5.4. Vertex correction to the SHC in TPSC arise from the excitation and reabsorption of spin, charge or mixed spin-charge excitations.

5.3.5 Evaluating the spin Hall conductivity expression with TPSC

In this section we explain how to calculate the SHC in TPSC with and without vertex corrections. We especially focus on the case of the Kane-Mele-Hubbard model. Since in our implementation we work in reduced units where $\hbar = k_{\mathrm{B}} = 1$ it is easiest to work with the spin Hall conductivity expression in the following form

$$\sigma_{xy}^{\mathrm{SH}} = \frac{e^2}{h}\frac{\pi T}{N V_{ez}}\mathrm{Im}\sum_{\omega_n \boldsymbol{k}\sigma}\mathrm{sign}(\sigma)\mathrm{Tr}\Big(\frac{\partial \tilde{G}_\sigma^{-1}(i\omega_n,\boldsymbol{k})}{\partial i\omega_n}\tilde{G}_\sigma(i\omega_n,\boldsymbol{k})\frac{\partial \tilde{G}_\sigma^{-1}(i\omega_n,\boldsymbol{k})}{\partial k_x}\tilde{G}_\sigma(i\omega_n,\boldsymbol{k})\frac{\partial \tilde{G}_\sigma^{-1}(i\omega_n,\boldsymbol{k})}{\partial k_y}\tilde{G}_\sigma(i\omega_n,\boldsymbol{k})$$
$$- \frac{\partial \tilde{G}_\sigma^{-1}(i\omega_n,\boldsymbol{k})}{\partial i\omega_n}\tilde{G}_\sigma(i\omega_n,\boldsymbol{k})\frac{\partial \tilde{G}_\sigma^{-1}(i\omega_n,\boldsymbol{k})}{\partial k_y}\tilde{G}_\sigma(i\omega_n,\boldsymbol{k})\frac{\partial \tilde{G}_\sigma^{-1}(i\omega_n,\boldsymbol{k})}{\partial k_x}\tilde{G}_\sigma(i\omega_n,\boldsymbol{k})\Big). \tag{5.82}$$

This expression was adapted from Eq. 5.46. One factor of $\frac{1}{\hbar}$ was absorbed in the frequency derivative, when switching to reduced units. $V = V_{ez}N$, where V_{ez} is the volume of the unit cell and N is the number of k-points. In the Kane-Mele model $V_{\mathrm{ez}}^{\mathrm{KM}} = \frac{\sqrt{3}}{2}a^2$, where a is the lattice constant that is set to $a = 1$. To evaluate this equation with TPSC we replace every $\tilde{G}$ by $\tilde{G}^{(2)}$. We changed $G \to \tilde{G}$ in this section to emphasize that we work in a gauge where the orbital positions in the unit cell are included in

the Fourier transforms (see Sec. 5.16). In the TPSC calculations are done in the gauge without a tilde, where all quantities are periodic in k-space. The gauge change can be performed by

$$\tilde{G}^{(2)}(k) = U^{\dagger}(\boldsymbol{k}) G^{(2)}(k) U(\boldsymbol{k}). \tag{5.83}$$

$U(\boldsymbol{k})$ is a k-dependent matrix that in the Kane-Mele model is given by

$$U(\boldsymbol{k}) = \begin{pmatrix} 1 & 0 & 0 & 0 \\ 0 & 1 & 0 & 0 \\ 0 & 0 & \phi(\boldsymbol{k}) & 0 \\ 0 & 0 & 0 & \phi(\boldsymbol{k}) \end{pmatrix}, \tag{5.84}$$

with $\phi(\boldsymbol{k})$ is given by

$$\phi(\boldsymbol{k}) = \exp(i\boldsymbol{k}\cdot\boldsymbol{r}_2) = \exp(i2\pi(\frac{1}{3}k_1 + \frac{1}{3}k_2)). \tag{5.85}$$

The derivatives act as

$$\partial_{k_\alpha}\tilde{G}^{(2)}(k) = U^{\dagger}(\boldsymbol{k})\left(\partial_{k_\alpha}G^{(2)}(k)\right)U(\boldsymbol{k}) + \left(\partial_{k_\alpha}U^{\dagger}(\boldsymbol{k})\right)G^{(2)}(k)U(\boldsymbol{k}) + U^{\dagger}(\boldsymbol{k})G^{(2)}(k)\left(\partial_{k_\alpha}U(\boldsymbol{k})\right). \tag{5.86}$$

$G^{(2)}$ is given by the Dyson equation

$$G^{(2)}_{\sigma}(i\omega_n, \boldsymbol{k}) = \left(i\omega_n - \mathcal{H}_{\sigma}(\boldsymbol{k}) + \mu - \Sigma^{(2)}_{\sigma}(i\omega_n, \boldsymbol{k})\right)^{-1}. \tag{5.87}$$

The TPSC self-energy $\Sigma^{(2)}$ in the Kane-Mele-Hubbard model where S^z is conserved simplifies to

$$\Sigma^{(2)ab}_{\sigma}(k) = U\delta_{ab}\langle n_{a-\sigma}\rangle + \frac{U}{8}\frac{T}{N}\sum_q G^{(1)ab}_{\sigma}(k+q)V^{ab}_{l\sigma}(q) + \frac{U}{8}\frac{T}{N}\sum_q G^{(1)ab}_{-\sigma}(k+q)V^{ab}_{t\sigma}(q) \tag{5.88}$$

with $k = ((i\omega_n, \boldsymbol{k})$, $q = (iq_m, \boldsymbol{k})$ and

$$V^{ab}_{l\sigma}(q) = \Gamma^{b}_{cc}\chi^{ba}_{cc}(q) + \Gamma^{b}_{zz}\chi^{ba}_{zz}(q) - \sigma\frac{1}{2}\left(\Gamma^{b}_{zz}\chi^{ba}_{zc}(q) + \Gamma^{b}_{ch}\chi^{ba}_{cz}(q) + \chi^{ba}_{zc}(q)\Gamma^{a}_{ch} + \chi^{ba}_{cz}(q)\Gamma^{a}_{zz}\right), \tag{5.89}$$

$$V^{ab}_{t\sigma}(q) = \Gamma^{b}_{xx}\chi^{ba}_{xx}(q) + \Gamma^{b}_{yy}\chi^{ba}_{yy}(q). \tag{5.90}$$

The derivatives of the Green's function can be evaluated from the corresponding TPSC expressions

$$\begin{aligned} \partial_{i\omega_n}G^{(2)-1}_{\sigma}(k) &= 1 - \partial_{i\omega_n}\Sigma^{(2)}(k), \\ \partial_{k_\alpha}G^{(2)-1}_{\sigma}(k) &= -\partial_{k_\alpha}\mathcal{H}(\boldsymbol{k}) - \partial_{k_\alpha}\Sigma^{(2)}(k). \end{aligned} \tag{5.91}$$

Note that in the approximation of the conductivity bubble one only takes into account the frequency derivative of the self-energy, but not the momentum derivatives of the self-energy. From TPSC self-energy expression in Eq. 5.88 we notice that derivatives of the argument of the self-energy act only on $G^{(1)}$. We have

$$\begin{aligned} \partial_{k_\alpha}\Sigma^{(2)ab}_{\sigma}(k) &= \frac{1}{2}\frac{T}{N}\sum_q\left(\partial_{k_\alpha}G^{(1)ab}_{\sigma}(k+q)V^{lab}_{\sigma}(q) + \partial_{k_\alpha}G^{(1)ab}_{-\sigma}(k+q)V^{tab}_{\sigma}(q)\right). \\ &= \frac{1}{2}\frac{T}{N}\sum_q\Big(G^{(1)a\bar{c}}_{\sigma}(k+q)\partial_{k_\alpha}\mathcal{H}^{\bar{c}\bar{d}}_{\sigma}(\boldsymbol{k}+\boldsymbol{q})G^{(1)\bar{d}b}_{\sigma}(k+q)V^{lab}_{\sigma}(q) \\ &\quad + G^{(1)a\bar{c}}_{-\sigma}(k+q)\partial_{k_\alpha}\mathcal{H}^{\bar{c}\bar{d}}_{-\sigma}(\boldsymbol{k}+\boldsymbol{q})G^{(1)\bar{d}b}_{-\sigma}(k+q)V^{tab}_{\sigma}(q)\Big) \end{aligned} \tag{5.92}$$

and similarly

$$\partial_{i\omega_n}\Sigma_\sigma^{(2)ab}(k) = -\frac{1}{2}\frac{T}{N}\sum_q \left(G_\sigma^{(1)a\bar{c}}(k+q)G_\sigma^{(1)\bar{c}b}(k+q)V_\sigma^{lab}(q) + G_{-\sigma}^{(1)a\bar{c}}(k+q)G_{-\sigma}^{(1)\bar{c}b}(k+q)V_\sigma^{tab}(q)\right). \tag{5.93}$$

The bare vertices can be evaluated analytically and are given by

$$\partial_{k_\alpha}\mathcal{H}(\boldsymbol{k}) = \begin{pmatrix} \partial_{k_\alpha}\gamma(\boldsymbol{k}) & 0 & \partial_{k_\alpha}h(\boldsymbol{k}) & 0 \\ 0 & -\partial_{k_\alpha}\gamma(\boldsymbol{k}) & 0 & \partial_{k_\alpha}h(\boldsymbol{k}) \\ \partial_{k_\alpha}h^*(\boldsymbol{k}) & 0 & -\partial_{k_\alpha}\gamma(\boldsymbol{k}) & 0 \\ 0 & \partial_{k_\alpha}h^*(\boldsymbol{k}) & 0 & \partial_{k_\alpha}\gamma(\boldsymbol{k}) \end{pmatrix} \tag{5.94}$$

where

$$\partial_{k_\alpha}h(\boldsymbol{k}) = -t\left(ia_{1\alpha}\exp(i\boldsymbol{k}\cdot\boldsymbol{a}_1) + ia_{2\alpha}\exp(i\boldsymbol{k}\cdot\boldsymbol{a}_2)\right), \tag{5.95}$$

$$\partial_{k_\alpha}\gamma(\boldsymbol{k}) = 2\lambda\left(a_{1\alpha}\cos(\boldsymbol{k}\cdot\boldsymbol{a}_1) - a_{2\alpha}\cos(\boldsymbol{k}\cdot\boldsymbol{a}_2) + (-a_{1\alpha}+a_{2\alpha})\cos(\boldsymbol{k}\cdot(-\boldsymbol{a}_1+\boldsymbol{a}_2))\right). \tag{5.96}$$

The derivative of the gauge matrix is given by

$$\partial_{k_\alpha}U(\boldsymbol{k}) = \begin{pmatrix} 0 & 0 & 0 & 0 \\ 0 & 0 & 0 & 0 \\ 0 & 0 & \partial_{k_\alpha}\phi(\boldsymbol{k}) & 0 \\ 0 & 0 & 0 & \partial_{k_\alpha}\phi(\boldsymbol{k}) \end{pmatrix}, \tag{5.97}$$

where

$$\partial_{k_\alpha}\phi(\boldsymbol{k}) = ir_{2\alpha}\exp(i\boldsymbol{k}\cdot\boldsymbol{r}_2). \tag{5.98}$$

In the implementation we take advantage of fast Fourier transformations and the sparse-ir library [187–189].

5.4 TPSC results for the Kane-Mele-Hubbard model

In the following we present results for the antiferromagnetic spin correlation length, the SHC with and without vertex corrections and the band gap renormalization for the Kane-Mele-Hubbard model. We consider different values for the Hubbard interaction, spin-orbit coupling strength and temperature. We also compute a phase diagram as a function of spin-orbit coupling and Hubbard interaction from the antiferromagnetic spin correlation length for transversal (spin direction in the x-y plane) spin fluctuations. All results are obtained for half-filling. The calculations are performed on a 300×300 k-point grid.

5.4.1 Correlation lengths

The correlation length is a measure for the distance in real space on which spins are correlated. Generally the correlation between spins is expected to drop of exponentially with the distance between the spins. Approaching a phase transition the spin correlation length diverges.

In the Kane-Mele Hubbard model with increasing U antiferromagnetic spin fluctuations are larger than the ferromagnetic fluctuations or charge fluctuations (see Sec. 4.14.5 and 4.14.6). Hence, we focus on the antiferromagnetic spin susceptibilities which are defined as

$$\chi_{\alpha\alpha}^{\mathrm{afm}}(q) = \chi_{\alpha\alpha}^{11}(q) - \chi_{\alpha\alpha}^{12}(q) - \chi_{\alpha\alpha}^{21}(q) + \chi_{\alpha\alpha}^{22}(q), \tag{5.99}$$

where $\alpha = x, y, z$ labels the components of the spin. Exponential decay in real space corresponds to a Lorenzian in momentum space. Hence, we calculate the antiferromagnetic spin correlation length by

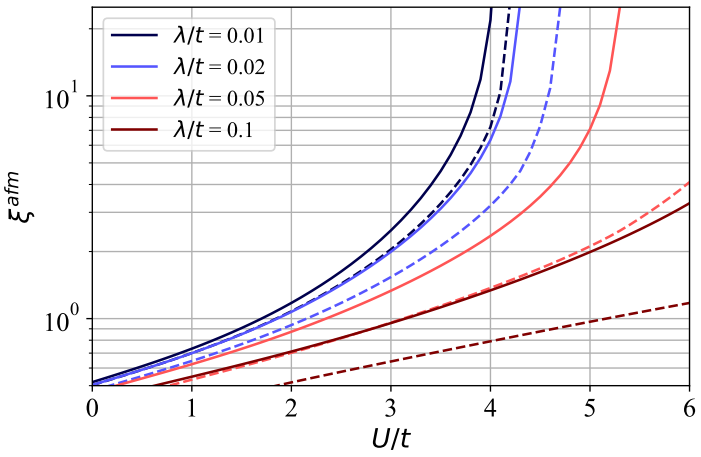

Figure 5.5: Antiferromagnetic spin correlation length $\xi_\alpha^{\mathrm{afm}}$ as a function of U/t for spins aligned in the x-y plane (solid lines) and in the z-direction (dashed lines) at $T/t = 0.001$ and various values of SOC λ/t.

$$\xi_\alpha^{\mathrm{afm}} = \frac{1}{|\boldsymbol{q}_\alpha^{HM}|}, \tag{5.100}$$

where $\boldsymbol{q}_\alpha^{HM}$ is determined from the condition

$$\chi_{\alpha\alpha}^{\mathrm{afm}}(0, \boldsymbol{q}_{\max} + \boldsymbol{q}_\alpha^{HM}) = \chi_{\alpha\alpha}^{\mathrm{afm}}(0, \boldsymbol{q}_{\max})/2. \tag{5.101}$$

Here, $\boldsymbol{q}_{\max}$ is the momentum at which $\chi_{\alpha\alpha}$ is largest. For the antiferromagnetic spin fluctuations in the Kane-Mele Hubbard model it holds $\boldsymbol{q}_{\max} = (0, 0)$. Note that $\xi_x^{\mathrm{afm}} = \xi_y^{\mathrm{afm}}$ in the Kane-Mele-Hubbard model due to spin rotation symmetry around the z-axis.

The results for the spin correlation lengths are shown in Fig. 5.5. The transversal spin correlation lengths ξ_x^{afm} and ξ_y^{afm} diverge at lower U values than the longitudinal one ξ_z^{afm}. Hence, the system undergoes a transition to an X-Y antiferromagnet. The corresponding divergence of the spin susceptibility indicates that the transition is of second order in TPSC. We can also observe that increasing SOC shifts the transition to higher values of U by decreasing the spin fluctuations.

Further, we find that the spin correlation lengths in TPSC as a function of temperature saturate at temperatures lower than $T/t = 0.01$. This is the case except very close to the phase transition, as already observed in Ref. [163].

5.4.2 Phase diagram

In Fig. 5.6, we show the $U - \lambda$ phase diagram for the KMH model obtained by estimating the critical value $U_c(\lambda)$ of the phase transition for various λ values as the linear extrapolation of $1/\xi_x^{\mathrm{afm}}$ to 0 at the lowest temperature we considered $T/t = 0.001$. Since the correlation lengths saturate at low temperatures this is a reasonable approximation for the $T = 0$ case. The phase transition line shown in the phase diagram is obtained from a quadratic fit. We only show critical U values for up to $\lambda/t = 0.05$, because for $U/t > 5$ TPSC loses its validity (see Sec. 4.14.10). The phase diagram also shows the phase transition between the semimetal and the antiferromagnet at zero SOC, where there is no easy plane for the spins. The exact location of the phase transition line is not known to the best of our knowledge. Refs. [197, 198, 201, 203] calculate the $U - \lambda$ phase diagram from quantum Monte Carlo (QMC) simulations, but they show an intermediate spin liquid phase, that could not be found by large scale QMC simulations [11].

Without SOC we obtain $U_c(\lambda = 0)/t = 3.72$ which agrees well with the previous TPSC result $U_c/t = 3.79 \pm 0.01$ [163] obtained from the zero temperature extrapolation for the crossover to the renormalized

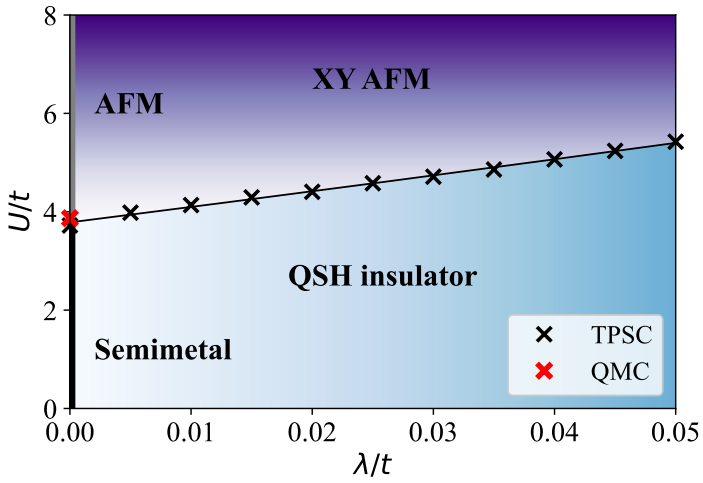

Figure 5.6: Phase diagram for the KMH model. Critical $U_c(\lambda)$ values (black crosses) are obtained from the linear extrapolation of the inverse antiferromagnetic correlation length $1/\xi_x^{afm}$ to 0 when U is increased at $T/t = 0.001$. The phase transition line is obtained from a quadratic fit. We also show the critical U_c (red cross) at zero spin-orbit coupling ($\lambda = 0$) for the transition between the semimetal and the antiferromagnet obtained by QMC in Ref. [11].

classical regime. Our result is also in reasonable good agreement with $U_c/t = 3.869 \pm 0.013$ [11] from Quantum Monte Carlo simulations.

5.4.3 Spin Hall conductivity

We calculate the spin Hall conductivity by evaluating the following expression valid in the presence of interactions and at finite temperature

$$\sigma^{\mathrm{SH}} = \frac{e^2}{h}\frac{\epsilon_{\mu\nu\rho}T}{12\pi}\mathrm{Im}\left(\sum_{\omega_n\sigma}\mathrm{sign}(\sigma)\int d\boldsymbol{k}\mathrm{Tr}\left(G_\sigma(k)\partial_\mu G_\sigma^{-1}(k)G_\sigma(k)\partial_\nu G_\sigma^{-1}(k)G_\sigma(k)\partial_\rho G_\sigma^{-1}(k)\right)\right), \quad (5.102)$$

where $\epsilon_{\mu\nu\rho}$ is the totally antisymmetric tensor. The μ, ν and ρ indices are summed over and stand for $i\omega_n, k_x, k_y$. The trace runs over the orbital indices. All matrices in the above equations are expressed in the gauge in momentum space which includes the site positions in the unit cell [228]. The expression is evaluated numerically as described in detail in Sec. 5.3.5. We note that the momentum-dependent vertex corrections show sharp point-like features at K and K' near (and beyond) the critical U_c which require a dense k-point grid to resolve. This procedure is similar to Ref. [234] where the finite temperature SHC is calculated from DMFT. In DMFT however there are no vertex corrections to the SHC, because the DMFT self-energy is constant in momentum space.

As explained in Sec. 5.3 the sum over Matsubara frequencies becomes an integral in the zero temperature limit. The resulting expression is a topological invariant expressed in terms of the Matsubara Green's function [107]. Hence, at zero temperature, σ^{SH} must always be an integer multiple of $2\frac{e^2}{h}$.

In Fig. 5.7 we show the results for the calculation of σ^{SH} with (solid lines) and without (dashed lines) momentum-dependent vertex corrections $\partial_{k_\alpha}\Sigma(k)$. The case without momentum-dependent vertex corrections corresponds to the so-called conductivity bubble. In the greyed out region TPSC is strictly not valid anymore, because the spin correlation length diverges and TPSC is not valid in the XY antiferromagnetic phase, since TPSC is a weak to intermediate coupling method. Nevertheless, we show this region because it is instructive to see what TPSC does in this region.

Let us first discuss the case without vertex corrections (dashed lines). At all temperatures considered, the spin Hall conductivity decreases smoothly as the Hubbard interaction increases towards the phase

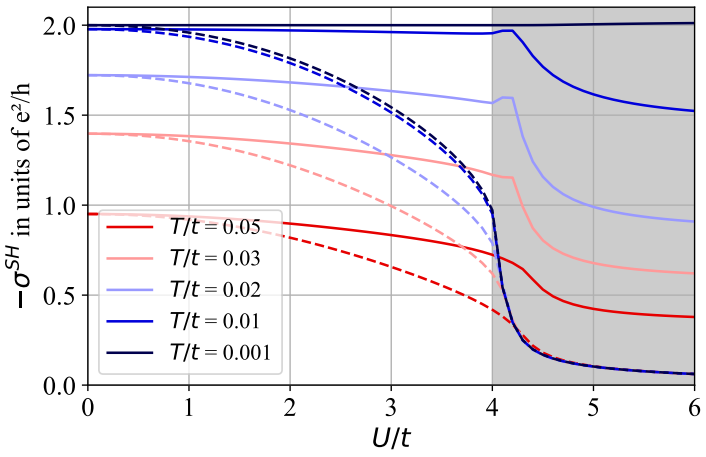

Figure 5.7: Spin Hall conductivity as a function of U/t calculated from Eq. 5.102 at $\lambda/t = 0.01$ and for different temperatures including momentum-dependent vertex corrections $\partial_{k_\alpha}\Sigma(k)$ (solid) and neglecting them (dashed). In the vicinity of the phase transition to the XY antiferromagnet at $U/t \approx 4$ the inclusion of vertex corrections almost doubles σ^{SH} at all temperatures. In the greyed out region TPSC is strictly not valid anymore, because the spin correlation length diverged and TPSC is only valid in the weak to intermediate coupling regime.

transition. At the phase transition, the drop in σ^{SH} becomes sharper. The drop is more pronounced at low temperatures. In the conductivity bubble, the main effect of the interactions is to broaden the interacting Green's function and make it smaller, since the self-energy enters in the denominator of the Green's function. This causes the phase transition to be visible in σ^{SH} with the conductivity bubble through a drop off, because there the self-energy constructed from the spin, charge and mixed spin-charge fluctuations becomes suddenly much larger. The main contributions, as we will see later, are the transversal, antiferromagnetic spin susceptibilities that diverge at the phase transition. Without vertex corrections, the quantized value of σ^{SH} is only reached in the limit where the Hubbard interaction goes to 0, where there are no vertex corrections and the conductivity bubble yields the exact result.

We now discuss the case with vertex corrections (solid lines). The spin Hall conductivity once again decreases with increasing U. However, this decrease is much slower than for the case without vertex corrections. With vertex corrections, the SHC converges to the quantized value of $-2e^2/h$ in the zero temperature limit at all values of U below the phase transition. This is in stark contrast to the case where the vertex corrections are not included. At larger temperatures, where there is no quantization, momentum-dependent vertex corrections also give a large contribution to σ^{SH}. In fact the inclusion of vertex corrections almost doubles the value of the spin Hall conductivity near the phase transition at all temperatures considered. In the vicinity of the phase transition to the XY antiferromagnet at $U/t \approx 4$, the inclusion of vertex corrections almost doubles the value of σ^{SH} at all temperatures.

The impact of the vertex corrections can be explained by the following: When approaching the phase transition, the antiferromagnetic spin fluctuations become strong and scattering of electrons on them yields a large contribution to σ^{SH}. Numerically, we see that the momentum dependence of the self-energy is rather strong near the phase transition, especially near $\boldsymbol{k} = K,\ K'$ (compare Fig. 4.18. Hence, vertex corrections corresponding to a momentum derivative of the self-energy become large near K and K'. This shows, that especially in the vicinity of the phase transition, where antiferromagnetic spin fluctuations are strong, using only the conductivity bubble is insufficient and vertex corrections become important. We note however, that in DMFT the neglect of vertex corrections is consistent since the DMFT self-energy is constant in momentum space. Hence, using the DMFT Green's function to evaluate Eq. 5.102 is consistent and also yields quantization with integer multiples of $2e^2/h$ in the zero temperature limit, Eq. 5.102 is a topological invariant of the Green's function.

We also note that, at the phase transition, the decrease in σ^{SH} is visible through a much smaller kink. The reason is that, through the enforcement of TR symmetry in the above TPSC self-consistency equations, the system cannot become magnetic even though the spin correlation length diverges. Note

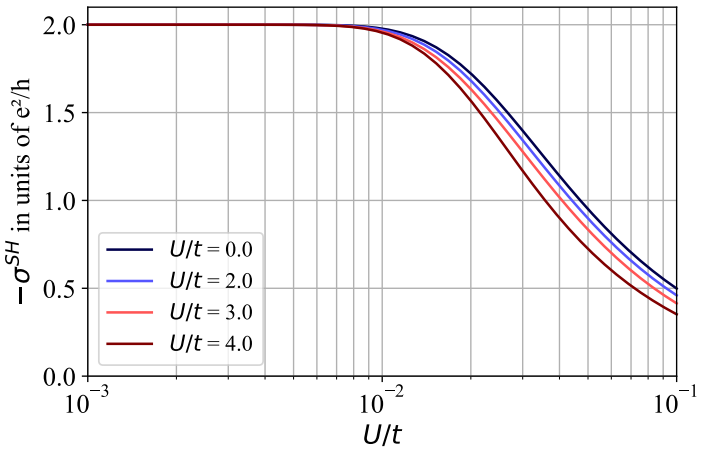

Figure 5.8: Spin Hall conductivity including vertex corrections as a function of T/t calculated from Eq. 5.82 at $\lambda/t = 0.01$ and for different values of the Hubbard U.

that the model possesses a continuous symmetry namely the spin rotation around z-axis. So strictly at finite temperature the Mermin-Wagner theorem holds and the system must not become magnetic. The small peak seen at certain temperatures in the greyed out region, where TPSC is not valid, could be caused by the averaging of the self-energy expressions expanded in the longitudinal and the transversal channels. Indeed, as discussed in section 5.4.1, with SOC the antiferromagnetic instability is reached first for transversal spin fluctuations and only at larger U values for longitudinal ones. However this peak is likely to be a unphysical phenomenon, because TPSC is not valid in the greyed out region.

In Fig. 5.8, we show the temperature dependence of σ^{SH} including vertex corrections for different values of U. At low temperatures, σ^{SH} goes to the quantized values of $-2e^2/h$. Deviations from the quantized value start when the temperature becomes of the order of the SOC which determines the band gap. Increasing the Hubbard U decreases σ^{SH} but the overall trend stays the same. We conclude that interactions destabilize the QSH state. The decrease can be explained with a renormalization of the band gap by interactions as we will see in more detail in Sec. 5.4.4. This can be seen as effectively increasing the temperature in the system. A higher temperature leads to more electrons occupying states above the band gap. The states above the band gap yield canceling contributions to the spin Hall conductivity. Hence, the spin Hall conductivity is decreased. Note that in a non-interacting lattice model if all bands are filled, the spin Hall conductivity, because all bands taken together must be topologically trivial.

In the case of the anomalous Hall conductivity, Ref. [235] attributes the decrease to a correlation-induced increase of spectral weight within the gap at finite temperatures. For the (spin) Hall conductivity, Refs. [234, 235] focus mainly on the topological insulator to Mott transition, which in the KMH model is overshadowed by the transition to the XY antiferromagnet. The suppression of σ^{SH} by interactions at finite temperatures has also been observed in DMFT calculations of the Bernevig-Hughes-Zhang-Hubbard model [234] and similarly for the anomalous Hall conductivity in the Hubbard model in the presence of a magnetic field [235].

5.4.4 Band renormalization

In the following, we discuss how interactions renormalize the band gap and thus affect σ^{SH}. The quasiparticle weight is defined as

$$Z(\omega, \boldsymbol{k}) = \left(1 - \partial_\omega \Sigma^{\mathrm{R}}(\omega, \boldsymbol{k})\right)^{-1}, \tag{5.103}$$

where $\Sigma^{\mathrm{R}}(\omega, \boldsymbol{k})$ is the retarded self-energy on the real frequency axis, indicated by ω. At $\boldsymbol{k} = K, K'$ we find the TPSC self-energy $\Sigma^{(2)}(i\omega_n, \boldsymbol{k})$ to be diagonal with identical entries that are purely imaginary, therefore $Z(0, K)$ becomes just a number Z. Expanding the self-energy linearly we can see that the band gap energy ΔE_g gets renormalized by the interactions by a factor of Z

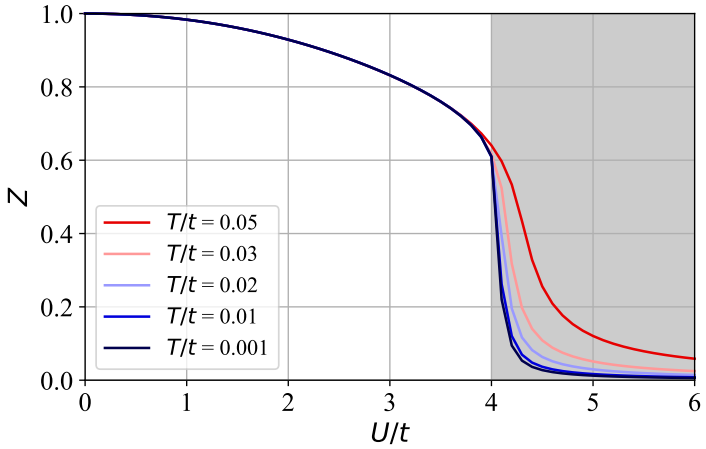

Figure 5.9: Band renormalization Z as a function of U/t for different temperatures and $\lambda/t = 0.01$. In the greyed out region TPSC is not valid anymore. At the phase transition we observe a sharp kink. The temperature dependence is very weak. This indicates that the stronger temperature dependence of σ^{SH} for higher values of U stems mostly from an effective increase of temperature by renormalizing the gap.

$$\begin{aligned} G_{\pm}(\omega, K) &= \left(\omega + i\eta \pm \frac{\Delta E_g}{2} + \mu - \Sigma(\omega, K)\right)^{-1} \\ &\approx \left((1 - \partial_\omega \Sigma(\omega, K)|_{\omega=0})\omega \pm \frac{\Delta E_g}{2} + \mu\right)^{-1} \\ &= \left(\omega \pm Z\frac{\Delta E_g}{2} + Z\mu\right)^{-1} Z \end{aligned} \tag{5.104}$$

For small SOC, the main contributions to σ^{SH} are localized around K and K', as can be seen in the noninteracting case (compare e.g. [231] for the Haldane model). Increasing SOC the region in momentum space contributing to σ^{SH} is broadened. At nonzero temperature, the band gap renormalization is crucial for σ^{SH} since the occupied states above the gap yield canceling contributions to it as discussed in Sec. 5.4.4. Renormalizing the gap hence can be seen as increasing the effective temperature in the system. To calculate Z numerically, the analytical continuation to real frequencies is performed using

$$\partial_\omega \mathrm{Re}\Sigma^{\mathrm{R}}(\omega, K)|_{\omega=0} \approx \mathrm{Im}\Sigma^{(2)}(i\omega_0, K)/\omega_0, \tag{5.105}$$

where $\omega_0 = \pi T$ is the lowest fermionic Matsubara frequency. In Fig. 5.9 we show the quasiparticle weight Z obtained from our TPSC calculations as a function of U. We observe a sharp drop at the phase transition. However, in contrast to σ^{SH}, Z is almost temperature independent below the phase transition. This indicates that the stronger temperature dependence of the spin Hall conductivity at larger values of U stems mostly from an effective increase of temperature by renormalizing the gap, since the Z itself shows no temperature dependence. In a quasiparticle picture it is easier to thermally excite electrons from the valence into the conduction band when the band gap is effectively reduced by the interactions. We note that the band gap renormalization and the corresponding decrease of the spin Hall conductivity at finite temperature was already observed in Ref. [234]. Here however, we can explicitly take into account the momentum dependence of the self-energy to calculate the band renormalization.

In the following we show that the antiferromagnetic spin fluctuations renormalize the band gap. $G^{(2)}$ and $\Sigma^{(2)}$ are diagonal in spin and orbital at $\boldsymbol{k} = K$. Hence, we consider the diagonal elements of the self-energy at zero frequency and $\boldsymbol{k} = K$ that are responsible for the band gap renormalization. The same arguments hold at $\boldsymbol{k} = K'$. From sublattice symmetry we have $\chi^{11}_{\alpha\alpha}(q) = \chi^{22}_{\alpha\alpha}(q)$ from which it follows that $\chi^{aa}_{\alpha\alpha}(q) \sim \chi^{\mathrm{afm}}_{\alpha\alpha}(q)/2$. Since the antiferromagnetic spin fluctuations dominate over charge

and ferromagnetic spin fluctuations in the system (see Sec. 4.14.5 and 4.14.6), especially at large U values, we only focus on them. The Hartee term can be absorbed in the chemical potential and is thus omitted from our discussion. Focusing only on χ_{xx} (the same holds for χ_{yy} and χ_{zz}) with our previous considerations we can write Eq. 4.183 for $\Sigma^{(2)}$ as

$$\Sigma_\sigma^{(2)aa}(i\omega_0, \boldsymbol{K}) \sim \frac{U}{16}\frac{T}{N}\sum_{iq_m,\boldsymbol{q}\alpha} G_{-\sigma}^{(1)aa}(i\omega_0 + i\boldsymbol{q}_m, \boldsymbol{K}+\boldsymbol{q})\Gamma_{xx}^a \chi_{xx}^{\mathrm{afm}}(iq_m, \boldsymbol{q}). \tag{5.106}$$

We conclude that the leading contribution to the self-energy comes from antiferromagnetic spin fluctuations.

On first sight it might be counter-intuitive that interactions make the band gap smaller, since the common picture in mind is that increasing interactions lead to a formation of Hubbard bands and thus increasing the band gap. However, a renormalization of the band structure accompanied by an increase of the effective electron mass through interactions is a common feature in correlated systems.

We can give a classical analogy for the renormalization of the band gap by spin fluctuations. However, the validity of the analogy is limited since it rather applies to phonons then Fermions. Consider a damped harmonic oscillator in one dimension. A friction term with friction constant γ will renormalize the oscillation frequency to $\omega_R = \sqrt{\omega_0^2 - \frac{\gamma^2}{4}}$, where $\omega_0 = \sqrt{k/m}$ is the oscillation frequency of the oscillator without damping. In the classical case the damping stems from the averaging of many microscopic particle collisions. In the case of the Kane-Mele-Hubbard model the damping microscopically originates from the interaction, which makes it possible for the electrons to excite and absorb spin fluctuations. Contrary to the simple classical case this effect is frequency dependent and leads to a frequency dependent renormalization of the quasi particle energy and hence also renormalizes the band gap.

5.4.5 Summary of the results

In this chapter we studied the spin Hall conductivity in the Kane-Mele-Hubbard model with TPSC. At zero temperature the Kane-Mele-Hubbard model shows a transition from a quantum spin Hall insulator to an XY antiferromagnet. The instability for the transition to the XY antiferromagnet was identified from the divergence of the antiferromagnetic spin correlation length for the spin components in the x-y plane. We calculated the SHC once using the conductivity bubble and once including vertex corrections. TPSC allows to take into account the full frequency and momentum dependence of the Green's function. Vertex corrections for the SHC within TPSC corresponds to the analogues of the Maki-Thompson contributions. Physically they describe the excitation and reabsorption of a spin, charge or mixed spin-charge excitation by an electron. With the conductivity bubble we saw a sharp drop at the phase transition, because the self-energy dampens the interacting Green's function. Including momentum dependent vertex corrections this picture changes. At all temperatures the vertex corrections have a large contribution near the instability to the XY antiferromagnet where antiferromagnetic spin fluctuations are large. Close to the phase transition the vertex corrections almost double the value of the spin Hall conductivity at all temperatures considered. Also, we did not see a drop at the phase transition when vertex corrections are included. The reason is that within TPSC we enforce TR symmetry and hence force the system to stay in the non-magnetic phase. TPSC is not valid anymore in the strong coupling limit, i.e. when the spin correlation length diverges. Further, we found that only with vertex corrections the SHC goes to the quantized value of $-2e^2/h$ in the zero temperature limit. At non-zero temperature increasing the Hubbard interaction leads to a decrease of the SHC. Further our results indicate that scattering of electrons of anti-ferromagnetic spin fluctuations renormalize the band gap. This can be interpreted as an effective increase of temperature leading to a decrease of the SHC. Hence, one needs to go to lower temperatures to see a the QSH when spin fluctuations become large.

Our main contribution is to show that nonlocal correlation effects, that result in a strong momentum dependence of the self-energy, can play an important role in the calculation of the spin Hall conductivity at finite temperature and that vertex corrections are extremely important to obtain the zero-temperature quantized value that corresponds to a topological invariant of the Matsubara Green's function. TPSC is well suited to study these effects quantitatively in the weak to intermediate coupling regime.

Chapter 6

Conclusion and Outlook

In this thesis we investigated certain aspects of the interplay of electronic correlation effects, spin-orbit coupling and topological properties. The model we considered is the Hubbard model, once in one dimension for the Su-Schriefer-Heeger model with Hubbard interactions and once in two dimensions for the Kane-Mele-Hubbard model. In the Kane-Mele-Hubbard model we specifically focused on the calculation of the spin Hall conductivity. In the following we summarize our main findings and give an outlook on possible future research avenues.

We investigated the applicability of elementary band representations (EBRs) to diagnose interacting topological phases that are protected by spatial symmetries and time-reversal-symmetry in terms of their single-particle Matsubara Green's functions. Assuming that there exists only a unique ground state of the interacting system, we showed how it is possible to define EBRs for the Matsubara Green's function in the zero temperature limit via the topological Hamiltonian. We found that the Green's function EBR classification can only change by (i) a gap closing in the spectral function at zero frequency, (ii) the Green's function becoming singular i.e. having a zero eigenvalue at zero frequency or (iii) the Green's function breaking a protecting symmetry. However, in which cases there is a strict correspondence between an EBR classification of Green's functions and SPT phases remains an open question. As an example, we demonstrated the use of the EBRs for Matsubara Green's functions on the Su-Schriefer-Heeger model with exact diagonalization. This model features a transition where the Green's function has zero eigenvalues at zero frequency. Although only demonstrated in one dimension, the procedure can be applied in any dimension. An EBR analysis of the topological Hamiltonian hence can become helpful in identifying topological phases in models and materials where electronic correlation effects are significant. The reason is that one only needs to calculate the Green's function and the topological Hamiltonian at a few high-symmetry k-points instead of on a dense k-grid. These results are published in Ref. [1].

An important topic of this work is the extension of the TPSC approach to include spin-orbit coupling (SOC). To do so, we took advantage of time-reversal symmetry that is preserved in the presence of SOC to derive new TPSC self-consistency equations including SOC. SOC breaks spin rotation symmetry which leads to a coupling of spin and charge sectors. We introduced an efficient matrix notation for susceptibilities and vertices. We showed that the local and constant TPSC vertex matrix in the particle-hole channel consists of three spin vertices and one charge vertex in the presence of time reversal symmetry. Together with spin and charge sum rules and an ansatz equation that relates the double occupancy to one of the vertices, this yields the new self-consistency equations. The derived self-consistency equations constitute a multidimensional root-finding problem for the four vertices that needs to be solved numerically. The self-energy is constructed from spin, charge and mixed spin-charge susceptibilities. In the absence of SOC, the derived equations reduce to the original TPSC self-consistency equations. We implemented the TPSC self-consistency equations for the special case of S_z conserved using the sparse-ir library [187–189].

As a test case to study the interplay of Hubbard interaction and SOC, we study the Kane-Mele-Hubbard model. With TPSC, we find that the antiferromagnetic spin fluctuations are the leading instability. This confirms that the Kane-Mele-Hubbard model is an XY antiferromagnet at zero tem-

perature. Mixed spin-charge fluctuations are found to be small. The transversal spin vertices are found to be more strongly renormalized than the longitudinal spin vertex. In TPSC we also see how higher SOC leads to a decrease of antiferromagnetic spin fluctuations, so that the phase transition is shifted to higher U values. The self-energy shows dispersion and sharp features in momentum space close to the phase transition. The $\mathrm{Tr}(G\Sigma)$ check shows that TPSC loses validity at the phase transition or if U gets to high.

As an application, we calculated the spin Hall conductivity in the Kane-Mele-Hubbard model at finite temperature with TPSC. At zero temperature, the Kane-Mele-Hubbard model shows a transition from a quantum spin Hall insulator to an XY antiferromagnet. Even though the Kane-Mele-Hubbard model is a simplified model, it allows us to understand systematically the interplay between correlation effects, here modeled by the Hubbard interaction that leads to an instability to a magnetically ordered phase, and a topological transport property i.e. the spin Hall conductivity in our case. In our calculations, the transition to the XY antiferromagnet was identified from the divergence of the antiferromagnetic spin correlation length for the spin components in the x-y plane, which allowed us to calculate a phase diagram from TPSC. We calculated the spin Hall conductivity once using the conductivity bubble and once including vertex corrections. Vertex corrections for the spin Hall conductivity within TPSC corresponds to the analogues of the Maki-Thompson contributions. Physically, vertex corrections in TPSC describe the excitation and reabsorption of a spin, charge or mixed spin-charge excitation by an electron. At all temperatures, the vertex corrections show a large contribution in the vicinity of the phase transition to the XY antiferromagnet where antiferromagnetic spin fluctuations are large. Close to the phase transition, the vertex corrections almost double the value of the spin Hall conductivity at all temperatures considered. We find that vertex corrections are crucial to recover the quantized value of $-2e^2/h$ in the zero temperature limit. Further, at non-zero temperature, increasing the Hubbard interaction leads to a decrease of the spin Hall conductivity. Our results indicate that scattering of electrons off antiferromagnetic spin fluctuations renormalize the band gap. Decreasing the gap can be interpreted as an effective increase of temperature leading to a decrease of the spin Hall conductivity. Hence, if the antiferromagnetic spin fluctuations are large, one needs to go to lower temperatures to observe the quantum spin Hall effect. These results emphasize the importance of vertex correction in the presence of strong spin fluctuations and help understanding the mechanism of decreasing the spin Hall conductivity in the presence of interactions. The results hence present valuable insights that might become important in spintronics applications based on the spin Hall effect. The developed method might also become important in a realistic modeling of the spin Hall conductivity at finite temperature and with interactions present in a real material. The results of this chapter are published in Ref. [2].

Besides the spin Hall effect, the interplay of SOC and correlation effects causes many interesting phenomena that can be studied with TPSC. Possible other applications are the study of spin textures in cuprates caused by SOC [81, 82], collective spin excitations in graphene due to the interplay of Rashba SOC and electron-electron interactions [83–88], magnetic anisotropy caused by SOC [140–142], the realization of a p-wave superconductor via proximity effects and gapless edgestates at the surface of a topological insulator [145, 146] or the superconductivity in Sr_2RuO_4 where SOC is important to describe the electronic structure [92–99].

Some of these application also necessitate progress on the method development side. The combination of TPSC multi-orbital extensions that also include U' and J [167–169] and SOC is a promising but challenging task. Here, the combination of DMFT with TPSC [5, 6, 159, 160], where occupation numbers and double occupancies from DMFT are used in the TPSC self-consistency equation, as well as the replacement of the local part of the self-energy by the DMFT self-energy, seems like a promising avenue. In this way, the ambiguity in the ansatz equation when including SOC can also be resolved.

We conclude that the interplay of electronic correlations, spin-orbit coupling and topology is very rich and has many exciting research avenues. TPSC is a suitable method to study this interplay in the weak to intermediate coupling regime.

Appendix A

List of definitions of susceptibilities

Here, we give a list of all susceptibilities formed by the operator set $\{S^x, S^y, S^z, n\}$ and also the susceptibilities in a different basis formed by the operator set $\{n_\uparrow, n_\downarrow, S^+, S^-\}$. We assume time reversal symmetry, so that certain expectation values vanish. We also explicitly give the basis transformation between both bases.

A.1 Physical susceptibilities

For the first set $\{S^x, S^y, S^z, n\}$ we have the following $4 \times 4 = 16$ susceptibilities. The purely longitudinal susceptibilities are

$$\chi^{ab}_{cc}(\tau, \boldsymbol{R}_i - \boldsymbol{R}_j) = \langle \mathcal{T}_\tau n_{ia}(\tau) n_{jb}(0) \rangle - \langle n \rangle^2 , \tag{A.1}$$
$$\chi^{ab}_{cz}(\tau, \boldsymbol{R}_i - \boldsymbol{R}_j) = \langle \mathcal{T}_\tau n_{ia}(\tau) S^z_{jb}(0) \rangle , \tag{A.2}$$
$$\chi^{ab}_{zc}(\tau, \boldsymbol{R}_i - \boldsymbol{R}_j) = \langle \mathcal{T}_\tau S^z_{ia}(\tau) n_{jb}(0) \rangle , \tag{A.3}$$
$$\chi^{ab}_{zz}(\tau, \boldsymbol{R}_i - \boldsymbol{R}_j) = \langle \mathcal{T}_\tau S^z_{ia}(\tau) S^z_{jb}(0) \rangle . \tag{A.4}$$

The pure transversal ones are

$$\chi^{ab}_{xx}(\tau, \boldsymbol{R}_i - \boldsymbol{R}_j) = \langle \mathcal{T}_\tau S^x_{ia}(\tau) S^x_{jb}(0) \rangle , \tag{A.5}$$
$$\chi^{ab}_{xy}(\tau, \boldsymbol{R}_i - \boldsymbol{R}_j) = \langle \mathcal{T}_\tau S^x_{ia}(\tau) S^y_{jb}(0) \rangle , \tag{A.6}$$
$$\chi^{ab}_{yx}(\tau, \boldsymbol{R}_i - \boldsymbol{R}_j) = \langle \mathcal{T}_\tau S^y_{ia}(\tau) S^x_{jb}(0) \rangle , \tag{A.7}$$
$$\chi^{ab}_{yy}(\tau, \boldsymbol{R}_i - \boldsymbol{R}_j) = \langle \mathcal{T}_\tau S^y_{ia}(\tau) S^y_{jb}(0) \rangle . \tag{A.8}$$

The susceptibilities coupling longitudinal and transversal channel are (first the upper right in the matrix notation)

$$\chi^{ab}_{cx}(\tau, \boldsymbol{R}_i - \boldsymbol{R}_j) = \langle \mathcal{T}_\tau n_{ia}(\tau) S^x_{jb}(0) \rangle , \tag{A.9}$$
$$\chi^{ab}_{cy}(\tau, \boldsymbol{R}_i - \boldsymbol{R}_j) = \langle \mathcal{T}_\tau n_{ia}(\tau) S^y_{jb}(0) \rangle , \tag{A.10}$$
$$\chi^{ab}_{zx}(\tau, \boldsymbol{R}_i - \boldsymbol{R}_j) = \langle \mathcal{T}_\tau S^z_{ia}(\tau) S^x_{jb}(0) \rangle , \tag{A.11}$$
$$\chi^{ab}_{zy}(\tau, \boldsymbol{R}_i - \boldsymbol{R}_j) = \langle \mathcal{T}_\tau S^z_{ia}(\tau) S^y_{jb}(0) \rangle , \tag{A.12}$$

as well as (lower left in the matrix notation)

$$\chi^{ab}_{xc}(\tau, \boldsymbol{R}_i - \boldsymbol{R}_j) = \langle \mathcal{T}_\tau S^x_{ia}(\tau) n_{jb}(0) \rangle \,, \tag{A.13}$$
$$\chi^{ab}_{xz}(\tau, \boldsymbol{R}_i - \boldsymbol{R}_j) = \langle \mathcal{T}_\tau S^x_{ia}(\tau) S^z_{jb}(0) \rangle \,, \tag{A.14}$$
$$\chi^{ab}_{yc}(\tau, \boldsymbol{R}_i - \boldsymbol{R}_j) = \langle \mathcal{T}_\tau S^y_{ia}(\tau) n_{jb}(0) \rangle \,, \tag{A.15}$$
$$\chi^{ab}_{yz}(\tau, \boldsymbol{R}_i - \boldsymbol{R}_j) = \langle \mathcal{T}_\tau S^y_{ia}(\tau) S^z_{jb}(0) \rangle \,. \tag{A.16}$$

A.2 Correlation functions of $n_\uparrow, n_\downarrow, S^+$ and S^-

In the other basis formed by $\{n_\uparrow, n_\downarrow, S^+, S^-\}$ one has 16 susceptibilities that in the presence of TR symmetry take the following form. Purely longitudinal one has

$$\chi^{ab}_{\uparrow\uparrow}(\tau, \boldsymbol{R}_i - \boldsymbol{R}_j) = \langle \mathcal{T}_\tau n_{ia\uparrow}(\tau) n_{jb\uparrow}(0) \rangle - \frac{\langle n \rangle^2}{4}, \tag{A.17}$$
$$\chi^{ab}_{\uparrow\downarrow}(\tau, \boldsymbol{R}_i - \boldsymbol{R}_j) = \langle \mathcal{T}_\tau n_{ia\uparrow}(\tau) n_{jb\downarrow}(0) \rangle - \frac{\langle n \rangle^2}{4}, \tag{A.18}$$
$$\chi^{ab}_{\downarrow\uparrow}(\tau, \boldsymbol{R}_i - \boldsymbol{R}_j) = \langle \mathcal{T}_\tau n_{ia\downarrow}(\tau) n_{jb\uparrow}(0) \rangle - \frac{\langle n \rangle^2}{4}, \tag{A.19}$$
$$\chi^{ab}_{\downarrow\downarrow}(\tau, \boldsymbol{R}_i - \boldsymbol{R}_j) = \langle \mathcal{T}_\tau n_{ia\downarrow}(\tau) n_{jb\downarrow}(0) \rangle - \frac{\langle n \rangle^2}{4}. \tag{A.20}$$

Here we used that $\langle n_\uparrow \rangle = \langle n_\downarrow \rangle$. The transversal susceptibilities are

$$\chi^{ab}_{++}(\tau, \boldsymbol{R}_i - \boldsymbol{R}_j) = \langle \mathcal{T}_\tau S^+_{ia}(\tau) S^+_{jb}(0) \rangle \,, \tag{A.21}$$
$$\chi^{ab}_{+-}(\tau, \boldsymbol{R}_i - \boldsymbol{R}_j) = \langle \mathcal{T}_\tau S^+_{ia}(\tau) S^-_{jb}(0) \rangle \,, \tag{A.22}$$
$$\chi^{ab}_{-+}(\tau, \boldsymbol{R}_i - \boldsymbol{R}_j) = \langle \mathcal{T}_\tau S^-_{ia}(\tau) S^+_{jb}(0) \rangle \,, \tag{A.23}$$
$$\chi^{ab}_{--}(\tau, \boldsymbol{R}_i - \boldsymbol{R}_j) = \langle \mathcal{T}_\tau S^-_{ia}(\tau) S^-_{jb}(0) \rangle \,. \tag{A.24}$$

Note that χ_{+-} and χ_{-+} are continuous at $\tau = 0$, because $[S^+, S^-] = S^z$ whose expectation value vanishes because of TR symmetry. Also note that because of TR symmetry $\langle S^+ \rangle = \langle S^- \rangle = 0$ and hence these terms are missing here in the susceptibilities. The mixed susceptibilities are

$$\chi^{ab}_{\uparrow+}(\tau, \boldsymbol{R}_i - \boldsymbol{R}_j) = \langle \mathcal{T}_\tau n_{ia\uparrow}(\tau) S^+_{jb}(0) \rangle \,, \tag{A.25}$$
$$\chi^{ab}_{\uparrow-}(\tau, \boldsymbol{R}_i - \boldsymbol{R}_j) = \langle \mathcal{T}_\tau n_{ia\uparrow}(\tau) S^-_{jb}(0) \rangle \,, \tag{A.26}$$
$$\chi^{ab}_{\downarrow+}(\tau, \boldsymbol{R}_i - \boldsymbol{R}_j) = \langle \mathcal{T}_\tau n_{ia\downarrow}(\tau) S^+_{jb}(0) \rangle \,, \tag{A.27}$$
$$\chi^{ab}_{\downarrow-}(\tau, \boldsymbol{R}_i - \boldsymbol{R}_j) = \langle \mathcal{T}_\tau n_{ia\downarrow}(\tau) S^-_{jb}(0) \rangle \,. \tag{A.28}$$

and

$$\chi^{ab}_{+\uparrow}(\tau, \boldsymbol{R}_i - \boldsymbol{R}_j) = \langle \mathcal{T}_\tau S^+_{ia}(\tau) n_{jb\uparrow}(0) \rangle \,, \tag{A.29}$$
$$\chi^{ab}_{+\downarrow}(\tau, \boldsymbol{R}_i - \boldsymbol{R}_j) = \langle \mathcal{T}_\tau S^+_{ia}(\tau) n_{jb\downarrow}(0) \rangle \,, \tag{A.30}$$
$$\chi^{ab}_{-\uparrow}(\tau, \boldsymbol{R}_i - \boldsymbol{R}_j) = \langle \mathcal{T}_\tau S^-_{ia}(\tau) n_{jb\uparrow}(0) \rangle \,, \tag{A.31}$$
$$\chi^{ab}_{-\downarrow}(\tau, \boldsymbol{R}_i - \boldsymbol{R}_j) = \langle \mathcal{T}_\tau S^-_{ia}(\tau) n_{jb\downarrow}(0) \rangle \,. \tag{A.32}$$

A.3 Basis transformation between susceptibilities

The susceptibilities are related to each other by (note again that $iS^y = S^+ - S^-$)

$$\chi_{cc} = \chi_{\uparrow\uparrow} + \chi_{\uparrow\downarrow} + \chi_{\downarrow\uparrow} + \chi_{\downarrow\downarrow}, \tag{A.33}$$
$$\chi_{cz} = \chi_{\uparrow\uparrow} - \chi_{\uparrow\downarrow} + \chi_{\downarrow\uparrow} - \chi_{\downarrow\downarrow}, \tag{A.34}$$
$$\chi_{zc} = \chi_{\uparrow\uparrow} + \chi_{\uparrow\downarrow} - \chi_{\downarrow\uparrow} - \chi_{\downarrow\downarrow}, \tag{A.35}$$
$$\chi_{zz} = \chi_{\uparrow\uparrow} - \chi_{\uparrow\downarrow} - \chi_{\downarrow\uparrow} + \chi_{\downarrow\downarrow}, \tag{A.36}$$

$$\chi_{xx} = \chi_{++} + \chi_{+-} + \chi_{-+} + \chi_{--}, \tag{A.37}$$
$$i\chi_{xy} = \chi_{++} - \chi_{+-} + \chi_{-+} - \chi_{--}, \tag{A.38}$$
$$i\chi_{yx} = \chi_{++} + \chi_{+-} - \chi_{-+} - \chi_{--}, \tag{A.39}$$
$$-\chi_{yy} = \chi_{++} - \chi_{+-} - \chi_{-+} + \chi_{--}, \tag{A.40}$$

$$\chi_{cx} = \chi_{\uparrow+} + \chi_{\uparrow-} + \chi_{\downarrow+} + \chi_{\downarrow-}, \tag{A.41}$$
$$i\chi_{cy} = \chi_{\uparrow+} - \chi_{\uparrow-} + \chi_{\downarrow+} - \chi_{\downarrow-}, \tag{A.42}$$
$$\chi_{zx} = \chi_{\uparrow+} + \chi_{\uparrow-} - \chi_{\downarrow+} - \chi_{\downarrow-}, \tag{A.43}$$
$$i\chi_{zy} = \chi_{\uparrow+} - \chi_{\uparrow-} - \chi_{\downarrow+} + \chi_{\downarrow-}, \tag{A.44}$$

$$\chi_{xc} = \chi_{+\uparrow} + \chi_{+\downarrow} + \chi_{-\uparrow} + \chi_{-\downarrow}, \tag{A.45}$$
$$\chi_{xz} = \chi_{+\uparrow} - \chi_{+\downarrow} + \chi_{-\uparrow} - \chi_{-\downarrow}, \tag{A.46}$$
$$i\chi_{yc} = \chi_{+\uparrow} + \chi_{+\downarrow} - \chi_{-\uparrow} - \chi_{-\downarrow}, \tag{A.47}$$
$$i\chi_{yz} = \chi_{+\uparrow} - \chi_{+\downarrow} - \chi_{-\uparrow} + \chi_{-\downarrow}. \tag{A.48}$$

Note that each S^y gets a factor i.

Appendix B

List of vertex elements

In this appendix we give a list of the matrix elements of the TPSC vertex in matrix notation. The TPSC vertex is defined as (disregarding all other indices but spin)

$$\Gamma_{\sigma_1\sigma_2,\sigma_4\sigma_3} := \Gamma_{\sigma_1\sigma_2\sigma_3\sigma_4} = \frac{\delta\Sigma_{\sigma_1\sigma_2}}{\delta G_{\sigma_3\sigma_4}}. \tag{B.1}$$

The first and last two indices separated by the comma, can be grouped together and be represented by the labels $\uparrow, \downarrow, +-$. Hence we have that

$$\Gamma_{\uparrow\uparrow} = \Gamma_{\uparrow\uparrow\uparrow\uparrow}, \tag{B.2}$$
$$\Gamma_{\uparrow\downarrow} = \Gamma_{\uparrow\uparrow\downarrow\downarrow}, \tag{B.3}$$
$$\Gamma_{\downarrow\uparrow} = \Gamma_{\downarrow\downarrow\uparrow\uparrow}, \tag{B.4}$$
$$\Gamma_{\downarrow\downarrow} = \Gamma_{\downarrow\downarrow\downarrow\downarrow}, \tag{B.5}$$

$$\Gamma_{++} = \Gamma_{\uparrow\downarrow\downarrow\uparrow}, \tag{B.6}$$
$$\Gamma_{+-} = \Gamma_{\uparrow\downarrow\uparrow\downarrow}, \tag{B.7}$$
$$\Gamma_{-+} = \Gamma_{\downarrow\uparrow\downarrow\uparrow}, \tag{B.8}$$
$$\Gamma_{--} = \Gamma_{\downarrow\uparrow\uparrow\downarrow}, \tag{B.9}$$

$$\Gamma_{\uparrow+} = \Gamma_{\uparrow\uparrow\downarrow\uparrow}, \tag{B.10}$$
$$\Gamma_{\uparrow-} = \Gamma_{\uparrow\uparrow\uparrow\downarrow}, \tag{B.11}$$
$$\Gamma_{\downarrow+} = \Gamma_{\downarrow\downarrow\downarrow\uparrow}, \tag{B.12}$$
$$\Gamma_{\downarrow-} = \Gamma_{\downarrow\downarrow\uparrow\downarrow}, \tag{B.13}$$

$$\Gamma_{+\uparrow} = \Gamma_{\uparrow\downarrow\uparrow\uparrow}, \tag{B.14}$$
$$\Gamma_{+\downarrow} = \Gamma_{\uparrow\downarrow\downarrow\downarrow}, \tag{B.15}$$
$$\Gamma_{-\uparrow} = \Gamma_{\downarrow\uparrow\uparrow\uparrow}, \tag{B.16}$$
$$\Gamma_{-\downarrow} = \Gamma_{\downarrow\uparrow\downarrow\downarrow}, \tag{B.17}$$

In the presence of time reversal symmetry the only non-vanishing physical vertex elements are (analogous to the susceptibilities)

$$\Gamma_{cc} = \Gamma_{\uparrow\uparrow} + \Gamma_{\uparrow\downarrow} + \Gamma_{\downarrow\uparrow} + \Gamma_{\downarrow\downarrow}, \tag{B.18}$$

$$\Gamma_{xx} = \Gamma_{++} + \Gamma_{+-} + \Gamma_{-+} + \Gamma_{--}, \tag{B.19}$$

$$-\Gamma_{yy} = \Gamma_{++} - \Gamma_{+-} - \Gamma_{-+} + \Gamma_{--}, \tag{B.20}$$

$$\Gamma_{zz} = \Gamma_{\uparrow\uparrow} - \Gamma_{\uparrow\downarrow} - \Gamma_{\downarrow\uparrow} + \Gamma_{\downarrow\downarrow}. \tag{B.21}$$

Appendix C

List of relations following from time reversal symmetry

In the following we list implications of TR on several quantities. For the expectation values of the occupation numbers and the spin operators one gets

$$\langle n_{a\sigma}\rangle = \langle n_{a-\sigma}\rangle = \frac{\langle n_a\rangle}{2}, \tag{C.1}$$

$$\langle S_a^+\rangle = \langle S_a^-\rangle = 0, \tag{C.2}$$

$$\langle S_a^x\rangle = \langle S_a^y\rangle = \langle S_a^z\rangle = 0. \tag{C.3}$$

For the Green's function and the self-energy one gets

$$G^{ab}_{\sigma\sigma'}(i\omega_n, \boldsymbol{k}) = \sigma\sigma' G^{ba}_{-\sigma'-\sigma}(i\omega_n, -\boldsymbol{k}), \tag{C.4}$$

$$\Sigma^{ab}_{\sigma\sigma'}(i\omega_n, \boldsymbol{k}) = \sigma\sigma' \Sigma^{ba}_{-\sigma'-\sigma}(i\omega_n, -\boldsymbol{k}). \tag{C.5}$$

For the susceptibility one gets

$$\chi^{ab}_{\sigma_1\sigma_2,\sigma_3\sigma_4}(iq_m, \boldsymbol{q}) = \sigma_1\sigma_2\sigma_3\sigma_4 \chi^{ba}_{-\sigma_3-\sigma_4,-\sigma_1-\sigma_2}(iq_m, -\boldsymbol{q}). \tag{C.6}$$

Note that the first two and the last two spin indices can be combined into one taking the values $\uparrow, \downarrow, +, -$. For the irreducible TPSC vertex one gets similarly

$$\Gamma^a_{\sigma_1\sigma_2,\sigma_3\sigma_4} = \sigma_1\sigma_2\sigma_3\sigma_4 \Gamma^a_{-\sigma_3-\sigma_4,-\sigma_1-\sigma_2}. \tag{C.7}$$

Appendix D

Fast Fourier transforms for convolution-like expressions

Often we need to evaluate expressions of the following one

$$(g \star f)(l) = \sum_j g(l+j) f(j). \tag{D.1}$$

Note that this expression is not a convolution, but convolution like. In a convolution one would have a minus sign instead of a plus sign. Of course in practice the indices l and j stand for either $q = (iq_m, \boldsymbol{q})$ or $k = (i\omega_n, \boldsymbol{k})$, where iq_m are bosonic and $i\omega_n$ fermionic Matsubara frequencies. To simplify the discussion we restrict ourselves here to the one-dimensional case with discrete indices. The computational effort for a direct evaluation of the above equation is $\mathcal{O}(N^2)$. With the use of fast Fourier transformation (FFT) the computational effort can be reduced to $\mathcal{O}(N \log(N))$. We define the discrete Fourier transform (FT) as

$$\hat{f}(k) = \sum_j f(j) e^{-2\pi i k j}. \tag{D.2}$$

The inverse FT is defined as

$$\check{f}(j) = \frac{1}{N} \sum_k f(k) e^{2\pi i j k}. \tag{D.3}$$

Obviously, it holds $f(j) = \check{\hat{f}}(i)$. Let us consider the FT of $(g \star f)(j)$

$$\begin{aligned}
\widehat{g \star f}(l) &= \sum_l e^{-2\pi i k l} \sum_j g(l+j) f(j) \\
&= \sum_{lj} e^{2\pi i k j} e^{-2\pi i k (l+j)} g(l+j) f(j) \\
&= \sum_j e^{2\pi i k j} \hat{g}(k) f(j) \\
&= \hat{g}(k) \check{f}(k).
\end{aligned} \tag{D.4}$$

Taking an inverse FT we finally obtain

$$(g \star f)(j) = \widetilde{(\hat{g} \cdot \check{f})}(j). \tag{D.5}$$

Note that with $\cdot$ we emphasize point wise multiplication. In our calculations we calculate in frequency momentum space. This corresponds to expressions of the following type

$$\frac{T}{N}\sum_{iq_m\boldsymbol{q}} f(i\omega_n + iq_m, \boldsymbol{k}+\boldsymbol{q})g(iq_m,\boldsymbol{q}) = \int_0^\beta d\tau e^{i\omega_n\tau}\sum_{\boldsymbol{R}_i} e^{-i\boldsymbol{k}\boldsymbol{R}_i} f(\tau,\boldsymbol{R}_i)g(-\tau,-\boldsymbol{R}_i). \tag{D.6}$$

The bosonic expression is analogous. Since we only store positive times, symmetry or antisymmetry can be used to relate negative τ the corresponding positive one (see Sec. 2.4).

Appendix E

Search interval for the spin vertex

To avoid numerical instabilities in the one dimensional root-finding problems, associated with the pole of the susceptibility regarded as a function of the spin vertices, it is possible to give a search interval for the spin vertex. However, this is only possible in the case where there is no coupling with charge or the other spins and hence the root-finding problem is one-dimensional. For example the expression for the spin susceptibility with spins aligned in x-direction for the case S^z conserved is given by

$$\chi_{xx}(iq_m, \boldsymbol{q}) = \left(1 - \frac{1}{2}\chi^{(1)}_{xx}(iq_m, \boldsymbol{q})\Gamma_{xx}\right)^{-1} \chi^{(1)}_{xx}(iq_m, \boldsymbol{q}). \tag{E.1}$$

One can give a search interval for Γ_{xx}. Remember that we assume Γ_{xx} to be diagonal with identical entries. From symmetry considerations one can see that $\chi_{xx}(iq_m, \boldsymbol{q})$ is a hermitian matrix i.e.

$$\chi^{a_1 a_2}_{xx}(iq_m, \boldsymbol{q}) = \left(\chi^{a_2 a_1}_{xx}(iq_m, \boldsymbol{q})\right)^* \tag{E.2}$$

Further the matrix must be positiv semidefinite i.e. all its eigenvalues must be greater or equal zero (this property is related to the positivity of energy dissipation (see Ref. [100].) These properties can also be checked numerically. A hermitian matrix can easily be inverted in its eigenbasis, as long as none of its eigenvalues is zero. We label the eigenvalues of $\chi^{(1)}_{xx}(q)$ by $\chi^{(1)n}_{xx}(q)$. To ensure positive eigenvalues we must have for every n

$$1 - \frac{1}{2}\chi^{(1)n}_{xx}(q)\Gamma^n_{xx} > 0. \tag{E.3}$$

Hence we get

$$\Gamma^c_{xx} = \frac{2}{\chi^{(1)n_{\max}}_{xx}}, \tag{E.4}$$

where $n_{\max}$ labels the largest eigenvalue. So the search interval for the matrix elements of Γ_{xx} is $[0, \Gamma^c_{xx})$.

Bibliography

[1] Dominik Lessnich, Stephen M. Winter, Mikel Iraola, Maia G. Vergniory, and Roser Valentí. Elementary band representations for the single-particle green's function of interacting topological insulators. *Phys. Rev. B*, 104:085116, Aug 2021. doi: 10.1103/PhysRevB.104.085116. URL https://link.aps.org/doi/10.1103/PhysRevB.104.085116.

[2] D. Lessnich, C. Gauvin-Ndiaye, Roser Valentí, and A.-M. S. Tremblay. Spin hall conductivity in the kane-mele-hubbard model at finite temperature. *Phys. Rev. B*, 109:075143, Feb 2024. doi: 10.1103/PhysRevB.109.075143. URL https://link.aps.org/doi/10.1103/PhysRevB.109.075143.

[3] D. Lessnich et al. Interplay of spin-orbit coupling and elctronic correlation effects with the two-particle self-consistent approach. *in preparation*, 2023.

[4] Mikel Iraola, Niclas Heinsdorf, Apoorv Tiwari, Dominik Lessnich, Thomas Mertz, Francesco Ferrari, Mark H. Fischer, Stephen M. Winter, Frank Pollmann, Titus Neupert, Roser Valentí, and Maia G. Vergniory. Towards a topological quantum chemistry description of correlated systems: The case of the hubbard diamond chain. *Phys. Rev. B*, 104:195125, Nov 2021. doi: 10.1103/PhysRevB.104.195125. URL https://link.aps.org/doi/10.1103/PhysRevB.104.195125.

[5] Karim Zantout, Steffen Backes, Aleksandar Razpopov, Dominik Lessnich, and Roser Valentí. Improved effective vertices in the multiorbital two-particle self-consistent method from dynamical mean-field theory. *Phys. Rev. B*, 107:235101, Jun 2023. doi: 10.1103/PhysRevB.107.235101. URL https://link.aps.org/doi/10.1103/PhysRevB.107.235101.

[6] C. Gauvin-Ndiaye, J. Leblanc, S. Marin, N. Martin, D. Lessnich, and A. M. S. Tremblay. The two-particle self-consistent approach for multiorbital models: application to the emery model, 2023.

[7] John Hubbard. Electron correlations in narrow energy bands. *Proc. R. Soc. Lond. A*, 276(1365): 238–257, 1963.

[8] Junjiro Kanamori. Electron Correlation and Ferromagnetism of Transition Metals. *Progress of Theoretical Physics*, 30(3):275–289, 09 1963. ISSN 0033-068X. doi: 10.1143/PTP.30.275. URL https://doi.org/10.1143/PTP.30.275.

[9] Martin C. Gutzwiller. Effect of correlation on the ferromagnetism of transition metals. *Phys. Rev. Lett.*, 10:159–162, Mar 1963. doi: 10.1103/PhysRevLett.10.159. URL https://link.aps.org/doi/10.1103/PhysRevLett.10.159.

[10] Mingpu Qin, Thomas Schäfer, Sabine Andergassen, Philippe Corboz, and Emanuel Gull. The hubbard model: A computational perspective. *Annual Review of Condensed Matter Physics*, 13 (1):275–302, 2022. doi: 10.1146/annurev-conmatphys-090921-033948. URL https://doi.org/10.1146/annurev-conmatphys-090921-033948.

[11] Sandro Sorella, Yuichi Otsuka, and Seiji Yunoki. Absence of a spin liquid phase in the hubbard model on the honeycomb lattice. *Scientific Reports*, 2(1):992, Dec 2012. ISSN 2045-2322. doi: 10.1038/srep00992. URL https://doi.org/10.1038/srep00992.

[12] Yoshiki Imai, Norio Kawakami, and Hirokazu Tsunetsugu. Low-energy excitations of the hubbard model on the kagomé lattice. *Phys. Rev. B*, 68:195103, Nov 2003. doi: 10.1103/PhysRevB.68.195103. URL https://link.aps.org/doi/10.1103/PhysRevB.68.195103.

[13] B. Kyung and A.-M. S. Tremblay. Mott transition, antiferromagnetism, and d-wave superconductivity in two-dimensional organic conductors. *Phys. Rev. Lett.*, 97:046402, Jul 2006. doi: 10.1103/PhysRevLett.97.046402. URL https://link.aps.org/doi/10.1103/PhysRevLett.97.046402.

[14] Takuma Ohashi, Norio Kawakami, and Hirokazu Tsunetsugu. Mott transition in kagomé lattice hubbard model. *Phys. Rev. Lett.*, 97:066401, Aug 2006. doi: 10.1103/PhysRevLett.97.066401. URL https://link.aps.org/doi/10.1103/PhysRevLett.97.066401.

[15] H. J. Liao, Z. Y. Xie, J. Chen, Z. Y. Liu, H. D. Xie, R. Z. Huang, B. Normand, and T. Xiang. Gapless spin-liquid ground state in the $s = 1/2$ kagome antiferromagnet. *Phys. Rev. Lett.*, 118:137202, Mar 2017. doi: 10.1103/PhysRevLett.118.137202. URL https://link.aps.org/doi/10.1103/PhysRevLett.118.137202.

[16] Josef Kaufmann, Klaus Steiner, Richard T. Scalettar, Karsten Held, and Oleg Janson. How correlations change the magnetic structure factor of the kagome hubbard model. *Phys. Rev. B*, 104:165127, Oct 2021. doi: 10.1103/PhysRevB.104.165127. URL https://link.aps.org/doi/10.1103/PhysRevB.104.165127.

[17] N. Bulut, W. Koshibae, and S. Maekawa. Magnetic correlations in the hubbard model on triangular and kagomé lattices. *Phys. Rev. Lett.*, 95:037001, Jul 2005. doi: 10.1103/PhysRevLett.95.037001. URL https://link.aps.org/doi/10.1103/PhysRevLett.95.037001.

[18] Kazushi Kanoda and Reizo Kato. Mott physics in organic conductors with triangular lattices. *Annual Review of Condensed Matter Physics*, 2(1):167–188, 2011. doi: 10.1146/annurev-conmatphys-062910-140521. URL https://doi.org/10.1146/annurev-conmatphys-062910-140521.

[19] Alexander Wietek, Riccardo Rossi, Fedor Šimkovic, Marcel Klett, Philipp Hansmann, Michel Ferrero, E. Miles Stoudenmire, Thomas Schäfer, and Antoine Georges. Mott insulating states with competing orders in the triangular lattice hubbard model. *Phys. Rev. X*, 11:041013, Oct 2021. doi: 10.1103/PhysRevX.11.041013. URL https://link.aps.org/doi/10.1103/PhysRevX.11.041013.

[20] Antoine Georges, Luca de' Medici, and Jernej Mravlje. Strong correlations from hund's coupling. *Annual Review of Condensed Matter Physics*, 4(1):137–178, 2013. doi: 10.1146/annurev-conmatphys-020911-125045. URL https://doi.org/10.1146/annurev-conmatphys-020911-125045.

[21] Elliott H. Lieb and F. Y. Wu. Absence of mott transition in an exact solution of the short-range, one-band model in one dimension. *Phys. Rev. Lett.*, 20:1445–1448, Jun 1968. doi: 10.1103/PhysRevLett.20.1445. URL https://link.aps.org/doi/10.1103/PhysRevLett.20.1445.

[22] Walter Metzner and Dieter Vollhardt. Correlated lattice fermions in $d = \infty$ dimensions. *Phys. Rev. Lett.*, 62:324–327, Jan 1989. doi: 10.1103/PhysRevLett.62.324. URL https://link.aps.org/doi/10.1103/PhysRevLett.62.324.

[23] Antoine Georges and Gabriel Kotliar. Hubbard model in infinite dimensions. *Phys. Rev. B*, 45:6479–6483, Mar 1992. doi: 10.1103/PhysRevB.45.6479. URL https://link.aps.org/doi/10.1103/PhysRevB.45.6479.

[24] M. Jarrell. Hubbard model in infinite dimensions: A quantum monte carlo study. *Phys. Rev. Lett.*, 69:168–171, Jul 1992. doi: 10.1103/PhysRevLett.69.168. URL https://link.aps.org/doi/10.1103/PhysRevLett.69.168.

[25] Steven R. White. Density matrix formulation for quantum renormalization groups. *Phys. Rev. Lett.*, 69:2863–2866, Nov 1992. doi: 10.1103/PhysRevLett.69.2863. URL https://link.aps.org/doi/10.1103/PhysRevLett.69.2863.

[26] Steven R. White. Density-matrix algorithms for quantum renormalization groups. *Phys. Rev. B*, 48:10345–10356, Oct 1993. doi: 10.1103/PhysRevB.48.10345. URL https://link.aps.org/doi/10.1103/PhysRevB.48.10345.

[27] Antoine Georges, Gabriel Kotliar, Werner Krauth, and Marcelo J. Rozenberg. Dynamical mean-field theory of strongly correlated fermion systems and the limit of infinite dimensions. *Rev. Mod. Phys.*, 68:13–125, Jan 1996. doi: 10.1103/RevModPhys.68.13. URL https://link.aps.org/doi/10.1103/RevModPhys.68.13.

[28] Y. M. Vilk, Liang Chen, and A.-M. S. Tremblay. Theory of spin and charge fluctuations in the hubbard model. *Phys. Rev. B*, 49:13267–13270, May 1994. doi: 10.1103/PhysRevB.49.13267. URL https://link.aps.org/doi/10.1103/PhysRevB.49.13267.

[29] Y. M. Vilk and A.-M. S. Tremblay. Destruction of fermi-liquid quasiparticles in two dimensions by critical fluctuations. *Europhysics Letters*, 33(2):159, jan 1996. doi: 10.1209/epl/i1996-00315-2. URL https://dx.doi.org/10.1209/epl/i1996-00315-2.

[30] Y.M. Vilk and A.-M.S. Tremblay. Non-perturbative many-body approach to the hubbard model and single-particle pseudogap. *J. Phys. I France*, 7(11):1309–1368, 1997. doi: 10.1051/jp1:1997135. URL https://doi.org/10.1051/jp1:1997135.

[31] A. Toschi, A. A. Katanin, and K. Held. Dynamical vertex approximation: A step beyond dynamical mean-field theory. *Phys. Rev. B*, 75:045118, Jan 2007. doi: 10.1103/PhysRevB.75.045118. URL https://link.aps.org/doi/10.1103/PhysRevB.75.045118.

[32] A. N. Rubtsov, M. I. Katsnelson, and A. I. Lichtenstein. Dual fermion approach to nonlocal correlations in the hubbard model. *Phys. Rev. B*, 77:033101, Jan 2008. doi: 10.1103/PhysRevB.77.033101. URL https://link.aps.org/doi/10.1103/PhysRevB.77.033101.

[33] S. Allen, A. M. S. Tremblay, and Y. M. Vilk. Conserving approximations vs two-particle self-consistent approach, 2003.

[34] A.-M. S. Tremblay. *Two-particle-self-consistent approach for the Hubbard model, in Strongly Correlated Systems: Theoretical Methods.* Edited by F. Mancini and A. Avella (Springer series, 2011) Chap. 13, pp. 409–455.

[35] B. Kyung, V. Hankevych, A.-M. Daré, and A.-M. S. Tremblay. Pseudogap and spin fluctuations in the normal state of the electron-doped cuprates. *Phys. Rev. Lett.*, 93:147004, Sep 2004. doi: 10.1103/PhysRevLett.93.147004. URL https://link.aps.org/doi/10.1103/PhysRevLett.93.147004.

[36] Dominic Bergeron, Vasyl Hankevych, Bumsoo Kyung, and A.-M. S. Tremblay. Optical and dc conductivity of the two-dimensional hubbard model in the pseudogap regime and across the antiferromagnetic quantum critical point including vertex corrections. *Phys. Rev. B*, 84:085128, Aug 2011. doi: 10.1103/PhysRevB.84.085128. URL https://link.aps.org/doi/10.1103/PhysRevB.84.085128.

[37] C. Gauvin-Ndiaye, M. Setrakian, and A.-M. S. Tremblay. Resilient fermi liquid and strength of correlations near an antiferromagnetic quantum critical point. *Phys. Rev. Lett.*, 128:087001, Feb 2022. doi: 10.1103/PhysRevLett.128.087001. URL https://link.aps.org/doi/10.1103/PhysRevLett.128.087001.

[38] A.-M. Daré, L. Raymond, G. Albinet, and A.-M. S. Tremblay. Interaction-induced adiabatic cooling for antiferromagnetism in optical lattices. *Phys. Rev. B*, 76:064402, Aug 2007. doi: 10.1103/PhysRevB.76.064402. URL https://link.aps.org/doi/10.1103/PhysRevB.76.064402.

[39] Nobel Prize Outreach AB. The nobel prize in physics 2016, 2023. URL https://www.nobelprize.org/prizes/physics/2016/summary/.

[40] Shinsei Ryu, Andreas P Schnyder, Akira Furusaki, and Andreas WW Ludwig. Topological insulators and superconductors: tenfold way and dimensional hierarchy. *New Journal of Physics*, 12(6):065010, 2010. doi: 10.1088/1367-2630/12/6/065010. URL https://doi.org/10.1088/1367-2630/12/6/065010.

[41] Xiao-Liang Qi and Shou-Cheng Zhang. Topological insulators and superconductors. *Rev. Mod. Phys.*, 83:1057–1110, Oct 2011. doi: 10.1103/RevModPhys.83.1057. URL https://link.aps.org/doi/10.1103/RevModPhys.83.1057.

[42] M. Zahid Hasan and Joel E. Moore. Three-dimensional topological insulators. *Annual Review of Condensed Matter Physics*, 2(1):55–78, 2011. doi: 10.1146/annurev-conmatphys-062910-140432. URL https://doi.org/10.1146/annurev-conmatphys-062910-140432.

[43] Joel E. Moore. The birth of topological insulators. *Nature*, 464(7286):194–198, Mar 2010. ISSN 1476-4687. doi: 10.1038/nature08916. URL https://doi.org/10.1038/nature08916.

[44] M. Z. Hasan and C. L. Kane. Colloquium: Topological insulators. *Rev. Mod. Phys.*, 82:3045–3067, Nov 2010. doi: 10.1103/RevModPhys.82.3045. URL https://link.aps.org/doi/10.1103/RevModPhys.82.3045.

[45] D. J. Thouless, M. Kohmoto, M. P. Nightingale, and M. den Nijs. Quantized hall conductance in a two-dimensional periodic potential. *Phys. Rev. Lett.*, 49:405–408, Aug 1982. doi: 10.1103/PhysRevLett.49.405. URL https://link.aps.org/doi/10.1103/PhysRevLett.49.405.

[46] R. Resta. Macroscopic electric polarization as a geometric quantum phase. *Europhysics Letters*, 22(2):133, apr 1993. doi: 10.1209/0295-5075/22/2/010. URL https://dx.doi.org/10.1209/0295-5075/22/2/010.

[47] R. D. King-Smith and David Vanderbilt. Theory of polarization of crystalline solids. *Phys. Rev. B*, 47:1651–1654, Jan 1993. doi: 10.1103/PhysRevB.47.1651. URL https://link.aps.org/doi/10.1103/PhysRevB.47.1651.

[48] C. L. Kane and E. J. Mele. Z_2 topological order and the quantum spin hall effect. *Phys. Rev. Lett.*, 95:146802, Sep 2005. doi: 10.1103/PhysRevLett.95.146802. URL https://link.aps.org/doi/10.1103/PhysRevLett.95.146802.

[49] C. L. Kane and E. J. Mele. Quantum spin hall effect in graphene. *Phys. Rev. Lett.*, 95:226801, Nov 2005. doi: 10.1103/PhysRevLett.95.226801. URL https://link.aps.org/doi/10.1103/PhysRevLett.95.226801.

[50] T. Thonhauser, Davide Ceresoli, David Vanderbilt, and R. Resta. Orbital magnetization in periodic insulators. *Phys. Rev. Lett.*, 95:137205, Sep 2005. doi: 10.1103/PhysRevLett.95.137205. URL https://link.aps.org/doi/10.1103/PhysRevLett.95.137205.

[51] Di Xiao, Junren Shi, and Qian Niu. Berry phase correction to electron density of states in solids. *Phys. Rev. Lett.*, 95:137204, Sep 2005. doi: 10.1103/PhysRevLett.95.137204. URL https://link.aps.org/doi/10.1103/PhysRevLett.95.137204.

[52] Alexander Altland and Martin R. Zirnbauer. Nonstandard symmetry classes in mesoscopic normal-superconducting hybrid structures. *Phys. Rev. B*, 55:1142–1161, Jan 1997. doi: 10.1103/PhysRevB.55.1142. URL https://link.aps.org/doi/10.1103/PhysRevB.55.1142.

[53] Andreas P. Schnyder, Shinsei Ryu, Akira Furusaki, and Andreas W. W. Ludwig. Classification of topological insulators and superconductors in three spatial dimensions. *Phys. Rev. B*, 78:195125, Nov 2008. doi: 10.1103/PhysRevB.78.195125. URL https://link.aps.org/doi/10.1103/PhysRevB.78.195125.

[54] Alexei Kitaev. Periodic table for topological insulators and superconductors. *AIP Conference Proceedings*, 1134(1):22–30, 2009. doi: 10.1063/1.3149495. URL https://aip.scitation.org/doi/abs/10.1063/1.3149495.

[55] Liang Fu. Topological crystalline insulators. *Phys. Rev. Lett.*, 106:106802, Mar 2011. doi: 10.1103/PhysRevLett.106.106802. URL https://link.aps.org/doi/10.1103/PhysRevLett.106.106802.

[56] Barry Bradlyn, L. Elcoro, Jennifer Cano, M. G. Vergniory, Zhijun Wang, C. Felser, M. I. Aroyo, and B. Andrei Bernevig. Topological quantum chemistry. *Nature*, 547(7663):298–305, 2017. ISSN 1476-4687. doi: 10.1038/nature23268. URL https://doi.org/10.1038/nature23268.

[57] Jennifer Cano, Barry Bradlyn, Zhijun Wang, L. Elcoro, M. G. Vergniory, C. Felser, M. I. Aroyo, and B. Andrei Bernevig. Building blocks of topological quantum chemistry: Elementary band representations. *Phys. Rev. B*, 97:035139, Jan 2018. doi: 10.1103/PhysRevB.97.035139. URL https://link.aps.org/doi/10.1103/PhysRevB.97.035139.

[58] J. Zak. Symmetry specification of bands in solids. *Phys. Rev. Lett.*, 45:1025–1028, Sep 1980. doi: 10.1103/PhysRevLett.45.1025. URL https://link.aps.org/doi/10.1103/PhysRevLett.45.1025.

[59] L. Michel and J. Zak. Connectivity of energy bands in crystals. *Phys. Rev. B*, 59:5998–6001, Mar 1999. doi: 10.1103/PhysRevB.59.5998. URL https://link.aps.org/doi/10.1103/PhysRevB.59.5998.

[60] L. Michel and J. Zak. Elementary energy bands in crystals are connected. *Physics Reports*, 341(1):377 – 395, 2001. ISSN 0370-1573. doi: https://doi.org/10.1016/S0370-1573(00)00093-4. URL http://www.sciencedirect.com/science/article/pii/S0370157300000934. Symmetry, invariants, topology.

[61] Hoi Chun Po, Ashvin Vishwanath, and Haruki Watanabe. Symmetry-based indicators of band topology in the 230 space groups. *Nature Communications*, 8(1):50, 2017. ISSN 2041-1723. doi: 10.1038/s41467-017-00133-2. URL https://doi.org/10.1038/s41467-017-00133-2.

[62] Eslam Khalaf, Hoi Chun Po, Ashvin Vishwanath, and Haruki Watanabe. Symmetry indicators and anomalous surface states of topological crystalline insulators. *Phys. Rev. X*, 8:031070, Sep 2018. doi: 10.1103/PhysRevX.8.031070. URL https://link.aps.org/doi/10.1103/PhysRevX.8.031070.

[63] Jorrit Kruthoff, Jan de Boer, Jasper van Wezel, Charles L. Kane, and Robert-Jan Slager. Topological classification of crystalline insulators through band structure combinatorics. *Phys. Rev. X*, 7:041069, Dec 2017. doi: 10.1103/PhysRevX.7.041069. URL https://link.aps.org/doi/10.1103/PhysRevX.7.041069.

[64] R. B. Laughlin. Anomalous quantum hall effect: An incompressible quantum fluid with fractionally charged excitations. *Phys. Rev. Lett.*, 50:1395–1398, May 1983. doi: 10.1103/PhysRevLett.50.1395. URL https://link.aps.org/doi/10.1103/PhysRevLett.50.1395.

[65] Xiao-Gang Wen. Colloquium: Zoo of quantum-topological phases of matter. *Rev. Mod. Phys.*, 89:041004, Dec 2017. doi: 10.1103/RevModPhys.89.041004. URL https://link.aps.org/doi/10.1103/RevModPhys.89.041004.

[66] Zheng-Cheng Gu and Xiao-Gang Wen. Tensor-entanglement-filtering renormalization approach and symmetry-protected topological order. *Phys. Rev. B*, 80:155131, Oct 2009. doi: 10.1103/PhysRevB.80.155131. URL https://link.aps.org/doi/10.1103/PhysRevB.80.155131.

[67] Frank Pollmann, Ari M. Turner, Erez Berg, and Masaki Oshikawa. Entanglement spectrum of a topological phase in one dimension. *Phys. Rev. B*, 81:064439, Feb 2010. doi: 10.1103/PhysRevB.81.064439. URL https://link.aps.org/doi/10.1103/PhysRevB.81.064439.

[68] Lukasz Fidkowski and Alexei Kitaev. Effects of interactions on the topological classification of free fermion systems. *Phys. Rev. B*, 81:134509, Apr 2010. doi: 10.1103/PhysRevB.81.134509. URL https://link.aps.org/doi/10.1103/PhysRevB.81.134509.

[69] Lukasz Fidkowski and Alexei Kitaev. Topological phases of fermions in one dimension. *Phys. Rev. B*, 83:075103, Feb 2011. doi: 10.1103/PhysRevB.83.075103. URL https://link.aps.org/doi/10.1103/PhysRevB.83.075103.

[70] Ari M. Turner, Frank Pollmann, and Erez Berg. Topological phases of one-dimensional fermions: An entanglement point of view. *Phys. Rev. B*, 83:075102, Feb 2011. doi: 10.1103/PhysRevB.83.075102. URL https://link.aps.org/doi/10.1103/PhysRevB.83.075102.

[71] Xie Chen, Zheng-Cheng Gu, and Xiao-Gang Wen. Classification of gapped symmetric phases in one-dimensional spin systems. *Phys. Rev. B*, 83:035107, Jan 2011. doi: 10.1103/PhysRevB.83.035107. URL https://link.aps.org/doi/10.1103/PhysRevB.83.035107.

[72] T. Senthil. Symmetry-protected topological phases of quantum matter. *Annual Review of Condensed Matter Physics*, 6(1):299–324, 2015. doi: 10.1146/annurev-conmatphys-031214-014740. URL https://doi.org/10.1146/annurev-conmatphys-031214-014740.

[73] G.E. Volovik. *The Universe in a helium droplet*. Oxford University Press, Oxford, 2003.

[74] G. E. Volovik. Topological invariant for superfluid 3he-b and quantum phase transitions. *JETP Letters*, 90(8):587–591, Dec 2009. ISSN 1090-6487. doi: 10.1134/S0021364009200089. URL https://doi.org/10.1134/S0021364009200089.

[75] G. E. Volovik. Topological invariants for standard model: From semi-metal to topological insulator. *JETP Letters*, 91(2):55–61, Jan 2010. ISSN 1090-6487. doi: 10.1134/S0021364010020013. URL https://doi.org/10.1134/S0021364010020013.

[76] V. Gurarie. Single-particle green's functions and interacting topological insulators. *Phys. Rev. B*, 83:085426, Feb 2011. doi: 10.1103/PhysRevB.83.085426. URL https://link.aps.org/doi/10.1103/PhysRevB.83.085426.

[77] Zhong Wang, Xiao-Liang Qi, and Shou-Cheng Zhang. Topological order parameters for interacting topological insulators. *Phys. Rev. Lett.*, 105:256803, Dec 2010. doi: 10.1103/PhysRevLett.105.256803. URL https://link.aps.org/doi/10.1103/PhysRevLett.105.256803.

[78] Zhong Wang, Xiao-Liang Qi, and Shou-Cheng Zhang. Topological invariants for interacting topological insulators with inversion symmetry. *Phys. Rev. B*, 85:165126, Apr 2012. doi: 10.1103/PhysRevB.85.165126. URL https://link.aps.org/doi/10.1103/PhysRevB.85.165126.

[79] Zhong Wang and Shou-Cheng Zhang. Simplified topological invariants for interacting insulators. *Phys. Rev. X*, 2:031008, Aug 2012. doi: 10.1103/PhysRevX.2.031008. URL https://link.aps.org/doi/10.1103/PhysRevX.2.031008.

[80] Zhong Wang and Binghai Yan. Topological hamiltonian as an exact tool for topological invariants. *Journal of Physics: Condensed Matter*, 25(15):155601, mar 2013. doi: 10.1088/0953-8984/25/15/155601. URL https://doi.org/10.1088%2F0953-8984%2F25%2F15%2F155601.

[81] Kenneth Gotlieb, Chiu-Yun Lin, Maksym Serbyn, Wentao Zhang, Christopher L. Smallwood, Christopher Jozwiak, Hiroshi Eisaki, Zahid Hussain, Ashvin Vishwanath, and Alessandra Lanzara. Revealing hidden spin-momentum locking in a high-temperature cuprate superconductor. *Science*, 362(6420):1271–1275, 2018. doi: 10.1126/science.aao0980. URL https://www.science.org/doi/abs/10.1126/science.aao0980.

[82] Xiancong Lu and David Sénéchal. Spin texture in a bilayer high-temperature cuprate superconductor. *Physical Review B*, 104(2):024502, Jul 2021. ISSN 2469-9950, 2469-9969. doi: 10.1103/PhysRevB.104.024502. arXiv:2102.12015 [cond-mat].

[83] Ali Ashrafi and Dmitrii L. Maslov. Chiral spin waves in fermi liquids with spin-orbit coupling. *Phys. Rev. Lett.*, 109:227201, Nov 2012. doi: 10.1103/PhysRevLett.109.227201. URL https://link.aps.org/doi/10.1103/PhysRevLett.109.227201.

[84] Ali Ashrafi, Emmanuel I. Rashba, and Dmitrii L. Maslov. Theory of a chiral fermi liquid: General formalism. *Phys. Rev. B*, 88:075115, Aug 2013. doi: 10.1103/PhysRevB.88.075115. URL https://link.aps.org/doi/10.1103/PhysRevB.88.075115.

[85] Shang-Shun Zhang, Xiao-Lu Yu, Jinwu Ye, and Wu-Ming Liu. Collective modes of spin-orbit-coupled fermi gases in the repulsive regime. *Phys. Rev. A*, 87:063623, Jun 2013. doi: 10.1103/PhysRevA.87.063623. URL https://link.aps.org/doi/10.1103/PhysRevA.87.063623.

[86] Saurabh Maiti, Vladimir Zyuzin, and Dmitrii L. Maslov. Collective modes in two- and three-dimensional electron systems with rashba spin-orbit coupling. *Phys. Rev. B*, 91:035106, Jan 2015. doi: 10.1103/PhysRevB.91.035106. URL https://link.aps.org/doi/10.1103/PhysRevB.91.035106.

[87] Saurabh Maiti, Muhammad Imran, and Dmitrii L. Maslov. Electron spin resonance in a two-dimensional fermi liquid with spin-orbit coupling. *Phys. Rev. B*, 93:045134, Jan 2016. doi: 10.1103/PhysRevB.93.045134. URL https://link.aps.org/doi/10.1103/PhysRevB.93.045134.

[88] Abhishek Kumar, Saurabh Maiti, and Dmitrii L. Maslov. Zero-field spin resonance in graphene with proximity-induced spin-orbit coupling. *Phys. Rev. B*, 104:155138, Oct 2021. doi: 10.1103/PhysRevB.104.155138. URL https://link.aps.org/doi/10.1103/PhysRevB.104.155138.

[89] M. I. D'Yakonov and V. I. Perel'. Possibility of Orienting Electron Spins with Current. *Soviet Journal of Experimental and Theoretical Physics Letters*, 13:467, June 1971.

[90] Markus König, Steffen Wiedmann, Christoph Brüne, Andreas Roth, Hartmut Buhmann, Laurens W. Molenkamp, Xiao-Liang Qi, and Shou-Cheng Zhang. Quantum spin hall insulator state in hgte quantum wells. *Science*, 318(5851):766–770, 2007. doi: 10.1126/science.1148047. URL https://www.science.org/doi/abs/10.1126/science.1148047.

[91] B. Andrei Bernevig, Taylor L. Hughes, and Shou-Cheng Zhang. Quantum spin hall effect and topological phase transition in hgte quantum wells. *Science*, 314(5806):1757–1761, 2006. doi: 10.1126/science.1133734. URL https://www.science.org/doi/abs/10.1126/science.1133734.

[92] Y. Maeno, H. Hashimoto, K. Yoshida, S. Nishizaki, T. Fujita, J. G. Bednorz, and F. Lichtenberg. Superconductivity in a layered perovskite without copper. *Nature*, 372(6506):532–534, Dec 1994. ISSN 1476-4687. doi: 10.1038/372532a0. URL https://doi.org/10.1038/372532a0.

[93] Andrew P. Mackenzie, Thomas Scaffidi, Clifford W. Hicks, and Yoshiteru Maeno. Even odder after twenty-three years: the superconducting order parameter puzzle of sr2ruo4. *npj Quantum Materials*, 2(1):40, Jul 2017. ISSN 2397-4648. doi: 10.1038/s41535-017-0045-4. URL https://doi.org/10.1038/s41535-017-0045-4.

[94] E. Pavarini and I. I. Mazin. First-principles study of spin-orbit effects and nmr in sr_2Ruo_4. *Phys. Rev. B*, 74:035115, Jul 2006. doi: 10.1103/PhysRevB.74.035115. URL https://link.aps.org/doi/10.1103/PhysRevB.74.035115.

[95] C. N. Veenstra, Z.-H. Zhu, M. Raichle, B. M. Ludbrook, A. Nicolaou, B. Slomski, G. Landolt, S. Kittaka, Y. Maeno, J. H. Dil, I. S. Elfimov, M. W. Haverkort, and A. Damascelli. Spin-orbital entanglement and the breakdown of singlets and triplets in sr_2ruo_4 revealed by spin- and angle-resolved photoemission spectroscopy. *Phys. Rev. Lett.*, 112:127002, Mar 2014. doi: 10.1103/PhysRevLett.112.127002. URL https://link.aps.org/doi/10.1103/PhysRevLett.112.127002.

[96] Emil J Rozbicki, James F Annett, Jean-René Souquet, and Andrew P Mackenzie. Spin–orbit coupling and k-dependent zeeman splitting in strontium ruthenate. *Journal of Physics: Condensed Matter*, 23(9):094201, feb 2011. doi: 10.1088/0953-8984/23/9/094201. URL https://dx.doi.org/10.1088/0953-8984/23/9/094201.

[97] M. W. Haverkort, I. S. Elfimov, L. H. Tjeng, G. A. Sawatzky, and A. Damascelli. Strong spin-orbit coupling effects on the fermi surface of sr_2ruo_4 and sr_2rho_4. *Phys. Rev. Lett.*, 101:026406, Jul 2008. doi: 10.1103/PhysRevLett.101.026406. URL https://link.aps.org/doi/10.1103/PhysRevLett.101.026406.

[98] A. Tamai, M. Zingl, E. Rozbicki, E. Cappelli, S. Riccò, A. de la Torre, S. McKeown Walker, F. Y. Bruno, P. D. C. King, W. Meevasana, M. Shi, M. Radović, N. C. Plumb, A. S. Gibbs, A. P. Mackenzie, C. Berthod, H. U. R. Strand, M. Kim, A. Georges, and F. Baumberger. High-resolution photoemission on sr_2ruo_4 reveals correlation-enhanced effective spin-orbit coupling and dominantly local self-energies. *Phys. Rev. X*, 9:021048, Jun 2019. doi: 10.1103/PhysRevX.9.021048. URL https://link.aps.org/doi/10.1103/PhysRevX.9.021048.

[99] O. Gingras, N. Allaglo, R. Nourafkan, M. Côté, and A.-M. S. Tremblay. Superconductivity in correlated multiorbital systems with spin-orbit coupling: Coexistence of even- and odd-frequency pairing, and the case of sr_2ruo_4. *Phys. Rev. B*, 106:064513, Aug 2022. doi: 10.1103/PhysRevB.106.064513. URL https://link.aps.org/doi/10.1103/PhysRevB.106.064513.

[100] André-Marie Tremblay. Phy-892 quantum materials theory, from perturbation theory to dynamical mean-field theory (lecture notes), April 2021.

[101] G.D. Mahan. *Many-Particle Physics*. Physics of Solids and Liquids. Springer, 2000. ISBN 9780306463389.

[102] P. Coleman. *Introduction to Many-Body Physics*. Cambridge University Press, 2015. ISBN 9780521864886.

[103] J.W. Negele. *Quantum Many-particle Systems*. CRC Press, 2018. ISBN 9780429966477.

[104] Paul C. Martin and Julian Schwinger. Theory of many-particle systems. i. *Phys. Rev.*, 115:1342–1373, Sep 1959. doi: 10.1103/PhysRev.115.1342. URL https://link.aps.org/doi/10.1103/PhysRev.115.1342.

[105] L.P. Kadanoff and G. Baym. *Quantum Statistical Mechanics: Green's Function Methods in Equilibrium and Nonequilibrium Problems*. Frontiers in Physics: Lecture note and reprint series, A. W.A. Benjamin, 1962. ISBN 9780805352016. URL https://books.google.de/books?id=1-FEAAAAIAAJ.

[106] W. P. Su, J. R. Schrieffer, and A. J. Heeger. Solitons in polyacetylene. *Phys. Rev. Lett.*, 42:1698–1701, Jun 1979. doi: 10.1103/PhysRevLett.42.1698. URL https://link.aps.org/doi/10.1103/PhysRevLett.42.1698.

[107] Kenzo Ishikawa and Toyoki Matsuyama. A microscopic theory of the quantum hall effect. *Nuclear Physics B*, 280:523–548, 1987. ISSN 0550-3213. doi: https://doi.org/10.1016/0550-3213(87)90160-X. URL https://www.sciencedirect.com/science/article/pii/055032138790160X.

[108] Kiaran B. Dave, Philip W. Phillips, and Charles L. Kane. Absence of luttinger's theorem due to zeros in the single-particle green function. *Phys. Rev. Lett.*, 110:090403, Feb 2013. doi: 10.1103/PhysRevLett.110.090403. URL https://link.aps.org/doi/10.1103/PhysRevLett.110.090403.

[109] J. M. Luttinger. Analytic properties of single-particle propagators for many-fermion systems. *Phys. Rev.*, 121:942–949, Feb 1961. doi: 10.1103/PhysRev.121.942. URL https://link.aps.org/doi/10.1103/PhysRev.121.942.

[110] Salvatore R. Manmana, Andrew M. Essin, Reinhard M. Noack, and Victor Gurarie. Topological invariants and interacting one-dimensional fermionic systems. *Phys. Rev. B*, 86:205119, Nov 2012. doi: 10.1103/PhysRevB.86.205119. URL https://link.aps.org/doi/10.1103/PhysRevB.86.205119.

[111] Tsuneya Yoshida, Robert Peters, Satoshi Fujimoto, and Norio Kawakami. Characterization of a topological mott insulator in one dimension. *Phys. Rev. Lett.*, 112:196404, May 2014. doi: 10.1103/PhysRevLett.112.196404. URL https://link.aps.org/doi/10.1103/PhysRevLett.112.196404.

[112] Yuan-Yao He, Han-Qing Wu, Zi Yang Meng, and Zhong-Yi Lu. Topological invariants for interacting topological insulators. i. efficient numerical evaluation scheme and implementations. *Phys. Rev. B*, 93:195163, May 2016. doi: 10.1103/PhysRevB.93.195163. URL https://link.aps.org/doi/10.1103/PhysRevB.93.195163.

[113] Thomas Mertz, Karim Zantout, and Roser Valentí. Statistical analysis of the chern number in the interacting haldane-hubbard model. *Phys. Rev. B*, 100:125111, Sep 2019. doi: 10.1103/PhysRevB.100.125111. URL https://link.aps.org/doi/10.1103/PhysRevB.100.125111.

[114] ZI YANG MENG, HSIANG-HSUAN HUNG, and THOMAS C. LANG. The characterization of topological properties in quantum monte carlo simulations of the kane–mele–hubbard model. *Modern Physics Letters B*, 28(01):1430001, 2014. doi: 10.1142/S0217984914300014. URL https://doi.org/10.1142/S0217984914300014.

[115] Hsiang-Hsuan Hung, Lei Wang, Zheng-Cheng Gu, and Gregory A. Fiete. Topological phase transition in a generalized kane-mele-hubbard model: A combined quantum monte carlo and green's function study. *Phys. Rev. B*, 87:121113, Mar 2013. doi: 10.1103/PhysRevB.87.121113. URL https://link.aps.org/doi/10.1103/PhysRevB.87.121113.

[116] Hsiang-Hsuan Hung, Victor Chua, Lei Wang, and Gregory A. Fiete. Interaction effects on topological phase transitions via numerically exact quantum monte carlo calculations. *Phys. Rev. B*, 89:235104, Jun 2014. doi: 10.1103/PhysRevB.89.235104. URL https://link.aps.org/doi/10.1103/PhysRevB.89.235104.

[117] Yao-Hua Chen, Hsiang-Hsuan Hung, Guoxiong Su, Gregory A. Fiete, and C. S. Ting. Cellular dynamical mean-field theory study of an interacting topological honeycomb lattice model at finite temperature. *Phys. Rev. B*, 91:045122, Jan 2015. doi: 10.1103/PhysRevB.91.045122. URL https://link.aps.org/doi/10.1103/PhysRevB.91.045122.

[118] Jan Carl Budich, Björn Trauzettel, and Giorgio Sangiovanni. Fluctuation-driven topological hund insulators. *Phys. Rev. B*, 87:235104, Jun 2013. doi: 10.1103/PhysRevB.87.235104. URL https://link.aps.org/doi/10.1103/PhysRevB.87.235104.

[119] A. Amaricci, J. C. Budich, M. Capone, B. Trauzettel, and G. Sangiovanni. First-order character and observable signatures of topological quantum phase transitions. *Phys. Rev. Lett.*, 114:185701, May 2015. doi: 10.1103/PhysRevLett.114.185701. URL https://link.aps.org/doi/10.1103/PhysRevLett.114.185701.

[120] Mois Ilia Aroyo, Juan Manuel Perez-Mato, Cesar Capillas, Eli Kroumova, Svetoslav Ivantchev, Gotzon Madariaga, Asen Kirov, and Hans Wondratschek. Bilbao crystallographic server: I. databases and crystallographic computing programs. *Zeitschrift für Kristallographie - Crystalline Materials*, 221(1):15–27, 2006. doi: doi:10.1524/zkri.2006.221.1.15. URL https://doi.org/10.1524/zkri.2006.221.1.15.

[121] Mois I. Aroyo, Asen Kirov, Cesar Capillas, J. M. Perez-Mato, and Hans Wondratschek. Bilbao Crystallographic Server. II. Representations of crystallographic point groups and space groups. *Acta Crystallographica Section A*, 62(2):115–128, Mar 2006. doi: 10.1107/S0108767305040286. URL https://doi.org/10.1107/S0108767305040286.

[122] Jan Carl Budich and Björn Trauzettel. From the adiabatic theorem of quantum mechanics to topological states of matter. *physica status solidi (RRL) – Rapid Research Letters*, 7(1-2):109–129, 2013. doi: 10.1002/pssr.201206416. URL https://onlinelibrary.wiley.com/doi/abs/10.1002/pssr.201206416.

[123] Yi-Zhuang You, Zhong Wang, Jeremy Oon, and Cenke Xu. Topological number and fermion green's function for strongly interacting topological superconductors. *Phys. Rev. B*, 90:060502, Aug 2014. doi: 10.1103/PhysRevB.90.060502. URL https://link.aps.org/doi/10.1103/PhysRevB.90.060502.

[124] Hong Yao and Steven A. Kivelson. Fragile mott insulators. *Phys. Rev. Lett.*, 105:166402, Oct 2010. doi: 10.1103/PhysRevLett.105.166402. URL https://link.aps.org/doi/10.1103/PhysRevLett.105.166402.

[125] Niklas Wagner, Lorenzo Crippa, Adriano Amaricci, Philipp Hansmann, Marcel Klett, Elio König, Thomas Schäfer, Domenico Di Sante, Jennifer Cano, Andrew Millis, Antoine Georges, and Giorgio Sangiovanni. Mott insulators with boundary zeros, 2023.

[126] C. Gauvin-Ndiaye. *L'approche auto-cohérente à deux particules : cuprates dopésen électrons et améliorations de la méthode*. Phd thesis, Université de Sherbrooke, Sherbrooke, Canada, July 2023.

[127] J. Sichau, M. Prada, T. Anlauf, T. J. Lyon, B. Bosnjak, L. Tiemann, and R. H. Blick. Resonance microwave measurements of an intrinsic spin-orbit coupling gap in graphene: A possible indication of a topological state. *Phys. Rev. Lett.*, 122:046403, Feb 2019. doi: 10.1103/PhysRevLett.122.046403. URL https://link.aps.org/doi/10.1103/PhysRevLett.122.046403.

[128] Cheng-Cheng Liu, Wanxiang Feng, and Yugui Yao. Quantum spin hall effect in silicene and two-dimensional germanium. *Phys. Rev. Lett.*, 107:076802, Aug 2011. doi: 10.1103/PhysRevLett.107.076802. URL https://link.aps.org/doi/10.1103/PhysRevLett.107.076802.

[129] Pantelis Bampoulis, Carolien Castenmiller, Dennis J. Klaassen, Jelle van Mil, Yichen Liu, Cheng-Cheng Liu, Yugui Yao, Motohiko Ezawa, Alexander N. Rudenko, and Harold J. W. Zandvliet. Quantum spin hall states and topological phase transition in germanene. *Phys. Rev. Lett.*, 130:196401, May 2023. doi: 10.1103/PhysRevLett.130.196401. URL https://link.aps.org/doi/10.1103/PhysRevLett.130.196401.

[130] B. J. Kim, Hosub Jin, S. J. Moon, J.-Y. Kim, B.-G. Park, C. S. Leem, Jaejun Yu, T. W. Noh, C. Kim, S.-J. Oh, J.-H. Park, V. Durairaj, G. Cao, and E. Rotenberg. Novel $J_{\text{eff}} = 1/2$ mott state induced by relativistic spin-orbit coupling in sr_2iro_4. *Phys. Rev. Lett.*, 101:076402, Aug 2008. doi: 10.1103/PhysRevLett.101.076402. URL https://link.aps.org/doi/10.1103/PhysRevLett.101.076402.

[131] K. Ishizaka, M. S. Bahramy, H. Murakawa, M. Sakano, T. Shimojima, T. Sonobe, K. Koizumi, S. Shin, H. Miyahara, A. Kimura, K. Miyamoto, T. Okuda, H. Namatame, M. Taniguchi, R. Arita, N. Nagaosa, K. Kobayashi, Y. Murakami, R. Kumai, Y. Kaneko, Y. Onose, and Y. Tokura. Giant rashba-type spin splitting in bulk bitei. *Nature Materials*, 10(7):521–526, Jul 2011. ISSN 1476-4660. doi: 10.1038/nmat3051. URL https://doi.org/10.1038/nmat3051.

[132] B. J. Kim, H. Ohsumi, T. Komesu, S. Sakai, T. Morita, H. Takagi, and T. Arima. Phase-sensitive observation of a spin-orbital mott state in sr¡sub¿2¡/sub¿iro¡sub¿4¡/sub¿. *Science*, 323(5919):1329–1332, 2009. doi: 10.1126/science.1167106. URL https://www.science.org/doi/abs/10.1126/science.1167106.

[133] M. K. Crawford, M. A. Subramanian, R. L. Harlow, J. A. Fernandez-Baca, Z. R. Wang, and D. C. Johnston. Structural and magnetic studies of sr_2iro_4. *Phys. Rev. B*, 49:9198–9201, Apr 1994. doi: 10.1103/PhysRevB.49.9198. URL https://link.aps.org/doi/10.1103/PhysRevB.49.9198.

[134] G. Cao, J. Bolivar, S. McCall, J. E. Crow, and R. P. Guertin. Weak ferromagnetism, metal-to-nonmetal transition, and negative differential resistivity in single-crystal sr_2iro_4. *Phys. Rev. B*, 57: R11039–R11042, May 1998. doi: 10.1103/PhysRevB.57.R11039. URL https://link.aps.org/doi/10.1103/PhysRevB.57.R11039.

[135] William Witczak-Krempa, Gang Chen, Yong Baek Kim, and Leon Balents. Correlated quantum phenomena in the strong spin-orbit regime. *Annual Review of Condensed Matter Physics*, 5(1):57–82, 2014. doi: 10.1146/annurev-conmatphys-020911-125138. URL https://doi.org/10.1146/annurev-conmatphys-020911-125138.

[136] Jeffrey G. Rau, Eric Kin-Ho Lee, and Hae-Young Kee. Spin-orbit physics giving rise to novel phases in correlated systems: Iridates and related materials. *Annual Review of Condensed Matter Physics*, 7(1):195–221, 2016. doi: 10.1146/annurev-conmatphys-031115-011319. URL https://doi.org/10.1146/annurev-conmatphys-031115-011319.

[137] Y. Mizukami, H. Shishido, T. Shibauchi, M. Shimozawa, S. Yasumoto, D. Watanabe, M. Yamashita, H. Ikeda, T. Terashima, H. Kontani, and Y. Matsuda. Extremely strong-coupling superconductivity in artificial two-dimensional kondo lattices. *Nature Physics*, 7(11):849–853, Nov 2011. ISSN 1745-2481. doi: 10.1038/nphys2112. URL https://doi.org/10.1038/nphys2112.

[138] M. Shimozawa, S. K. Goh, R. Endo, R. Kobayashi, T. Watashige, Y. Mizukami, H. Ikeda, H. Shishido, Y. Yanase, T. Terashima, T. Shibauchi, and Y. Matsuda. Controllable rashba spin-orbit interaction in artificially engineered superlattices involving the heavy-fermion superconductor $cecoin_5$. *Phys. Rev. Lett.*, 112:156404, Apr 2014. doi: 10.1103/PhysRevLett.112.156404. URL https://link.aps.org/doi/10.1103/PhysRevLett.112.156404.

[139] A. D. Caviglia, M. Gabay, S. Gariglio, N. Reyren, C. Cancellieri, and J.-M. Triscone. Tunable rashba spin-orbit interaction at oxide interfaces. *Phys. Rev. Lett.*, 104:126803, Mar 2010. doi: 10.1103/PhysRevLett.104.126803. URL https://link.aps.org/doi/10.1103/PhysRevLett.104.126803.

[140] Sarnjeet S. Dhesi, Gerrit van der Laan, Esther Dudzik, and Alexander B. Shick. Anisotropic spin-orbit coupling and magnetocrystalline anisotropy in vicinal co films. *Phys. Rev. Lett.*, 87: 067201, Jul 2001. doi: 10.1103/PhysRevLett.87.067201. URL https://link.aps.org/doi/10.1103/PhysRevLett.87.067201.

[141] A. B. Shick, S. Khmelevskyi, O. N. Mryasov, J. Wunderlich, and T. Jungwirth. Spin-orbit coupling induced anisotropy effects in bimetallic antiferromagnets: A route towards antiferromagnetic spintronics. *Phys. Rev. B*, 81:212409, Jun 2010. doi: 10.1103/PhysRevB.81.212409. URL https://link.aps.org/doi/10.1103/PhysRevB.81.212409.

[142] Yang Li, Zeyu Jiang, Jiaheng Li, Shengnan Xu, and Wenhui Duan. Magnetic anisotropy of the two-dimensional ferromagnetic insulator $mnbi_2te_4$. *Phys. Rev. B*, 100:134438, Oct 2019. doi: 10.1103/PhysRevB.100.134438. URL https://link.aps.org/doi/10.1103/PhysRevB.100.134438.

[143] Y. K. Kato, R. C. Myers, A. C. Gossard, and D. D. Awschalom. Observation of the spin hall effect in semiconductors. *Science*, 306(5703):1910–1913, 2004. doi: 10.1126/science.1105514. URL https://www.science.org/doi/abs/10.1126/science.1105514.

[144] J. Wunderlich, B. Kaestner, J. Sinova, and T. Jungwirth. Experimental observation of the spin-hall effect in a two-dimensional spin-orbit coupled semiconductor system. *Phys. Rev. Lett.*, 94: 047204, Feb 2005. doi: 10.1103/PhysRevLett.94.047204. URL https://link.aps.org/doi/10.1103/PhysRevLett.94.047204.

[145] Liang Fu and C. L. Kane. Superconducting proximity effect and majorana fermions at the surface of a topological insulator. *Phys. Rev. Lett.*, 100:096407, Mar 2008. doi: 10.1103/PhysRevLett.100.096407. URL https://link.aps.org/doi/10.1103/PhysRevLett.100.096407.

[146] Mehdi Kargarian, Dmitry K. Efimkin, and Victor Galitski. Amperean pairing at the surface of topological insulators. *Phys. Rev. Lett.*, 117:076806, Aug 2016. doi: 10.1103/PhysRevLett.117.076806. URL https://link.aps.org/doi/10.1103/PhysRevLett.117.076806.

[147] Manuel Laubach, Johannes Reuther, Ronny Thomale, and Stephan Rachel. Rashba spin-orbit coupling in the kane-mele-hubbard model. *Phys. Rev. B*, 90:165136, Oct 2014. doi: 10.1103/PhysRevB.90.165136. URL https://link.aps.org/doi/10.1103/PhysRevB.90.165136.

[148] Andrés Greco and Andreas P. Schnyder. Mechanism for unconventional superconductivity in the hole-doped rashba-hubbard model. *Phys. Rev. Lett.*, 120:177002, Apr 2018. doi: 10.1103/PhysRevLett.120.177002. URL https://link.aps.org/doi/10.1103/PhysRevLett.120.177002.

[149] Andrés Greco, Matías Bejas, and Andreas P. Schnyder. Ferromagnetic fluctuations in the rashba-hubbard model. *Phys. Rev. B*, 101:174420, May 2020. doi: 10.1103/PhysRevB.101.174420. URL https://link.aps.org/doi/10.1103/PhysRevB.101.174420.

[150] Rasoul Ghadimi, Mehdi Kargarian, and S. Akbar Jafari. Competing superconducting phases in the interacting two-dimensional electron gas with strong rashba spin-orbit coupling. *Phys. Rev. B*, 99:115122, Mar 2019. doi: 10.1103/PhysRevB.99.115122. URL https://link.aps.org/doi/10.1103/PhysRevB.99.115122.

[151] Sebastian Wolf and Stephan Rachel. Spin-orbit coupled superconductivity: Rashba-hubbard model on the square lattice. *Phys. Rev. B*, 102:174512, Nov 2020. doi: 10.1103/PhysRevB.102.174512. URL https://link.aps.org/doi/10.1103/PhysRevB.102.174512.

[152] Jacob Beyer, Jonas B. Hauck, Lennart Klebl, Tilman Schwemmer, Dante M. Kennes, Ronny Thomale, Carsten Honerkamp, and Stephan Rachel. Rashba spin-orbit coupling in the square-lattice hubbard model: A truncated-unity functional renormalization group study. *Phys. Rev. B*, 107:125115, Mar 2023. doi: 10.1103/PhysRevB.107.125115. URL https://link.aps.org/doi/10.1103/PhysRevB.107.125115.

[153] Erik Wegner Hodt, Jabir Ali Ouassou, and Jacob Linder. Transient dynamics and quantum phase diagram for the square lattice rashba-hubbard model at arbitrary hole doping. *Phys. Rev. B*, 107:224427, Jun 2023. doi: 10.1103/PhysRevB.107.224427. URL https://link.aps.org/doi/10.1103/PhysRevB.107.224427.

[154] Lorenzo Del Re and Alessandro Toschi. Dynamical vertex approximation for many-electron systems with spontaneously broken su(2) symmetry. *Physical Review B*, 104(8):085120, Aug 2021. doi: 10.1103/PhysRevB.104.085120.

[155] Thomas Schäfer, Nils Wentzell, Fedor Šimkovic, Yuan-Yao He, Cornelia Hille, Marcel Klett, Christian J. Eckhardt, Behnam Arzhang, Viktor Harkov, François-Marie Le Régent, Alfred Kirsch, Yan Wang, Aaram J. Kim, Evgeny Kozik, Evgeny A. Stepanov, Anna Kauch, Sabine Andergassen, Philipp Hansmann, Daniel Rohe, Yuri M. Vilk, James P. F. LeBlanc, Shiwei Zhang, A.-M. S. Tremblay, Michel Ferrero, Olivier Parcollet, and Antoine Georges. Tracking the footprints of spin fluctuations: A multimethod, multimessenger study of the two-dimensional hubbard model. *Physical Review X*, 11(1):011058, Mar 2021. doi: 10.1103/PhysRevX.11.011058.

[156] Alain F. Veilleux, Anne-Marie Daré, Liang Chen, Y. M. Vilk, and A.-M. S. Tremblay. Magnetic and pair correlations of the hubbard model with next-nearest-neighbor hopping. *Phys. Rev. B*, 52:16255–16263, Dec 1995. doi: 10.1103/PhysRevB.52.16255. URL https://link.aps.org/doi/10.1103/PhysRevB.52.16255.

[157] S. Moukouri, S. Allen, F. Lemay, B. Kyung, D. Poulin, Y. M. Vilk, and A.-M. S. Tremblay. Many-body theory versus simulations for the pseudogap in the hubbard model. *Phys. Rev. B*, 61:7887–7892, Mar 2000. doi: 10.1103/PhysRevB.61.7887. URL https://link.aps.org/doi/10.1103/PhysRevB.61.7887.

[158] B. Kyung, S. Allen, and A.-M. S. Tremblay. Pairing fluctuations and pseudogaps in the attractive hubbard model. *Phys. Rev. B*, 64:075116, Jul 2001. doi: 10.1103/PhysRevB.64.075116. URL https://link.aps.org/doi/10.1103/PhysRevB.64.075116.

[159] N. Martin, C. Gauvin-Ndiaye, and A.-M. S. Tremblay. Nonlocal corrections to dynamical mean-field theory from the two-particle self-consistent method. *Phys. Rev. B*, 107:075158, Feb 2023. doi: 10.1103/PhysRevB.107.075158. URL https://link.aps.org/doi/10.1103/PhysRevB.107.075158.

[160] Olivier Simard and Philipp Werner. Dynamical mean field theory extension to the nonequilibrium two-particle self-consistent approach, 2023.

[161] C. Gauvin-Ndiaye, C. Lahaie, Y. M. Vilk, and A. M. S. Tremblay. An improved two-particle self-consistent approach, 2023.

[162] Olivier Simard and Philipp Werner. Nonequilibrium two-particle self-consistent approach. *Phys. Rev. B*, 106:L241110, Dec 2022. doi: 10.1103/PhysRevB.106.L241110. URL https://link.aps.org/doi/10.1103/PhysRevB.106.L241110.

[163] S. Arya, P. V. Sriluckshmy, S. R. Hassan, and A.-M. S. Tremblay. Antiferromagnetism in the hubbard model on the honeycomb lattice: A two-particle self-consistent study. *Phys. Rev. B*, 92:045111, Jul 2015. doi: 10.1103/PhysRevB.92.045111. URL https://link.aps.org/doi/10.1103/PhysRevB.92.045111.

[164] Hirohito Aizawa, Kazuhiko Kuroki, and Jun-ichi Yamada. Enhancement of electron correlation due to the molecular dimerization in organic superconductors $\beta - (\mathrm{BDA} - \mathrm{TTP})_2 x$ ($x = \mathrm{i}_3, \mathrm{sbf}_6$). *Physical Review B*, 92(15):155108, Oct 2015. doi: 10.1103/PhysRevB.92.155108.

[165] Daisuke Ogura and Kazuhiko Kuroki. Asymmetry of superconductivity in hole- and electron-doped cuprates: Explanation within two-particle self-consistent analysis for the three-band model. *Physical Review B*, 92(14):144511, Oct 2015. doi: 10.1103/PhysRevB.92.144511.

[166] Karim Zantout, Michaela Altmeyer, Steffen Backes, and Roser Valentí. Superconductivity in correlated bedt-ttf molecular conductors: Critical temperatures and gap symmetries. *Physical Review B*, 97(1):014530, Jan 2018. doi: 10.1103/PhysRevB.97.014530.

[167] Hideyuki Miyahara, Ryotaro Arita, and Hiroaki Ikeda. Development of a two-particle self-consistent method for multiorbital systems and its application to unconventional superconductors. *Phys. Rev. B*, 87:045113, Jan 2013. doi: 10.1103/PhysRevB.87.045113. URL https://link.aps.org/doi/10.1103/PhysRevB.87.045113.

[168] Karim Zantout, Steffen Backes, and Roser Valentí. Effect of nonlocal correlations on the electronic structure of lifeas. *Phys. Rev. Lett.*, 123:256401, Dec 2019. doi: 10.1103/PhysRevLett.123.256401. URL https://link.aps.org/doi/10.1103/PhysRevLett.123.256401.

[169] Karim Zantout, Steffen Backes, and Roser Valentí. Two-particle self-consistent method for the multi-orbital hubbard model. *Annalen der Physik*, 533(2):2000399, 2021.

[170] B. Davoudi and A.-M. S. Tremblay. Nearest-neighbor repulsion and competing charge and spin order in the extended hubbard model. *Phys. Rev. B*, 74:035113, Jul 2006. doi: 10.1103/PhysRevB.74.035113. URL https://link.aps.org/doi/10.1103/PhysRevB.74.035113.

[171] B. Davoudi and A.-M. S. Tremblay. Non-perturbative treatment of charge and spin fluctuations in the two-dimensional extended hubbard model: Extended two-particle self-consistent approach. *Phys. Rev. B*, 76:085115, Aug 2007. doi: 10.1103/PhysRevB.76.085115. URL https://link.aps.org/doi/10.1103/PhysRevB.76.085115.

[172] B. Davoudi, S. R. Hassan, and A.-M. S. Tremblay. Competition between charge and spin order in the $t-u-v$ extended hubbard model on the triangular lattice. *Phys. Rev. B*, 77:214408, Jun 2008. doi: 10.1103/PhysRevB.77.214408. URL https://link.aps.org/doi/10.1103/PhysRevB.77.214408.

[173] S. Allen and A.-M. S. Tremblay. Nonperturbative approach to the attractive hubbard model. *Phys. Rev. B*, 64:075115, Jul 2001. doi: 10.1103/PhysRevB.64.075115. URL https://link.aps.org/doi/10.1103/PhysRevB.64.075115.

[174] V. Hankevych, B. Kyung, and A.-M. S. Tremblay. Weak ferromagnetism and other instabilities of the two-dimensional $t - t'$ hubbard model at van hove fillings. *Phys. Rev. B*, 68:214405, Dec 2003. doi: 10.1103/PhysRevB.68.214405. URL https://link.aps.org/doi/10.1103/PhysRevB.68.214405.

[175] Anne-Marie Daré, Y. M. Vilk, and A. M. S. Tremblay. Crossover from two- to three-dimensional critical behavior for nearly antiferromagnetic itinerant electrons. *Phys. Rev. B*, 53:14236–14251, Jun 1996. doi: 10.1103/PhysRevB.53.14236. URL https://link.aps.org/doi/10.1103/PhysRevB.53.14236.

[176] Anne-Marie Daré and Gilbert Albinet. Magnetic properties of the three-dimensional hubbard model at half filling. *Phys. Rev. B*, 61:4567–4575, Feb 2000. doi: 10.1103/PhysRevB.61.4567. URL https://link.aps.org/doi/10.1103/PhysRevB.61.4567.

[177] Bumsoo Kyung, Jean-Sébastien Landry, and A.-M. S. Tremblay. Antiferromagnetic fluctuations and d-wave superconductivity in electron-doped high-temperature superconductors. *Phys. Rev. B*, 68:174502, Nov 2003. doi: 10.1103/PhysRevB.68.174502. URL https://link.aps.org/doi/10.1103/PhysRevB.68.174502.

[178] S. R. Hassan, B. Davoudi, B. Kyung, and A.-M. S. Tremblay. Conditions for magnetically induced singlet d-wave superconductivity on the square lattice. *Phys. Rev. B*, 77:094501, Mar 2008. doi: 10.1103/PhysRevB.77.094501. URL https://link.aps.org/doi/10.1103/PhysRevB.77.094501.

[179] Junya Otsuki. Two-particle self-consistent approach to unconventional superconductivity. *Phys. Rev. B*, 85:104513, Mar 2012. doi: 10.1103/PhysRevB.85.104513. URL https://link.aps.org/doi/10.1103/PhysRevB.85.104513.

[180] Daisuke Ogura and Kazuhiko Kuroki. Asymmetry of superconductivity in hole- and electron-doped cuprates: Explanation within two-particle self-consistent analysis for the three-band model. *Phys. Rev. B*, 92:144511, Oct 2015. doi: 10.1103/PhysRevB.92.144511. URL https://link.aps.org/doi/10.1103/PhysRevB.92.144511.

[181] H. Nélisse, C. Bourbonnais, H. Touchette, Y. M. Vilk, and A.-M. S. Tremblay. Spin susceptibility of interacting electrons in one dimension: Luttinger liquid and lattice effects. *The European Physical Journal B - Condensed Matter and Complex Systems*, 12(3):351–365, Dec 1999. ISSN 1434-6036. doi: 10.1007/s100510051016. URL https://doi.org/10.1007/s100510051016.

[182] J. M. Luttinger and J. C. Ward. Ground-state energy of a many-fermion system. ii. *Phys. Rev.*, 118:1417–1427, Jun 1960. doi: 10.1103/PhysRev.118.1417. URL https://link.aps.org/doi/10.1103/PhysRev.118.1417.

[183] Gordon Baym and Leo P. Kadanoff. Conservation laws and correlation functions. *Phys. Rev.*, 124:287–299, Oct 1961. doi: 10.1103/PhysRev.124.287. URL https://link.aps.org/doi/10.1103/PhysRev.124.287.

[184] Gordon Baym. Self-consistent approximations in many-body systems. *Phys. Rev.*, 127:1391–1401, Aug 1962. doi: 10.1103/PhysRev.127.1391. URL https://link.aps.org/doi/10.1103/PhysRev.127.1391.

[185] Michael Potthoff. Non-perturbative construction of the luttinger-ward functional, 2004.

[186] C. Gauvin-Ndiaye. A python library that allows the computation of hubbard model related functions and quantities (such as the self-energy and green's function) using the two-particle-self-consistent (TPSC) approach first described in [vilk and tremblay, 1997]. https://github.com/amstremblay/TPSC, 2023.

[187] Markus Wallerberger, Samuel Badr, Shintaro Hoshino, Sebastian Huber, Fumiya Kakizawa, Takashi Koretsune, Yuki Nagai, Kosuke Nogaki, Takuya Nomoto, Hitoshi Mori, Junya Otsuki, Soshun Ozaki, Thomas Plaikner, Rihito Sakurai, Constanze Vogel, Niklas Witt, Kazuyoshi Yoshimi, and Hiroshi Shinaoka. sparse-ir: Optimal compression and sparse sampling of many-body propagators. *SoftwareX*, 21:101266, 2023. ISSN 2352-7110. doi: https://doi.org/10.1016/j.softx.2022.101266. URL https://www.sciencedirect.com/science/article/pii/S2352711022001844.

[188] Hiroshi Shinaoka, Junya Otsuki, Masayuki Ohzeki, and Kazuyoshi Yoshimi. Compressing green's function using intermediate representation between imaginary-time and real-frequency domains. *Phys. Rev. B*, 96:035147, Jul 2017. doi: 10.1103/PhysRevB.96.035147. URL https://link.aps.org/doi/10.1103/PhysRevB.96.035147.

[189] Jia Li, Markus Wallerberger, Naoya Chikano, Chia-Nan Yeh, Emanuel Gull, and Hiroshi Shinaoka. Sparse sampling approach to efficient ab initio calculations at finite temperature. *Phys. Rev. B*, 101:035144, Jan 2020. doi: 10.1103/PhysRevB.101.035144. URL https://link.aps.org/doi/10.1103/PhysRevB.101.035144.

[190] Yugui Yao, Fei Ye, Xiao-Liang Qi, Shou-Cheng Zhang, and Zhong Fang. Spin-orbit gap of graphene: First-principles calculations. *Phys. Rev. B*, 75:041401, Jan 2007. doi: 10.1103/PhysRevB.75.041401. URL https://link.aps.org/doi/10.1103/PhysRevB.75.041401.

[191] Hongki Min, J. E. Hill, N. A. Sinitsyn, B. R. Sahu, Leonard Kleinman, and A. H. MacDonald. Intrinsic and rashba spin-orbit interactions in graphene sheets. *Phys. Rev. B*, 74:165310, Oct 2006. doi: 10.1103/PhysRevB.74.165310. URL https://link.aps.org/doi/10.1103/PhysRevB.74.165310.

[192] Daniel Huertas-Hernando, F. Guinea, and Arne Brataas. Spin-orbit coupling in curved graphene, fullerenes, nanotubes, and nanotube caps. *Phys. Rev. B*, 74:155426, Oct 2006. doi: 10.1103/PhysRevB.74.155426. URL https://link.aps.org/doi/10.1103/PhysRevB.74.155426.

[193] F. D. M. Haldane. Model for a quantum hall effect without landau levels: Condensed-matter realization of the "parity anomaly". *Phys. Rev. Lett.*, 61:2015–2018, Oct 1988. doi: 10.1103/PhysRevLett.61.2015. URL https://link.aps.org/doi/10.1103/PhysRevLett.61.2015.

[194] Dung-Hai Lee. Effects of interaction on quantum spin hall insulators. *Phys. Rev. Lett.*, 107:166806, Oct 2011. doi: 10.1103/PhysRevLett.107.166806. URL https://link.aps.org/doi/10.1103/PhysRevLett.107.166806.

[195] Christian Griset and Cenke Xu. Phase diagram of the kane-mele-hubbard model. *Phys. Rev. B*, 85:045123, Jan 2012. doi: 10.1103/PhysRevB.85.045123. URL https://link.aps.org/doi/10.1103/PhysRevB.85.045123.

[196] Joel Hutchinson, Philipp W. Klein, and Karyn Le Hur. Analytical approach for the mott transition in the kane-mele-hubbard model. *Phys. Rev. B*, 104:075120, Aug 2021. doi: 10.1103/PhysRevB.104.075120. URL https://link.aps.org/doi/10.1103/PhysRevB.104.075120.

[197] M. Hohenadler, T. C. Lang, and F. F. Assaad. Correlation effects in quantum spin-hall insulators: A quantum monte carlo study. *Phys. Rev. Lett.*, 106:100403, Mar 2011. doi: 10.1103/PhysRevLett.106.100403. URL https://link.aps.org/doi/10.1103/PhysRevLett.106.100403.

[198] M. Hohenadler, Z. Y. Meng, T. C. Lang, S. Wessel, A. Muramatsu, and F. F. Assaad. Quantum phase transitions in the kane-mele-hubbard model. *Phys. Rev. B*, 85:115132, Mar 2012. doi: 10.1103/PhysRevB.85.115132. URL https://link.aps.org/doi/10.1103/PhysRevB.85.115132.

[199] Stephan Rachel and Karyn Le Hur. Topological insulators and mott physics from the hubbard interaction. *Phys. Rev. B*, 82:075106, Aug 2010. doi: 10.1103/PhysRevB.82.075106. URL https://link.aps.org/doi/10.1103/PhysRevB.82.075106.

[200] Johannes Reuther, Ronny Thomale, and Stephan Rachel. Magnetic ordering phenomena of interacting quantum spin hall models. *Phys. Rev. B*, 86:155127, Oct 2012. doi: 10.1103/PhysRevB.86.155127. URL https://link.aps.org/doi/10.1103/PhysRevB.86.155127.

[201] Shun-Li Yu, X. C. Xie, and Jian-Xin Li. Mott physics and topological phase transition in correlated dirac fermions. *Phys. Rev. Lett.*, 107:010401, Jun 2011. doi: 10.1103/PhysRevLett.107.010401. URL https://link.aps.org/doi/10.1103/PhysRevLett.107.010401.

[202] Dong Zheng, Guang-Ming Zhang, and Congjun Wu. Particle-hole symmetry and interaction effects in the kane-mele-hubbard model. *Phys. Rev. B*, 84:205121, Nov 2011. doi: 10.1103/PhysRevB.84.205121. URL https://link.aps.org/doi/10.1103/PhysRevB.84.205121.

[203] Wei Wu, Stephan Rachel, Wu-Ming Liu, and Karyn Le Hur. Quantum spin hall insulators with interactions and lattice anisotropy. *Phys. Rev. B*, 85:205102, May 2012. doi: 10.1103/PhysRevB.85.205102. URL https://link.aps.org/doi/10.1103/PhysRevB.85.205102.

[204] Manuel Laubach, Johannes Reuther, Ronny Thomale, and Stephan Rachel. Rashba spin-orbit coupling in the kane-mele-hubbard model. *Phys. Rev. B*, 90:165136, Oct 2014. doi: 10.1103/PhysRevB.90.165136. URL https://link.aps.org/doi/10.1103/PhysRevB.90.165136.

[205] Hsiang-Hsuan Hung, Lei Wang, Zheng-Cheng Gu, and Gregory A. Fiete. Topological phase transition in a generalized kane-mele-hubbard model: A combined quantum monte carlo and green's function study. *Phys. Rev. B*, 87:121113, Mar 2013. doi: 10.1103/PhysRevB.87.121113. URL https://link.aps.org/doi/10.1103/PhysRevB.87.121113.

[206] Markus Richter, Johannes Graspeuntner, Thomas Schäfer, Nils Wentzell, and Markus Aichhorn. Comparing the effective enhancement of local and nonlocal spin-orbit couplings on honeycomb lattices due to strong electronic correlations. *Phys. Rev. B*, 104:195107, Nov 2021. doi: 10.1103/PhysRevB.104.195107. URL https://link.aps.org/doi/10.1103/PhysRevB.104.195107.

[207] Peizhi Mai, Jinchao Zhao, Benjamin E. Feldman, and Philip W. Phillips. 1/4 is the new 1/2: Interaction-induced unification of quantum anomalous and spin hall effects, 2023.

[208] M Hohenadler and F F Assaad. Correlation effects in two-dimensional topological insulators. *Journal of Physics: Condensed Matter*, 25(14):143201, mar 2013. doi: 10.1088/0953-8984/25/14/143201. URL https://dx.doi.org/10.1088/0953-8984/25/14/143201.

[209] Stephan Rachel. Interacting topological insulators: a review. *Reports on Progress in Physics*, 81(11):116501, oct 2018. doi: 10.1088/1361-6633/aad6a6. URL https://dx.doi.org/10.1088/1361-6633/aad6a6.

[210] ZI YANG MENG, HSIANG-HSUAN HUNG, and THOMAS C. LANG. The characterization of topological properties in quantum monte carlo simulations of the kane–mele–hubbard model. *Modern Physics Letters B*, 28(01):1430001, 2014. doi: 10.1142/S0217984914300014. URL https://doi.org/10.1142/S0217984914300014.

[211] Youhei Yamaji and Masatoshi Imada. Mott physics on helical edges of two-dimensional topological insulators. *Phys. Rev. B*, 83:205122, May 2011. doi: 10.1103/PhysRevB.83.205122. URL https://link.aps.org/doi/10.1103/PhysRevB.83.205122.

[212] Tsuneya Yoshida and Norio Kawakami. Topological edge mott insulating state in two dimensions at finite temperatures: Bulk and edge analysis. *Phys. Rev. B*, 94:085149, Aug 2016. doi: 10.1103/PhysRevB.94.085149. URL https://link.aps.org/doi/10.1103/PhysRevB.94.085149.

[213] Onur Hosten and Paul Kwiat. Observation of the spin hall effect of light via weak measurements. *Science*, 319(5864):787–790, 2008. doi: 10.1126/science.1152697. URL https://www.science.org/doi/abs/10.1126/science.1152697.

[214] M. C. Beeler, R. A. Williams, K. Jiménez-García, L. J. LeBlanc, A. R. Perry, and I. B. Spielman. The spin hall effect in a quantum gas. *Nature*, 498(7453):201–204, Jun 2013. ISSN 1476-4687. doi: 10.1038/nature12185. URL https://doi.org/10.1038/nature12185.

[215] M. Aidelsburger, M. Atala, M. Lohse, J. T. Barreiro, B. Paredes, and I. Bloch. Realization of the hofstadter hamiltonian with ultracold atoms in optical lattices. *Phys. Rev. Lett.*, 111:185301, Oct 2013. doi: 10.1103/PhysRevLett.111.185301. URL https://link.aps.org/doi/10.1103/PhysRevLett.111.185301.

[216] Zui Tao, Bowen Shen, Wenjin Zhao, Nai Chao Hu, Tingxin Li, Shengwei Jiang, Lizhong Li, Kenji Watanabe, Takashi Taniguchi, Allan H. MacDonald, Jie Shan, and Kin Fai Mak. Giant spin hall effect in ab-stacked mote2/wse2 bilayers, 2023.

[217] Andreas Roth, Christoph Brüne, Hartmut Buhmann, Laurens W. Molenkamp, Joseph Maciejko, Xiao-Liang Qi, and Shou-Cheng Zhang. Nonlocal transport in the quantum spin hall state. *Science*, 325(5938):294–297, 2009. doi: 10.1126/science.1174736. URL https://www.science.org/doi/abs/10.1126/science.1174736.

[218] Tingxin Li, Pengjie Wang, Hailong Fu, Lingjie Du, Kate A. Schreiber, Xiaoyang Mu, Xiaoxue Liu, Gerard Sullivan, Gábor A. Csáthy, Xi Lin, and Rui-Rui Du. Observation of a helical luttinger liquid in InAs/GaSb quantum spin hall edges. *Phys. Rev. Lett.*, 115:136804, Sep 2015. doi: 10.1103/PhysRevLett.115.136804. URL https://link.aps.org/doi/10.1103/PhysRevLett.115.136804.

[219] Ivan Knez, Rui-Rui Du, and Gerard Sullivan. Evidence for helical edge modes in inverted InAs/GaSb quantum wells. *Phys. Rev. Lett.*, 107:136603, Sep 2011. doi: 10.1103/PhysRevLett.107.136603. URL https://link.aps.org/doi/10.1103/PhysRevLett.107.136603.

[220] Sanfeng Wu, Valla Fatemi, Quinn D. Gibson, Kenji Watanabe, Takashi Taniguchi, Robert J. Cava, and Pablo Jarillo-Herrero. Observation of the quantum spin hall effect up to 100 kelvin in a monolayer crystal. *Science*, 359(6371):76–79, 2018. doi: 10.1126/science.aan6003. URL https://www.science.org/doi/abs/10.1126/science.aan6003.

[221] Shujie Tang, Chaofan Zhang, Dillon Wong, Zahra Pedramrazi, Hsin-Zon Tsai, Chunjing Jia, Brian Moritz, Martin Claassen, Hyejin Ryu, Salman Kahn, Juan Jiang, Hao Yan, Makoto Hashimoto, Donghui Lu, Robert G. Moore, Chan-Cuk Hwang, Choongyu Hwang, Zahid Hussain, Yulin Chen, Miguel M. Ugeda, Zhi Liu, Xiaoming Xie, Thomas P. Devereaux, Michael F. Crommie, Sung-Kwan Mo, and Zhi-Xun Shen. Quantum spin hall state in monolayer 1t'-wte2. *Nature Physics*, 13(7):683–687, Jul 2017. ISSN 1745-2481. doi: 10.1038/nphys4174. URL https://doi.org/10.1038/nphys4174.

[222] Zaiyao Fei, Tauno Palomaki, Sanfeng Wu, Wenjin Zhao, Xinghan Cai, Bosong Sun, Paul Nguyen, Joseph Finney, Xiaodong Xu, and David H. Cobden. Edge conduction in monolayer wte2. *Nature Physics*, 13(7):677–682, Jul 2017. ISSN 1745-2481. doi: 10.1038/nphys4091. URL https://doi.org/10.1038/nphys4091.

[223] James L. Collins, Anton Tadich, Weikang Wu, Lidia C. Gomes, Joao N. B. Rodrigues, Chang Liu, Jack Hellerstedt, Hyejin Ryu, Shujie Tang, Sung-Kwan Mo, Shaffique Adam, Shengyuan A. Yang, Michael S. Fuhrer, and Mark T. Edmonds. Electric-field-tuned topological phase transition in ultrathin na3bi. *Nature*, 564(7736):390–394, Dec 2018. ISSN 1476-4687. doi: 10.1038/s41586-018-0788-5. URL https://doi.org/10.1038/s41586-018-0788-5.

[224] J. O. Island, X. Cui, C. Lewandowski, J. Y. Khoo, E. M. Spanton, H. Zhou, D. Rhodes, J. C. Hone, T. Taniguchi, K. Watanabe, L. S. Levitov, M. P. Zaletel, and A. F. Young. Spin–orbit-driven band inversion in bilayer graphene by the van der waals proximity effect. *Nature*, 571 (7763):85–89, Jul 2019. ISSN 1476-4687. doi: 10.1038/s41586-019-1304-2. URL https://doi.org/10.1038/s41586-019-1304-2.

[225] Philipp Eck, Carmine Ortix, Armando Consiglio, Jonas Erhardt, Maximilian Bauernfeind, Simon Moser, Ralph Claessen, Domenico Di Sante, and Giorgio Sangiovanni. Real-space obstruction in quantum spin hall insulators. *Phys. Rev. B*, 106:195143, Nov 2022. doi: 10.1103/PhysRevB.106.195143. URL https://link.aps.org/doi/10.1103/PhysRevB.106.195143.

[226] Maximilian Bauernfeind, Jonas Erhardt, Philipp Eck, Pardeep K. Thakur, Judith Gabel, Tien-Lin Lee, Jörg Schäfer, Simon Moser, Domenico Di Sante, Ralph Claessen, and Giorgio Sangiovanni. Design and realization of topological dirac fermions on a triangular lattice. *Nature Communications*, 12(1):5396, Sep 2021. ISSN 2041-1723. doi: 10.1038/s41467-021-25627-y. URL https://doi.org/10.1038/s41467-021-25627-y.

[227] Cedric Schmitt, Jonas Erhardt, Philipp Eck, Matthias Schmitt, Kyungchan Lee, Tim Wagner, Philipp Keßler, Martin Kamp, Timur Kim, Cephise Cacho, Tien-Lin Lee, Giorgio Sangiovanni, Simon Moser, and Ralph Claessen. Stabilizing an atomically thin quantum spin hall insulator at ambient conditions: Graphene-intercalation of indenene, 2023.

[228] R. Nourafkan and A.-M. S. Tremblay. Hall and faraday effects in interacting multiband systems with arbitrary band topology and spin-orbit coupling. *Phys. Rev. B*, 98:165130, Oct 2018. doi: 10.1103/PhysRevB.98.165130. URL https://link.aps.org/doi/10.1103/PhysRevB.98.165130.

[229] A.-M. S. Tremblay. private communication, 2023.

[230] William Witczak-Krempa, Michael Knap, and Dmitry Abanin. Interacting weyl semimetals: Characterization via the topological hamiltonian and its breakdown. *Physical Review Letters*, 113(13): 136402, Sep 2014. doi: 10.1103/PhysRevLett.113.136402.

[231] David Vanderbilt. *Berry Phases in Electronic Structure Theory: Electric Polarization, Orbital Magnetization and Topological Insulators*. Cambridge University Press, 2018. doi: 10.1017/9781316662205.

[232] Shiing-Shen Chern. A simple intrinsic proof of the gauss-bonnet formula for closed riemannian manifolds. *Annals of Mathematics*, 45(4):747–752, 1944. ISSN 0003486X. URL http://www.jstor.org/stable/1969302.

[233] Zhong Wang and Shou-Cheng Zhang. Simplified topological invariants for interacting insulators. *Phys. Rev. X*, 2:031008, Aug 2012. doi: 10.1103/PhysRevX.2.031008. URL https://link.aps.org/doi/10.1103/PhysRevX.2.031008.

[234] Tsuneya Yoshida, Satoshi Fujimoto, and Norio Kawakami. Correlation effects on a topological insulator at finite temperatures. *Phys. Rev. B*, 85:125113, Mar 2012. doi: 10.1103/PhysRevB.85.125113. URL https://link.aps.org/doi/10.1103/PhysRevB.85.125113.

[235] A. A. Markov, G. Rohringer, and A. N. Rubtsov. Robustness of the topological quantization of the hall conductivity for correlated lattice electrons at finite temperatures. *Phys. Rev. B*, 100: 115102, Sep 2019. doi: 10.1103/PhysRevB.100.115102. URL https://link.aps.org/doi/10.1103/PhysRevB.100.115102.